



TECHNISCHE UNIVERSITÄT MÜNCHEN

Physik Department

Lehrstuhl für Topologie Korrelierter Systeme

**Investigation of
Antiferromagnetic Superstructures
in Rare-Earth Compounds**

Dipl.-Phys. Univ. Wolfgang Simeth

Vollständiger Abdruck der von der
Fakultät für Physik der Technischen Universität München
zur Erlangung des akademischen Grades eines

Doktors der Naturwissenschaften (Dr. rer. nat.)

genehmigten Dissertation.

Vorsitzender: Prof. Dr. Johannes Knolle

Prüfer der Dissertation: 1. Prof. Christian Pfleiderer, Ph.D.
2. Priv.-Doz. Dr. Hans-Gregor Hübl

Die Dissertation wurde am 19.11.2019 an der Technischen Universität München
eingereicht und durch die Fakultät für Physik am 06.12.2019 angenommen.

Contents

1. Motivation	1
2. Experimental Methods	3
2.1. Neutron Diffraction	3
2.1.1. Nuclear Scattering	3
2.1.2. Magnetic Scattering	4
2.2. Magnetic Structure Determination	7
2.2.1. Fourier Decomposition of a Magnetic Structure	8
2.2.2. Experimental Determination of the Irreducible Representations	11
2.2.3. Multiple Periodic Structures	12
2.3. Single Crystalline Samples	14
3. Magnetic Superstructures in Rare-Earth Copper Compounds	17
3.1. Introduction to Rare-Earth Intermetallics	17
3.2. Properties of $(\pi\pi_0)$ Antiferromagnets	22
3.3. The Compound HoCu	27
3.3.1. Introduction to HoCu	27
3.3.2. Objectives and Outline	33
3.3.3. Neutron Diffraction in Zero Magnetic Field	36
3.3.4. Neutron Diffraction in Magnetic Fields	71
3.3.5. Magnetic Structures in Zero Magnetic Field	107
3.3.6. Topological and Geometric Properties	121
3.3.7. The Conduction Electrons	141
3.4. The Compound TmCu	153
3.4.1. Introduction to TmCu	153
3.4.2. Magnetic Propagation Vectors in Zero Magnetic Field	156
3.4.3. Neutron Diffraction in Magnetic Fields	159
3.5. The Compound ErCu	171
3.5.1. Introduction to ErCu	171
3.5.2. Neutron Diffraction Study	175
3.6. Summary and Outlook	199

4. Incommensurate Antiferromagnetism in EuPtSi₃	203
4.1. Introduction to EuPtSi ₃	203
4.2. Magnetic Long-Range Order in Zero Magnetic Field	206
4.2.1. Magnetic Propagation Vectors	206
4.2.2. Representational Analysis for Magnetic Structures	211
4.2.3. Magnetic Structure Determination	212
4.3. Summary, Outlook and Open Questions	219
5. Conclusions	221
A. Appendix	223
A.1. Magnetic Structure Factors in the RCu Compounds	223
A.2. Polarization Matrices in the RCu Compounds	225
A.3. Stoke's Theorem for Chern Numbers	229
A.4. Neutron Diffraction on HoCu with Magnetic Field along Twofold Directions	231
A.5. Neutron Diffraction on TmCu with Field along Twofold Directions	233
Bibliography	235
List of publications	253
Acknowledgements	255

1. Motivation

The ideas of topology were adapted in the field of condensed matter physics in the nineteen seventies, prominently through the famous works of Kosterlitz and Thouless [1, 2], and were employed in a series of seminal studies, e.g., by Thouless *et al.* in order to explain the quantization of the Hall conductance in a two dimensional electron gas [3] or by Haldane in order to derive a theory for spin chains [4, 5]. The concepts of topology not only are of high importance for the theoretical understanding of phase transitions, but also for applications, as states of matter with nontrivial topology often offer remarkable material properties.

The Skyrmion lattice in MnSi [6] is an intensively investigated example for such a state of matter with non-trivial topology. In the Skyrmion lattice phase the magnetic moments form a hexagonal lattice of whirls, which are topologically protected against unwinding into a conventional ferromagnet. The Skyrmion lattice is a multi- k structure that may be approximated by a superposition of three helices (cf. Ref. [7]), as reflected by a sixfold pattern in neutron diffraction [6]. Establishing the multi- k nature of the Skyrmion lattice, in contrast to a putative state consisting of multiple domains of a single- k structure, requires a sophisticated study of higher harmonics [8] or the study of the topological Hall effect [9], the latter of which arises as a direct consequence of the emergent electrodynamics associated with the nontrivial topology of the magnetic ground state [10]. Skyrmion lattice phases arise in a wide range of cubic chiral magnets, regardless whether they are metallic [6], semiconducting [11], or insulating [12]. In these noncentrosymmetric compounds the stabilization of Skyrmion lattice order is based on a hierarchy of energies [13] comprising exchange interactions, Dzyaloshinski-Moriya interactions [14, 15], and magnetocrystalline anisotropies. Rather recently, topologically nontrivial magnetic structures were also detected in substances such as GaV₄S₈ [16] or tetragonal Heusler materials [17], where other stabilization mechanisms play a role.

In this thesis, we investigate a new class of materials as possible host for ground states with nontrivial topology. First, the centrosymmetric cubic rare-earth intermetallics HoCu, TmCu, and ErCu, in which a complex magnetic phase diagram arises from competing interactions rather than a hierarchy of energy scales are studied. Despite the lack of Dzyaloshinski-Moriya interactions, transport measurements suggested the emergence of

magnetic ground states possessing nontrivial topology (cf. Ref. [18]). Second, the noncentrosymmetric compound EuPtSi_3 , where Dzyaloshinski-Moriya interactions presumably favor cycloidal modulations, is studied. Again transport measurements, supported by early neutron experiments, suggested the emergence of antiferromagnetic multi- k order with nontrivial topology (cf. Ref. [19]).

In this work, microscopic studies of the four compounds are presented. Therefore, magnetic ground states were determined by means of single-crystal neutron diffraction. A particular concern was the identification of multi- k structures. In all four compounds we detected antiferromagnetic superstructures. The identified structures were studied with respect to their topological properties and their interplay with the electronic structure.

Outline of the thesis

The thesis is organized as follows. In the first chapter (Sec. 2), experimental techniques are introduced. It is explained, how magnetic ground states may be determined by means of neutrons, and how multi- k structures may be distinguished from multi-domain states of single- k structures. The second chapter (Sec. 3) is devoted to the intermetallic compounds RCu . Comprehensive studies of the compounds HoCu , TmCu , and ErCu are presented. As the main results of our microscopic studies we identified multitudinous magnetic ground states, including multi- k states, structures with nontrivial topology, structures that are modulated with a large wavelength in real-space, and structures that give rise to a complex electronic structure. In the third chapter (Sec. 4), we present a microscopic study of the compound EuPtSi_3 . We identified a multi- k state with long wavelength in real-space, which may possibly be portrayed as a lattice of antiferromagnetic Skyrmions. In the last chapter (Sec. 5), a conclusion of the thesis is drawn.

2. Experimental Methods

Neutron scattering is a powerful tool in experimental condensed matter physics to study microscopic properties of materials. In this thesis it is used to study antiferromagnetic ground states (cf. Ref. [20]) of relatively localized $4f$ ions in rare-earth compounds. In the following chapter it is explained, how magnetic ground states may be determined by means of neutrons. Furthermore, it is established, how multi- k states may be identified.

The chapter is organized as follows. First, the properties of nuclear Bragg scattering and magnetic Bragg scattering are introduced in Sec. 2.1. Second, concepts required for magnetic structure determinations are presented in Sec. 2.2. It is addressed, how multi- k states may be distinguished from single- k states. Third, an overview of the single-crystalline samples that were used for our neutron experiments is given in Sec. 2.3.

2.1. Neutron Diffraction

In the following, the basic concepts of neutron scattering from crystal structures, i.e., nuclear Bragg scattering, as well as from static magnetic ground states are presented. Comprehensive introductions into these topics are, e.g., found in Refs. [21, 22].

2.1.1. Nuclear Scattering

The compounds studied in this thesis represent crystalline solids [23]. Their crystal structure may be described by means of a Bravais lattice together with an atomic basis [24]. Neutrons couple to the nuclei on the lattice and may be scattered. The interaction between an incoming neutron of mass m and a nucleus is typically described in terms of a point-like Fermi pseudopotential $V(\mathbf{x}) = \frac{2\pi\hbar^2}{m}b \cdot \delta(\mathbf{x})$ [23]. The scattering lengths b for specific nuclei are, e.g., listed in Ref. [25]. Due to the periodicity of the crystalline structure, constructive interference with material specific structure factors results in nuclear Bragg scattering.

The cross section for coherent, elastic Bragg scattering from a Bravais lattice with an atomic basis, as derived in first-order perturbation theory, i.e., in the Born approximation (cf. Ref. [22]), using Fermi's golden rule [26], is given by [22]:

$$\left(\frac{d\sigma}{d\Omega}\right)_{\text{coh,el}} = N \frac{(2\pi)^3}{\nu_0} \sum_{\mathbf{G}} \delta(\boldsymbol{\kappa} - \mathbf{G}) |F_N(\boldsymbol{\kappa})|^2, \quad (2.1)$$

where N is the number of unit cells and ν_0 the volume of a unit cell. The nuclear structure factor $F_N(\boldsymbol{\kappa}) = \sum_{\mathbf{d}} \bar{b}_{\mathbf{d}} \exp(i\boldsymbol{\kappa} \cdot \mathbf{d}) \exp(-W_{\mathbf{d}})$ in the cross-section is calculated from the nuclei in one unit cell. As the nuclei in the crystal are assumed to be point-like, the structure factor is not q -dependent. The Debye Waller factor $W_{\mathbf{d}}$, which decreases as a function of q , describes the change of the cross section as a function of temperature [24, 27, 28].

Due to the term $\sum_{\mathbf{G}} \delta(\boldsymbol{\kappa} - \mathbf{G})$ in the nuclear cross section, each reciprocal lattice vector \mathbf{G} gives rise to a nuclear scattering process [24]. The condition for constructive interference can be expressed in terms of the Laue condition $\mathbf{k}_f - \mathbf{k}_i = \mathbf{G}$ [24] or the Bragg condition, which has the form $2d \sin(\theta) = \lambda$. In this thesis, Bragg's law for a scattering process with wave vector $\mathbf{G} = \mathbf{G}_{h,k,l} = (h, k, l)$ is used in the following form $2d_{hkl} \sin(\theta) = \lambda$ (cf. Ref. [24]). The distance of adjacent lattice planes $d_{hkl} = \frac{2\pi}{|\mathbf{G}_{h,k,l}|}$ for certain Bravais lattices is given by:

$$\frac{1}{d_{hkl}} = \frac{\sqrt{h^2 + k^2 + l^2}}{a} \quad (\text{cubic}) \quad (2.2)$$

$$\frac{1}{d_{hkl}} = \sqrt{\frac{h^2 + k^2}{a^2} + \frac{l^2}{c^2}} \quad (\text{tetragonal}) \quad (2.3)$$

2.1.2. Magnetic Scattering

The compounds studied in this thesis host antiferromagnetic long-range order of rare-earth ions, which may be portrayed as relatively localized moments. As neutrons also carry a magnetic moment, they may interact both with orbital and spin contributions of $4f$ moments of the rare earths [21]. Accordingly, neutrons prove useful for the investigation of the magnetic ground states and the spectrum of magnetic excitations. In particular, neutrons prove useful for the study of antiferromagnets, which was first demonstrated by Shull *et al.* [29].

The magnetic moment of a neutron may be described in terms of the operator $\boldsymbol{\mu}_n = -\gamma \cdot \frac{e\hbar}{2m_p} \boldsymbol{\sigma}$, where m_p is the mass of a proton, e its charge, γ is a positive constant, where $\gamma = 1.913$, and $\boldsymbol{\sigma}$ the vector of Pauli matrices.

Coherent, elastic Bragg scattering from a magnetic structure \mathbf{S} may be expressed in terms of a cross section given by [22]:

$$\left(\frac{d\sigma}{d\Omega}\right)_{\text{el}} = (\gamma r_0)^2 N \left\{ \frac{1}{2} g F_M(\boldsymbol{\kappa}) \right\}^2 \exp(-2W) \sum_{\alpha, \beta} \left(\delta_{\alpha\beta} - \frac{\kappa_\alpha \kappa_\beta}{\kappa^2} \right) \cdot \sum_{\mathbf{R}_1, \mathbf{R}_2} \exp(i\boldsymbol{\kappa} \cdot (\mathbf{R}_1 - \mathbf{R}_2)) \langle \mathbf{S}_{\mathbf{R}_1}^\alpha \rangle \langle \mathbf{S}_{\mathbf{R}_2}^\beta \rangle. \quad (2.4)$$

Here, r_0 is the classical radius of an electron and g is the Landé splitting factor. The factor $\left(\delta_{\alpha\beta} - \frac{\kappa_\alpha \kappa_\beta}{\kappa^2}\right)$ is typically referred to as polarization factor. As for the nuclear cross section, the magnetic cross section in Eq. (2.4) is derived in first-order perturbation theory. In particular, the cross section does not distinguish between single- k structures with equally populated domains and multi- k structures, which consist of the same wave-vector type as the single- k structure.

In contrast to nuclear scattering, magnetic scattering is strongly q -dependent, resulting in a non constant form factor $F_M(\boldsymbol{\kappa})$ that vanishes asymptotically in the limit of backscattering, i.e., when $\sin(\theta)/\lambda \rightarrow \frac{1}{\lambda}$. The form factor for $4f$ ions, which have both spin and orbital contributions, may be described in the dipole approximation as follows [30]:

$$F_M(\boldsymbol{\kappa}) = \langle j_0 \rangle + \left(1 - \frac{2}{g}\right) \langle j_2 \rangle. \quad (2.5)$$

The Lande g factor for rare-earth ions may be calculated by means of Hund's rules [30]. Explicit analytic approximations of $\langle j_1 \rangle$ and $\langle j_2 \rangle$ as a function of $s = \frac{\sin(\theta)}{\lambda}$ are given by [31]:

$$\langle j_0(s) \rangle = A \exp(-as^2) + B \exp(-bs^2) + C \exp(-cs^2) + D \quad (2.6)$$

$$\langle j_2(s) \rangle = As^2 \exp(-as^2) + Bs^2 \exp(-bs^2) + Cs^2 \exp(-cs^2) + Ds^2. \quad (2.7)$$

The coefficients A, B, \dots, a, b, \dots are summarized for a multitude of different atoms in Ref. [25].

An important property of neutron scattering from magnetic order is the dependence of the scattered neutron polarization on the magnetic structure. Hence, an analysis of spin-flip and non-spin-flip ratios of different directions of the polarization for a Bragg scattering process may provide detailed information about a magnetic ground state (cf. Refs. [32, 33]).

In the following it is addressed, how the scattered neutron polarization may be calculated, when the magnetic structure as well as the incoming neutron polarization are known. In this work, neutron experiments are carried out with an incoming neutron beam that is, as possible as it gets, fully polarized $\sim |\mathbf{P}_i| = 1$ along a certain direction

\mathbf{e}_n . Detailed introductions how to mathematically describe a polarized beam may, e.g., be found in Refs. [21, 34].

For a Bragg scattering process \mathbf{Q} from a given magnetic structure \mathbf{m} , the (final) polarization \mathbf{P}_f of the scattered beam may be calculated by means of the Blume-Maleev equations [35, 36]. One therefore defines $\mathbf{M}_\perp = \hat{\mathbf{Q}} \times (\mathbf{M}(\mathbf{Q}) \times \hat{\mathbf{Q}})$, where

$$\mathbf{M}(\mathbf{Q}) = \int \mathbf{m}(\mathbf{R}) \cdot \exp(-i\mathbf{Q} \cdot \mathbf{R}) d^3R. \quad (2.8)$$

As is common for polarization studies with neutrons, Cartesian coordinates are defined with respect to the scattering vector, such that \hat{e}_z is vertical, $\hat{e}_x \parallel \hat{\mathbf{Q}}$ and $\hat{e}_y = \hat{e}_z \times \hat{e}_x$. The polarization of the scattered beam is calculated by means of the Blume-Maleev equations as follows:

$$\mathbf{P}_f = \tilde{P}\mathbf{P}_i + \mathbf{P}'', \quad (2.9)$$

where

$$\tilde{P} = \begin{pmatrix} \frac{1}{I_x} (N - |M_\perp|^2) & \frac{i}{I_x} \cdot J_n^z & \frac{i}{I_x} \cdot J_n^y \\ -\frac{i}{I_y} \cdot J_n^z & \frac{1}{I_y} (N^2 + |M_{\perp y}|^2 - |M_{\perp z}|^2) & \frac{1}{I_y} R_{yz} \\ -\frac{1}{I_z} \cdot J_{ny} & \frac{1}{I_z} \cdot R_{zy} & \frac{1}{I_z} (N^2 - |M_{\perp y}|^2 + |M_{\perp z}|^2) \end{pmatrix} \quad (2.10)$$

and

$$\mathbf{P}'' = \begin{pmatrix} -\frac{1}{I} \cdot J_{yz} \\ \frac{1}{I} \cdot R_{ny} \\ \frac{1}{I} \cdot R_{nz} \end{pmatrix}. \quad (2.11)$$

Therefore the following abbreviations were used:

$$I_x = M^2 + N^2 + \hat{P}_x J_{yz} \quad R_{ij} = 2 \frac{1}{I_x} \text{Re}(M_{\perp i}^* \cdot M_{\perp j}) \quad (2.12)$$

$$I_y = M^2 + N^2 + \hat{P}_y R_{ny} \quad J_{ij} = 2 \frac{1}{I_x} \text{Im}(M_{\perp i}^* \cdot M_{\perp j}) \quad (2.13)$$

$$I_z = M^2 + N^2 + \hat{P}_z R_{nz} \quad R_{ni} = 2 \text{Re}(M_{\perp i}^*) \quad (2.14)$$

$$I = M^2 + N^2 + \hat{P}_x J_{yz} + \hat{P}_y R_{ny} + \hat{P}_z R_{nz} \quad J_{ni} = 2 \text{Im}(M_{\perp i}^*) \quad (2.15)$$

The nuclear-magnetic interference terms R_{ni} and J_{ni} are finite when magnetic intensities coincide with nuclear peak intensities, as is the case for ferromagnetic peaks. The off-diagonal terms R_{yz} are called mixed magnetic terms and the J_{yz} are known as chiral

terms. Comprehensive studies discussing the meaning of each of the contributions may be found in Refs. [33, 37–39].

For purely magnetic scattering processes, the equations reduce to:

$$\sigma \tilde{P} = \begin{pmatrix} -|M_{\perp}|^2 & 0 & 0 \\ 0 & |M_{\perp y}|^2 - |M_{\perp z}|^2 & 2\text{Re}(M_{\perp y}^* \cdot M_{\perp z}) \\ 0 & 2\text{Re}(M_{\perp y}^* \cdot M_{\perp z}) & -|M_{\perp y}|^2 + |M_{\perp z}|^2 \end{pmatrix} \quad (2.16)$$

$$\sigma \mathbf{P}'' = -2\text{Im}(M_{\perp y}^* \cdot M_{\perp z}) \cdot \hat{e}_x, \quad \sigma = |M_{\perp}|^2 + P_{0x} \cdot 2\text{Im}(M_{\perp y}^* \cdot M_{\perp z}) \quad (2.17)$$

At zero magnetic field, the calculated matrices need to be averaged over all possible magnetic domains \mathbf{m}_d :

$$P^c = \langle P_{\mathbf{m}}^c \rangle_d = \sum_{\mathbf{m}_d} r_d \cdot P_{\mathbf{m}}^c \Big|_{\mathbf{m}=\mathbf{m}_d}, \quad (2.18)$$

with $r_d = \sigma_d(\mathbf{Q}) \cdot V_d / \sum_{d'} [V_{d'} \sigma_{d'}(\mathbf{Q})]$, where $V_{d'}$ are the volumes of the domains and $\sigma_{d'}(\mathbf{Q}) = C \cdot F^2(h, k, l)|_{\mathbf{m}=\mathbf{m}_{d'}}$ the structure factor for each domain, as calculated from Eq. (2.4).

In our polarization experiments presented further below, the initial polarization $\mathbf{P}_i = \mathbf{e}_n$ is successively adjusted parallel to \mathbf{e}_x , \mathbf{e}_y , and \mathbf{e}_z , respectively. The scattered (final) polarization \mathbf{P}_f is always analyzed along the same axis as the initial polarization and the corresponding matrix elements are inferred via $P_{nn}^o = |\mathbf{P}_f| / |\mathbf{P}_i|$ for the three directions \mathbf{e}_x , \mathbf{e}_y , and \mathbf{e}_z . Hence, the experiments allow to determine diagonal elements of polarization matrices only. The corresponding matrix P^o is referred to in the text as observed polarization matrix.

2.2. Magnetic Structure Determination

In the following, some basic concepts behind magnetic structure determinations with neutrons are presented. First, basic ideas of representational analysis are introduced. Second, the concepts behind Rietveld refinements and polarization analysis are presented. Third, it is discussed, how multi- k structures may be distinguished from single- k structures by means of neutrons.

There are two common approaches how to perform a magnetic structure determination. One method is based on the theory of Shubnikov space groups (cf. Ref. [40]), the other method, which was used for the studies presented in this thesis, is based on representa-

tional theory [40]. In many cases there is a correspondence between the two methods and same results are obtained. However, there are many cases, such as incommensurate magnetic structures, that cannot be treated with the conventional Shubnikov method [40]. To handle incommensurate structures, the theory of superspace groups, an extended version of the Shubnikov method, has been developed recently [41]. For instance, Refs. [42, 43] discuss the two methods in detail.

A short outline, as given in the following, shall motivate the concepts, which were used for the determination of magnetic structures. In this thesis, we assume that all magnetic ground states may be portrayed as static magnetic structures, which may in a classical sense be described by a vectorfield $\mathbf{m}(\mathbf{R})$ on a spatial lattice [42]. This vectorfield may be decomposed into a Fourier series (cf. Ref. [44]). The wave vectors of the sinusoidal terms in this series are called propagation vectors. As first step of a magnetic structure determination, the magnetic propagation vectors that describe the magnetic ground state have to be determined (cf. Ref. [45]). As second step, the pre-factors of the sinusoidal terms in the Fourier series are determined. Representational theory provides all pre-factors that are allowed by symmetry (cf. Ref. [46]). Rietveld refinements or polarized neutrons may allow to experimentally determine those pre-factors that in fact appear in the Fourier decomposition of the ground state. Third, the number of propagation vectors has to be determined (cf. Ref. [42]). When more than one propagation vectors are involved, a structure is called multi- k [44]. In zero magnetic field, when magnetic domains are in equilibrium, it is difficult to experimentally distinguish between a multi- k state and a multi-domain state of a single- k structure. In this thesis we distinguish the two cases experimentally by symmetry breaking fields and by means of higher-harmonic peaks.

2.2.1. Fourier Decomposition of a Magnetic Structure

The determination of magnetic propagation vectors, which appear in the Fourier decomposition of a magnetic structure, may be highly nontrivial. Typically, magnetic propagation vectors are determined by indexation of magnetic Bragg peaks, which are observed in a neutron diffraction experiment. A propagation vector \mathbf{k}_0 , which has been inferred from a Bragg peak, defines a whole set of Q -positions $[\mathbf{k}_0]_{\sim} = \{\mathbf{k}_0 + \mathbf{G}\}$, which is called k -arm (cf. Ref. [47]). The k -arm contains all Q -positions, which differ from \mathbf{k}_0 by only reciprocal lattice vectors. Accordingly, all Q -positions of a k -arm represent the same propagation vector in the Fourier decomposition and Bragg peaks are present at all Q -position of a k -arm, as long as the polarization factor in the structure factor Eq. (2.4) is not suppressed.

A propagation vector and its arm give rise to a set of other propagation vectors, which is labeled $\{\mathbf{k}_0\}$ and called propagation vector star [47]. The star contains all k -arms of nonequivalent wave vectors, which are obtained from \mathbf{k}_0 by the action of all the elements of the space group G [48]. If magnetic domains are equally populated, Bragg peaks are present at all k -arms of a star. Accordingly, k -arms are sometimes also called k -domains. When dealing with single- k structures, this phrasing may be intuitive. However, it is misleading, when dealing with multi- k structures.

In principle, all k -arms of a star $\{\mathbf{k}\}$ should be considered as possible propagation vectors in the Fourier decomposition of a ground state. Representational theory, which was developed by Bertaut [40], Izyumov [48–50], and others, provides for a given propagation vector \mathbf{k} and a given space group G a decomposition of the magnetic representation into irreducible representations (IRs). Each IR $\Gamma_i(\mathbf{k})$ is related to a set of basis functions $\Psi_\nu^{\mathbf{k}}$ allowed in the Fourier decomposition of a magnetic ground state.

Accordingly, a magnetic structure may be decomposed into a Fourier series of basis functions given by:

$$\mathbf{m}(\mathbf{R}) = \sum_{\mathbf{k}, \nu} \left[C_\nu^{\mathbf{k}} \Psi_\nu^{\mathbf{k}} \exp(i\mathbf{k} \cdot \mathbf{R}) + C_\nu^{-\mathbf{k}} \Psi_\nu^{-\mathbf{k}} \exp(-i\mathbf{k} \cdot \mathbf{R}) \right] \quad (2.19)$$

where the sum is over all basis functions indexed ν and over all k -arms of the corresponding k -vector star $\{\mathbf{k}\}$.

If the sum in Eq. (2.19) goes over a single k -arm, the structure is a single- k structure. A structure, which is a superposition of not conjugated propagation vectors of different arms, represents a multi- k structure [51].

For the study presented in this thesis, we will not distinguish between conjugated k -arms, if an inversion center is present, as explained in the following. The conjugated k -arms $[\mathbf{k}]_\sim$ and $[-\mathbf{k}]_\sim$ belong to the same star, if the space group G has an inversion symmetry center [47]. For some propagation vectors, such as $(\frac{1}{2}, \frac{1}{2}, 0)$, the two arms $[\mathbf{k}]_\sim$ and $[-\mathbf{k}]_\sim$ are equivalent, i.e., they represent the same k -arm. However, for incommensurate propagation vectors the arms $[\mathbf{k}]_\sim$ and $[-\mathbf{k}]_\sim$ are nonequivalent, i.e., they represent different arms of the star $\{\mathbf{k}\}$. Note, that a Fourier series of a ground state, which contains \mathbf{k} , also contains $-\mathbf{k}$. This follows from the fact that $\mathbf{m}(\mathbf{R})$ must be real-valued implying $C_\nu^{-\mathbf{k}} = (C_\nu^{\mathbf{k}})^*$ for the mixing coefficients in Eq. (2.19). Accordingly, also the magnetic structure factor, as measured in a scattering experiment, is equivalent on conjugated k -arms.

As we will not distinguish between conjugated k -arms, such as $[\mathbf{k}]_\sim$ and $[-\mathbf{k}]_\sim$, we may identify them as a single set $A = [\mathbf{k}]_\sim \cup [-\mathbf{k}]_\sim$. Such unions of conjugated k -arms will be called Ω -arms. When dealing with incommensurate structures in this thesis, the

Ω -arms will also be referred to as arms or wave-vector arms. The number of Ω -arms of a star determines, how many different propagation vectors a multi- k structure may have, as explained in the following.

A multi- k structure with propagation vectors of a single star may have at most $\mathcal{N}(\mathbf{k})$ different propagation vectors, where $\mathcal{N}(\mathbf{k})$ is the number of (not conjugated) k -arms of the star $\{\mathbf{k}\}$ (cf. Ref. [47]). Accordingly, the maximum number of propagation vectors is given by the number of Ω -arms of a star. For the propagation vector $\mathbf{k} = \left(\frac{1}{2}, \frac{1}{2}, 0\right)$ there are $|\{\mathbf{k}\}| = 3$ different k -arms and they are not conjugated. Accordingly, a structure with propagation vector $\left(\frac{1}{2}, \frac{1}{2}, 0\right)$ may be single- k , double- k , or triple- k . For incommensurate propagation vectors, the number of Ω arms is half of the number of k -arms, which is given by $\mathcal{N}(\mathbf{k}) = |\{\mathbf{k}\}|/2$.

The k -arms, which display finite mixing coefficients $C_\nu^{\mathbf{k}}$ in the Fourier decomposition Eq. (2.19), may be called participating k -arms of the star $\{\mathbf{k}\}$ (cf. Ref. [47]). For a complete magnetic structure determination, the transition channel [47, 52], i.e., all k -arms, which are participating in a magnetic phase transition, have to be figured out.

Note, that in principle, a magnetic ground state may be a superposition of propagation vectors, which belong to different k -stars. A magnetic ground state involving different stars may be automatically multi- k . However, the variety of structures involving several different stars reported in literature is small. As pointed out in Ref. [51] conical structures, which are, for instance, hosted in helimagnets, are an example for magnetic structures involving two wave-vector stars. In this study we report a couple of magnetic ground states involving several different k -stars.

If \mathbf{k} is an incommensurate propagation vector it is instructive to decompose the mixing coefficients into real and imaginary part $C_\nu^{\mathbf{k}} = \alpha_\nu^{\mathbf{k}} + i \cdot \beta_\nu^{\mathbf{k}}$:

$$\mathbf{m}(\mathbf{R}) = \sum_{\mathbf{k}, \nu} 2\Psi_\nu^{\mathbf{k}} \left[\alpha_\nu^{\mathbf{k}} \cos(\mathbf{k}\mathbf{R}) + \beta_\nu^{\mathbf{k}} \sin(\mathbf{k}\mathbf{R}) \right] = \quad (2.20)$$

$$= \sum_{\mathbf{k}, \nu} A_\nu^{\mathbf{k}} \cdot \Psi_\nu^{\mathbf{k}} \cos(\mathbf{k}\mathbf{R} + \delta_\nu^{\mathbf{k}}) \quad (2.21)$$

where

$$A_\nu^{\mathbf{k}} = 2 \cdot \text{sgn}(\alpha_\nu^{\mathbf{k}}) \sqrt{(\alpha_\nu^{\mathbf{k}})^2 + (\beta_\nu^{\mathbf{k}})^2} \quad (2.22)$$

$$\delta_\nu^{\mathbf{k}} = \delta = \arctan\left(-\frac{\beta_\nu^{\mathbf{k}}}{\alpha_\nu^{\mathbf{k}}}\right) \quad (2.23)$$

The decomposition into Bloch waves does not provide any simplification, as it only changed the mathematical parametrization. However, Landau theory implies that only one IR can become critical at each second-order phase transition (cf. Ref. [53]). Hence,

if the ordering temperature possesses second-order origin, only basis functions from one IR may occur in the Fourier decomposition of the magnetic structure in the phase just below the ordering temperature. At each further second-order transition one further IR can become critical. In many cases, magnetic structures follow this rule, even though the transition does not possess second-order origin. In turn, it proves useful to always consider magnetic ground states first, that are related to one IR only.

In this thesis, representational analysis is used as a tool and the analysis itself is carried out by means of the software package *SARAH* [54]. The labelling of IRs follows the conventions introduced by Kovalev [55]. Other crystallographic properties, concerning, e.g., crystallographic stars, are determined by means of the online software ISODISTORT [56]. For further information we refer to literature.

Note that in this thesis, the following conventions are used: Q -positions in the reciprocal space are denoted by letters \mathbf{q} . Propagation vectors are denoted by round brackets, if a specific representative of a k -arm shall be denoted, such as $\mathbf{k}_1 = (\frac{1}{2}, \frac{1}{2}, 0)$. The corresponding k -arm shall be denoted by $[\frac{1}{2}, \frac{1}{2}, 0]_{\sim}$. The star $\{(\frac{1}{2}, \frac{1}{2}, 0)\}$ may also be denoted by $\langle \pi\pi 0 \rangle$.

Note, that some studies do not distinguish between propagation vectors and their arms [44]. In the present thesis, we distinguish between the two cases, as we will perform vector calculations with specific representatives of k -arms.

2.2.2. Experimental Determination of the Irreducible Representations

Neutron diffraction may allow to experimentally determine the irreducible representations, which are associated with a magnetic ground state. In particular, the pre-factors $\sum_{\nu} C_{\nu}^{\mathbf{k}} \Psi_{\nu}^{\mathbf{k}}$ in the Fourier decomposition Eq. (2.19) may be specified.

Let \mathcal{M} be a set containing different physically reasonable ground states $\mathbf{M} \in \mathcal{M}$. The ground states in this set may be associated with different irreducible representations. The structures in $\mathbf{M} \in \mathcal{M}$ may be probed experimentally by means of Rietveld refinements or by means of polarized neutrons. Accordingly, this may allow to experimentally probe the different irreducible representations.

In the following, the two experimental methods are briefly presented:

- **Rietveld Refinements** For a Rietveld refinement, magnetic and nuclear structure factors, i.e., $F_{\mathbf{o}}^2$, are measured using single crystal neutron diffraction. Therefore, a large set of integrated intensities $I(h, k, l)$ of both nuclear and magnetic Bragg reflections may be recorded at a single crystal diffractometer. The observed values

$F_o^2 := I(h, k, l)$ may then be compared with the structure factor $F_c^2(h, k, l)$, calculated for each magnetic structure $\in \mathcal{M}$ by means of Eq. (2.4). Therefore Rietveld refinements [57] are carried out and the free parameters of the magnetic structures are refined by means of least squares fits, such that the values F_c^2 give a good approximation to the values F_o^2 . The goodness of a Rietveld refinement is given by the R -value:

$$R = 100 \cdot \frac{\sum_{\{h,k,l\}} \left(F_o^2(h, k, l) - \frac{1}{c} F_c^2(h, k, l) \right)}{\sum_{\{h,k,l\}} F_o^2(h, k, l)}, \quad (2.24)$$

where c is a scale parameter, optimized such that the R -value is minimized.

- **Polarization Analysis** For the second approach typically a few Bragg peaks are considered only. For each of the chosen Bragg peaks, a polarization matrix $M_o^{\hat{n}}(h, k, l)$ is measured. The entries are inferred from spin-flip and non-spin-flip scattering ratios for various incoming neutron polarizations. In turn, the expected polarization matrices $M_c^{\hat{n}}(h, k, l)$ may be calculated by means of the Blume-Maleev equations for each magnetic structure $\in \mathcal{M}$. The structures may be compared with the experimental data by minimization of $\sum_{\{h,k,l\}} \left\| M_c^{\hat{n}}(h, k, l) - M_o^{\hat{n}}(h, k, l) \right\|$.

In our study, polarization matrices were calculated by means of Mathematica [58]. Rietveld refinements were carried out by means of the Software Jana2006 [59], which is optimized for single-crystal data. The symmetry analysis of Jana2006 is based on Shubnikov space groups and not on representational theory. For this thesis, the symmetry analysis by means of representational theory was simultaneously carried out by means of SARA h [54]. Another prominent refinement software is Fullprof, which is based on representational theory. However it was not used in the present study, as it is optimized for refinements on powder diffraction data [60].

2.2.3. Multiple Periodic Structures

In the following, two strategies are presented, how multi- k structures may be distinguished from single- k structures. In particular, we will consider the case, where two propagation vectors \mathbf{k}_1 and \mathbf{k}_2 , which belong to the same star $\{\mathbf{k}\}$, are superposed to a multi- k structure. In zero magnetic field, where magnetic domains are in equilibrium, there are typically single- k structures, which have the same magnetic structure factor as multi- k structures (Eq. (2.4)). In this case, the fundamental Bragg peaks are the same for the multi- k structure and for the single- k structure.

In order to distinguish, whether two wave vectors \mathbf{k}_1 and \mathbf{k}_2 from the same star form a multi- k state or a multi-domain state, we present the following two methods:

- **Mixed Higher Harmonics**

Multi- k structures may lead to odd mixed higher harmonics [30, 61], which are not present for single- k structures. In particular, for a multi- k structure with two propagation vectors \mathbf{k}_1 and \mathbf{k}_2 , mixed higher harmonics may be present at reciprocal space positions such as $Q = m \cdot \mathbf{k}_1 + n \cdot \mathbf{k}_2$, where $m, n \in \mathbb{Z}$ and $m + n \in 2\mathbb{Z} + 1$. These mixed higher orders are not accounted for by the magnetic structure factor in Eq. (2.4), which was derived in the Born approximation. Accordingly, their scattering intensity may be relatively weak and in experiments it may be difficult to separate real scattering intensities due to higher orders from multiple scattering contributions. Experimentally this may be done, e.g., by Renninger scans [62] or the study of dependences on the neutron wavelength. Higher harmonics were studied, e.g., in the Skyrmion phase of MnSi [8], which may be viewed as a triple- k state, or in the multi- k phase of Neodymium [63, 64].

- **Symmetry Breaking Field**

A multi- k structure, which is a superposition of two propagation vectors \mathbf{k}_1 and \mathbf{k}_2 , has two participating k -arms, which may be labeled $K_1 = [\mathbf{k}_1]_{\sim}$ and $K_2 = [\mathbf{k}_2]_{\sim}$. In order to distinguish this multi- k structure from a single- k structure, it may prove useful to break the symmetry between the two k -arms K_1 and K_2 , either by means of a field along a direction \hat{n} or by means of uniaxial pressure along \hat{n} . When symmetries are broken, a multi- k structure may display a different behavior than a single- k structure [64–66]. Below, we will give a definition of what it means to break the symmetry between k -arms. Equivalent to that, we may define, when two propagation vectors have the same symmetry in a field.

The symmetry between the two k -arms K_1 and K_2 is broken by a field along \hat{n} , if the following condition is fulfilled:

There is neither a reflection nor a rotation operator $\mathcal{O} \in G$, which leaves \hat{n} invariant, i.e., $\mathcal{O}\hat{n} = \hat{n}$, and maps the k -arm K_1 on $\pm K_2$, i.e., $\mathcal{O}K_1 = \pm K_2$.

For propagation-vector arms K_1 and K_2 , for which the symmetry is not broken by a magnetic field, we will use the following phrasing:

- The symmetry between K_1 and K_2 is preserved by the field or in the field.
- The k -arms K_1 and K_2 have the same orientation in the field.

The symmetry between two propagation vectors \mathbf{k}_1 and \mathbf{k}_2 is broken by a field along \hat{n} , if the following condition is fulfilled:

There is neither a reflection nor a rotation operator $\mathcal{O} \in G$, which leaves \hat{n} invariant, i.e., $\mathcal{O}\hat{n} = \hat{n}$, such that there exists a reciprocal lattice vector \mathbf{G} satisfying

$$\mathcal{O}\mathbf{k}_1 = \pm\mathbf{k}_2 + \mathbf{G}.$$

Note, that by these definitions conjugated k -arms have the same orientation in a field.

2.3. Single Crystalline Samples

For the present thesis, neutron experiment were carried out on single crystals. The samples were grown in a zone floating furnace [67] by M. Rahn, M. Wagner, and A. Bauer. Tab. 2.1 gives an overview over all single-crystalline samples studied in this thesis. HoCu, TmCu, and ErCu crystallize in a cubic, EuPtSi₃ in a tetragonal crystal structure. In the following, the geometry of the samples is briefly described:

HoCu

- OFZ95-3-3-h: The sample represents a cuboid $2 \times 2 \times 1\text{mm}^3$. One of the two facets ($2 \times 1\text{mm}^2$) corresponds to a (100) plane, and the other two facets correspond to (110) planes.
- OFZ95-3-2-1-a: The sample resembles a slate cylinder. The top and bottom bases, both of which correspond roughly to (110) planes, are slightly inclined with respect to each other.

TmCu

- OFZ107-2-a: The sample represents a cuboid $2.35 \times 1 \times 3\text{mm}^3$. One of the facets ($3 \times 1\text{mm}^2$) corresponds to a (100) plane, and the other facets to (110) planes.

ErCu

- OFZ104-3-4-1: The sample represents a cuboid $1.75 \times 1.5 \times 1\text{mm}^3$. One of the facets ($1.75 \times 1\text{mm}^2$) corresponds to a (100) plane, the other two facets to (110) planes.
- OFZ104-3-3: The sample has two flat facets. One corresponds to a (100) plane, the other one to a (110) plane

EuPtSi₃

- OFZ97-3-1-cb: The sample represents a cuboid $1 \times 2 \times 0.02\text{mm}^3$. One of the facets ($1 \times 0.02\text{mm}^2$) corresponds to the (001) plane. The other two facets correspond to the planes (110) and ($1\bar{1}0$), respectively.

Sample	Shape
HoCu	
OFZ95-3-3-h	cuboid ($1 \times 2 \times 2 \text{ mm}^3$)
OFZ95-3-2-1	oblique prism with a circle as base ($\sim 0.2 \text{ cm}^3$)
ErCu	
OFZ104-3-4-1	cuboid ($1 \times 1.5 \times 1.75 \text{ mm}^3$)
OFZ104-3-3	no symmetric form ($\sim 0.1 \text{ cm}^3$)
TmCu	
OFZ107-2-a	cuboid ($3 \times 1 \times 2.35 \text{ mm}^3$)
EuPtSi₃	
OFZ97-3-1-cb	cuboid ($2 \times 1 \times 0.02 \text{ mm}^3$)

Table 2.1.: Single-crystal samples of HoCu, ErCu, TmCu, and EuPtSi₃ that were used for the experimental study further below. The samples were grown in a zone floating furnace [67] by M. Rahn, M. Wagner, and A. Bauer.

3. Magnetic Superstructures in Rare-Earth Copper Compounds

In this chapter, we present microscopic studies on the antiferromagnetic compounds HoCu, TmCu, and ErCu. All three materials display a complex magnetic phase diagram arising from competing interactions rather than a hierarchy of energies. Despite the inversion symmetry of the compounds, transport measurements suggested the emergence of ground states possessing non-trivial topology (cf. Ref. [18]). Previous magnetic structure determinations were mainly using neutron powder diffraction and focused on commensurate magnetic ground states [68]. In our study, magnetic structures were determined using single-crystal neutron diffraction. As the main results of our studies we identified a multitude of ground states, including numerous multi- k states, structures with long wavelengths in real-space, and structures with non-trivial topology.

The chapter is organized as follows. First, an introduction to rare-earth intermetallics is given in Sec. 3.1. Second, profound microscopic studies on the three compounds HoCu (Sec. 3.3), TmCu (Sec. 3.4), and ErCu (Sec. 3.5) are presented. The chapter concludes with a summary in Sec. 3.6.

3.1. Introduction to Rare-Earth Intermetallics

We now turn to the rare-earth intermetallics HoCu, TmCu, and ErCu. As explained in the following, the compounds are promising candidate materials for hosting antiferromagnetic ground states with non-trivial topology, even though they are centrosymmetric. Our study, focusing predominantly on the determination of magnetic ground states, was inspired by recently observed unconventional transport properties [18] suggestive of Berry phases that may possibly originate in the topology of magnetic ground states. Furthermore, the three compounds feature complex magnetic properties characteristic of rare-earth intermetallics, such as multi-step magnetism, complex magnetic phase diagrams, and long-wavelength modulations (cf. Ref. [69]). These remarkable properties are suggestive of multitudinous competing interactions and underscore that the rare-earth copper

compounds are a promising playground for detecting novel magnetic ground states, as well as novel mechanisms stabilizing topological ground states.

In the following, key properties of rare-earth copper compounds and rare-earth intermetallics are presented. First, the highly symmetric crystal structures of the compounds and second, their magnetism with high-symmetry points as magnetic propagation vectors, which are typically of type $(\frac{1}{2}, \frac{1}{2}, 0)$ in the rare-earth copper compounds, are discussed. Comments are also made on rare-earth intermetallics in general. Third, the characteristic interactions on the rare-earth ions, which are typically competing in rare-earth intermetallics, are presented. Fourth, specific properties, which are important for the study of $(\pi\pi 0)$ antiferromagnets by means of neutrons, are discussed.

Crystal Structure of Rare-Earth Intermetallics The binary intermetallic compounds HoCu, TmCu, and ErCu crystallize in the cubic CsCl structure, which is related to the centrosymmetric space group $Pm\bar{3}m$. RCu compounds, which range from GdCu to TmCu, occur also in a CsCl structure (cf. Refs. [69, 70]). In contrast, some equiatomic RCu alloys with lighter rare-earths have a FeB structure [69–71]. The two boundary compounds GdCu [72] and TbCu [73] undergo a martensitic transition, whereas all other compounds of the series were reported to have a stable crystal structure [69].

Crystallization in relatively simple crystal structures is characteristic of rare-earth intermetallics. A compound R_0M_0 , where R_0 is a specific rare-earth element and M_0 a metal, often gives rise to a whole series of intermetallic compounds RM_0 , where R may be any other rare-earth atom. The compounds of a series often crystallize in the same crystal structure, as the chemical properties, which are predominantly determined by the outer electron shells, are mainly unaffected over the series of rare-earth elements [71]. Examples are series of compounds such as RCu , RZn , RAg , RZn , RMg [69]. Many of them crystallize in the cubic CsCl structure. The compounds RX_3 , where X is Pb, In, Tl, Pd, Sn, Ga [69], often feature the cubic AuCu₃ structure. An impression of the plethora of intermetallic materials is, e.g., provided by Morin and Schmitt [69] or by Buschow *et al.* giving systematic overviews of, e.g., rare-earth compounds with $3d$ transition metals [74], with non-magnetic metals [71] or with specific elements like aluminum [75].

Magnetic Long-Range Order of Rare-Earth Intermetallics The three compounds HoCu, TmCu, and ErCu establish magnetic long-range order of tripositive rare-earth ions at temperatures below 30 K. All ground states in the three compounds, which have so far been reported, have propagation vectors, which are approximately of type $(\frac{1}{2}, \frac{1}{2}, 0)$ [68, 69]. Accordingly, the ground states are variations of $(\pi\pi 0)$ antiferromagnets (cf. Ref. [76]).

Magnetic propagation vectors in rare-earth intermetallics often correspond to high symmetry points in the reciprocal space, such as the points M, X, and Γ . Which of the high symmetry points in the reciprocal space is favored as magnetic propagation vector in first instance depends on the Fermi energy of the compound. The energy of collinear magnetic structures in a CsCl crystal structure with high symmetry points M, X, and Γ as magnetic propagation vectors may be compared in a simple exchange model (cf. Refs. [68, 77]). In this model, indirect exchange interactions between localised f -electrons are mediated by delocalised electrons through RKKY exchange. As elaborated in Ref. [77], as a function of increasing Fermi energy E_F , first antiferromagnets with \mathbf{k} -vector $(\frac{1}{2}, 0, 0)$ should be favoured, second antiferromagnets with \mathbf{k} -vector $(\frac{1}{2}, \frac{1}{2}, 0)$, and third ferromagnets with \mathbf{k} -vector $(0, 0, 0)$. Although there are many deviations from this result, the model may provide a qualitative explanation for the experimentally observed sequence of propagation vectors in the rare-earth intermetallics RM , where M is non-magnetic and $R = \text{Rh, Ag, Cu, Zn, Mg, Cd}$, when the number of electrons increases [68, 77].

Magnetic Interactions in Rare-Earth Intermetallics A multitude of interactions typically affects magnetic moments in rare-earth intermetallics. A detailed discussion of the magnetic interactions, which may be relevant, is, e.g., found in Refs. [30, 69]. The Hamiltonian describing the magnetic rare-earth ions may be described as follows (cf. Ref. [69, 78]):

$$\mathcal{H} = \mathcal{H}_{\text{CEF}} + \mathcal{H}_{\text{B}} + \mathcal{H}_{\text{Q}} + \mathcal{H}_{\text{ME}} + \mathcal{H}_{\text{Z}}. \quad (3.1)$$

The contributions have the following physical origin:

- **Crystal Electric Field \mathcal{H}_{CEF}**

The crystal electric field (CEF) originates in the surrounding point charges on the lattice [79] and induces single-ion anisotropies. The contribution in the Hamiltonian is usually expressed by means of Stevens operators O_i^m and may in cubic symmetry contain terms up to sixth order. The following conventions are in common:

$$\mathcal{H}_{\text{CEF}} = A_4 \langle r^4 \rangle \beta_J (O_4^0 + 5O_4^4) + A_6 \langle r^6 \rangle \gamma_J (O_6^0 - 21O_6^4) = \quad (3.2)$$

$$= \frac{Wx}{F_4} (O_4^0 + 5O_4^4) + \frac{W(1-|x|)}{F_6} (O_6^0 - 21O_6^4) \quad (3.3)$$

The conventions are taken from Ref. [79] and from Ref. [80], respectively.

- **Bilinear Heisenberg Exchange \mathcal{H}_{B}**

Bilinear exchange interactions between localized moments may in the isotropic form be written as follows:

$$H_B = \sum_{\langle i,j \rangle} J_{ij} \mathbf{J}_i \cdot \mathbf{J}_j \quad (3.4)$$

Since the spatial overlap of $4f$ orbitals is negligible, the exchange constants J_{ij} have vanishingly small contributions from direct $4f$ - $4f$ exchange. Finite contributions arise mainly due to indirect exchange, mediated by conduction electrons [30].

- **Quadrupolar Interactions \mathcal{H}_Q**

In f -electron materials electric multipole interactions as well as multipolar order may play an important role (cf. Ref. [81]). In rare earth compounds electric quadrupoles may interact with each other mostly through two-ion interactions mediated by conduction electrons [82]. Quadrupolar interactions in rare-earth intermetallics were discussed in detail, for instance, in Ref. [69].

- **Magnetoelastic Couplings \mathcal{H}_{ME}**

Magnetoelastic effects, which arise due to couplings between magnetic moments and lattice strains, may be important in rare-earth compounds [30]. An account of magnetoelastic couplings in rare-earth intermetallics is, for instance, found in Ref. [69]. The magnetoelastic Hamiltonian may contain both one-ion contributions \mathcal{H}_{ME1} and two-ion contributions \mathcal{H}_{ME2} [69].

- **Zeeman Energy \mathcal{H}_Z**

The energy of the moments in magnetic fields is accounted for by the ordinary Zeeman term.

Magnetic interactions are often viewed in a hierarchy. Typically, bilinear Heisenberg exchange and crystal electric fields are the dominant interactions that drive magnetic long-range order defining type of propagation vectors and direction of the easy axis, whereas quadrupolar interactions are thought of as small perturbations. However, this simple picture is often insufficient in rare-earth intermetallics. The hierarchy of bilinear exchange, crystal electric fields, and quadrupolar interactions, if even well defined, may be entirely different from compound to compound, as the following examples, including the series RCu , illustrate.

The quadrupolar interactions may, e.g., affect easy axis in a system and hence compete with crystal electric fields. In $DyCd$, crystal electric fields would provide threefold directions as easy axes [83]. However, due to quadrupolar interactions, the fourfold directions are preferred to the threefold directions [83]. In $TmCu$ [84], and possibly also in other RCu compounds, quadrupolar interactions appear strong enough to compete with bilinear exchange. In $TmCd$, the quadrupolar interactions are strong enough to stabilize

quadrupolar order, whereas magnetic order is absent [78]. In TmZn [85], two successive transitions, first a quadrupolar at higher and then a ferromagnetic transition at slightly lower temperature were observed. In dysprosium compounds, bilinear exchange is typically dominant but the quadrupolar interactions may be important to understand the stabilization of magnetic order. In DyZn and DyCd, the stabilization of collinear magnetic structures may be explained by means of positive quadrupolar interactions, whereas in DyAg and DyCu the formation of noncollinear multi- k states may be explained by negative antiferro-quadrupolar interactions [86]. Quadrupolar order, which occurs in TmZn [87], TmCd [78], and CeAg [88] may be ferro-quadrupolar [69], whereas quadrupolar order which occurs in TmGa₃ [89, 90] or PrBb₃ [91] may be antiferro-quadrupolar [69]. In CeB₆ [92], first commensurate antiferro-quadrupolar order is established and then at lower temperatures multi- k magnetic order with the same wave vector as for the multipole-order.

The competition of numerous interactions acting on the $4f$ shell often causes intriguing magnetic properties, like the formation of multi- k magnetic ground states, as e.g., reported in DyCu [93], metamagnetic behaviour, which refers to a transition as a function of field of an antiferromagnet to a state with a large net magnetization [94], multi-step metamagnetic behavior, which may occur in compounds such as DyCu [93], NdIn₃ [95], or DyAg [96], the occurrence of incommensurate magnetic structures, or the interplay of magnetism with quadrupolar interactions [97]. Furthermore, complex magnetic phase diagrams evolve in rare-earth intermetallics [98]. In fact, in rare-earth intermetallics magnetic ground states are typically commensurate at low temperatures in zero magnetic field and become incommensurate just below the Néel temperature T_N and as a function of field [99]. Even the pure rare-earth elements may have rich magnetic properties, like holmium where a helifan structure is established [100] or neodymium [63, 101] which establishing multi- k order has been a riddle over decades [98, 102]. Another prominent material hosting multi- k order in zero magnetic field is CeAl₂, which is still subject on ongoing research [103]. The structure has early been portrayed as triple- k structure [104]. A decade later, Forgan and coworkers argued that the magnetic structure of this centrosymmetric compound is double- k and a non-chiral spiral [105].

The phenomena of numerous competing interactions, complex magnetic phase diagrams, incommensurate modulations with large wavelengths, and the tendency to form canted multi- k structures are promising prerequisites to detect magnetic ground states with non-trivial topology. This possibility of topological states in rare-earth intermetallics has mainly escaped notice, even though the formation of multi- k states has been explicitly considered in early studies (cf. Ref. [69]).

3.2. Properties of $(\pi\pi 0)$ Antiferromagnets

The rare earth copper compounds, which were studied for this thesis, display variations of $(\pi\pi 0)$ antiferromagnetism. In the following, basic properties of $(\pi\pi 0)$ antiferromagnets are discussed.

Antiferromagnets of type $(\pi\pi 0)$ are commensurate and characteristically have magnetic propagation vectors of the star $\left\{\left(\frac{1}{2}, \frac{1}{2}, 0\right)\right\}$. This star, which is often denoted by $\left\langle\frac{1}{2}\frac{1}{2}0\right\rangle$, has three different k -arms [56]. Representatives of these k -arms are, for instance, given by $\mathbf{k}_1^c = \left(\frac{1}{2}, \frac{1}{2}, 0\right)$, $\mathbf{k}_2^c = \left(0, \frac{1}{2}, \frac{1}{2}\right)$, and $\mathbf{k}_3^c = \left(\frac{1}{2}, 0, \frac{1}{2}\right)$. The k -arms may be denoted by $A_1^c := \left[\frac{1}{2}, \frac{1}{2}, 0\right]_{\sim}$, $A_2^c := \left[0, \frac{1}{2}, \frac{1}{2}\right]_{\sim}$, and $A_3^c := \left[\frac{1}{2}, 0, \frac{1}{2}\right]_{\sim}$.

Accordingly, $(\pi\pi 0)$ antiferromagnets may be written in terms of a Fourier series as follows:

$$\mathbf{m}(\mathbf{R}) = \sum_{i=0}^{N_k} \mathbf{r}^T(\mathbf{k}_i^c) \exp(i \cdot \mathbf{k}_i^c \cdot \mathbf{R}) . \quad (3.5)$$

As the $\left\langle\frac{1}{2}\frac{1}{2}0\right\rangle$ star has three k -arms, $(\pi\pi 0)$ antiferromagnets may be single- k , double- k , or triple- k . Note that the single- k , double- k , and triple- k $(\pi\pi 0)$ antiferromagnets, are collinear, coplanar but noncollinear, and noncoplanar, respectively.

There are in principle infinitely many different commensurate $(\pi\pi 0)$ structures. However, in the rare-earth copper compounds a finite set containing 21 structures may be physically reasonable, as explained in the following. As pointed out in Ref. [106], it is instructive to make the two assumptions, namely that the magnetic moments of a commensurate $(\pi\pi 0)$ antiferromagnet:

- have equal modulus on each crystallographic site.
- are all directed along directions within a unique crystallographic star, which is either $\langle 100 \rangle$, $\langle 110 \rangle$ or $\langle 111 \rangle$.

The authors of Ref. [106] argued that the first assumption comes from the minimization of the bilinear exchange term in the case of a high symmetry propagation vector at the border of the Brillouin zone. The second condition may be related to crystal electric fields, which should define a unique direction of easy magnetization. The authors inferred for propagation vectors $\left(\frac{1}{2}, 0, 0\right)$ that there are 21 different antiferromagnetic structures of type $(\pi 00)$ that satisfy the two conditions. The authors pointed out, that the treatment of $(\pi\pi 0)$ structures is entirely analogous.

Tab. 3.1 gives an overview of the 21 commensurate $(\pi\pi 0)$ structures, which fulfill the two conditions (cf. Ref. [18]). Each of the structures in Tab. 3.1 may be defined by the number of propagation vectors, as well as by the pre-factors that are required for the

Fourier decomposition according to Eq. (3.5). Note, that the 21 commensurate structures have the same isotropic bilinear exchange energy [106, 107]. Hence, for the stabilization of specific $(\pi\pi 0)$ structures, the competition of crystal electric fields and quadrupolar interactions may be important.

In this thesis, antiferromagnetic $(\pi\pi 0)$ ground states in rare-earth copper compounds were studied by means of neutrons. In the following, some basic properties of neutron scattering from $(\pi\pi 0)$ antiferromagnets are discussed. In particular, it is addressed, how $(\pi\pi 0)$ ground states may be determined by polarized neutron diffraction at zero magnetic field. Further, the effect of symmetry breaking fields on $(\pi\pi 0)$ antiferromagnets is discussed.

In neutron diffraction from $(\pi\pi 0)$ antiferromagnets, Bragg peaks are characteristically observed at Q -positions, which are related to the star $\left\{\left(\frac{1}{2}, \frac{1}{2}, 0\right)\right\}$. The distinction of $(\pi\pi 0)$ structures by means of neutrons may be difficult, as many of them exhibit the same structure factor (cf. Ref. [108]). The criteria, for two $(\pi\pi 0)$ structures to exhibit the same structure factors in zero magnetic field were discussed in detail by Wintenberger in Ref. [107].

In this thesis, $(\pi\pi 0)$ antiferromagnets were determined by means of Rietveld refinements and by means of polarized neutrons, the latter is explained in the following. For the polarization analysis, we determined the diagonal entries of polarization matrices of scattering processes $\mathbf{Q} = \left(\frac{1}{2}, \frac{1}{2}, 0\right)$ by means of polarized neutron scattering. Therefore, the samples were oriented such that the crystallographic (001) plane corresponded to the scattering plane.

These polarization matrices may also be calculated for the 21 commensurate $(\pi\pi 0)$ structures listed in Tab. 3.1. For the calculation by means of the Blume-Maleev equations all possible domains must be taken into account. The polarization matrices of a Bragg peak located at $\mathbf{Q} = \left(\frac{1}{2}, \frac{1}{2}, 0\right)$ is given by:

$$P = \frac{\sum_d \sigma_d \cdot P_d}{\sum_d \sigma_d} = \begin{pmatrix} -1 & * & * \\ * & \alpha & * \\ * & * & -\alpha \end{pmatrix}. \quad (3.6)$$

The values α for the 21 commensurate $(\pi\pi 0)$ structures are given in Tab. 3.1.

To distinguish multi- k $(\pi\pi 0)$ structures from single- k $(\pi\pi 0)$ structures, we performed neutron experiments under broken symmetries. When symmetries are broken, single- k structures may feature different temperature or field dependences than multi- k structures (cf. Refs. [64, 65]). For our neutron studies, fields were applied along major cubic directions $\langle 100 \rangle$, $\langle 110 \rangle$, and $\langle 111 \rangle$.

In the following, the possible orientations of k -arms (cf. Sec. 2.2.3 for further information) of the $\langle \frac{1}{2}\frac{1}{2}0 \rangle$ star in the presence of fields along major cubic directions are discussed:

- In a field, which is applied along the threefold $[111]$ axis, the three k -arms A_1^c , A_2^c , and A_3^c have the same orientation. The k -arms A_2^c and A_3^c are namely mapped onto A_1^c by the rotation operators $R_{\mathbf{n}}\left(\theta = \frac{2\pi}{3}\right)$ and $R_{\mathbf{n}}\left(\theta = -\frac{2\pi}{3}\right)$ ($\hat{n} \parallel [111]$), respectively. As these rotation operators do not affect the field direction, i.e., $R_{\mathbf{n}}(\theta)\mathbf{B} = \mathbf{B}$, the symmetry between the three k -arms is preserved.
- In a field, which is applied along the twofold $[110]$ axis, the symmetry is preserved between the k -arms A_2^c and A_3^c . However, the symmetry is broken between A_1^c and A_2^c , and it is also broken between A_1^c and A_3^c . The k -arms A_2^c and A_3^c have the same orientation in the field, as the rotation operator $R_{\mathbf{n}}^{\theta=\pi}$ ($\hat{n} \parallel [110]$) maps A_2^c on A_3^c . Further, this rotation operator leaves the field invariant.
- In a field, which is applied along the fourfold $[001]$ axis, the symmetry is preserved between the k -arms A_2^c and A_3^c . However, the symmetry is broken between A_1^c and A_2^c , and it is broken between A_1^c and A_3^c . The k -arms A_2^c and A_3^c have the same orientation in the field, as the rotation operator $R_{\mathbf{n}}^{\theta=\frac{\pi}{2}}$ ($\hat{n} \parallel [001]$) maps A_2^c on A_3^c . Further, this rotation operator leaves the field invariant.

Accordingly, there is one possible orientation of $(\pi\pi 0)$ arms in a field along a threefold $\langle 111 \rangle$ axis, there are two possible orientations of $(\pi\pi 0)$ arms in a field along a twofold $\langle 110 \rangle$ axis, and there are two possible orientations of $(\pi\pi 0)$ arms in a field along a fourfold $\langle 100 \rangle$ axis

Hence, in order to distinguish multi- k from single- k structures, it may prove useful to apply fields either along $\langle 100 \rangle$ or $\langle 110 \rangle$ directions, rather than $\langle 111 \rangle$ directions.

single- k structures, $N_k = 1$						
	s1	s2	s3	s4	s5	
$\mathbf{r}(\mathbf{k}_1^c)$	$(0, 0, 1)$	$(1, 0, 0)$	$(\frac{1}{\sqrt{2}}, 0, \frac{1}{\sqrt{2}})$	$(\frac{1}{\sqrt{2}}, \frac{1}{\sqrt{2}}, 0)$	$(\frac{1}{\sqrt{3}}, \frac{1}{\sqrt{3}}, \frac{1}{\sqrt{3}})$	
α	-1	1	$-\frac{1}{3}$	1	0	
$\mathbf{m} \parallel$	$\langle 100 \rangle$	$\langle 100 \rangle$	$\langle 110 \rangle$	$\langle 110 \rangle$	$\langle 111 \rangle$	
double- k structures, $N_k = 2$						
	d1	d2	d3	d4	d5	
$\mathbf{r}(\mathbf{k}_1^c)$	$(0, 0, \frac{1}{\sqrt{2}})$	$(\frac{1}{\sqrt{2}}, 0, 0)$	$(0, \frac{1}{\sqrt{2}}, 0)$	$(0, \frac{1}{\sqrt{3}}, \frac{1}{\sqrt{3}})$	$(\frac{1}{\sqrt{3}}, 0, 0)$	
$\mathbf{r}(\mathbf{k}_2^c)$	$(\frac{1}{\sqrt{2}}, 0, 0)$	$(0, 0, \frac{1}{\sqrt{2}})$	$(\frac{1}{\sqrt{2}}, 0, 0)$	$(\frac{1}{\sqrt{3}}, 0, 0)$	$(0, \frac{1}{\sqrt{3}}, \frac{1}{\sqrt{3}})$	
α	-1	1	$-\frac{1}{3}$	$-\frac{3}{5}$	1	
$\mathbf{m} \parallel$	$\langle 110 \rangle$	$\langle 110 \rangle$	$\langle 110 \rangle$	$\langle 111 \rangle$	$\langle 111 \rangle$	
double- k structures, $N_k = 2$						
	d6	d7	d8	d9	d10	
$\mathbf{r}(\mathbf{k}_1^c)^T$	$(0, \frac{1}{\sqrt{3}}, 0)$	$(\frac{1}{2}, 0, -\frac{1}{2})$	$(\frac{1}{2}, -\frac{1}{2}, 0)$	$(\frac{1}{2\sqrt{2}}, \frac{1}{\sqrt{2}}, -\frac{1}{2\sqrt{2}})$	$(\frac{1}{2\sqrt{2}}, -\frac{1}{2\sqrt{2}}, \frac{1}{\sqrt{2}})$	
$\mathbf{r}(\mathbf{k}_2^c)^T$	$(\frac{1}{\sqrt{3}}, 0, \frac{1}{\sqrt{3}})$	$(\frac{1}{2}, 0, \frac{1}{2})$	$(\frac{1}{2}, \frac{1}{2}, 0)$	$(\frac{1}{2\sqrt{2}}, 0, \frac{1}{2\sqrt{2}})$	$(\frac{1}{2\sqrt{2}}, \frac{1}{2\sqrt{2}}, 0)$	
α	0	$-\frac{1}{3}$	$\frac{1}{5}$	$\frac{1}{5}$	$-\frac{7}{13}$	
$\mathbf{m} \parallel$	$\langle 111 \rangle$	$\langle 100 \rangle$	$\langle 100 \rangle$	$\langle 110 \rangle$	$\langle 110 \rangle$	
double- k structures, $N_k = 2$						
	d11					
$\mathbf{r}(\mathbf{k}_1^c)$	$(\frac{1}{2\sqrt{2}}, \frac{1}{2\sqrt{2}}, 0)$					
$\mathbf{r}(\mathbf{k}_2^c)$	$(\frac{1}{2\sqrt{2}}, -\frac{1}{2\sqrt{2}}, \frac{1}{\sqrt{2}})$					
α	$\frac{5}{9}$					
$\mathbf{m} \parallel$	$\langle 110 \rangle$					
triple- k structures, $N_k = 3$						
	t1	t2	t3	t4	t5	
$\mathbf{r}(\mathbf{k}_1^c)$	$(0, 0, \frac{1}{\sqrt{3}})$	$(0, \frac{1}{\sqrt{3}}, 0)$	$(0, \frac{1}{\sqrt{3}}, 0)$	$(0, \frac{1}{2\sqrt{2}}, \frac{1}{2\sqrt{2}})$	$(\frac{1}{\sqrt{2}}, 0, 0)$	
$\mathbf{r}(\mathbf{k}_2^c)$	$(\frac{1}{\sqrt{3}}, 0, 0)$	$(0, 0, \frac{1}{\sqrt{3}})$	$(\frac{1}{\sqrt{3}}, 0, 0)$	$(\frac{1}{\sqrt{2}}, 0, 0)$	$(0, -\frac{1}{2\sqrt{2}}, \frac{1}{2\sqrt{2}})$	
$\mathbf{r}(\mathbf{k}_3^c)$	$(0, \frac{1}{\sqrt{3}}, 0)$	$(\frac{1}{\sqrt{3}}, 0, 0)$	$(0, 0, \frac{1}{\sqrt{3}})$	$(0, -\frac{1}{2\sqrt{2}}, \frac{1}{2\sqrt{2}})$	$(0, \frac{1}{2\sqrt{2}}, \frac{1}{2\sqrt{2}})$	
α	-1	+1	0	$-\frac{5}{7}$	$\frac{5}{9}$	
$\mathbf{m} \parallel$	$\langle 111 \rangle$	$\langle 111 \rangle$	$\langle 111 \rangle$	$\langle 110 \rangle$	$\langle 110 \rangle$	

Table 3.1.: There are 21 commensurate $(\pi\pi 0)$ structures fulfilling the two conditions that all moments have equal modulus and all moments are directed along a unique crystallographic star, which is either $\mathbf{M} \parallel \langle 100 \rangle$, $\langle 110 \rangle$, or $\langle 111 \rangle$. The 21 structures can be classified with respect to the number of k -vectors N_k , which are participating in the Fourier description $\mathbf{m} = \sum_{j=1}^{N_k} \mathbf{r}^T(\mathbf{k}_j^c) \exp(i\mathbf{k}_j^c \cdot \mathbf{R})$. The prefactors \mathbf{r} are given for each structure. The diagonals of the polarization matrices of a Bragg peak located at $\mathbf{Q} = (\frac{1}{2}, \frac{1}{2}, 0)$ and measured such that (001) corresponds to the scattering plane are given by $(-1, \alpha, -\alpha)$. The values α , as calculated by means of the Blume-Maleev equations and averaged over all possible magnetic domains, are given for each structure.

3.3. The Compound HoCu

In the following, a microscopic study of the magnetic properties of HoCu is presented. HoCu is antiferromagnetic and one of three RCu compounds, studied as part of this thesis. As a main result, a complex magnetic phase diagram, which arises due to competing interactions, has been studied in detail and magnetic structures were determined. Despite the centrosymmetry of the space group of HoCu, transport measurements performed by Rahn suggested the emergence of ground states with non-trivial topology [18]. Previous magnetic structure determinations used neutron diffraction from polycrystalline samples and resolved commensurate magnetic ground states [68]. As the main results of single crystal neutron diffraction performed in the context of this thesis, a variety of magnetic ground states could be identified, including several multi- k structures, long-wavelength modulations, and structures with non-trivial topology. Furthermore, an important interplay between magnetic order and the electronic structure could be identified. Namely, antiferromagnetic ground states may give rise to a finite Berry curvature with an assembly of magnetic charges in the electronic structure, an orbital magnetization, and an anomalous Hall effect.

The presentation of the study of HoCu is organised as follows. First, an introduction to the literature of HoCu is given in Sec. 3.3.1. The specific measurements presented in this chapter, as well as a more detailed outline are motivated in Sec. 3.3.2. Neutron scattering data measured in zero magnetic field are presented in Sec. 3.3.3, followed by the neutron scattering data under magnetic fields in Sec. 3.3.4. The results of the neutron scattering experiments are then combined to determine the magnetic ground states of the zero field phases in Sec. 3.3.5. The topological and geometric properties of the ground states in zero magnetic field and the interplay of magnetic long-range order with the conduction electrons and the electronic structure are discussed in Secs. 3.3.6 and 3.3.7, respectively.

3.3.1. Introduction to HoCu

Centrosymmetric HoCu is prototypical for the complexity of rare-earth magnetism. It is a candidate material for hosting novel antiferromagnetic ground states with non-trivial topology, even though the crystal structure is centrosymmetric. Complex magnetic phase diagrams, as observed recently [18], reflect the presence of competing interactions and a variety of magnetic ground states. The unconventional Hall effect, reported in Ref. [18], is clearly related to the antiferromagnetic properties of HoCu, but does not arise due to an ordinary anomalous Hall effect. The additional contributions to the Hall effect may be related to non-trivial Berry phases and may possess topological origin. In particular,

when arising from real-space Berry phases, the Hall effect may be an indication of magnetic ground states with non-trivial topology (cf. Refs. [9, 109, 110]).

HoCu crystallizes in the cubic CsCl crystal structure [70] with lattice constant $a = 3.447 \text{ \AA}$ [71]. The Ho^{3+} ions may be portrayed as free ions with moment $g\sqrt{J \cdot (J + 1)} = 10.61 \mu_{\text{B}}/\text{f.u.}$, as inferred from Hund's rules ($L = 6$, $S = 2$, $J = 8$, and $g = \frac{5}{4}$ [30]). They carry antiferromagnetic long-range order at temperatures below 28 K [68, 111, 112]. Complex magnetic phase diagrams evolve, as shown in Fig. 3.1 for the major cubic directions and may be inferred from the magnetization, ac susceptibility, and electrical transport measurements (cf. Ref. [18]). Qualitative differences of the three diagrams reflect the importance of cubic anisotropies. Critical fields are lower for $\langle 110 \rangle$ and $\langle 111 \rangle$ directions, whereas for $\langle 100 \rangle$ they are considerably larger. This may suggest fourfold $\langle 100 \rangle$ directions as hard axes, as well as a binary easy plane, in agreement with previous findings of neutron spectroscopy measurements, as reported in Ref. [113].

In zero magnetic field, three magnetically ordered phases with transition temperatures $T_{t_1} = 13.4 \text{ K}$, $T_{t_2} = 20 \text{ K}$, and $T_{\text{N}} = 26.5 \text{ K}$ have been observed [68]. The specific heat features a lambda-anomaly at T_{N} , which is characteristic of a second-order phase transition, as well as signatures of a first-order phase transition at T_{t_1} [68]. At T_{t_2} the specific heat features a relatively broad anomaly. The authors of Ref. [68] noticed that the latent heat $L = 3.2 \frac{\text{J}}{\text{mol}}$ at the transition $T_{t_1} = 13.4 \text{ K}$, if related to a change in the magnetic structure, is small compared to the values observed in related compounds ($L = 33 \frac{\text{J}}{\text{mol}}$ in TbZn [114], $L = 8 \frac{\text{J}}{\text{mol}}$ in HoZn [114]).

The susceptibility as a function of temperature features Curie-Weiss behavior with $\theta \approx -12 \text{ K}$, a typical value for non-frustrated antiferromagnets, as well as a fluctuating moment $\mu_{\text{eff}} = 10.65 \mu_{\text{B}}$, which is slightly larger than the free-ion value of Ho^{3+} [18] (cf. Ref. [70]).

Typical magnetization data as a function of field are shown in Fig. 3.2 (top). The magnetization displays a sequence of step-like increases. The behavior is akin to the multi-step behavior, which was reported in compounds such as DyCu [115], PrAg [116] or NdIn₃ [95].

Measurements of resistivity, magnetoresistance, and Hall effect were reported in Refs. [18, 112]. Notable is the unconventional behavior of the Hall resistivity ρ_{xy} in the magnetically ordered regime [18]. Typical field dependences of the Hall resistivity are shown in Fig. 3.2 (bottom). In the paramagnetic regime, the Hall resistivity depends linearly on magnetic fields characteristic of a normal metal. In the magnetically ordered regime, a negative contribution to the Hall effect is present, being large enough such that the total Hall signal becomes negative. This additional contribution is clearly related to the magnetic long-range order but does not arise due to an ordinary anomalous Hall effect as

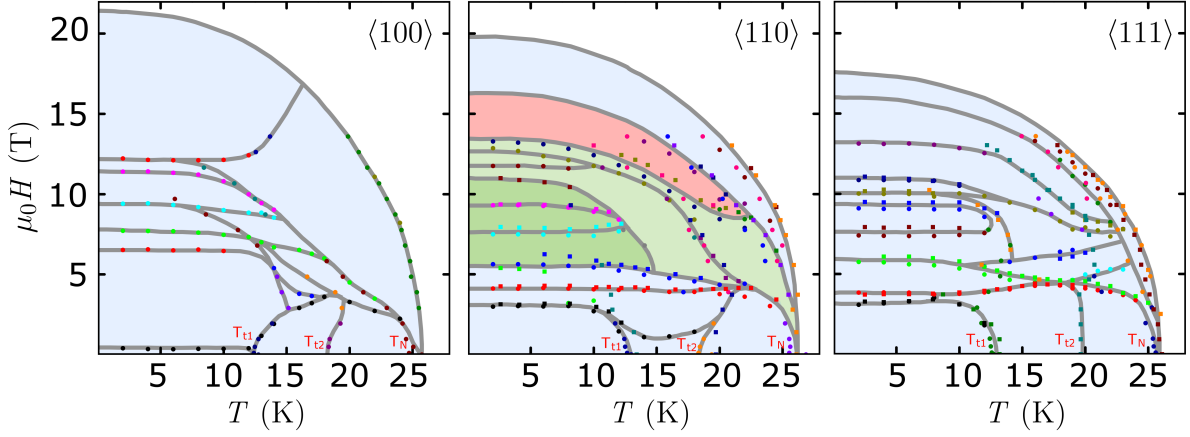


Figure 3.1.: Magnetic phase diagrams of HoCu for the major cubic directions $\langle 100 \rangle$, $\langle 110 \rangle$ and $\langle 111 \rangle$. Data were inferred by Rahn from measurements of the magnetization, ac susceptibility, resistivity and Hall effect. The figure is taken from Ref. [18].

it does not scale linearly with the net magnetization. The author of Ref. [18] noted that unconventional contributions may be possible, arising from real-space, reciprocal-space, or mixed Berry phases (cf. Refs. [109, 110, 117]). When associated with real-space Berry phases, the Hall effect may be an indication of magnetic ground states with a non-trivial topology [9].

Magnetic structure determinations in zero magnetic field using neutron diffraction on polycrystalline samples were carried out by Morin *et al.* [68]. The authors suggested commensurate $(\pi\pi 0)$ structures as magnetic ground states in the three ordered phases. However, the description of the ground states proves to be insufficient, as reported in this thesis further below. Fig. 3.3 (a) shows the diffraction spectra recorded by Morin *et al.* [68]. At $T = 10.5 \text{ K} < T_{t1}$ in the phase, which is further below labeled phase C, the inferred ordered moment is given by $7.5 \mu_B$ [68]. The structure was not determined unambiguously suffering ambiguities arising due to polycrystalline neutron diffraction (cf. Ref. [108]). Fig. 3.3 (b) shows the possible solutions suggested as magnetic ground state by Morin *et al.* [68]. The first possibility is a single- k structure, which is classified by an angle $\theta \approx 56^\circ$, the magnetic moments being parallel to one of the $\langle 111 \rangle$ directions. The other possibilities are a double- k , as well as a triple- k structure, which have the same magnetic structure factor as the single- k structure. For both of them, the moments are directed along the $\langle 111 \rangle$ axes. From the absence of an asymmetric broadening of nuclear peaks at 10.5 K it was inferred, that there is no noticeable distortion of the cubic lattice, which is particularly consistent with moments pointing along the threefold $\langle 111 \rangle$ directions. In the second phase, which will be labeled IC1 below, the diffraction pattern was recorded at $T = 14.5 \text{ K}$. The inferred ordered moment is here $7.1 \mu_B$. Further, Morin *et al.* [68] found commensurate magnetic propagation vectors of type $(\pi\pi 0)$ only. As a

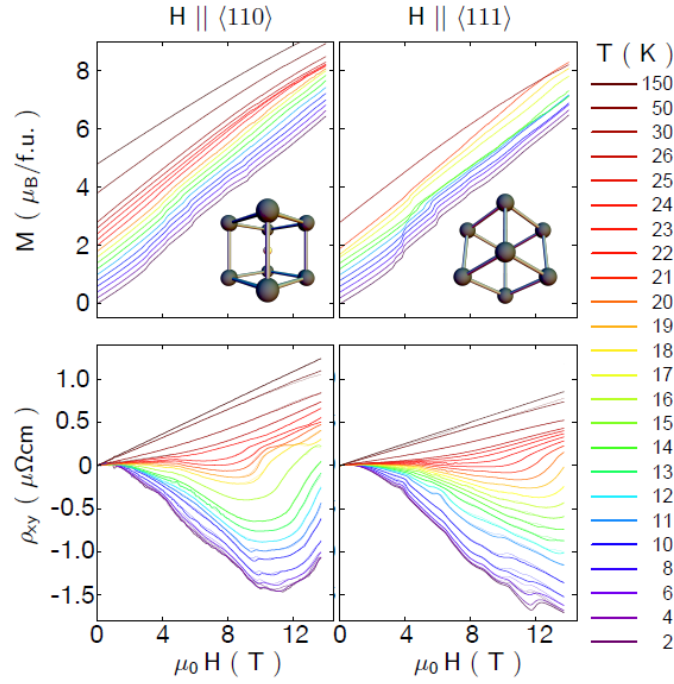


Figure 3.2.: Magnetization M (top) and Hall resistivity ρ_{xy} (bottom) of HoCu at different temperatures as a function of magnetic field as reported by Rahn [118]. The field was applied along the two cubic directions $\langle 110 \rangle$ and $\langle 111 \rangle$. Typical magnetization data is monotonic and features steps. The Hall resistivity ρ_{xy} as a function of field is linear in the paramagnetic regime, which is characteristic of conductors. In the ordered regime ($T < T_N$) a negative contribution evolves, large enough that the whole Hall signal becomes negative. This negative contribution does not arise due to an ordinary anomalous Hall effect depending linearly on the net magnetization. The figures are taken from Ref. [118].

key result of the work reported here, this description is incomplete, due to the presence of additional incommensurate propagation vectors. In addition, Morin *et al.* [68] found that the moments are tilted towards $\langle 110 \rangle$ directions, when compared with the ground state in phase C. The suggested structure candidates were classified by an angle, which is either $\theta \approx 45^\circ$ or $\theta \approx 48^\circ$ [68]. An illustration of suggested solutions, notably single- k , double- k , and triple- k , is given in Fig. 3.3 (c).

In the third phase, which will be labeled IC2 below, the diffraction pattern presented in Ref. [68] was recorded at $T = 19.7$ K. The ordered moment amounted to $6.3 \mu_B$. The ground state was also described as commensurate antiferromagnet, which turns out to be incomplete further below in our study. In Ref. [68] the magnetic structure was classified by an angle $\theta \approx 50^\circ$, being again either single- k , double- k , or triple- k [68].

Crystal electric fields were studied by neutron spectroscopy measurements of diluted compounds [113]. As mentioned before, it was inferred, that $\langle 100 \rangle$ directions are clearly the hard axes, whereas $\langle 110 \rangle$ and $\langle 111 \rangle$ directions have similar energies suggesting a

binary easy-magnetization plane between the [101] and [111] directions in the presence of predominantly isotropic bilinear exchange interactions [68, 113].

Magnetostriction of polycrystalline HoCu and related compounds such as DyCu, as measured in pulsed magnetic fields, exhibit a rich dependence on magnetic fields [119]. In particular, a volume magnetostriction and an anisotropic magnetostriction were observed. Accordingly, in a magnetic field the lattice of the compounds is differently distorted parallel and perpendicular to the field direction.

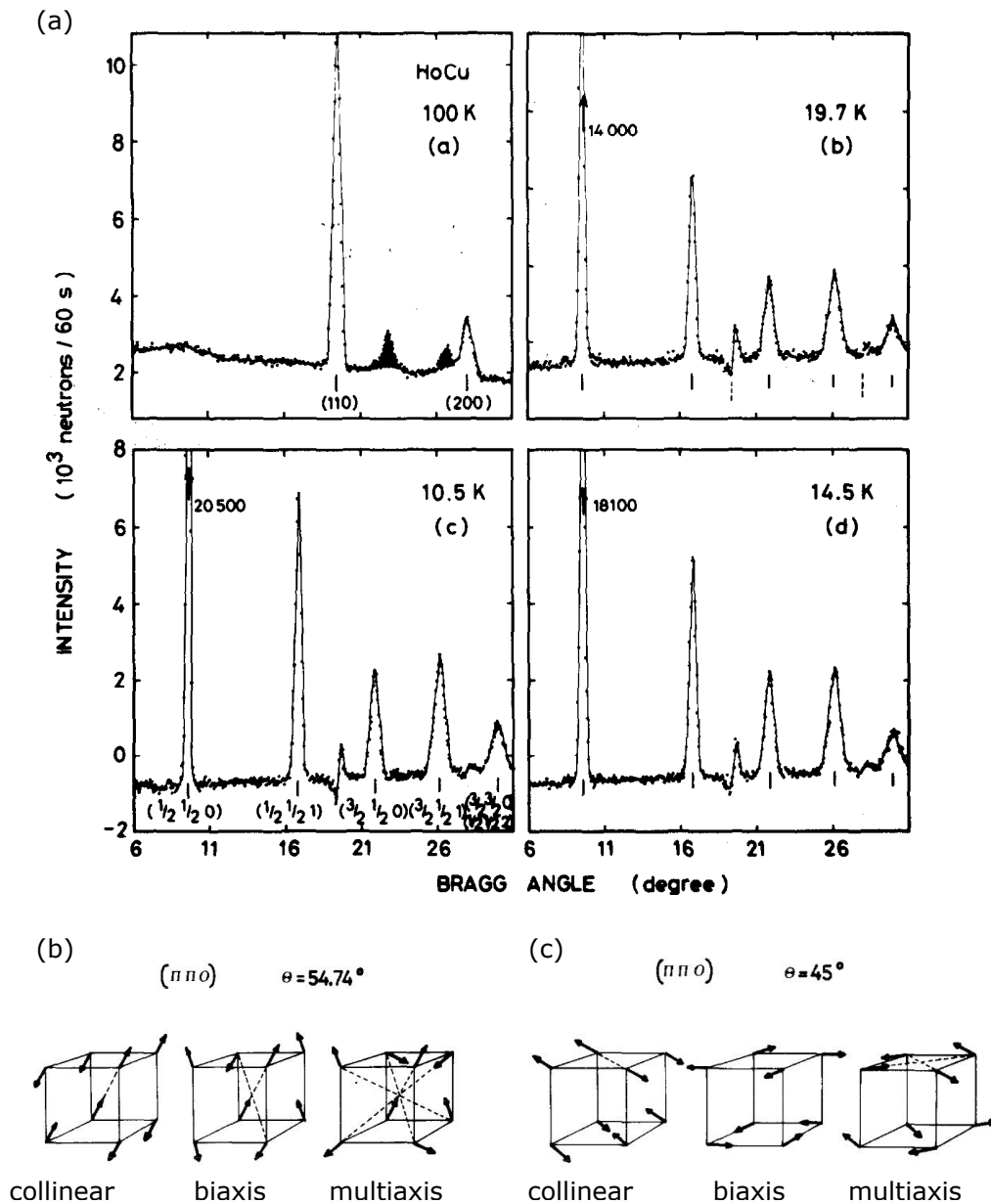


Figure 3.3.: Magnetic structure determinations in zero magnetic field using polycrystalline neutron diffraction as reported by Morin *et al.* [68]. (a) Diffraction data were recorded in each of the four zero field phases. The three data sets taken within the magnetically ordered regime exhibit six magnetic Bragg reflections. Magnetic structure determinations were carried out. (b) The magnetic structure in phase C at $T = 10.5$ K is related to an angle $\theta = 54^\circ$ and may be collinear and single- k , biaxis and double- k , or multiaxis and triple- k . (c) The magnetic structure in phase IC1 at $T = 14.5$ K is either related to an angle $\theta = 45^\circ$ or an angle $\theta = 48^\circ$. The first case is illustrated in the figure. The structure is either single- k and collinear, double- k and biaxis, or triple- k and multiaxis. The figures are taken from Ref. [68]

3.3.2. Objectives and Outline

In the following, we provide a short summary of the objectives of our study, followed by an outline of this chapter, as well as a brief summary of some major results.

As reported in the first part of this chapter, magnetic ground states were determined using single crystal neutron diffraction. As a major result, magnetic structures of HoCu were determined in the three magnetically ordered phases at zero magnetic field. All three phases display variations of $(\pi\pi0)$ antiferromagnetism. Fig. 3.4 illustrates the emergence of the three ordered phases showing the temperature dependence of the magnetic $(\pi\pi0)$ order parameter at zero magnetic field. One commensurate phase, labeled phase C, as well as two incommensurate phases, labeled phases IC1 and IC2, emerge at temperatures below 28 K. Residual scattering above the ordering temperature is suggestive of strong spin fluctuations (cf. Ref. [120]).

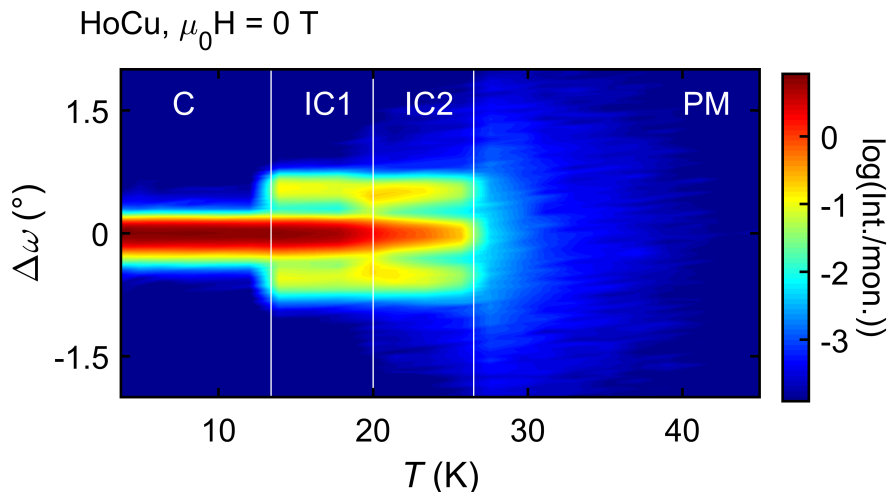


Figure 3.4.: Temperature dependence of the magnetic $(\pi\pi0)$ order parameter in zero magnetic field. Shown is the temperature dependence of the $(\frac{3}{3}, \frac{3}{2}, 1)$ Bragg peak position reflecting the emergence of three magnetically ordered phases below the ordering temperature T_N . In phase C, the magnetic order parameter is commensurate. In phases IC1 and IC2, incommensurate satellites in the vicinity of the commensurate peak evolve. The diffuse signal as observed well above the onset of long-range order provides evidence of strong spin fluctuations in the paramagnetic regime. The measurements were performed together with the experiments in Sec. 3.3.3.2. The figure was inferred from rocking scans around the magnetic Bragg peak $(\frac{3}{3}, \frac{3}{2}, 1)$ carried out at the diffractometer HEiDi while cooling down from 45 K to 2.5 K.

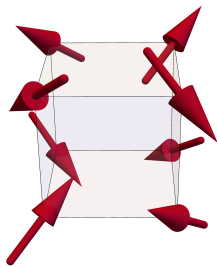
Fig. 3.5 illustrates the ground states of phases C, IC1, and IC2 of HoCu, as inferred from single crystal neutron diffraction and as depicted for one magnetic unit cell. All three ground states are multi- k and noncoplanar. In phase C, the magnetic structure is commensurate of type $(\pi\pi0)$. It combines three propagation vectors and has a relatively small unit cell. In phase IC1, the magnetic ground state is a superposition of commensurate

and incommensurate propagation vectors. The ground state is topologically protected against unwinding into a collinear antiferromagnet and has a large wavelength along one spatial direction of the order of 90 \AA . Locally, the structure is akin to commensurate $(\pi\pi 0)$ antiferromagnets. In phase IC2, the ground state is a complex superposition of several propagation vectors. The unit cell has a long wavelength of the order of 90 \AA along two different spatial directions. Locally, the structure is also akin to commensurate $(\pi\pi 0)$ antiferromagnets. Depicted is an educated guess, which may possibly represent the ground state in IC2.

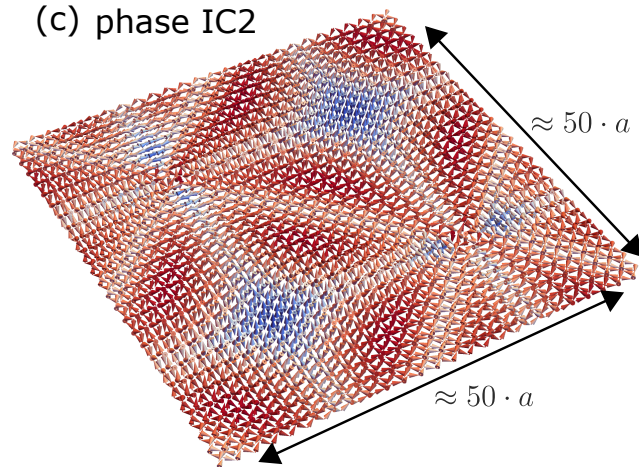
HoCu

ground states at zero magnetic field

(a) phase C



(c) phase IC2



(b) phase IC1

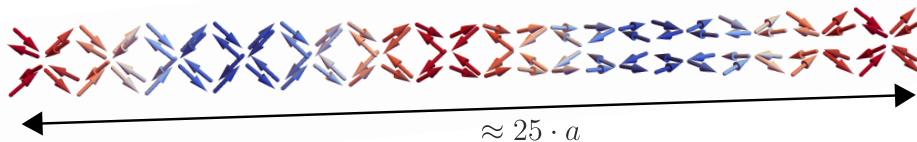


Figure 3.5.: Magnetic structures in the three ordered phases at zero magnetic field. (a) In phase C the ground state is a triple- k antiferromagnet of type $(\pi\pi 0)$ having a relatively small unit cell of size $2a \cdot 2a \cdot 2a$. (b) In phase IC1, the ground state is a triple- k structure, combining commensurate and incommensurate propagation vectors. The structure is a highly noncollinear antiferromagnet which is locally akin to commensurate $(\pi\pi 0)$ antiferromagnets. The structure has a long wavelength of the order of $\approx 90 \text{ \AA}$ along one spatial direction. (c) In phase IC2, the ground state is more complex. A likely structure candidate is shown. The structure is multi- k combining commensurate and incommensurate propagation vectors. Locally the structure is akin to commensurate $(\pi\pi 0)$ antiferromagnets. The structure is incommensurate with respect to two different spatial directions. It has a long wavelength of the order of $\approx 90 \text{ \AA}$ along two spatial directions.

The presentation of the detailed observations that allowed to identify these ground states in the three ordered phases at zero field is organized as follows. In Sec. 3.3.3, single crystal neutron diffraction is presented. We determined the stars of the magnetic

propagation vectors and specified the magnetic ground states by means of representational analysis, Rietveld refinements, polarization analysis, and the study of higher-order peak positions. The number of propagation vectors of the ground states were determined by means of symmetry breaking magnetic fields, as reported in Sec. 3.3.4. In the same set of measurements the ground states under magnetic fields were investigated. In Sec. 3.3.5, magnetic structure determinations are reported, gathering the results from single crystal neutron diffraction. In Sec 3.3.6, the topological and geometric properties of the ground states in zero magnetic field are addressed.

Neutron scattering under field along $\langle 110 \rangle$ and $\langle 111 \rangle$ are presented in Sec. 3.3.4. The neutron studies reveal a variety of magnetic structures, including numerous multi- k states and ground states possessing long-wavelength modulations.

Sec. 3.3.7 addresses the interplay of magnetic order and the electronic structure. This concerns the role of the conduction electrons in the presence of antiferromagnetic $(\pi\pi 0)$ order. First, a theoretical model is suggested of the conduction electrons in the presence of noncoplanar $(\pi\pi 0)$ order. A finite Berry curvature with a complex assembly of monopoles and antimonopoles in the electronic structure, an orbital magnetization, as well as an unconventional Hall effect are predicted within this model. An anomalous Hall effect, which does not originate from an ordinary anomalous Hall effect depending linearly on the net magnetization, may arise due to noncoplanar magnetic long-range order. Second, it is reported, that also noncollinear $(\pi\pi 0)$ order may possibly cause a finite Berry curvature and an anomalous Hall effect, which is not ordinary. Third, the emergence of a topological Hall effect in the presence of ground states with a long wavelength in real-space and a magnetic field is discussed.

3.3.3. Neutron Diffraction in Zero Magnetic Field

In the following, data recorded in HoCu under zero magnetic field by means of several complementary neutron techniques are reported. The CsCl crystal structure was confirmed, as summarized in Sec. 3.3.3.1. The magnetic propagation vectors of the ground states in zero magnetic field were determined, as presented in Sec. 3.3.3.2. The results of small angle neutron scattering are presented in Sec. 3.3.3.3. By a combination of representational analysis (Sec. 3.3.3.4), polarization analysis (Sec. 3.3.3.5), and Rietveld refinements (Sec. 3.3.3.6), the ground states in the three phases are specified. A study on higher-order peaks in phases IC1 and IC2 is presented in Sec. 3.3.3.7.

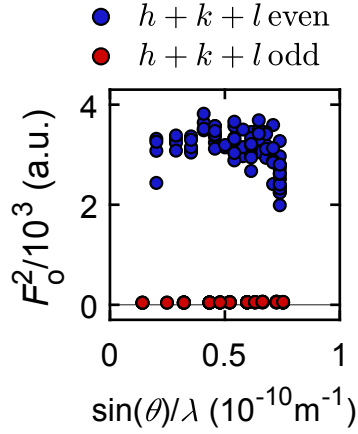
3.3.3.1. Determination of the Crystal Structure

The crystal structure of the single-crystal sample OFZ95-3-2-1-a was determined at the four-circle neutron diffractometer HEiDi [121]. As the main result, these measurements confirm a CsCl crystal structure in excellent agreement with the literature [70, 71], as well as a high sample quality. For these measurements neutrons with a wavelength $\lambda = 1.16 \text{ \AA}$ were used. Due to the relatively small lattice constant a of HoCu, only a small volume in reciprocal space, $\sqrt{h^2 + k^2 + l^2} \leq 2a/\lambda \approx 5.93$, is accessible for Bragg scattering. At $T = 30 \text{ K}$ a value of $a = 3.45(3) \text{ \AA}$ was inferred, consistent with the literature ($a = 3.440 \text{ \AA}$ [68, 71]). For further analysis, a limited set of 161 nuclear Bragg reflections was recorded at $T = 45 \text{ K}$, well above the magnetic transition temperature, in order to avoid remanent diffuse magnetic scattering. To obtain the structure factor, integrated intensities $F_o^2(h, k, l) = I$ were inferred from the measured Bragg peaks with the instrument software at HEiDi. For $(2, 0, 0)$ a large peak intensity of 7.1/std.mon. with a small FWHM of 0.42° was observed. All values reflected the high crystalline quality and low mosaicity of the specimen.

Further, the structure factor for the CsCl structure of HoCu, as inferred from Eq. (2.1), is given by

$$F_{\text{HoCu}}^2(h, k, l) = \begin{cases} (b_{\text{Ho}} + b_{\text{Cu}})^2 & h + k + l \in 2\mathbb{Z} \\ (b_{\text{Ho}} - b_{\text{Cu}})^2 & h + k + l \in 2\mathbb{Z} + 1 \end{cases} . \quad (3.7)$$

For the scattering lengths of Ho and Cu, $b_{\text{Ho}} = 8.01 \text{ fm}$ and $b_{\text{Cu}} = 7.718 \text{ fm}$ [122], being very similar, the nuclear reflections with odd values of $h + k + l$ are strongly suppressed, whereas those with even values of $h + k + l$ are strongly enhanced. Thus, the structure factor is approximately that of a bcc lattice with a one-atomic basis. As shown in Fig. 3.6,



Model	$Pm\bar{3}m$
No. of measured reflections	161
No. of refined parameters	4
$R [F^2 \geq 3\sigma(F^2)]$	3.91
$wR(F^2)$	9.99
Extinction correction	Isotropic, Lorentzian
Extinction coefficient	0.000276
$U_{iso} (\text{\AA}^2)$	0.0051

Figure 3.6.: Determination of the crystal structure of HoCu. The nuclear structure factor was measured in the paramagnetic regime at $T = 45$ K. A set of 161 structural Bragg reflections was measured at the four-circle diffractometer HEiDi and integrated intensities $I \sim F_o^2(h, k, l)$ were inferred. The measured structure factor follows the behavior expected for the CsCl crystal structure splitting into a group of strongly enhanced and a group of strongly suppressed reflections satisfying $h + k + l \in 2\mathbb{Z}$ and $h + k + l \in 2\mathbb{Z} + 1$, respectively (figure on the left). A Rietveld refinement was carried out on the 161 structural reflections by means of the software JANA2006 [59] (table on the right). The low R -value of 3.91 reflects the excellent agreement of the measured data with the CsCl crystal structure. The extinction was accounted for by an isotropic Lorentzian parameter.

the measured Bragg peaks are in excellent agreement with Eq. (3.7), featuring two groups of strongly enhanced and strongly suppressed reflections.

In addition, a Rietveld refinement [123] was carried out using JANA2006 [59]. The measured integrated intensities F_o^2 , shown in Fig. 3.6, were fitted according to space group $Pm\bar{3}m$. Excellent agreement with the experimental data is indicated by the low R -value of 3.91. A mean square displacement $U_{iso} = \langle u^2 \rangle \approx 0.0051 \text{\AA}^2$ was obtained from the refinement. The integrated intensities F_o^2 (Fig. 3.6) decrease to higher scattering angles due the Debye-Waller factor [24, 27, 28], which is given by $\exp(-\frac{1}{3}\mathbf{G}^2 \langle u^2 \rangle) \approx 0.9$ for the largest scattering angles $2\theta \approx 180^\circ$.

3.3.3.2. Magnetic Propagation Vectors

To determine the magnetic propagation vectors of the three phases C, IC1, and IC2 at zero magnetic field, single crystal neutron diffraction of sample OFZ95-3-2-1-a was performed at HEiDi and of sample OFZ95-3-3-h at BIODIFF [124]. The main results of these experiments, as explained in detail further below, may be summarized as follows:

- The phases C, IC1, and IC2 all display variations of $(\pi\pi 0)$ antiferromagnetism.
- The ground state of phase C is commensurate. The structure is single- k or multi- k with up to three commensurate propagation vectors of the star $\langle \frac{1}{2} \frac{1}{2} 0 \rangle = \left\{ \left(\frac{1}{2}, \frac{1}{2}, 0 \right) \right\}$.
- The ground states of phases IC1 and IC2 are modulated with an incommensurate superstructure. Both are multi- k , combining up to three commensurate propagation vectors of the star $\langle \frac{1}{2} \frac{1}{2} 0 \rangle$ and up to six incommensurate propagation vectors of the star $\langle \frac{1}{2} - \delta, \frac{1}{2}, 0 \rangle = \left\{ \left(\frac{1}{2} - \delta, \frac{1}{2}, 0 \right) \right\}$. These maximum numbers of propagation vectors are inferred from the number of k -arms of the crystallographic stars $\langle \frac{1}{2} \frac{1}{2} 0 \rangle$ and $\langle \frac{1}{2} - \delta, \frac{1}{2}, 0 \rangle$.
- The intensity at the nuclear peak positions is temperature dependent. This dependence, however, is not related to ferromagnetic Bragg scattering, but presumably arises due to multiple scattering associated with the antiferromagnetic order or magnetoelastic effects.

The determination of propagation vectors in zero magnetic field was carried out in three steps. First, specific high symmetry points of the simple cubic lattice were investigated as the putative location of propagation vectors, namely the critical points Γ , M, R, and X in the first Brillouin zone (cf. Ref. [125] for further information). However, only Γ and M were found to be relevant, as temperature dependences were only present at positions associated with the set of $(\pi\pi 0)$ reflections and at the nuclear positions. Second, the propagation vectors of phase C were determined. It was shown that peaks from the set of $(\pi\pi 0)$ reflections are due to magnetic Bragg scattering, whereas temperature dependent contributions at structural positions do not display magnetic Bragg scattering. Therefore, the form factor [21, 22] was measured for a large set of $(\pi\pi 0)$ reflections, as well as for the temperature dependent contribution observed at structural positions. The $(\pi\pi 0)$ reflections were found to follow the square of the magnetic form factor of Ho^{3+} . This confirmed the magnetic origin of the $(\pi\pi 0)$ reflections. In contrast, the temperature dependent contributions at structural positions do not follow the square of the form factor of Ho^{3+} , suggesting that the ground state in phase C has magnetic propagation vectors of the star $\langle \frac{1}{2} \frac{1}{2} 0 \rangle$ only. Third, incommensurate propagation vectors were determined in phases IC1 and IC2. Measurements with a counting tube revealed an incommensurate splitting of the $(\pi\pi 0)$ ordering vectors in phases IC1 and IC2. The precise position of all

magnetic satellites in the vicinity of $(\frac{1}{2}, \frac{1}{2}, 0)$ was determined at BIODIFF with an area detector allowing accurate identification of the magnetic satellites. These measurements confirmed that the ground states in IC1 and IC2 are superpositions of commensurate and incommensurate propagation vectors.

For the measurements at HEiDi, neutrons with a wavelength $\lambda = 1.16 \text{ \AA}$ were used. To establish the magnetic ordering vectors the following critical k -points were investigated as a function of temperature (cf. Fig. 3.7): (i) $(\frac{1}{2}, \frac{1}{2}, 0)$ of the set of $(\pi\pi 0)$ positions, i.e., the M point. As shown in Fig. 3.7 (a) a temperature dependence was present. (ii) The ferromagnetic $(1, 1, 0)$ position. This was done to obtain information on the related Γ point. A temperature dependent contribution, which is shown in Fig. 3.7 (b), is present at temperatures below T_{t2} . In phase C, at $T = 2.5 \text{ K}$, the integrated intensity of the $(1, 1, 0)$ reflection was roughly 10 % larger than at $T = 45 \text{ K}$ in the paramagnetic state, i.e.,

$$\frac{I_{2.5 \text{ K}}^{(110)}}{I_{45 \text{ K}}^{(220)}} = 1.095 \pm 0.027. \quad (3.8)$$

(iii) Selected positions of the set of $(\pi\pi\pi)$ reflections, where no temperature dependence was observed. This was confirmed at positions such as the M point, i.e., $(\frac{1}{2}, \frac{1}{2}, \frac{1}{2})$, in IC2 at 22 K, in IC1 at 15 K, and in C at 2.5 K. (iv) Selected positions from the set of $(\pi 0 0)$ reflections, where no temperature dependence was observed. This was confirmed at positions such as the R point, i.e. $(\frac{1}{2}, 0, 0)$, in IC2 at 22 K, in IC1 at 15 K, and in C at 2.5 K.

Next, the form factor was determined for $(\pi\pi 0)$ reflections and temperature dependent contributions at structural positions. The measurements showed that the temperature dependent scattering at the $(\pi\pi 0)$ positions in phase C is due to magnetic Bragg scattering with propagation vectors of the star $\langle \frac{1}{2} \frac{1}{2} 0 \rangle$. In contrast, the temperature dependent intensities observed at nuclear Bragg positions were found to exhibit no magnetic Bragg scattering. Instead, the remaining temperature dependence may be due to multiple scattering or magnetoelastic effects. A set of 500 magnetic $(\pi\pi 0)$ Bragg reflections and the 181 structural reflections, identical to those investigated in the paramagnetic regime (cf. Fig. 3.6), were studied in phase C at $T = 2.5 \text{ K}$ at HEiDi. For $(\frac{1}{2}, \frac{1}{2}, 0)$ a large peak intensity of 5.4/std.mon. with a small FWHM of 0.57° was observed. Similar values were observed for nuclear Bragg reflections (cf. Sec. 3.3.3.1). Integrated intensities $F_o^2(h, k, l) = I$ were inferred from the measured Bragg peaks with the instrument software of HEiDi. To obtain the temperature dependent contributions of structural peak positions in phase C, a data set containing 161 structural reflections, recorded in the paramagnetic state at $T = 45 \text{ K}$, was subtracted from a data set containing the same 161 structural reflections,

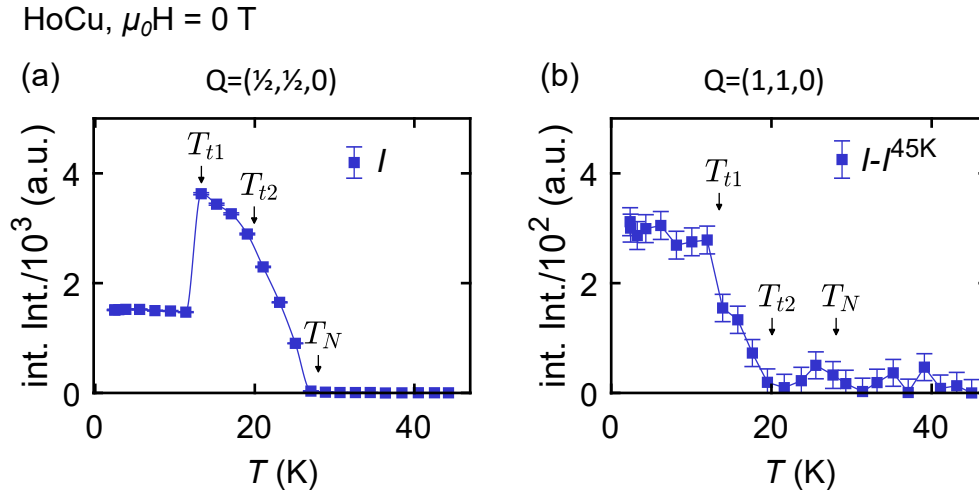


Figure 3.7.: Investigation of the k -points M and Γ as putative magnetic propagation vectors. (a) Temperature dependence of the integrated intensity at the antiferromagnetic peak position $(\frac{1}{2}, \frac{1}{2}, 0)$ (M point), which arises due to magnetic Bragg scattering. The temperature dependence was inferred from rocking scans, which were fitted with single Gaussian profiles and integrated. This Gaussian fit provided a good approximation in phase C and a rough approximation in phases IC1 and IC2. (b) Temperature dependent contribution of integrated intensity at the nuclear position $(1, 1, 0)$. To obtain the temperature dependent contribution, all integrated intensities were subtracted by the integrated intensity in the paramagnetic state at 45 K. This temperature dependence at structural positions arises presumably due to multiple scattering or magnetoelastic couplings. To obtain integrated intensities, rocking scans were carried out, fitted with Gaussian profiles and integrated. Measurements were carried out at HEiDi.

recorded in phase C at $T = 2.5$ K, i.e., $I^{2.5\text{K}} - I^{45\text{K}}$. The strongest temperature dependent contributions at nuclear peak positions were at least one order of magnitude weaker than the strongest antiferromagnetic $(\pi\pi 0)$ peaks.

Figs. 3.8 (a) and (b) show the integrated intensities at the antiferromagnetic positions and of temperature dependent contributions at nuclear positions, respectively, as a function of $\sin(\theta)/\lambda$, where 2θ is the scattering angle. If the intensities were due to magnetic Bragg scattering they must follow the square of the magnetic form factor of Ho^{3+} as a function of $\sin(\theta)/\lambda$ (cf. Ref. [126]). As shown in Fig. 3.8 (a), the temperature dependence follows that of Ho^{3+} at the antiferromagnetic peaks of the set of $(\pi\pi 0)$ positions (Fig. 3.8). This confirms that the intensities are due to magnetic Bragg scattering. In contrast, the temperature dependent contribution at the structural positions exhibits distinctly different behavior, as shown in Fig. 3.8 (b). In particular, the intensities do not vanish even in the limit of backscattering, $\sin(\theta)/\lambda \rightarrow \frac{1}{\lambda} \approx 0.86 \text{ \AA}^{-1}$. The additional contribution at nuclear peak positions is thus not originating from a ferromagnetic contribution to the magnetic structure, but may be due to a change of the crystal structure driven by magnetoelastic coupling or multiple scattering from the antiferromagnetic $(\pi\pi 0)$ peaks.

Hence, all magnetic propagation vectors in phase C are of the star $\langle \frac{1}{2} \frac{1}{2} 0 \rangle$. As the corresponding k -star comprises three different arms, multi- k textures with up to three propagation vectors are possible in principle. The number of k -arms was determined by hand at first and checked with the online tool ISODISTORT [56]. The three k -arms of the star $\langle \pi\pi 0 \rangle$, which contain the vectors $\mathbf{k}_1^c = (\frac{1}{2}, \frac{1}{2}, 0)$, $\mathbf{k}_2^c = (0, \frac{1}{2}, \frac{1}{2})$, and $\mathbf{k}_3^c = (\frac{1}{2}, 0, \frac{1}{2})$, may be labeled A_1^c , A_2^c , and A_3^c , respectively.

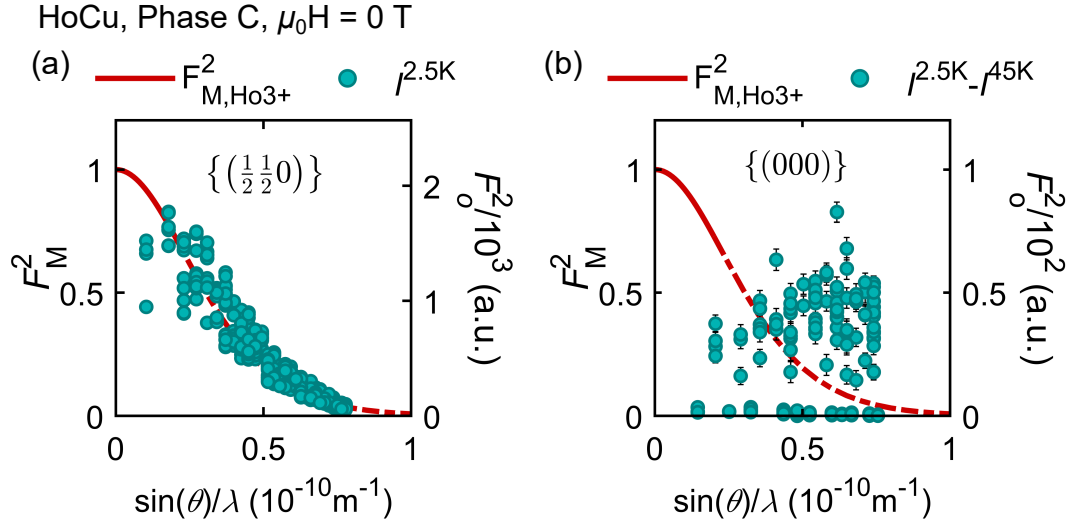


Figure 3.8.: Form factors as a function of $\sin(\theta)/\lambda$, measured for magnetic $(\pi\pi 0)$ positions and for temperature dependent contributions at structural positions in phase C. (a) Integrated intensities $F_o^2(h, k, l) = I$ of $(\pi\pi 0)$ positions ($\mathbf{q} \in \{(\frac{1}{2}, \frac{1}{2}, 0)\}$) as a function of $\sin(\theta)/\lambda$. 500 $(\pi\pi 0)$ Bragg peaks were recorded at $T = 2.5 \text{K}$ by means of rocking scans, fitted with Gaussian profiles and integrated. The intensity at $(\pi\pi 0)$ positions arises due to magnetic Bragg scattering, as it follows the square of the form factor of Ho^{3+} . (b) Temperature dependent contributions at structural peak positions as a function of $\sin(\theta)/\lambda$. To obtain the temperature dependent contributions at structural peak positions ($\mathbf{q} \in \{(0, 0, 0)\}$), a data set containing 161 structural reflections, recorded in the paramagnetic state at $T = 45 \text{K}$, was subtracted from a data set containing the same 161 structural reflections, recorded in phase C at $T = 2.5 \text{K}$, i.e., $I^{2.5 \text{K}} - I^{45 \text{K}}$. These temperature dependent contributions at nuclear positions do not follow the square of the form factor of Ho^{3+} indicating that this temperature dependence does not arise from magnetic Bragg scattering.

As the ensuing discussion illustrates, phases IC1 and IC2 exhibit $(\pi\pi 0)$ antiferromagnetism with a modulated superstructure. A combination of both commensurate and incommensurate propagation vectors is needed to describe the magnetic ground states. The incommensurate splitting of magnetic propagation vectors is shown in Fig. 3.9. Reciprocal space was mapped out in the vicinity of the antiferromagnetic $(\frac{1}{2}, \frac{1}{2}, 0)$ position for the three zero field phases C, IC1, and IC2 by means of a counting tube detector at HEiDI. Q -scans were performed in the $(h, k, 0)$ plane at the temperatures $T = 2.5 \text{K}$, $T = 15 \text{K}$, and $T = 22 \text{K}$. In particular, scattering intensity was recorded at each discrete position on a grid with $0.45 \leq h, k \leq 0.55$, $\Delta h = 0.005$, and $\Delta k = 0.005$.

In phase C, the intensity at the Bragg peak $(\frac{1}{2}, \frac{1}{2}, 0)$ appears to be elongated towards the reciprocal (110) direction (Fig. 3.9 (a)). However, this is due to the resolution of HEiDi and the intensity corresponds to commensurate $(\pi\pi 0)$ antiferromagnetism.

In phase IC1, two incommensurate satellites that are shifted by ~ 0.02 r.l.u. within the $(h, k, 0)$ plane, as well as a commensurate peak (Fig. 3.9 (b)), weaker than in phase C, suggest $(\pi\pi 0)$ antiferromagnetism with a superstructure that is modulated over distances ~ 50 unit cells. In IC2, incommensurate satellites with a splitting (Fig. 3.9 (c)), similar to phase IC1, also reflect $(\pi\pi 0)$ antiferromagnetism with a modulated superstructure.

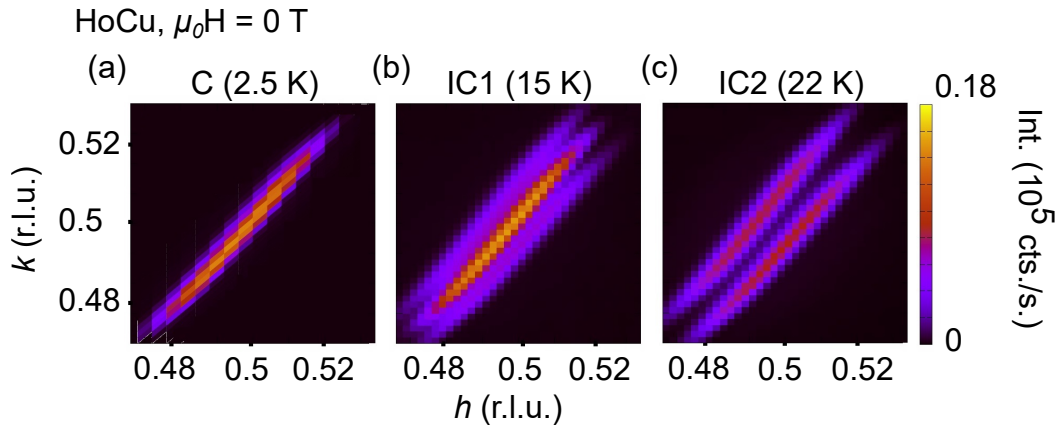


Figure 3.9.: Incommensurate modulation of the ground states in IC1 and IC2. Reciprocal space was mapped out in the vicinity of $(\frac{1}{2}, \frac{1}{2}, 0)$ in phase C at 2.5 K, in phase IC1 at 15 K, and in IC2 at 22 K. Data were recorded by means of a single point detector at the diffractometer HEiDi. (a) The commensurate peak in phase C, stretched along (110) due to the instrumental resolution, reflects commensurate $(\pi\pi 0)$ antiferromagnetism. (b,c) Incommensurate satellites in IC1 and IC2 are shifted by roughly ~ 0.02 within the $(h, k, 0)$ plane, and are due to $(\pi\pi 0)$ antiferromagnetism with a modulated superstructure.

In order to determine the propagation vectors in IC1 and IC2 accurately, the reciprocal space in the vicinity of $(\frac{1}{2}, \frac{1}{2}, 0)$ was mapped out at BIODIFF using neutrons with a wavelength $\lambda = 3.4 \text{ \AA}$ and an area detector. The sample was oriented such that the crystallographic plane $(1\bar{1}0)$ corresponded to the horizontal scattering plane. Intensities were recorded by means of rocking scans around the rocking angle ω_0 , under which the Bragg condition for the $(\frac{1}{2}, \frac{1}{2}, 0)$ reflection is fulfilled. For each Bragg peak identified in one of the rocking scans corresponding scattering vectors $\mathbf{k}_f - \mathbf{k}_i$ were calculated by means of Bragg's law, $\mathbf{k}_f - \mathbf{k}_i = \mathbf{G}$.

Fig. 3.11 shows sums over detector images for the rocking scans, recorded in the three phases C, IC1, and IC2 at $T \approx 5 \text{ K}$, $T \approx 15 \text{ K}$, and $T \approx 22 \text{ K}$, respectively. In phase C, the single Bragg peak at $(\frac{1}{2}, \frac{1}{2}, 0)$ reflects commensurate $(\pi\pi 0)$ magnetism. In phase IC1, the combination of a commensurate Bragg peak at $(\frac{1}{2}, \frac{1}{2}, 0)$, with four satellite Bragg peaks at $(\frac{1}{2} \pm \delta, \frac{1}{2}, 0)$ and $(\frac{1}{2}, \frac{1}{2} \pm \delta, 0)$ forms a fourfold pattern. The splitting parameter

is given by $\delta_{15\text{K}} = (0.023 \pm 0.003)$ r.l.u.. The diffraction pattern suggests a superposition of commensurate and incommensurate propagation vectors as the magnetic ground state. Weak intensities measured at higher-order positions may be due to multiple scattering. In phase IC2, a commensurate Bragg peak at $(\frac{1}{2}, \frac{1}{2}, 0)$ and incommensurate satellites at the positions $(\frac{1}{2} \pm \delta, \frac{1}{2}, 0)$ and $(\frac{1}{2}, \frac{1}{2} \pm \delta, 0)$ again form a fourfold pattern, similar to IC1. Here, the splitting parameter is given by $\delta_{22\text{K}} = (0.022 \pm 0.003)$ r.l.u.. Residual intensities, as observed at higher-order positions, may again arise due to multiple scattering effects. The two phases IC1 and IC2 may be directly compared as follows. The incommensurate shift along the fourfold directions (100) and (010) has a slightly smaller value in IC2 than in IC1. The intensity measured for the commensurate peak is considerably weaker in IC2 compared to IC1, while the four incommensurate satellites only have a slightly weaker intensity in IC2 than in IC1.

Propagation vectors of the two stars $\{(\frac{1}{2}, \frac{1}{2}, 0)\}$ and $\{(\frac{1}{2} - \delta, \frac{1}{2}, 0)\}$ are required to index the magnetic Bragg peaks in phases IC1 and IC2. The incommensurability is given by $\delta_{15\text{K}} \approx 0.023$ r.l.u. in IC1 and by $\delta_{22\text{K}} \approx 0.022$ r.l.u. in IC2. The ground states in IC1 and IC2 are multi- k , as they are a superposition of commensurate and incommensurate propagation vectors. The star $\{(\frac{1}{2} - \delta, \frac{1}{2}, 0)\}$, which is defined by the incommensurate propagation vectors, may also be labeled $\langle \frac{1}{2} - \delta, \frac{1}{2}, 0 \rangle$. This crystallographic $\langle \frac{1}{2} - \delta, \frac{1}{2}, 0 \rangle$ star has 12 different k -arms. For the present study we do not distinguish between conjugated k -arms, as their experimental signatures are equivalent. Accordingly, we consider unions, such as $[\mathbf{k}]_{\sim} \cup [-\mathbf{k}]_{\sim}$. These unions, which may be called Ω -arms, will in the present study simply be referred to as arms. Accordingly, the crystallographic star $\langle \frac{1}{2} - \delta, \frac{1}{2}, 0 \rangle$ has six different Ω -arms, which may be labeled $A_{1,x}^{ic} := [\frac{1}{2} \pm \delta, \frac{1}{2}, 0]_{\sim}$, $A_{1,y}^{ic} := [\frac{1}{2}, \frac{1}{2} \pm \delta, 0]_{\sim}$, $A_{2,y}^{ic} := [0, \frac{1}{2} \pm \delta, \frac{1}{2}]_{\sim}$, $A_{2,z}^{ic} := [0, \frac{1}{2}, \frac{1}{2} \pm \delta]_{\sim}$, $A_{3,z}^{ic} := [\frac{1}{2}, 0, \frac{1}{2} \pm \delta]_{\sim}$, and $A_{3,x}^{ic} := [\frac{1}{2} \pm \delta, 0, \frac{1}{2}]_{\sim}$. For the present study we choose the following conventions for specific representatives of these k -arms: $\mathbf{k}_{1,x}^{ic} = (\frac{1}{2} - \delta, \frac{1}{2}, 0)$, $\mathbf{k}_{1,y}^{ic} = (\frac{1}{2}, \frac{1}{2} - \delta, 0)$, $\mathbf{k}_{2,y}^{ic} = (0, \frac{1}{2} - \delta, \frac{1}{2})$, $\mathbf{k}_{2,z}^{ic} = (0, \frac{1}{2}, \frac{1}{2} - \delta)$, $\mathbf{k}_{3,z}^{ic} = (\frac{1}{2}, 0, \frac{1}{2} - \delta)$, and $\mathbf{k}_{3,x}^{ic} = (\frac{1}{2} - \delta, 0, \frac{1}{2})$.

Fig. 3.10 shows an illustration of the k -arms of magnetic propagation vectors at zero magnetic field. Shown in Fig. 3.10 (a) are Q -positions of all k -arms of the stars $\langle \frac{1}{2} \frac{1}{2} 0 \rangle$ and $\langle \frac{1}{2} - \delta, \frac{1}{2}, 0 \rangle$, respectively. Shown in Fig. 3.10 (b1), (b2), and (b3) are Q -positions, which belong to the k -arms A_1^c , A_2^c , and A_3^c , respectively. Shown in Fig. 3.10 (c1), (c2), (c3), (c4), (c5), and (c6) are Q -positions, which belong to the arms $A_{1,x}^{ic}$, $A_{1,y}^{ic}$, $A_{2,y}^{ic}$, $A_{1,z}^{ic}$, $A_{3,z}^{ic}$, and $A_{3,x}^{ic}$, respectively.

The fourfold pattern around commensurate $(\pi\pi 0)$ positions may be understood as follows. The two spots at $(\frac{1}{2} - \delta, \frac{1}{2}, 0)$ and $(\frac{1}{2} + \delta, \frac{1}{2}, 0)$ belong to the same Ω -arm $A_{1,x}^{ic}$, i.e., they belong to conjugated k -arms, and are indexed by the vectors $(0, 0, 0) + \mathbf{k}_{1,x}^{ic}$ and

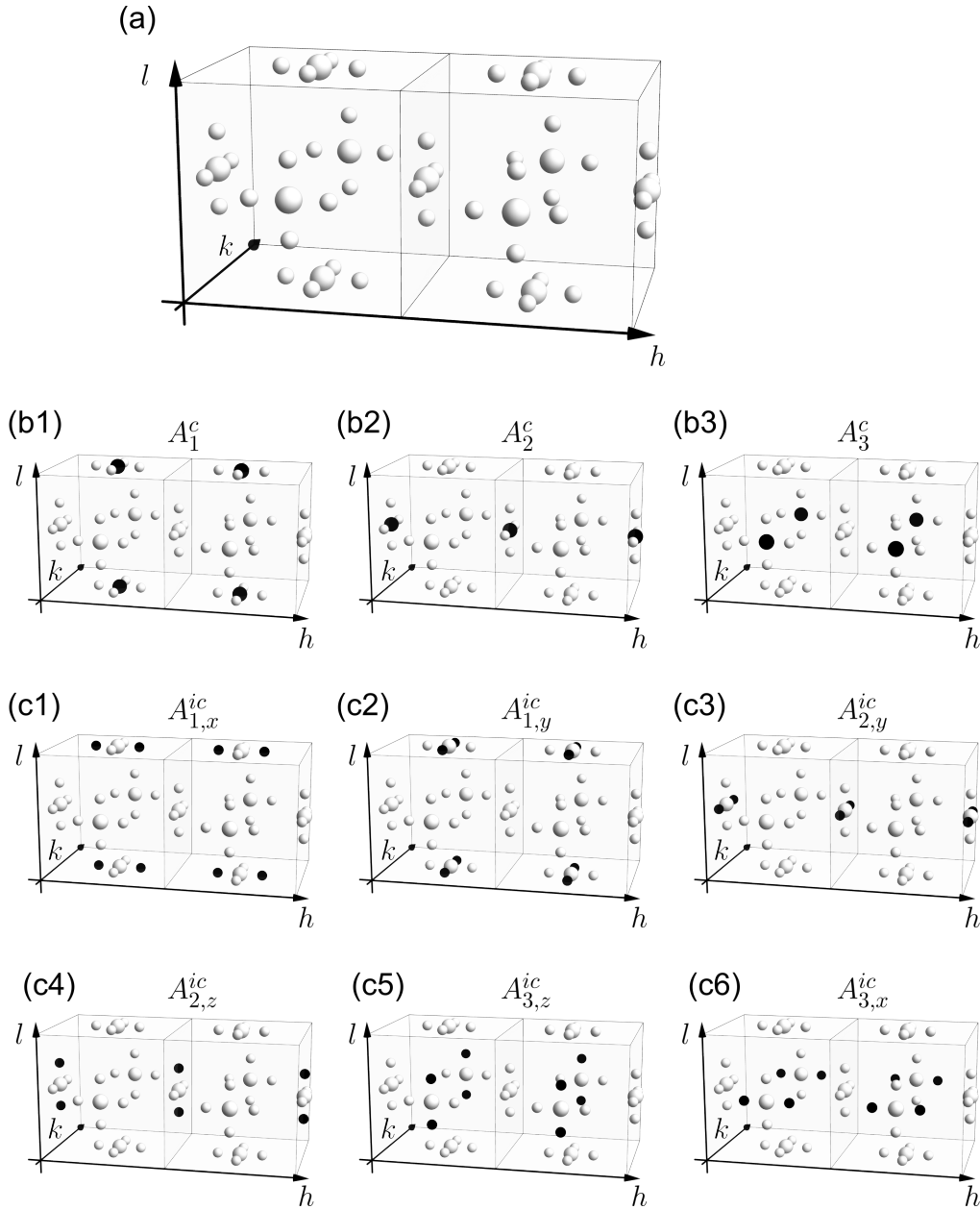


Figure 3.10.: Illustration of the three arms of the star $\langle \frac{1}{2} \frac{1}{2} 0 \rangle$ and the arms of the star $\langle \frac{1}{2} - \delta, \frac{1}{2}, 0 \rangle$. (a) Illustration of Q -positions, as indicated by grey spheres, of all k -vector arms of the two stars. (b1)-(b3) The Q -positions, which belong to the k -arms A_1^c , A_2^c , and A_3^c , respectively, are filled black. (c1)-(c6) The Q -positions, which belong to the arms $A_{1,x}^{ic}$, $A_{1,y}^{ic}$, $A_{2,y}^{ic}$, $A_{2,z}^{ic}$, $A_{3,z}^{ic}$, and $A_{3,x}^{ic}$, respectively, are filled black.

$(1, 1, 0) - \mathbf{k}_{1,x}^{ic}$, respectively, coming from two different structural positions. In contrast, peaks such as $(\frac{1}{2}, \frac{1}{2} - \delta, 0)$ and $(\frac{1}{2} - \delta, \frac{1}{2}, 0)$ belong to the arms $A_{1,y}^{ic}$ and $A_{1,x}^{ic}$, respectively. Accordingly, they belong to different Ω -arms of the star $\langle \frac{1}{2} - \delta, \frac{1}{2}, 0 \rangle$. They may be indexed by means of $(0, 0, 0) + \mathbf{k}_{1,y}^{ic}$ and $(0, 0, 0) + \mathbf{k}_{1,x}^{ic}$, respectively.

As the star $\langle \frac{1}{2} \frac{1}{2} 0 \rangle$ has three k -arms and $\langle \frac{1}{2} - \delta, \frac{1}{2}, 0 \rangle$ has six pairs of conjugated k -

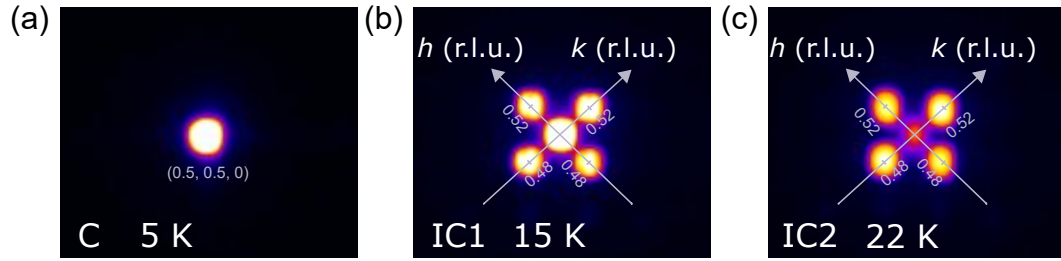
HoCu, $\mu_0 H = 0$ T

Figure 3.11.: Magnetic propagation vectors in the three zero field phases C, IC1, and IC2. Reciprocal space in the vicinity of $(\frac{1}{2}, \frac{1}{2}, 0)$ was mapped out at the temperatures $T = 5$ K, $T = 15$ K, and $T = 22$ K with a large area detector covering both vertical and horizontal angle. (a) In phase C, a single Bragg peak at $(\frac{1}{2}, \frac{1}{2}, 0)$ reflects commensurate $(\pi\pi 0)$ antiferromagnetism. (a,b) In phases IC1 and IC2, Bragg peaks were observed at the commensurate position $(\frac{1}{2}, \frac{1}{2}, 0)$, as well as at the incommensurate positions $(\frac{1}{2} \pm \delta, \frac{1}{2}, 0)$ and $(\frac{1}{2}, \frac{1}{2} \pm \delta, 0)$, where $\delta \approx 0.02$. In IC1 and IC2, the magnetic ground state is a superposition of commensurate and incommensurate propagation vectors of the stars $\langle \frac{1}{2} \frac{1}{2} 0 \rangle$ and $\langle \frac{1}{2} - \delta, \frac{1}{2}, 0 \rangle$, respectively. In particular, the ground state has a modulated superstructure.

arms, the ground states in IC1 and IC2 may have up to three commensurate propagation vectors of the star $\langle \frac{1}{2} \frac{1}{2} 0 \rangle$ and up to six incommensurate propagation vectors of the star $\langle \frac{1}{2} - \delta, \frac{1}{2}, 0 \rangle$. In particular, this points to, that the ground states in IC1 and IC2 are multi- k .

3.3.3.3. Small Angle Neutron Scattering

To determine, whether there is a ferromagnetic superstructure, small-angle neutron scattering (SANS) on the single crystal OFZ95-3-2-1-a was carried out at SANS-1 [127–129]. As the main result, these measurements established multiple scattering processes of the incommensurate antiferromagnetic $(\pi\pi 0)$ reflections causing strong SANS signals in phases IC1 and IC2. This is reflected by the strong wavelength dependence of the SANS intensities [130, 131]. No evidence for SANS signals due to Bragg scattering from ferromagnetic order was found. These phenomena are reminiscent of related studies on potassium, for which an experimental study by Giebultowicz *et al.* initially inferred from scattering data the existence of charge density waves [132]. Pintschovius *et al.* [133], however, found a strong wavelength dependence of scattering intensities that cannot arise due to Bragg scattering.

Multiple scattering as the origin of SANS in phases IC1 and IC2 of HoCu was identified by the strong wavelength dependence of the SANS signals, as explained further below, and by Renninger scans. That this multiple scattering observed in SANS is caused by incommensurate antiferromagnetic $(\pi\pi 0)$ peaks is indicated by the following observations. In rocking scans, the peaks in the SANS display their maxima roughly at rocking angles, where the Bragg position is also fulfilled for peaks at antiferromagnetic $(\pi\pi 0)$ positions. The splitting parameters δ for incommensurate peaks in the SANS correspond to the parameters, which were observed for incommensurate $(\pi\pi 0)$ reflections in IC1 and IC2 (cf. Sec. 3.3.3.2)

To establish the strong wavelength dependence of SANS, rocking scans were performed with two different neutron wavelengths. First, SANS was carried out with neutrons of wavelength 4.5 Å. Strong SANS was observed in both phases, IC1 and IC2. Second, SANS was carried out with neutrons of wavelength 5.5 Å in phase IC1. The comparison of the two sets of measurements revealed a strong wavelength dependence. Further, the rocking scans corresponded to Renninger scans for SANS caused by a putative wavevector $\mathbf{Q}_{1/2}$ with a small q -value as arising due to a ferromagnetic superstructure. The wavevectors $\mathbf{Q}_{1/2}$ are specified further below. As a function of rocking angle, the SANS intensity, which may be caused by $\mathbf{Q}_{1/2}$, becomes vanishingly small for large angle ranges. All observed SANS intensities as a function of rocking angle featured maxima at angles, where the Bragg condition is fulfilled for antiferromagnetic $(\pi\pi 0)$ positions. This finding suggests that the SANS signals arise not from magnetic Bragg scattering of small q values, but from multiple scattering at incommensurate antiferromagnetic $(\pi\pi 0)$ reflections.

For the SANS experiments the sample was oriented such that the scattering plane corresponded to the crystallographic (001) plane. In the first set of measurements with

wavelength $\lambda = 4.5 \text{ \AA}$, rocking scans were carried out in the range $\omega = 46^\circ \pm 7.5^\circ$. SANS recorded in phase C did not display scattering different from the paramagnetic state. For the SANS measurements carried out in phases IC1 and IC2, at $T = 15 \text{ K}$ and $T = 22 \text{ K}$, sums over detector images are shown in Fig. 3.12. In IC1 (Fig. 3.12 (a)), at $T = 15 \text{ K}$, relatively strong peaks appeared at the detector positions $(q_x, q_y) = (\pm\delta, 0)$, $(0, \pm\delta)$, as well as at the diagonal positions $\pm(\delta, \pm\delta)$. Peaks at the second-order positions $(\pm 2\delta, 0)$ and $(0, \pm 2\delta)$ were weaker by one order of magnitude. The splitting parameter is given by $\delta = (0.4346 \pm 0.0002) \text{ \AA}^{-1}$. In phase IC2 (Fig. 3.12 (b)), peaks at diagonal positions, i.e., $\pm(\delta, \pm\delta)$, were relatively strong with intensities one order of magnitude stronger than at first-order positions and second-order positions. The splitting in IC2 is given by $\delta = (0.0399 \pm 0.0001) \text{ \AA}^{-1}$. In both phases, IC1 and IC2, the splitting parameters δ correspond to the values observed for antiferromagnetic satellites in the vicinity of $(\frac{1}{2}, \frac{1}{2}, 0)$ (cf. Sec. 3.3.3.2).

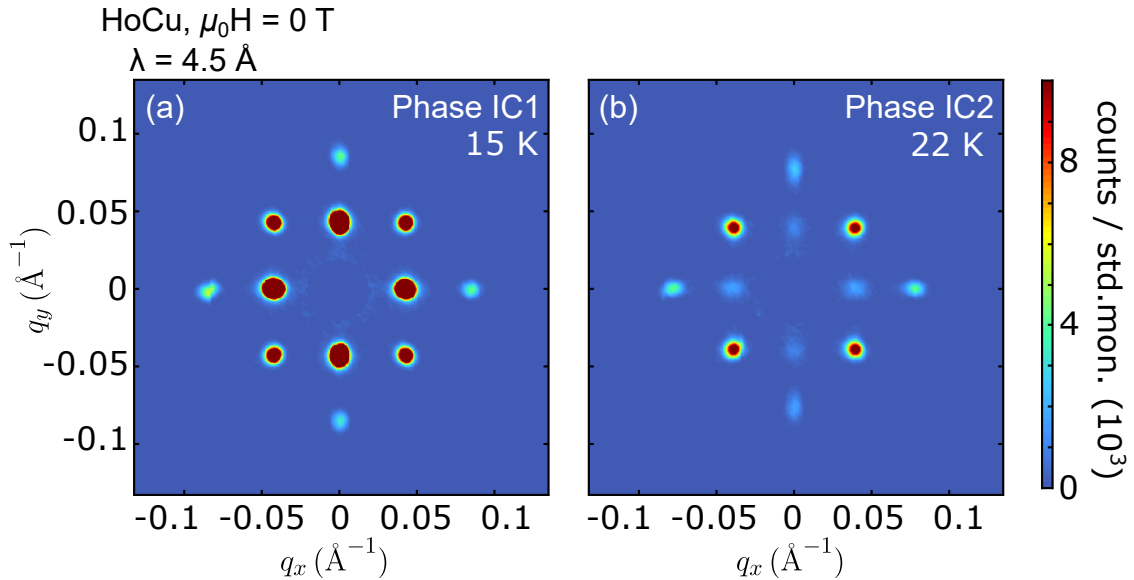


Figure 3.12.: SANS measured in phases IC1 and IC2 with neutrons of wavelength $\lambda = 4.5 \text{ \AA}$. Shown are sums of detector images for a rocking scan $\omega = 46^\circ \pm 7.5^\circ$ carried out (a) in phase IC1 at $T = 15 \text{ K}$ and (b) in phase IC2 at $T = 22 \text{ K}$. The crystallographic $[001]$ direction was perpendicular to the scattering plane. As discussed in the text, SANS arises due to multiple scattering at incommensurate $(\pi\pi 0)$ peaks.

In the second set of measurements with a wavelength $\lambda = 5.5 \text{ \AA}$ a large rocking scan through $\omega = \pm 180^\circ$ was carried out in phase IC1 at $T = 15 \text{ K}$. Fig. 3.13 (a) shows the sum over corresponding detector images. The vertical peaks $(0, \pm\delta)$ were distinctively weaker than the horizontal peaks $(\pm\delta, 0)$. In contrast, in the first set of measurements with wavelength $\lambda = 4.5 \text{ \AA}$ horizontal and vertical peaks featured similar intensities (cf. Fig. 3.12 (a)).

For wavevectors $\mathbf{Q}_{1/2} = (0, 0, \pm\delta)$, the rocking scan in Fig. 3.12 corresponded to a

HoCu, Phase IC1, $T = 15$ K, $\mu_0 H = 0$ T

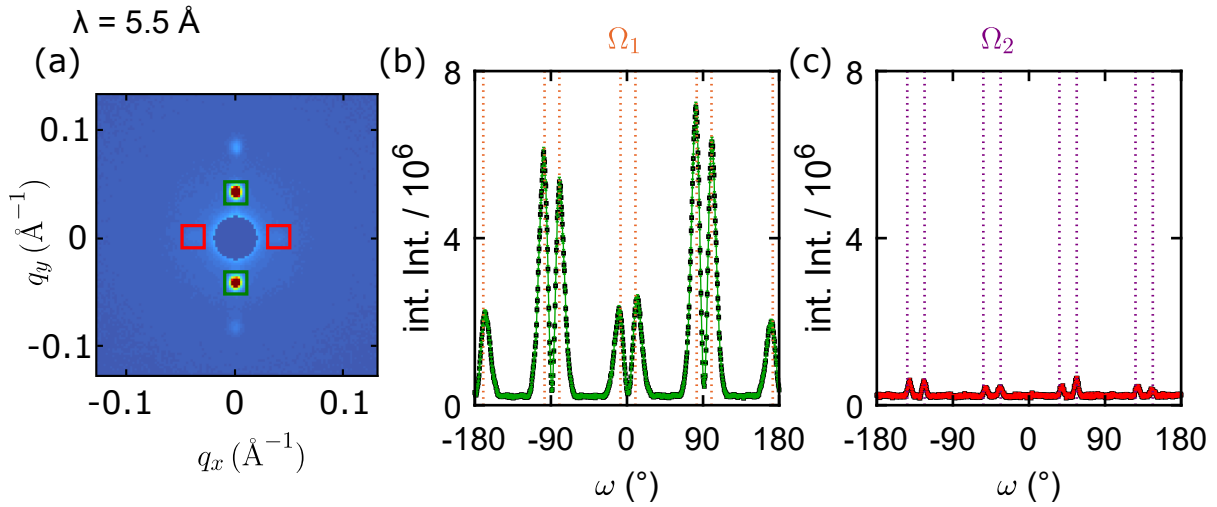


Figure 3.13.: Evidence for multiple scattering in SANS in HoCu. SANS was measured in IC1 with a neutron wavelength of $\lambda = 5.5$ \AA . Therefore, a large rocking scan was carried out $\omega = \pm 180^\circ$ at $T = 15$ K. (a) Sum of detector images for the rocking scan. (b) Average of integrated intensities for the green regions of interest (ROIs), which were defined in (a). The orange lines indicate the positions Ω_1 of rocking angles, where the Bragg condition is fulfilled for one of the four peaks $(\frac{1}{2}, 0, \pm\frac{1}{2})$ and $-(\frac{1}{2}, 0, \pm\frac{1}{2})$. (c) Average of integrated intensities for the red ROIs, which were defined in (a). The purple lines indicate the positions Ω_2 of rocking angles, where the Bragg condition is fulfilled for one of the peaks $(\frac{1}{2}, \pm\frac{1}{2}, 0)$ and $-(\frac{1}{2}, \pm\frac{1}{2}, 0)$.

Renninger scan. If peaks at $(0, \pm\delta)$ in the detector images were due to Bragg scattering from $\mathbf{Q}_{1/2}$ the intensity must not change for rotations of the sample around \mathbf{Q} , as the rotations do not affect the Bragg condition for wave vectors $\mathbf{Q}_{1/2}$ (cf. Refs. [8, 62]). However, as established in the following, the intensity at $(0, \pm\delta)$ becomes vanishingly small for various rocking angles.

Figs. 3.13 (b) and (c) show the intensities of regions of interest at $(\pm\delta, 0)$ and $(0, \pm\delta)$ as a function of ω for the large rocking scan with wavelength 5.5 \AA . Notably, horizontal and vertical intensities, $(\pm\delta, 0)$ and $(0, \pm\delta)$, never appeared simultaneously within an ω -range $\pm 7.5^\circ$, other than for neutrons with wavelength $\lambda = 4.5$ \AA (Fig. 3.12 (a)). This reflects the strong wavelength dependence of SANS. For $(0, \pm\delta)$, the intensity as a function of rocking angle has pairs of maxima and displays vanishingly small intensities for large angle ranges (cf. Fig. 3.12 (b)). This indicates, that the intensity at $(0, \pm\delta)$ is not caused by Bragg scattering from $\mathbf{Q}_{1/2}$, but by multiple scattering.

The vertical peaks $(0, \pm\delta)$ appeared at exactly those rocking angles $\in \Omega_1$, where the Bragg condition is fulfilled for one of the antiferromagnetic peaks $(\frac{1}{2}, 0, \pm\frac{1}{2})$, $-(\frac{1}{2}, 0, \pm\frac{1}{2})$, $\pm(0, \frac{1}{2}, \pm\frac{1}{2})$, and $-(0, \frac{1}{2}, \pm\frac{1}{2})$. In contrast, the horizontal peaks $(\pm\delta, 0)$ appeared at rocking angles Ω_2 , where the Bragg condition is fulfilled for one of the wave vectors

$\pm (\frac{1}{2}, \pm \frac{1}{2}, 0)$. This confirms that the SANS signals are due to multiple scattering from antiferromagnetic $(\pi\pi 0)$ Bragg peaks.

3.3.3.4. Representational Analysis of the Magnetic Structures

Magnetic structures may be decomposed into a Fourier series of basis functions that are associated with irreducible representations (IRs). The IRs may be calculated, when spacegroup and magnetic propagation vectors are given. IRs and their basis functions represent natural normal modes of a magnetic structure. To determine all IRs as well as the corresponding basis functions for the two types of propagation vectors, which are present in HoCu at zero magnetic field, a representational analysis was carried out by means of the software *SARAh* [54]. A representational analysis provides all IRs that are allowed by symmetry. The IRs that are physically relevant and that, in fact, describe the ground states are determined further below by a polarization analysis (cf. Sec. 3.3.3.5) and Rietveld refinements (cf. Sec. 3.3.3.6).

As the main results this analysis shows that:

- The magnetic ground state in phase C may be decomposed into a Fourier series with up to three propagation vectors of the star $\{\mathbf{k}_c\}$, where $\mathbf{k}_c = \left(\frac{1}{2}, \frac{1}{2}, 0\right)$. Each Fourier component can be written as superposition of $\Gamma_3(\mathbf{k}_c)$ and $\Gamma_9(\mathbf{k}_c)$ basis functions.
- The magnetic ground states in phases IC1 and IC2 may be decomposed into a Fourier series with up to three propagation vectors of the star $\{\mathbf{k}_c\}$ and six propagation vectors of the star $\{\mathbf{k}_{ic}\}$, where $\mathbf{k}_{ic} = \left(\frac{1}{2} - \delta, \frac{1}{2}, 0\right)$. Each commensurate Fourier component may be decomposed analogously to phase C. Each incommensurate Fourier component is a superposition of $\Gamma_2(\mathbf{k}_{ic})$, $\Gamma_3(\mathbf{k}_{ic})$, and $\Gamma_4(\mathbf{k}_{ic})$ basis functions.

Propagation vector	IR	BV	BV components					
			$m_{\parallel a}$	$m_{\parallel b}$	$m_{\parallel c}$	$im_{\parallel a}$	$im_{\parallel b}$	$im_{\parallel c}$
$\mathbf{k}_c = \left(\frac{1}{2}, \frac{1}{2}, 0\right)$	Γ_3	$\Psi_1^{\mathbf{k}_c}$	0	0	16	0	0	0
	Γ_9	$\Psi_2^{\mathbf{k}_c}$	8	0	0	0	0	0
		$\Psi_3^{\mathbf{k}_c}$	0	-8	0	0	0	0
$\mathbf{k}_{ic} = \left(\frac{1}{2} - \delta, \frac{1}{2}, 0\right)$	Γ_2	$\Psi_1^{\mathbf{k}_{ic}}$	4	0	0	0	0	0
	Γ_3	$\Psi_2^{\mathbf{k}_{ic}}$	0	4	0	0	0	0
	Γ_4	$\Psi_3^{\mathbf{k}_{ic}}$	0	0	4	0	0	0

Table 3.2.: Analysis of representations of the magnetic Ho site in space group $Pm\bar{3}m$. For each magnetic propagation vector \mathbf{k} that was detected in one of the zero field phases of HoCu, the IRs $\Gamma(\mathbf{k})$ containing non-trivial basis functions $\Psi^{\mathbf{k}}$ are listed. The analysis was carried out by means of the software *SARAh* [54].

Tab. 3.2 summarizes the results of the representational analysis as obtained for propagation vectors \mathbf{k}_c , \mathbf{k}_{ic} , and space group $Pm\bar{3}m$. For the commensurate propagation vector $\mathbf{k}_c = \left(\frac{1}{2}, \frac{1}{2}, 0\right)$ the magnetic representation splits into $\Gamma = 1\Gamma_3^1 + 1\Gamma_9^2$. The IR Γ_3 has the order $\nu = 1$ containing one basis function which is perpendicular to the basal plane of

the propagation vector. In contrast, Γ_9 has the order $\nu = 2$ and contains the two basis functions $\Psi_2^{\mathbf{k}^c}$ and $\Psi_3^{\mathbf{k}^c}$, both of which lie within the basal plane of the propagation vector. For incommensurate propagation vectors \mathbf{k}_{ic} , the magnetic representation is decomposed into $\Gamma = 1\Gamma_2^1 + 1\Gamma_3^1 + 1\Gamma_4^1$. Each IR has the order $\nu = 1$ and contains one basis function only. The most general magnetic structure in the zero field phases of HoCu can thus be written as follows:

$$\mathbf{m}(\mathbf{R}) = \sum_{\mathbf{k} \in \Omega, l} C_l^{\mathbf{k}} \Psi_l^{\mathbf{k}} (\exp(i\mathbf{k} \cdot \mathbf{R}) + \exp(-i\mathbf{k} \cdot \mathbf{R})) . \quad (3.9)$$

In phase C, the sum $\sum_{\mathbf{k} \in \Omega, l}$ goes over the (representatives of) three k -arms of the $\langle \frac{1}{2} \frac{1}{2} 0 \rangle$ star, i.e., \mathbf{k}_i^c ($1 \leq i \leq 3$). As the three commensurate propagation vectors fulfil the relationship $\exp(i\mathbf{k}_c \mathbf{R}) = \exp(-i\mathbf{k}_c \mathbf{R})$, the magnetic ground state in phase C can be written as follows:

$$\mathbf{m}(\mathbf{R}) = \sum_{j=1}^{N_k} \mathbf{r}(\mathbf{k}_j^c) \cdot \exp(i\mathbf{k}_j^c \cdot \mathbf{R}) . \quad (3.10)$$

In the incommensurate phases IC1 and IC2, the sum $\sum_{\mathbf{k} \in \Omega, l}$ goes over (representatives of) the three k -arms of the $\langle \frac{1}{2} \frac{1}{2} 0 \rangle$ star and over the six Ω -arms of the $\langle \frac{1}{2} - \delta, \frac{1}{2}, 0 \rangle$ star. In principle each superposition in Eq. (3.9) may give rise to a conceivable magnetic structure [134]. However, Landau theory often narrows down the number of possible structures. In phases, for which Landau theory is applicable, only superpositions with basis functions associated with one IR only should be allowed (cf. Sec. 2.2). As in HoCu only the transition at T_N is clearly of second order, Landau theory may be applied in IC2 only. However, in practice Landau theory often applies, even if the transitions are not of second order.

3.3.3.5. Polarization Analysis

In the representational analysis, which was reported in Sec. 3.3.3.4, all IRs were determined that are allowed by symmetry. Typically only very few of them are relevant and describe the magnetic ground states. To experimentally determine the IRs that describe the magnetic ground states in phases C, IC1, and IC2, polarized neutron diffraction of the sample OFZ95-3-3-h was carried out at the diffractometer DNS [135]. In particular, this study provides the pre-factors to each sinusoidal term in the Fourier series of the ground states.

The main results of these experiments may be summarized as follows:

- The intensity at the position $(1, 1, 0)$ is purely structural in phases C, IC1, and IC2. Scattering processes are purely non-spin-flip for incident neutron spins $\parallel \hat{Q}$, which is characteristic of scattering at structural Bragg peaks. In particular, no ferromagnetic component contributes to the magnetic ground state in phase C.
- The intensity at the position $(1, 1, 0)$ is temperature dependent. This dependence, however, does not arise due to multiple scattering, but presumably due to magnetoelastic effects.
- All Bragg peaks in the vicinity of $(\frac{1}{2}, \frac{1}{2}, 0)$, commensurate and incommensurate, are purely magnetic in phases C, IC1, and IC2. The scattering processes are namely purely spin-flip for incident neutron spins $\parallel \hat{Q}$, which is characteristic of magnetic scattering.
- In phase C, the magnetic ground state consists of only $\Gamma_9(\mathbf{k}_c)$ basis functions. There are five structures, two being single- k , two double- k , and one triple- k , among the 21 $(\pi\pi 0)$ structures in Tab. 3.1 that meet this condition.
- In phase IC1, the magnetic ground state consists of $\Gamma_3(\mathbf{k}_c)$ basis functions and $\Gamma_4(\mathbf{k}_{ic})$ basis functions. Hence, for given propagation vectors the pre-factors in the Fourier decomposition of the ground state are known up to complex phase shifts. The number of k -vectors, however, cannot be inferred from the polarization analysis.
- In phase IC2, the magnetic ground state consists of $\Gamma_4(\mathbf{k}_{ic})$ basis functions and commensurate contributions. These commensurate contributions may be a pure superposition of only $\Gamma_3(\mathbf{k}_c)$ or only $\Gamma_9(\mathbf{k}_c)$ basis functions, or they may be a mixture of both.

The irreducible representations that describe the ground states in phases C, IC1, and IC2, were inferred from polarization experiments as follows. First, the experimental polarization rate α of the incident beam at the DNS instrument was determined in the paramagnetic regime at the structural peak $(1, 1, 0)$, for which all scattering processes are expected to be purely non-magnetic and non-spin-flip. Second, the diagonal entries

of polarization matrices were determined in phases C, IC1, and IC2 for all first-order magnetic Bragg peaks in the vicinity of $(\frac{1}{2}, \frac{1}{2}, 0)$ as well as for the structural position $(1, 1, 0)$. Third, the irreducible representations that describe the magnetic ground states in phases C, IC1, and IC2 were inferred from the polarization matrices by means of the Blume-Maleev equations [35, 36] (cf. Secs. 2.1.2 and 3.2 for further information).

For these measurements, the sample was oriented such that the scattering plane corresponded to the crystallographic (001) plane. Neutrons with wavelength $\lambda \approx 4.2 \text{ \AA}$ were used. Only magnetic peaks in the vicinity of $(\frac{1}{2}, \frac{1}{2}, 0)$ were accessible. As is common for polarized neutrons, a set of Cartesian coordinates was defined with respect to the scattering vector $\mathbf{Q} = (h, k, l)$, such that \hat{e}_z is vertical, $\hat{e}_x \parallel \mathbf{Q}$ and $\hat{e}_y = \hat{e}_z \times \hat{e}_x$. At DNS, the initial polarization \mathbf{P}_i of the incident neutron beam may be adjusted parallel to one of the three Cartesian axes, i.e., $\mathbf{P}_i = \hat{n}$ with $\hat{n} \in \{\mathbf{e}_x, \mathbf{e}_y, \mathbf{e}_z\}$. The polarization \mathbf{P}_f of the scattered neutrons may then be analyzed with respect to the direction \hat{n} , along which the incoming beam is polarized. This procedure allows to determine the diagonal elements of polarization matrices only. In the following, the three different polarizations are referred to as polarization channels.

Polarization matrices were inferred from the data by the following procedure. For each Bragg peak, maps with both spin-flip and non-spin-flip intensities were recorded for the surrounding reciprocal space region within the $(h, k, 0)$ plane. Therefore, rocking scans were carried out and the scattered beam was analyzed at different detector bank positions. For all three polarization channels, maps for both spin-flip (–) and non-spin-flip (+) scattering were inferred by the software available at DNS, providing:

$$J_n^-(h, k, 0) = J_n^{\text{sf}} = J_{n \rightarrow \bar{n}} \quad (3.11)$$

$$J_n^+(h, k, 0) = J_n^{\text{nsf}} = J_{n \rightarrow n}. \quad (3.12)$$

Each Bragg peak was approximated with a two-dimensional Gaussian profile by a least squares fit:

$$a_0^\pm \exp \left[-\frac{1}{2} \left(\frac{h - h_0}{\sigma_h} \right)^2 - \frac{1}{2} \left(\frac{k - k_0}{\sigma_k} \right)^2 \right] \xrightarrow{\text{fit}} J^\pm(h, k, 0). \quad (3.13)$$

Integrated intensities $I^\pm = \int J^\pm(h, k, 0) dh dk$ of spin-flip and non-spin-flip channels were inferred from the Gaussian profiles. To obtain the diagonal elements of the polarization matrix, intensities were corrected by a factor $\gamma = \frac{1}{1-2\epsilon}$ that accounts for the polarization rate $\alpha = 1 - \epsilon < 1$ of the incident beam:

$$P_{nn}^o = \gamma (I_n^+ - I_n^-) / (I_n^+ + I_n^-). \quad (3.14)$$

For our data analysis we assume that the incident beam is not fully polarized, whereas other corrections are neglected. To determine the polarization rate α of the incident beam, the nuclear peak $(1, 1, 0)$ was investigated in the paramagnetic regime at $T = 45$ K. The polarization, as measured in the x -channel, was given by $P'_{xx} = (I_x^+ - I_x^-) / (I_x^+ + I_x^-) = 0.94 \pm 0.01$. For a fully polarized beam, one expects $P_{xx}^c = +1$, as the scattering process is purely non-spin-flip. It was inferred that a polarization rate $\alpha = 1 - \epsilon = 0.97$ is in agreement with the analyzed polarization P'_{xx} . Consequently, all experimental polarization matrices were corrected by a factor $\gamma = \frac{1}{1-2\epsilon} \approx 1.06$ to compensate for this lack of full polarization.

Tab. 3.3 summarizes all polarization matrices that were measured for magnetic and structural reflections in phases C, IC1, and IC2. For the structural reflection $(1, 1, 0)$ the entries of the polarization matrices were 1 in all phases, implying that the scattering processes are all purely non-spin-flip. This reflects the purely non-magnetic origin of the Bragg peak at the $(1, 1, 0)$ position. In particular, the ground states in C, IC1, and IC2 do not have any ferromagnetic component. However, the intensity at the position $(1, 1, 0)$ is temperature dependent, in agreement with the data presented in Fig. 3.7:

$$\frac{I^{(110)}(T)}{I_{45\text{K}}^{(110)}} = \begin{cases} 1.096 \pm 0.006 & , T = 5 \text{ K} \\ 1.078 \pm 0.006 & , T = 15 \text{ K} \\ 1.056 \pm 0.006 & , T = 22 \text{ K} \end{cases} . \quad (3.15)$$

No multiple scattering processes were identified to explain these temperature dependent contributions at the position $(1, 1, 0)$ in C, IC1, and IC2 suggesting magnetoelastic effects as the plausible origin. In contrast, all Bragg peaks in the vicinity of $(\frac{1}{2}, \frac{1}{2}, 0)$ were purely spin-flip in the x -channel $P_{xx} \approx -1$ reflecting their purely magnetic origin (cf. Ref. [136]).

In phase C, the polarization matrix of the commensurate Bragg peak fulfills $P_{yy} \approx -P_{zz} \approx -0.85$ indicating that moments corresponding to a propagation vector $\mathbf{k}_c = (\frac{1}{2}, \frac{1}{2}, 0)$ of the magnetic ground state in phase C lie mainly in the crystallographic (001) plane, whereas projections along [001] are small. In phase IC1, the polarization matrix of the commensurate Bragg peak fulfills $P_{yy} \approx -P_{zz} \approx +0.85$ indicating that moments corresponding to a propagation vector \mathbf{k}_c of the magnetic ground state in phase IC1 are mainly directed along the [001] axis, whereas projections in the (001) plane are small (cf. Ref. [137]).

The incommensurate Bragg peaks have a polarization matrix consistent with $P_{yy} = -P_{zz} = -1$ implying that magnetic moments corresponding to a propagation vector $\mathbf{k}_{ic} = (\frac{1}{2} - \delta, \frac{1}{2}, 0)$ of the magnetic ground state in phase IC1 are directed along the [001] axis. In phase IC2, the polarization matrix of the commensurate Bragg peak fulfills

$P_{yy} \approx P_{zz} \approx -0.4$ indicating that moments corresponding to a commensurate propagation vector \mathbf{k}_c of the magnetic ground state in phase IC2 have finite projections both along [001] and within the plane (001). The incommensurate Bragg peaks have a polarization matrix consistent with $P_{yy} = -P_{zz} = -1$ implying that moments corresponding to a propagation vector \mathbf{k}_{ic} of the magnetic ground state in phase IC2 are directed along the [001] axis.

Q-position	Phase C	Phase IC1	Phase IC2
(1, 1, 0)	(1.00, 1.00, 1.00)	(1.00, 1.01, -)	(1.00, 1.00, -)
$\left(\frac{1}{2}, \frac{1}{2}, 0\right)$	(-1, +0.85, -0.88)	(-1.02, -0.87, +0.87)	(-1.01, -0.39, +0.41)
$\left(\frac{1}{2} - \delta, \frac{1}{2}, 0\right)$	-	(-1.02, -0.99, +1.00)	(-1.02, -0.99, +1.00)
$\left(\frac{1}{2} + \delta, \frac{1}{2}, 0\right)$	-	(-1.02, -0.99, +0.99)	(-1.02, -0.99, +0.99)
$\left(\frac{1}{2}, \frac{1}{2} - \delta, 0\right)$	-	(-1.02, -1.00, +1.00)	(-1.02, -0.99, +0.98)
$\left(\frac{1}{2}, \frac{1}{2} + \delta, 0\right)$	-	(-1.02, -0.96, +0.96)	(-1.02, -0.96, +0.97)

Table 3.3.: Polarization matrices determined experimentally for nuclear as well as magnetic peaks in phases C, IC1, and IC2, at 5 K, 15 K, and 22 K, respectively. For the measurements, the HoCu sample was oriented such that the scattering plane corresponded to the crystallographic (001) plane. Shown are the diagonals of the polarization matrices only. The statistical errors are all smaller than ± 0.02 .

The irreducible representations that describe the magnetic ground states may be determined from Tab. 3.3 by means of the Blume-Maleev equations (cf. Sec. 2.1.2). As argued in the following, the magnetic ground state in phase C represents a superposition of basis functions from $\Gamma_9(\mathbf{k}_c)$ only. In particular, no basis functions from $\Gamma_3(\mathbf{k}_c)$ occur in the Fourier series, which is equivalent to $C_1^{\mathbf{k}_c^i} = 0$. The commensurate ground state in phase C may then be expanded as follows:

$$\mathbf{m}(\mathbf{R}) = \sum_j \left[C_2^{\mathbf{k}_c^j} \Psi_2^{\mathbf{k}_c^j} + C_3^{\mathbf{k}_c^j} \Psi_3^{\mathbf{k}_c^j} \right] \exp(i\mathbf{k}_j^c \cdot \mathbf{R}). \quad (3.16)$$

From the measurements this may be inferred as follows. The polarization matrix measured at the commensurate peak $\left(\frac{1}{2}, \frac{1}{2}, 0\right)$ fulfills $P_{yy}^o \approx -P_{zz}^o \approx 0.85$ (Tab. 3.3). As shown in Sec. A.2, a polarization matrix fulfilling $P_{yy} = -P_{zz} = +1$ would in fact imply that only the basis functions Ψ_2 and Ψ_3 , which are associated with $\Gamma_9(\mathbf{k}_c)$, can contribute to the Fourier decomposition of \mathbf{m} . For each of the 21 commensurate $(\pi\pi 0)$ structures in Tab. 3.1 the polarization matrices were calculated by means of Eq. (2.16). All calculated matrices have diagonals of shape $(-1, \alpha, -\alpha)$. Fig. 3.14 shows the calculated values α for each of the 21 $(\pi\pi 0)$ structures (cf. Tab. 3.1) in comparison with the measured value $P_{yy}^o \approx 0.85$. The structures that agree best with the experimental data, are s2, s4, d2, d5

and t2. All of them are superpositions of $\Gamma_9(\mathbf{k}_c)$ basis functions only, which implies that $P_{yy} = -P_{zz} = +1$.

In fact, the five structures s2, s4, d2, d5, and t2 are the only structures among the 21 structures in Tab. 3.1 that are superpositions of only $\Gamma_9(\mathbf{k}_c)$ basis functions. It is inferred that the ground state in phase C represents one of the five structures s2, s4, d2, d5 and t2. The mismatch between $P_{yy}^o \approx 0.85$ and $P_{yy}^c = 1$ may be explained due to double spin-flip scattering. As explained in Sec. 3.3.3.3, double scattering is relatively strong in HoCu. In particular, multiple scattering processes of third order may lead to additional double spin-flip intensities at the $(\frac{1}{2}, \frac{1}{2}, 0)$ position. A simulation of such processes would be difficult. However, as illustrated by the red area in Fig. 3.14, an additional double spin-flip contribution at the commensurate peak position amounting to approximately 10% of the pure $(\frac{1}{2}, \frac{1}{2}, 0)$ peak signal would lead to a difference $\Delta_{2sf} \approx 0.2$ in the measured polarization P^o and may explain the mismatch between $P_{yy}^o \approx 0.85$ and $P_{yy}^c = 1$.

Accordingly, the ground state in C is associated with an angle $\theta = 90^\circ$, in contrast to 56° , which was reported in Ref. [68] for phase C and inferred by means of polycrystalline neutron diffraction.

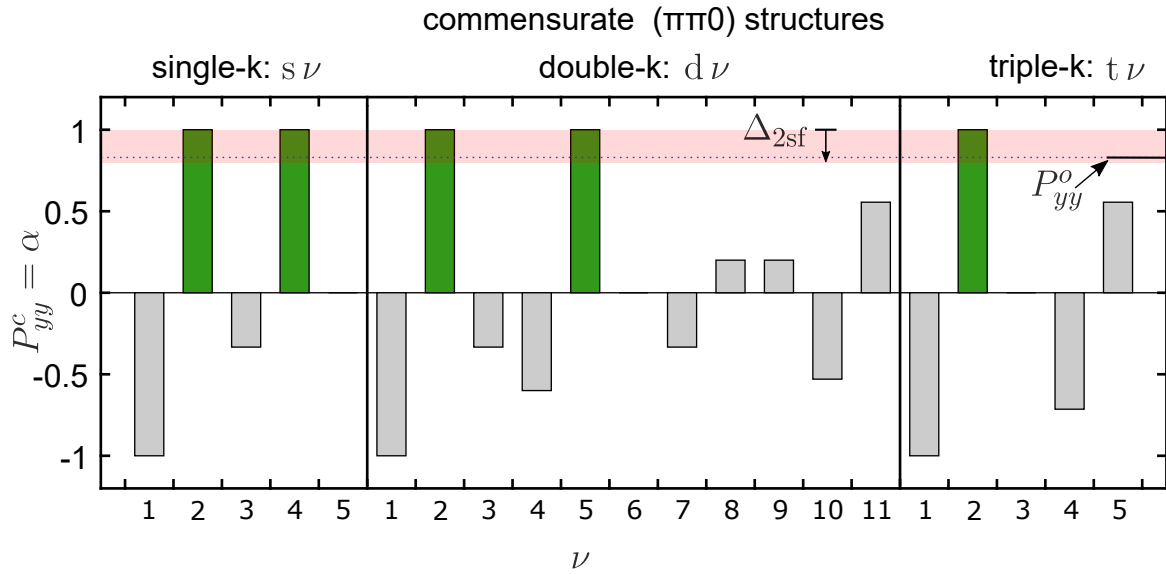


Figure 3.14.: Comparison of measured vs. calculated polarization matrices in phase C. For the 21 commensurate $(\pi\pi0)$ structures in Tab. 3.1, the polarization matrix elements $\alpha = P_{yy}^c$ were calculated by means of the Blume-Maleev equations (cf. Sec. 3.2) for a scattering process with $\mathbf{Q} = (\frac{1}{2}, \frac{1}{2}, 0)$, the sample oriented such that $[001]$ is vertical. The experimental values P_{yy}^o were inferred from the data, recorded by means of polarized neutrons. The five structures s2, s4, d2, d5, and t5 yield $P_{yy}^c = \alpha = +1$ and fit best to the measured polarization $P_{yy}^o = +0.85$. As indicated by the red area, a double spin-flip signal that is roughly 10% of the pure magnetic signal may explain the discrepancy between measured and calculated values.

As shown further, the commensurate contributions to the magnetic ground state in

phase IC1 are a superposition of only $\Gamma_3(\mathbf{k}_c)$ basis functions and the incommensurate contributions a superposition of only $\Gamma_4(\mathbf{k}_{ic})$ basis functions. In particular, no basis functions from $\Gamma_9(\mathbf{k}_c)$ contribute to the commensurate propagation and no basis functions from $\Gamma_2(\mathbf{k}_{ic})$ and $\Gamma_3(\mathbf{k}_{ic})$ contribute to the incommensurate propagation in the Fourier series. The ground state in phase IC1 may then be expanded as follows:

$$\begin{aligned} \mathbf{m}(\mathbf{R}) &= \sum_{\mathbf{k} \in \{\mathbf{k}_c\}} C^{\mathbf{k}} \Psi_1^{\mathbf{k}} \cdot \exp(i\mathbf{k} \cdot \mathbf{R}) + \sum_{\mathbf{k} \in \{\mathbf{k}_{ic}\}} \Psi_3^{\mathbf{k}} \left(C^{\mathbf{k}} \exp(i\mathbf{k}) + C^{-\mathbf{k}} \exp(-i\mathbf{k}) \right) = \\ &= \sum_{\mathbf{k} \in \{\mathbf{k}_c\}} \alpha^{\mathbf{k}} \Psi_1^{\mathbf{k}}(\mathbf{k}) \cdot \exp(i\mathbf{k} \cdot \mathbf{R}) + \sum_{\mathbf{k} \in \{\mathbf{k}_{ic}\}} \alpha^{\mathbf{k}} \Psi_3^{\mathbf{k}} \cdot \cos(\mathbf{k} \cdot \mathbf{R} + \phi(\mathbf{k})). \end{aligned} \quad (3.17)$$

From the measurements this was inferred as follows. The polarization matrix measured at the commensurate peak $(\frac{1}{2}, \frac{1}{2}, 0)$ fulfills $P_{yy}^o \approx -P_{zz}^o \approx -0.85$ (Tab. 3.3). One may assume that the ground state actually implies a polarization $P_{yy} = -P_{zz} = -1$ and that the mismatch between measured and calculated values may again be caused by double spin-flip scattering, as is the case in phase C. The assumption $P_{yy} = -P_{zz} = -1$ implies that the commensurate contributions to the ground state are superpositions of only $\Gamma_3(\mathbf{k}_c)$ basis functions (cf. Sec. A.2). For the incommensurate peaks in phase IC1, the measured polarization matrices are consistent with $P_{yy} = -P_{zz} = -1$, implying that incommensurate contributions to the ground state in IC1 are superpositions of only $\Gamma_4(\mathbf{k}_{ic})$ basis functions (cf. Sec. A.2).

As shown further, the incommensurate contributions to the magnetic ground state in phase IC2 prove to be a superposition of $\Gamma_4(\mathbf{k}_{ic})$ basis functions only. This may be inferred from the polarization matrices measured at incommensurate positions in IC2, which are consistent with $P_{yy} = -P_{zz} = -1$. In contrast, the polarization matrix measured at the commensurate peak position fulfills $P_{yy} = -P_{zz} \approx -0.4$ suggesting that commensurate contributions to the ground state are mixtures of several IRs. This is at odds with Landau theory, which requires that only one IR is involved in phase IC2. The two cases $P_{yy} = -P_{zz} = \pm 1$ only, may be in agreement with Landau theory. Presumably, the polarization data was again contaminated with double spin-flip scattering signals.

3.3.3.6. Magnetic Rietveld Refinements

To perform magnetic Rietveld refinements in phases C and IC1, neutron diffraction on sample OFZ95-3-2-1-a was carried out at HEiDi. The results of the experiments may be summarized as follows:

- The magnetic ground state in phase C is represented by one of the five $(\pi\pi 0)$ structures s2, s4, d2, d5, and t2. This was confirmed by magnetic Rietveld refinements.
- Among the 21 commensurate $(\pi\pi 0)$ structures in Tab. 3.1 these five structures represent the ones that contain Γ_9 basis functions only. The Rietveld refinements are thus in excellent agreement with the polarization analysis in Sec. 3.3.3.5.
- The structures s2 and s4 are single- k , d2 and d5 are double- k , and t2 is triple- k . As these structures have the same magnetic structure factor when magnetic domains are equally populated, they may not be distinguished by means of Rietveld refinements in zero magnetic field.
- The magnetic structure factor in phase IC1 may be approximated by that of the commensurate, single- k $(\pi\pi 0)$ structure s1. This was confirmed by Rietveld refinements.
- The commensurate structure s1 consists of basis functions only that are associated with $\Gamma_3(\mathbf{k}_c)$. As the only basis function, associated with $\Gamma_4(\mathbf{k}_{ic})$, is parallel to the only basis function, associated with $\Gamma_3(\mathbf{k}_c)$, the Rietveld refinement is in excellent agreement with the polarization analysis in Sec. 3.3.3.5.
- There is a multitude of multi- k structures that may describe the magnetic ground state in phase IC1. Rietveld refinements in zero field, however, do not allow to distinguish them.

In phase C, magnetic Rietveld refinements were carried out on the data sets recorded at HEiDi at $T = 2.5 K$ (cf. Fig. 3.8), containing 500 commensurate $(\pi\pi 0)$ reflections as well as 181 structural reflections. As in phase C the structural reflections are purely non-magnetic and the $(\pi\pi 0)$ reflections are purely magnetic, the integrated intensities represent nuclear and magnetic structure factors F_o^2 , respectively.

Refinements were conducted by means of the software Jana2006 [59]. For the refinement of the crystal structure, $Pm\bar{3}m$, a scale parameter, a quadratic (isotropic) displacement parameter, and an isotropic Lorentzian extinction were introduced. For the magnetic refinements the (uniform) size of the magnetic moments, an isotropic Lorentzian extinction parameter, and $d - 1$ ratio parameters for d possible magnetic domains were introduced.

The five commensurate $(\pi\pi 0)$ structures s2, s4, d2, d5, and t2 that are in agreement with the polarization analysis were considered as magnetic ground state in phase C. As

Magnetic Structure:	s2	s4	d2	d5	t2
Number of k -vectors N:	1	1	2	2	3
Number of domains:	6	6	3	12	2
$\mathbf{r}(\mathbf{k}_1^c)$	(1, 0, 0)	$(\frac{1}{\sqrt{2}}, \frac{-1}{\sqrt{2}}, 0)$	$(\frac{1}{\sqrt{2}}, 0, 0)$	$(\frac{1}{\sqrt{2}}, 0, 0)$	$(\frac{1}{\sqrt{3}}, 0, 0)$
$\mathbf{r}(\mathbf{k}_2^c)$	-	-	$(0, 0, \frac{1}{\sqrt{2}})$	$(0, \frac{1}{\sqrt{2}}, \frac{-1}{\sqrt{2}})$	$(0, \frac{1}{\sqrt{3}}, 0)$
$\mathbf{r}(\mathbf{k}_3^c)$	-	-	-	-	$(0, 0, \frac{1}{\sqrt{3}})$
Allover refinement:					
$R[F^2 \geq 3\sigma(F^2)]$:	5.97	5.22	5.24	5.22	6.28
$wR(F^2)$:	14.45	13.07	13.13	13.03	15.88
Nuclear refinement:					
$R[F^2 \geq 3\sigma(F^2)]$:	6.81	6.19	5.70	5.88	5.91
$wR(F^2)$:	16.85	16.00	16.00	14.62	15.24
Magnetic refinement:					
$R[F^2 \geq 3\sigma(F^2)]$:	5.43	4.60	4.54	4.17	8.91
$wR(F^2)$:	13.50	11.85	11.86	10.96	19.25
mag. moment (μ_B):	6.133(2)	6.241(2)	6.256(2)	6.258(2)	6.335(3)
nuc. ext. Giso:	0.123	0.136	0.138	0.128	0.140
mag. ext. Gmag:	0.090	0.120	0.240	0.214	0.414
Uiso	0.0025	0.0039	0.0040	0.0040	0.0047

Table 3.4.: Magnetic Rietveld refinements for the ground state in phase C. Integrated intensities F_o^2 of 500 magnetic ($\pi\pi 0$) reflections, as well as 161 structural reflections, which were inferred from diffraction data recorded at HEiDi, were used for the refinements. The five magnetic structures s2, s4, d2, d5, and t2 that were considered here are the only structures among the 21 commensurate ($\pi\pi 0$) structures in Tab. 3.1, which are in agreement with the polarization analysis. The structures may be expanded into Fourier series by means of $\mathbf{m}(\mathbf{R}) = \sum_n \mathbf{r}(\mathbf{k}_n^c) \exp(i\mathbf{k}_n^c \cdot \mathbf{r})$. For the refinement of the crystal structure, $Pm\bar{3}m$, a scale parameter, a quadratic (isotropic) displacement parameter, and an isotropic Lorentzian extinction were introduced. For the magnetic refinements the (uniform) size of the magnetic moment, an isotropic Lorentzian extinction parameter, and $d - 1$ ratio parameters for the d possible domains were introduced.

these five structures for equally distributed domains all share the same structure factor, Rietveld refinements are expected to be similar.

Tab. 3.4 shows the results of the magnetic Rietveld refinements in phase C. A stable refinement was obtained for each of the five magnetic structures. The low R -values, which range from 5.1 to 6.2, reflect the excellent agreement between calculated and measured structure factors in phase C. The R -values were slightly lower for the structures s4, d2, and d5. The mean quadratic displacement has the smallest value for the structure s2, namely $U_{iso} \approx 0.0024$. For all other structures it amounts to ≈ 0.0040 . The magnetic moments vary between $6.13 \mu_B$ and $6.35 \mu_B$ for the five structures. All of them are smaller than $(7.5 \pm 0.1) \mu_B/\text{f.u.}$, the value determined in Ref. [68] at $T = 10.5 \text{ K}$ in phase C, and considerably smaller than $10.61 \mu_B/\text{f.u.}$, the free-ion value of Ho^{3+} calculated from

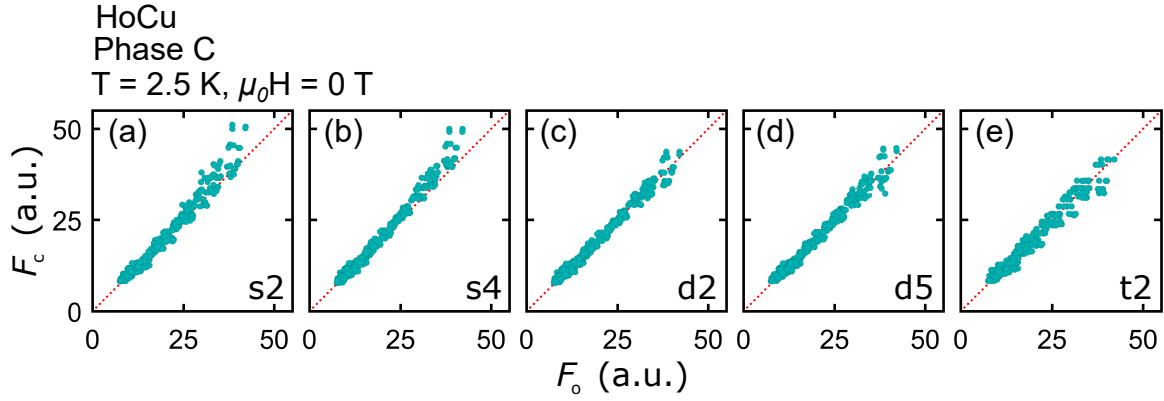


Figure 3.15.: Calculated vs. observed magnetic structure factors F_c/F_o for the magnetic Rietveld refinements in phase C. For the refinement, the five structures of Tab. 3.1, which consist of only Γ_9 functions, were considered. Shown are the structure factors F_c , as calculated for each of the five magnetic structures, and the values F_o inferred from the 500 recorded magnetic Bragg reflections. Similarly good were the results obtained for (a),(b) the single- k structures s2 and s4, (c),(d) the double- k structures d2 and d5, and (e) the triple- k structure t2, reflecting the agreement of the experimental data with structures that consist of only Γ_9 basis functions.

Hund's rules. Extinction parameters for the structural refinements are given by ≈ 0.1 . The magnetic extinction parameters were ≈ 0.1 for single- k structures, ≈ 0.2 for double- k structures, and ≈ 0.3 for triple- k structures. Fig. 3.15 illustrates the excellent agreement of the magnetic structure factor F_c , calculated for each of the five magnetic structures, with the structure factor F_o , inferred from the recorded data. For each of the five structures the data points of the 500 magnetic reflections are almost perfectly on the bisetrix reflecting the excellent agreement with the experimental data.

For the magnetic Rietveld refinements in phase IC1, rocking scans were carried out for 180 structural and 499 magnetic $(\pi\pi 0)$ positions at $T = 15 \text{ K}$. Integrated intensities F_o^2 for structural and magnetic $(\pi\pi 0)$ reflections were inferred by means of the data reduction software available at HEiDi, fitting the data at each position with a single-peak profile function. For most of the $(\pi\pi 0)$ positions this provided a good approximation of the total scattering intensity. Note, however, that the approximation was bad at low q -values, such as in the vicinity of $(\frac{1}{2}, \frac{1}{2}, 0)$. In these cases, the rocking scans had several maxima and were badly approximated by a single-peak function. An accurate measurement of both incommensurate and commensurate magnetic structure factors would be tedious, as it requires both a high q -resolution and coverage of a large volume in q -space.

As an approximation to the magnetic ground state in IC1, the three commensurate single- k structures s1, s2, and s4 were considered. The three structures represent all single- k structures among the 21 structures in Tab. 3.1, which contain basis functions associated with one IR only. s1 contains only $\Gamma_3(\mathbf{k}_c)$ basis functions, s2 and s4 only

Magnetic Structure:	s1	s2	s4
Number of domains:	3	6	6
\mathbf{r}_i	(0, 0, 1)	(1, 0, 0)	$\frac{1}{\sqrt{2}}(1, 1, 0)$
Magnetic refinement:			
$R [F^2 \geq 3\sigma (F^2)]:$	7.42	26.86	26.56
$wR (F^2):$	10.50	30.40	30.49
Nuclear refinement:			
$R [F^2 \geq 3\sigma (F^2)]:$	5.16	4.81	6.20
$wR (F^2):$	7.59	7.45	9.75
Allover refinement:			
$R [F^2 \geq 3\sigma (F^2)]:$	6.52	18.08	18.46
$wR (F^2):$	9.77	26.47	26.69
Magnetic moment (μ_B):	6.393	6.723	6.768
Extinction coefficient (nuclear):	0.097702	0.136271	0.055549
Extinction coefficient (magnetic):	0.028359	0.481687	0.010686

Table 3.5.: Magnetic Rietveld refinements in phase IC1. The magnetic ground state in IC1 was approximated by three commensurate single- k structures. The three structures s1, s2, and s4 are the only single- k structures among the 21 structures in Tab. 3.1 that contain basis functions from one IR only. Their Fourier series may be represented by $\mathbf{m}_i(\mathbf{R}) = \mathbf{r}_i (\exp(i\mathbf{k}_1^c \cdot \mathbf{R}))$. Integrated intensities were inferred from a data set containing 499 magnetic ($\pi\pi 0$) positions and 180 structural peaks, which was recorded at $T = 15$ K at HEiDi. For each ($\pi\pi 0$) position intensities of both commensurate and incommensurate contributions were fitted with a single peak profile. For magnetic peak positions with low q -values this gives a rough approximation, for larger q -values the approximation is good. For the refinement of the crystal structure, $Pm\bar{3}m$, a scale parameter and an isotropic Lorentzian extinction were introduced. For the magnetic refinements the (uniform) size of the magnetic moment, an isotropic Lorentzian extinction parameter, and $d - 1$ ratio parameters for the d possible domains were introduced. The refinements were carried out by means of JANA2006 [59].

$\Gamma_9(\mathbf{k}_{ic})$ basis functions. The Fourier decompositions of the three structures have the form:

$$\mathbf{m}_j(\mathbf{R}) = \mathbf{r}_j \cdot \exp(i\mathbf{k}_1^c \cdot \mathbf{R}) . \quad (3.18)$$

with $\mathbf{r}_1 = (0, 0, 1)$, $\mathbf{r}_2 = (1, 0, 0)$, $\mathbf{r}_3 = \frac{1}{\sqrt{2}}(1, 1, 0)$. The structure \mathbf{m}_1 corresponds to s1, \mathbf{m}_2 to s2, and \mathbf{m}_3 to s4 in Tab. 3.1. As shown further, the Rietveld refinement confirmed, that the structure factor of \mathbf{m}_1 gives the best approximation to the measured data. In particular, this finding is in excellent agreement with the polarization measurements, as the only basis functions associated with $\Gamma_4(\mathbf{k}_{ic})$ is parallel to the only basis function, associated with $\Gamma_3(\mathbf{k}_c)$.

Tab. 3.5 shows the results of the magnetic Rietveld refinements in phase IC1. For the structure \mathbf{m}_1 , good refinement results were obtained, For \mathbf{m}_2 and for \mathbf{m}_3 the refinements were considerably worse. The R -value 6.52 reflects a good approximation of the mea-

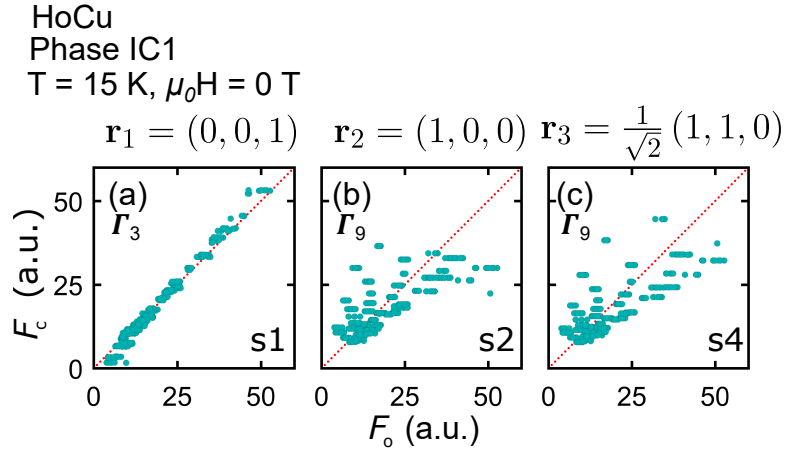


Figure 3.16.: Calculated vs. observed magnetic structure factors F_c/F_o for the magnetic Rietveld refinements in phase IC1. The magnetic ground state in IC1 was approximated by the commensurate $(\pi\pi 0)$ structures (a) s1, (b) s2, and (c) s4. The three structures are the only single- k structures among the 21 structures in Tab. 3.1 that contain basis functions associated with a single IR only. Each of the structures may be represented by a Fourier series $\mathbf{m}_i(\mathbf{R}) = \mathbf{r}_i (\exp(i\mathbf{k}_1^c \cdot \mathbf{R}))$. Shown for the three refinements is the comparison of the magnetic structure factor F_c , calculated for the magnetic structures s1, s2, and s4, respectively, with the structure factor F_o , inferred from the 499 magnetic Bragg peaks. The refinement yields relatively good results for the structure s1, which is associated with the IR Γ_3 , the magnetic moments pointing along the c -axis. In contrast, the refinement is worse for the structures s2 and s4, which are associated with the IR Γ_9 , the magnetic moments located in the ab -plane.

sured structure factor by the commensurate magnetic structure s1. The refined magnetic moment $6.393 \mu_B$ is smaller than the value $(7.1 \pm 0.1) \mu_B/\text{f.u.}$ observed in Ref. [68] at $T = 14.5 \text{ K}$ in phase IC1, but is considerably smaller than $10.61 \mu_B/\text{f.u.}$, the value inferred for tripositive holmium by means of Hund's rules. Fig. 3.16 illustrates graphically the good agreement of the magnetic structure factor F_c , calculated for the structure \mathbf{m}_1 , with the structure factor F_o , inferred from the recorded data. In contrast, F_c and F_o are distinctively different for the structures \mathbf{m}_2 and \mathbf{m}_3 .

3.3.3.7. Higher Harmonic Peaks

In order to investigate higher-order magnetic peaks, which may be important for the identification of multi- k structures [30, 61, 63], neutron diffraction on the sample OFZ95-3-2-1-a was carried out at MIRA [138]. The main results of these experiments, as explained further below, may be summarized as follows:

- In phase C, higher harmonics were not investigated, as they are expected either at the same position as structural peaks or as $(\pi\pi 0)$ peaks, both of which are relatively strong, rendering the separation of intensities difficult.
- In phase IC1, higher-order peaks were detected at the positions $(\frac{1}{2} \pm 3\delta, \frac{1}{2}, 0)$ and $(\frac{1}{2}, \frac{1}{2} \pm 3\delta, 0)$. They reflect either the anharmonicity of the magnetic ground state or they arise due to mixed higher harmonics from a multi- k ground state combining several wave vectors of the star $\langle \frac{1}{2} - \delta, \frac{1}{2}, 0 \rangle$.
- In phase IC1, no peaks were detected at the mixed positions $(\frac{1}{2} + \delta, \frac{1}{2} \pm 2\delta, 0)$, $(\frac{1}{2} - \delta, \frac{1}{2} \pm 2\delta, 0)$, $(\frac{1}{2} + 2\delta, \frac{1}{2} \pm \delta, 0)$, or $(\frac{1}{2} - 2\delta, \frac{1}{2} \pm \delta, 0)$.
- In phase IC2, higher-order peaks were detected at the positions $(\frac{1}{2} \pm 3\delta, \frac{1}{2}, 0)$ and $(\frac{1}{2}, \frac{1}{2} \pm 3\delta, 0)$. They reflect either the anharmonicity of the magnetic ground state or they arise due to mixed higher harmonics from a multi- k ground state combining several wave vectors of the star $\langle \frac{1}{2} - \delta, \frac{1}{2}, 0 \rangle$.
- In phase IC2, peaks were also detected at mixed positions $(\frac{1}{2} + \delta, \frac{1}{2} \pm 2\delta, 0)$, $(\frac{1}{2} - \delta, \frac{1}{2} \pm 2\delta, 0)$, $(\frac{1}{2} + 2\delta, \frac{1}{2} \pm \delta, 0)$, and $(\frac{1}{2} - 2\delta, \frac{1}{2} \pm \delta, 0)$. They establish that the ground state in IC2 is a multi- k state combining several wave vectors of the star $\langle \frac{1}{2} - \delta, \frac{1}{2}, 0 \rangle$.
- In phase IC2, the ground state is at least a triple- k structure consisting of at least one commensurate propagation vector of the star $\langle \frac{1}{2} \frac{1}{2} 0 \rangle$ and more than one incommensurate propagation vectors of the star $\langle \frac{1}{2} - \delta, \frac{1}{2}, 0 \rangle$.

The investigation of higher harmonics was carried out as follows. First, the resolution of the instrument MIRA was determined in the vicinity of the magnetic Bragg peak $(\frac{1}{2}, \frac{1}{2}, 0)$. Therefore, the Bragg peak $(\frac{1}{2}, \frac{1}{2}, 0)$ was properly mapped out by means of q -scans in phase C. It was assumed that the profile of the Bragg peak $(\frac{1}{2}, \frac{1}{2}, 0)$ represents the resolution of the instrument. This provided as resolution a Gaussian profile function that gave a remarkably good approximation to all magnetic peaks, measured in the vicinity of $(\frac{1}{2}, \frac{1}{2}, 0)$ in phases IC1 and IC2. Second, higher harmonics were studied in phases IC1 and IC2, by scanning the reciprocal space in the vicinity of $(\frac{1}{2}, \frac{1}{2}, 0)$. Therefore, q -scans were carried out along several high symmetric directions through $Q_0 = (\frac{1}{2}, \frac{1}{2}, 0)$. Each peak P_m at a position Q_m , which was observed in one of the scans, was fitted with a profile

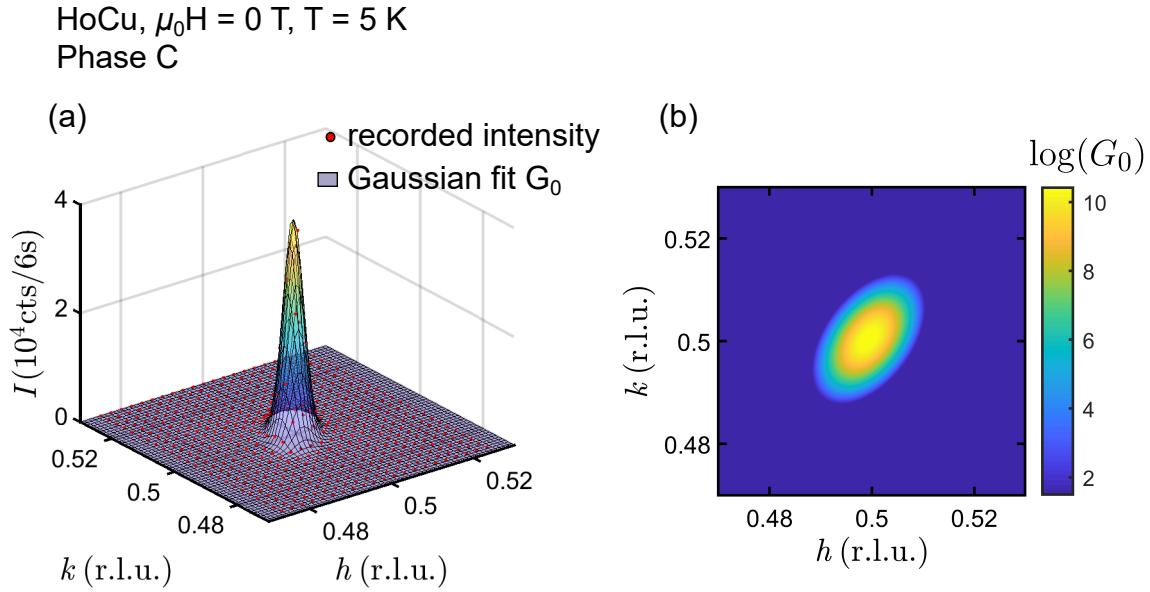


Figure 3.17.: Instrumental resolution of MIRA at the position $(\frac{1}{2}, \frac{1}{2}, 0)$. In phase C, the reciprocal space position $(\frac{1}{2}, \frac{1}{2}, 0)$ was accurately mapped out by means of q -scans at constant h values, i.e., q -scans were carried out along lines $(h_0, k, 0)$. (a) The commensurate magnetic Bragg peak at $(\frac{1}{2}, \frac{1}{2}, 0)$ features a Gaussian profile reflecting the resolution of the instrument. (b) The Gaussian fit function G_0 located at $(\frac{1}{2}, \frac{1}{2}, 0)$ as illustrated in terms of a color plot. The function was used as a model fit function for all other Bragg peaks in the vicinity of the $(\frac{1}{2}, \frac{1}{2}, 0)$ position.

function inferred from the resolution by means of $G_m(Q - Q_m) = j(Q_m) \cdot G_0(Q - Q_0)$. Integrated intensities were inferred further below for each magnetic peak by integration of these Gaussian fit functions.

For the measurements, the instrument MIRA was used as a triple-axis-spectrometer, as in this mode the background is strongly suppressed [138]. However, only elastic experiments (zero energy transfer) were performed. Neutrons with a wavelength $\lambda \approx 4.33$ Å were used. The sample was oriented such that the crystallographic (001) plane corresponded to the scattering plane.

For the determination of the resolution around $(\frac{1}{2}, \frac{1}{2}, 0)$, diffraction intensity was measured on a discrete grid with step size $\Delta h = \Delta k = 0.0025$ r.l.u. at $T = 5$ K in phase C. In particular, for each fixed reciprocal space coordinate $h_0(i) = 0.475 + i \cdot 0.0025$ ($i \in [0, 20]$), a q -scan was performed along lines $(h_0, k, 0)$ within the range $k \in [0.45, 0.55]$ and with

$Q_m - \left(\frac{1}{2}, \frac{1}{2}, 0\right)$	Phase IC1: $j(Q_m)$	Phase IC2: $j(Q_m)$
$(0, 0, 0)$	0.8387 ± 0.0085	0.1077 ± 0.0012
$(\bar{\delta}, 0, 0)$	0.5855 ± 0.0060	0.5265 ± 0.0056
$(\delta, 0, 0)$	0.6363 ± 0.0065	0.5499 ± 0.0054
$(0, \bar{\delta}, 0)$	0.6367 ± 0.0065	0.5608 ± 0.0057
$(0, \delta, 0)$	0.6650 ± 0.0068	0.5693 ± 0.0058
$(3\bar{\delta}, 0, 0)$	0.00170 ± 0.0001	0.00533 ± 0.00012
$(3\delta, 0, 0)$	0.001420 ± 0.0001	0.00503 ± 0.00013
$(0, 3\bar{\delta}, 0)$	0.00190 ± 0.0001	0.0047 ± 0.00012
$(0, 3\delta, 0)$	0.0015 ± 0.0001	0.0050 ± 0.00012
$(\delta, 2\bar{\delta}, 0)$	$< 5.5 \cdot 10^{-5}$	$5.0 \cdot 10^{-4} \pm 3.6 \cdot 10^{-5}$
$(\delta, 2\delta, 0)$	$< 2.9 \cdot 10^{-5}$	$6.7 \cdot 10^{-4} \pm 4.1 \cdot 10^{-5}$
$(\bar{\delta}, 2\delta, 0)$	$< 5.5 \cdot 10^{-5}$	$4.8 \cdot 10^{-4} \pm 3.5 \cdot 10^{-5}$
$(\bar{\delta}, 2\bar{\delta}, 0)$	$< 5.5 \cdot 10^{-5}$	$5.5 \cdot 10^{-4} \pm 3.8 \cdot 10^{-5}$
$(2\bar{\delta}, \delta, 0)$	$< 6.8 \cdot 10^{-5}$	$5.2 \cdot 10^{-4} \pm 3.7 \cdot 10^{-5}$
$(2\delta, \delta, 0)$	$< 7.0 \cdot 10^{-5}$	$7.1 \cdot 10^{-4} \pm 4.3 \cdot 10^{-5}$
$(2\delta, \bar{\delta}, 0)$	$< 4.3 \cdot 10^{-5}$	$7.0 \cdot 10^{-4} \pm 4.2 \cdot 10^{-5}$
$(2\bar{\delta}, \bar{\delta}, 0)$	$< 6.7 \cdot 10^{-5}$	$6.9 \cdot 10^{-4} \pm 4.2 \cdot 10^{-5}$

Table 3.6.: Integrated intensities of Bragg peaks in the vicinity of $\left(\frac{1}{2}, \frac{1}{2}, 0\right)$ in phases IC1 and IC2. Shown are the integrated intensities divided by the integrated peak intensity of the peak $\left(\frac{1}{2}, \frac{1}{2}, 0\right)$ in phase C at 5 K. Both phases IC1 and IC2 exhibit peaks at third-order positions with incommensurability $\sim (3\delta, 0, 0)$. Peaks at positions with mixed incommensurability $\sim (2\delta, \delta, 0)$ were detected only in phase IC2.

the step size $\Delta k = 0.0025$ r.l.u.. The recorded data were fitted with a two dimensional Gaussian profile G_0 , located at $\left(\frac{1}{2}, \frac{1}{2}, 0\right)$ (Fig. 3.17):

$$G_0\left(h - \frac{1}{2}, k - \frac{1}{2}\right) = a_0 \cdot \exp\left\{-\frac{1}{\sigma_1^2} \cdot \tilde{h}^2 - \frac{1}{\sigma_2^2} \cdot \tilde{k}^2\right\}, \quad (3.19)$$

$$\text{where } \begin{pmatrix} \tilde{h} \\ \tilde{k} \end{pmatrix} = \begin{pmatrix} \cos(\phi_0) & -\sin(\phi_0) \\ \sin(\phi_0) & \cos(\phi_0) \end{pmatrix} \cdot \begin{pmatrix} h - \frac{1}{2} \\ k - \frac{1}{2} \end{pmatrix}. \quad (3.20)$$

The parameters, as obtained from the least squares fit, were found to be $a_0 = 4.02 \cdot 10^4$ cts/6s, $\sigma_1 = 0.002004$ r.l.u., $\sigma_2 = 0.003419$ r.l.u., and $\phi_0 = -36.73^\circ$. The value $R^2 = 0.9941$ indicates remarkable agreement of the Gaussian profile with the recorded data. The value ϕ_0 is presumably not intrinsic, but is related to the instrumental resolution. Accordingly, it was assumed that the Gaussian function G_0 , which has the widths σ_1 and σ_2 along minor and major ellipse axis, respectively, may represent the resolution of the instrument.

Higher orders were not investigated in phase C for the following reasons. As the propagation vectors of the ground state are all of the star $\left\langle \frac{1}{2}, \frac{1}{2}, 0 \right\rangle$, higher orders either have

the same position as $(\pi\pi 0)$ peaks or as structural peaks. Since higher-order intensities are typically relatively weak, their intensities can hardly be separated from structural and magnetic $(\pi\pi 0)$ intensities, respectively. As example a commensurate multi- k structure with propagation vectors $\mathbf{k}_a = \left(\frac{1}{2}, \frac{1}{2}, 0\right)$, $\mathbf{k}_b = \left(\frac{1}{2}, 0, \frac{1}{2}\right)$, and $\mathbf{k}_c = \left(0, \frac{1}{2}, \frac{1}{2}\right)$ may be considered. Higher orders may then be present at positions such as $2\mathbf{k}_a + \mathbf{k}_b = \left(\frac{3}{2}, 1, \frac{1}{2}\right)$ or $\mathbf{k}_a + \mathbf{k}_b + \mathbf{k}_c = (1, 1, 1)$.

To study higher orders in phases IC1 and IC2, reciprocal space scans at $T = 15$ K and $T = 22$ K were carried out through $\left(\frac{1}{2}, \frac{1}{2}, 0\right)$ along the high-symmetry directions $(h, 0, 0)$, $(0, k, 0)$, $(h, h, 0)$, $(h, \bar{h}, 0)$, $(h, \pm 2h, 0)$, and $(2h, \pm h, 0)$. Accordingly, we define as scan-directions the vectors $\mathbf{e}_{\text{dir}} = (1, 0, 0)$, $(0, 1, 0)$, $\frac{1}{\sqrt{2}}(1, 1, 0)$, $\frac{1}{\sqrt{2}}(1, -1, 0)$, $\frac{1}{\sqrt{5}}(1, \pm 2, 0)$, and $\frac{1}{\sqrt{5}}(2, \pm 1, 0)$. Each peak P_m that was identified at a position $Q_m = (h_m, k_m, 0)$ in a q -scan was then separately fitted by a slice through the Gaussian peak function $G_m(Q - Q_m) = j(Q_m) \cdot G_0(Q - Q_0)$, which is located at Q_m . In particular, each peak identified in a one-dimensional q -scan with scan direction \mathbf{e}_{dir} was fitted with the one-dimensional profile:

$$g_m(t - t_m) = G_m \left(t \cdot \hat{e}_h \cdot \hat{e}_{\text{dir}} - \frac{1}{2}, t \cdot \hat{e}_k \cdot \hat{e}_{\text{dir}} - \frac{1}{2} \right) = \quad (3.21)$$

$$= j(Q_m) \cdot G_0 \left(t \cdot \hat{e}_h \cdot \hat{e}_{\text{dir}} - \frac{1}{2}, t \cdot \hat{e}_k \cdot \hat{e}_{\text{dir}} - \frac{1}{2} \right). \quad (3.22)$$

The fit functions G_m , which are multiples of G_0 , have the same widths along major and minor ellipse axes as G_0 . Accordingly, the integrated intensity of the peak P_m is given by $j(Q_m) \cdot I_0$, where I_0 is the integrated intensity of the peak $\left(\frac{1}{2}, \frac{1}{2}, 0\right)$ in phase C.

Total fit functions for the scattering intensity in the vicinity of the $\left(\frac{1}{2}, \frac{1}{2}, 0\right)$ position in phases IC1 and IC2 were obtained via $F_{\text{fit}}^{\text{IC1}}(h, k, 0) = \sum_m G_m^{\text{IC1}}(h - h_m, k - k_m)$ and $F_{\text{fit}}^{\text{IC2}}(h, k, 0) = \sum_m G_m^{\text{IC2}}(h - h_m, k - k_m)$, respectively. These fit functions are illustrated in Fig. 3.18 (a1) and (b1) for phases IC1 and IC2, respectively. A comparison of the data, recorded along the line $\left(h, \frac{1}{2}, 0\right)$, and the fit function along this line, i.e., $F_{\text{fit}}\left(h, \frac{1}{2}, 0\right)$, is shown in Fig. 3.18 (b1) and (b2) for IC1 and IC2, respectively. In particular, this illustrates that the fit functions are in excellent agreement with the recorded diffraction data.

In both phases IC1 and IC2, five relatively strong Bragg peaks build the fourfold pattern, which was also detected in Sec. 3.3.3.2 and which may be indexed with propagation vectors of the stars $\left\{\left(\frac{1}{2}, \frac{1}{2}, 0\right)\right\}$ and $\left\{\left(\frac{1}{2} - \delta, \frac{1}{2}, 0\right)\right\}$. The splitting parameters are given by $\delta_{15\text{K}} = 0.023 \pm 10^{-3}$ and $\delta_{22\text{K}} = 0.019 \pm 10^{-3}$ in phase IC1 at $T = 15$ K and in phase IC2 at $T = 22$ K, respectively. As explained further, a multitude of higher-order peaks was detected in the vicinity of $\left(\frac{1}{2}, \frac{1}{2}, 0\right)$.

In phase IC1, faint intensities were detected at the higher-order positions $(\frac{1}{2} \pm 3\delta, \frac{1}{2}, 0)$ and $(\frac{1}{2}, \frac{1}{2} \pm 3\delta, 0)$. Magnetic satellites at those positions typically reflect the anharmonicity of the magnetic ground state. For instance, \cos^3 terms in the Fourier decomposition of the ground state make for intensities at positions shifted by 3δ with respect to the commensurate position. However, they may also arise due to mixed higher harmonics from multi- k states with different incommensurate wave vectors of the star $\langle \frac{1}{2} - \delta, \frac{1}{2}, 0 \rangle$ that lie in the vicinity of different $(\pi\pi 0)$ positions, but for which the incommensurate splitting is parallel. Examples are multi- k states with wave vectors such as $\mathbf{k}_d = (\frac{1}{2} - \delta, \frac{1}{2}, 0)$, $\mathbf{k}_e = (\frac{1}{2} + \delta, 0, \frac{1}{2})$, as corresponding mixed higher-order peaks may be present at $-\mathbf{k}_d + 2 \cdot \mathbf{k}_e + (0, 1, 1) = (\frac{1}{2} - \delta, 0, \frac{1}{2}) = (\frac{1}{2} + 3\delta, \frac{1}{2}, 0)$. In phase IC1, no peaks were detected at the mixed positions $(\frac{1}{2} + \delta, \frac{1}{2} \pm 2\delta, 0)$, $(\frac{1}{2} - \delta, \frac{1}{2} \pm 2\delta, 0)$, $(\frac{1}{2} + 2\delta, \frac{1}{2} \pm \delta, 0)$, or $(\frac{1}{2} - 2\delta, \frac{1}{2} \pm \delta, 0)$. This may indicate, that the multi- k ground state in IC1 does not combine k -vectors of the star $\langle \frac{1}{2} - \delta, \frac{1}{2}, 0 \rangle$, for which the incommensurate splitting is noncollinear.

In phase IC2, faint intensities were detected at the higher-order positions $(\frac{1}{2} \pm 3\delta, \frac{1}{2}, 0)$ and $(\frac{1}{2}, \frac{1}{2} \pm 3\delta, 0)$. Magnetic satellites at those positions may again either reflect the anharmonicity of the magnetic structure due to \cos^3 terms in the Fourier decomposition of the ground state or they may arise due to mixed higher harmonics from multi- k states with incommensurate wavevectors of the star $\langle \frac{1}{2} - \delta, \frac{1}{2}, 0 \rangle$ that lie in the vicinity of different $(\pi\pi 0)$ positions, but for which the incommensurate splitting is parallel. In IC2, peaks were also detected at mixed positions $(\frac{1}{2} + \delta, \frac{1}{2} \pm 2\delta, 0)$, $(\frac{1}{2} - \delta, \frac{1}{2} \pm 2\delta, 0)$, $(\frac{1}{2} + 2\delta, \frac{1}{2} \pm \delta, 0)$, and $(\frac{1}{2} - 2\delta, \frac{1}{2} \pm \delta, 0)$. Peaks at those positions establish that the ground state is multi- k with propagation vectors of the star $\langle \frac{1}{2} - \delta, \frac{1}{2}, 0 \rangle$, for which the incommensurate splitting is noncollinear, such as $(\frac{1}{2} - \delta, \frac{1}{2}, 0)$ and $(0, \frac{1}{2} - \delta, \frac{1}{2})$. In particular, the magnetic ground state in IC2 is a multi- k state with at least three propagation vectors, at least two are incommensurate and one commensurate.

Integrated intensities were inferred for all peaks in phases C, IC1, and IC2. For each peak P_m integration of the corresponding fit function G_m gives as integrated intensity $I_0 \cdot j(Q_m)$, where I_0 is the integrated intensity of the Bragg peak $(\frac{1}{2}, \frac{1}{2}, 0)$ in phase C. Tab. 3.6 shows the values $j(Q_m)$ for each peak in phases IC1 and IC2, respectively.

In phase IC1, the peaks with incommensurability $(3\delta, 0, 0)$ were approximately three orders of magnitude smaller than the first-order peaks with incommensurability $(\delta, 0, 0)$, $I_{15K}^{3\delta} / I_{15K}^{1st} \approx 2.6 \cdot 10^{-3}$. In phase IC2, this ratio is much larger, $I_{22K}^{3\delta} / I_{22K}^{1st} \approx 9 \cdot 10^{-3}$. In phase IC1, intensities at positions with mixed incommensurability were vanishingly small within the error bars. In contrast, finite integrated intensities were observed at positions with mixed incommensurability $(2\delta, \delta, 0)$ in phase IC2.

It may be noted that all intensities at higher-order positions may have contributions due to multiple scattering. However, as argued further, the intensities are mostly due to Bragg scattering. Notably, in IC1 all peaks at third-order positions with incommensurability 3δ feature similar intensities $\approx 1.5 \cdot 10^{-3}$. The same holds true for the peaks at third-order positions in IC2 and the peaks at positions with mixed incommensurability in IC2. This may reflect the non multiple-scattering origin of the peaks, as multiple scattering intensities typically strongly depend on the exact orientation of a single crystal in the neutron beam, which was different for the measurement of each higher-order intensity. Further, it may be inferred from temperature dependences, that the intensities at higher-order positions do not arise due to multiple scattering. If the intensities at higher-order positions were due to multiple scattering effects, the ratios of third-order peaks must scale monotonically with the ratio of first-order peaks at different temperatures. However, it is found $I_{22\text{K}}^{3\delta} / I_{15\text{K}}^{3\delta} \approx 3.1$ for the higher-order positions with incommensurability $(3\delta, 0, 0)$ and $I_{22\text{K}}^{1st} / I_{15\text{K}}^{1st} \approx 0.87$ for the first-order positions with incommensurability $(\delta, 0, 0)$.

The direct comparison of the diffraction data, recorded in IC1 and IC2 at mixed positions with incommensurability $(\delta, 2\delta, 0)$, further indicate the existence of higher harmonics at mixed higher-order positions in phase IC2 but not in IC1 (Fig. 3.19). Shown in Figs. 3.19 (a1,a2), (b1,b2), (c1,c2), and (d1,d2) are q -scans through $(\frac{1}{2}, \frac{1}{2}, 0)$ along the lines $(h, k) = (\frac{1}{2}, \frac{1}{2}) + t \cdot \frac{1}{\sqrt{5}} (2, 1)$, $(h, k) = (\frac{1}{2}, \frac{1}{2}) + t \cdot \frac{1}{\sqrt{5}} (2, -1)$, $(h, k) = (\frac{1}{2}, \frac{1}{2}) + t \cdot \frac{1}{\sqrt{5}} (1, 2)$, and $(h, k) = (\frac{1}{2}, \frac{1}{2}) + t \cdot \frac{1}{\sqrt{5}} (1, -2)$, respectively. Mixed higher harmonics may be present at positions, where $t_0 = \pm\sqrt{5} \cdot \delta \approx 0.045$ r.l.u.. Peaks were observed at each of those mixed position in IC2, but not in IC1. Further, mixed higher-order positions in phase IC2 like, e.g., $(\frac{1}{2} \pm \delta, \frac{1}{2} \pm 2\delta, 0)$ feature integrated intensities distinctively different from the background. Again, these intensities cannot be explained by multiple scattering effects, as their intensity would then scale monotonically with the ratio of first-order peaks. However, it was found $I_{15\text{K}}^{\text{mixed}} / I_{22\text{K}}^{\text{mixed}} < 0.08$, whereas $I_{15\text{K}}^{1st} / I_{22\text{K}}^{1st} \approx 1.15$.

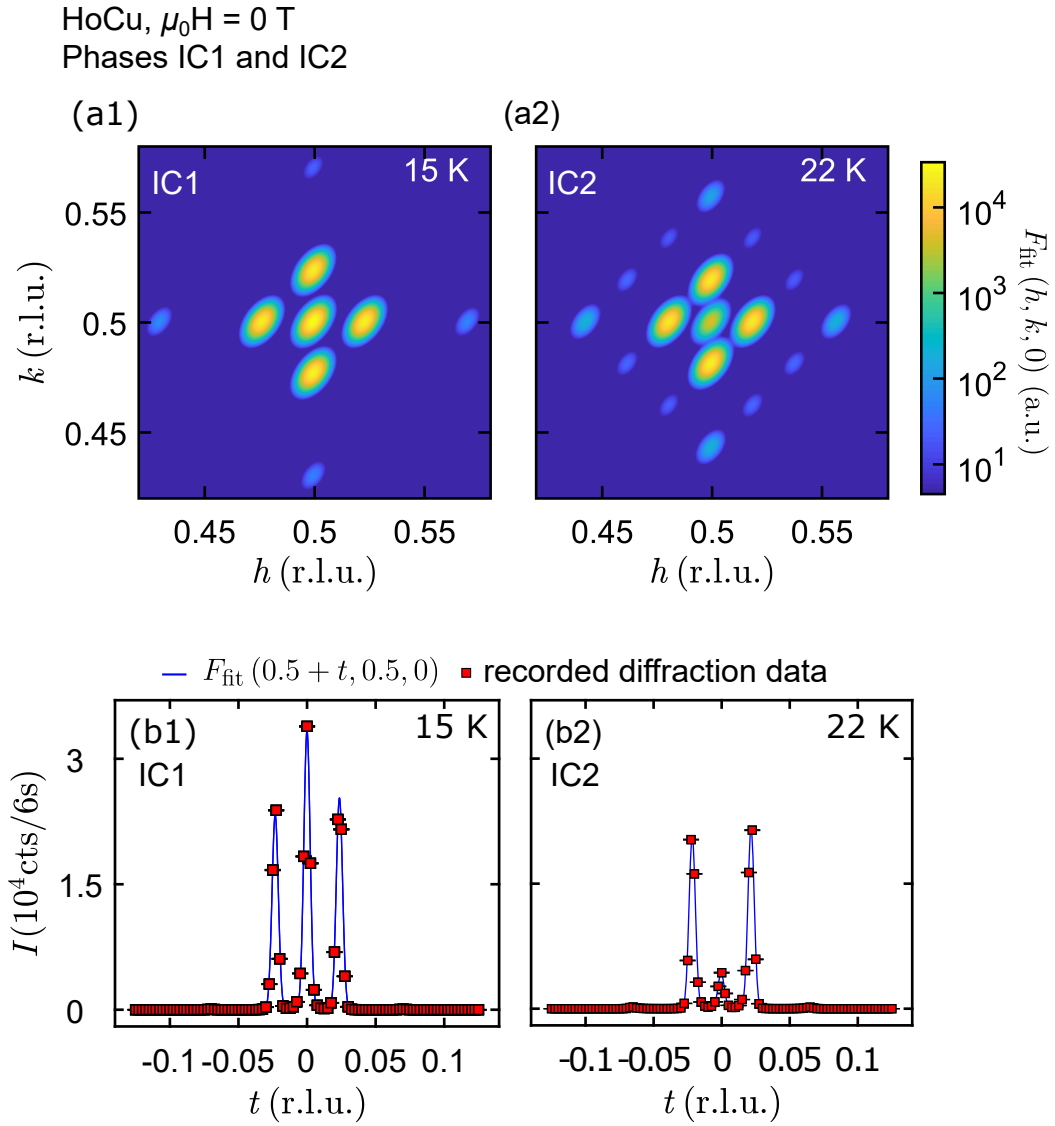


Figure 3.18.: Higher-order peaks in phases IC1 and IC2. (a1) Total fit function approximating the diffraction data in the $(h, k, 0)$ plane, as recorded in phase IC1. Higher orders are present at positions $(\frac{1}{2} \pm 3\delta, \frac{1}{2}, 0)$ and $(\frac{1}{2}, \frac{1}{2} \pm 3\delta, 0)$. (a2) Total fit function approximating the diffraction data in the $(h, k, 0)$ plane, as recorded in phase IC2. Higher orders were observed at positions $(\frac{1}{2} \pm 3\delta, \frac{1}{2}, 0)$ and $(\frac{1}{2}, \frac{1}{2} \pm 3\delta, 0)$, and at mixed higher-order positions $(\frac{1}{2}\delta, \frac{1}{2} \pm 2\delta, 0)$, $(\frac{1}{2} - \delta, \frac{1}{2} \pm 2\delta, 0)$, $(\frac{1}{2} + 2\delta, \frac{1}{2} \pm \delta, 0)$, or $(\frac{1}{2} - 2\delta, \frac{1}{2} \pm \delta, 0)$. Scattering data were recorded by means of q -scans, which contain the position $(\frac{1}{2}, \frac{1}{2}, 0)$ and which are directed along $(h, 0, 0)$, $(0, k, 0)$, $(h, h, 0)$, $(h, \bar{h}, 0)$, and $(h, \pm 2h, 0)$, $(2h, \pm h, 0)$. (b1), (b2) Comparison of the fit functions in phases IC1 and IC2 with the diffraction data, recorded by means of q -scans along the line $(h, \frac{1}{2}, 0)$. Excellent agreement between fit functions F_{fit} and data recorded at $T = 15$ K and 22 K, respectively, is indicated by the illustration.

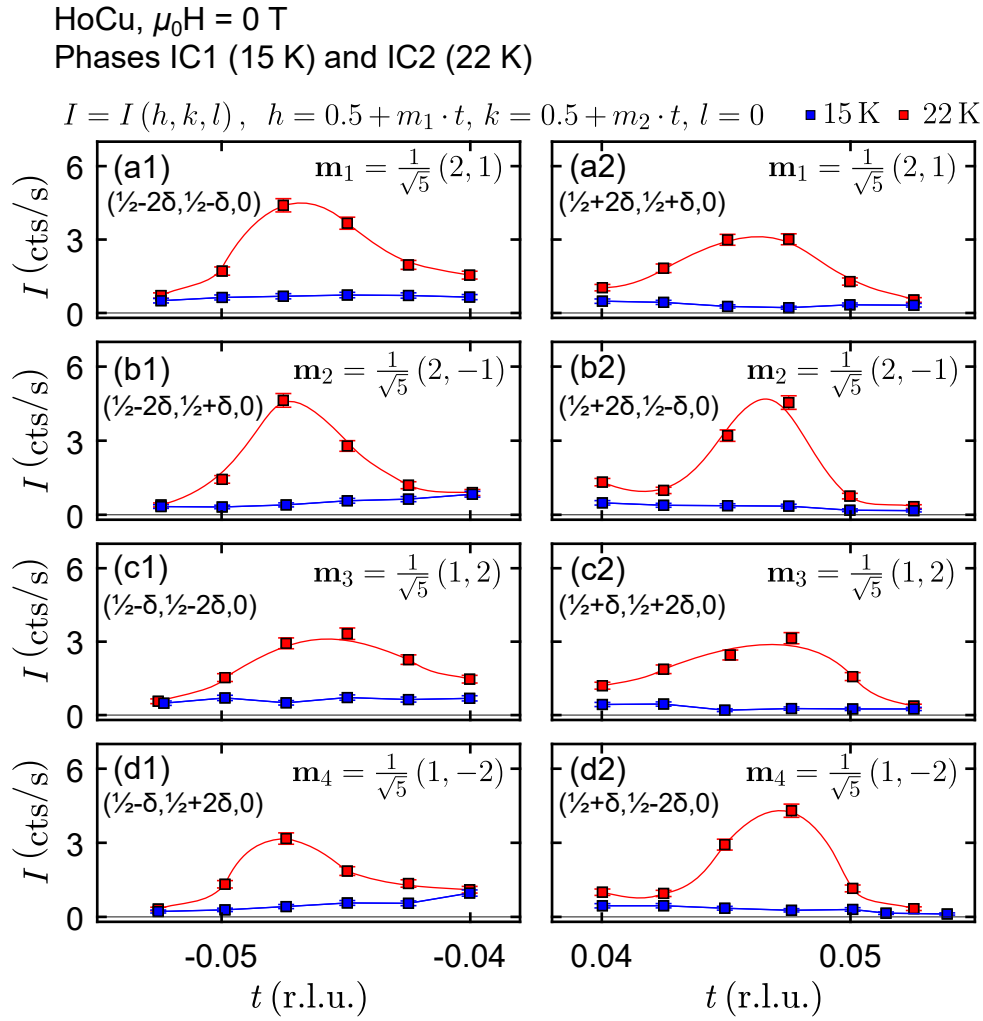


Figure 3.19.: Diffraction intensities in phases IC1 and IC2 recorded at higher-order positions with mixed incommensurability. Reciprocal space scans through $(\frac{1}{2}, \frac{1}{2}, 0)$ were performed along the lines, which are located in the (001) plane and which are defined by means of $(h - \frac{1}{2}, k - \frac{1}{2}) =$ (a) $t \cdot \mathbf{m}_1$, (b) $t \cdot \mathbf{m}_2$, (c) $t \cdot \mathbf{m}_3$, and (d) $t \cdot \mathbf{m}_4$. For approximately (a1),(b1),(c1),(d1) $t_0 = -\sqrt{5} \cdot \delta \approx -0.045$ r.l.u. and for (a2),(b2),(c2),(d2) $t_0 = +\sqrt{5} \cdot \delta \approx +0.045$ r.l.u., where mixed higher harmonics may appear, pronounced peaks were detected in IC2, at $T = 22$ K, but not in IC1, at $T = 15$ K.

3.3.4. Neutron Diffraction in Magnetic Fields

To study the evolution of magnetic order as a function of field and the magnetic phase diagram, neutron diffraction was carried out in magnetic fields along the three major cubic directions. First, fields were applied along the twofold $\langle 110 \rangle$ directions, second along the fourfold $\langle 100 \rangle$ directions, and third along the threefold $\langle 111 \rangle$ directions. As shown in the following, a strong dependence on the field history for fields along twofold directions permitted to specify the number of propagation vectors of the magnetic ground states in the zero field phases C, IC1, and IC2.

3.3.4.1. Fields Along Twofold Directions

To investigate the evolution of magnetic order for fields along twofold $\langle 110 \rangle$ directions, neutron diffraction of the single crystal OFZ95-3-2-1-a was carried out at D10 at the ILL. Magnetic fields vertical to the scattering plane were applied along the $[110]$ direction.

The $\langle 110 \rangle$ phase diagram, which was determined by Rahn (cf. Refs. [18, 118]), is shown in Fig. 3.20. The regions in this phase diagram were assigned colors and labels. The capital letters M shall indicate, that magnetic fields are applied along a cubic face diagonal. In the following presentation, the regions in the phase diagram will be referred to as "phases" or "phase pockets". Note, however, that these "phases" are not necessarily phases in a thermodynamic sense, i.e., they are not necessarily thermodynamically separated by phase transitions [139].

These experiments had two main purposes. On the one hand, magnetic ground states in different phase pockets of the $\langle 110 \rangle$ phase diagram were studied. On the other hand, the experiments allowed to specify the number of commensurate and incommensurate propagation vectors of the ground states in the zero-field phases C, IC1, and IC2.

As a major result, ground states in many phases of the $\langle 110 \rangle$ phase diagram of HoCu were specified. Tab. 3.7 summarizes these main results. For each of the phase pockets listed in the first column, the stars of the propagation vectors, which were inferred from the neutron diffraction data, are given in the second column. In the third column it is indicated, whether a ground state is single- k or multi- k . All the propagation vectors, which were observed in this study, belong to one of the four stars $\langle \frac{1}{2} \frac{1}{2} 0 \rangle$, $\langle \frac{1}{2} - \delta, \frac{1}{2}, 0 \rangle$, $\langle \mathbf{q}_{I,\alpha} \rangle$, or $\langle \mathbf{q}_{I,\beta} \rangle$, the latter two are introduced below.

The number of propagation vectors in phases C, IC1, and IC2 may be specified by these experiments, as the $[110]$ field direction breaks the symmetry between k -arms of the propagation vector stars, which were observed in phases C, IC1, and IC2. The propagation vectors in these three phases belong to the stars $\langle \frac{1}{2} \frac{1}{2} 0 \rangle$ and $\langle \frac{1}{2} - \delta, \frac{1}{2}, 0 \rangle$, respectively, as reported in Sec. 3.3.3.2. By means of temperature and field dependences of magnetic

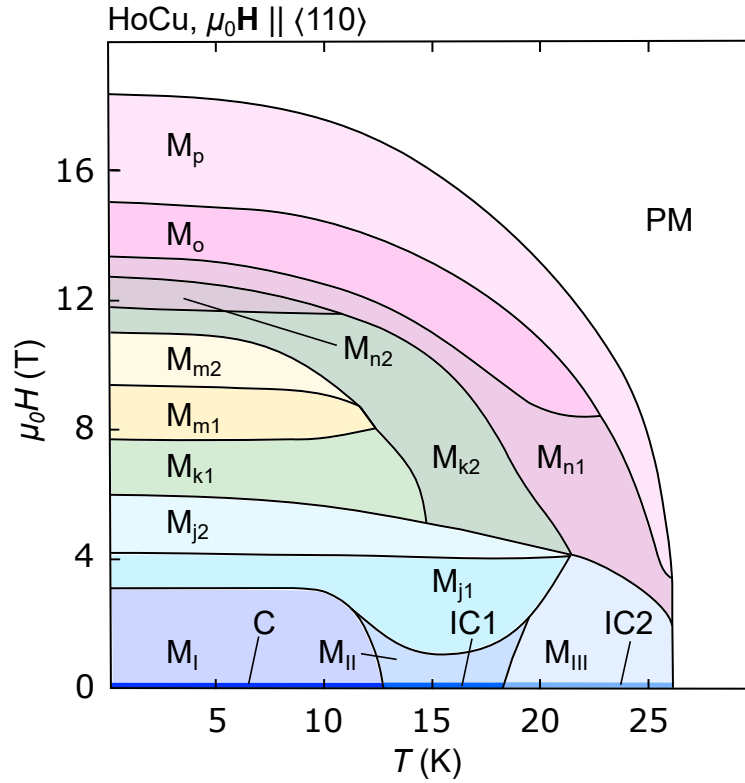


Figure 3.20.: Phase pockets in the $\langle 110 \rangle$ phase diagram of HoCu. The phase diagram was determined by Rahn in Refs. [18, 118]. For this study the phase pockets were labeled and filled with colors.

Bragg peaks, the k -arms participating in a phase may be determined (cf. Sec. 2.2). Each k -arm featuring finite intensities may correspond to one participating propagation vector in the Fourier decomposition of the ground state in a phase. In particular, the number of propagation vectors in a phase may be specified, when symmetries between different k -arms are broken (cf. Sec. 2.2.3 for further information). For instance, there are two possible orientations of commensurate $(\pi\pi 0)$ arms (cf. Sec. 3.2 for further information) and three possible orientations of $(\pi - \delta, \pi, 0)$ arms in a field directed along a twofold axis, cf. Sec. 3.2 for more details. Note, that the orientation of these k -arms in the magnetic field is illustrated, for instance, in Fig. 3.10 (c).

In the study reported here, it is helpful to assign the arms of the $\langle \frac{1}{2} \frac{1}{2} 0 \rangle$ star and of the $\langle \frac{1}{2} - \delta, \frac{1}{2}, 0 \rangle$ star, respectively, to sets, such that the magnetic field does not break the symmetry between arms of the same set, but between arms of two different sets it does break the symmetry. These sets represent the different orientations in the field of arms of the $\langle \frac{1}{2} \frac{1}{2} 0 \rangle$ star and $\langle \frac{1}{2} - \delta, \frac{1}{2}, 0 \rangle$ star, respectively. Accordingly, the commensurate k -arms of the $\langle \frac{1}{2} \frac{1}{2} 0 \rangle$ star may in terms of a partition be assigned to the sets $\mathcal{S}_1^c = \{A_1^c\}$ and $\mathcal{S}_2^c = \{A_2^c, A_3^c\}$. For the incommensurate propagation vector arms of the $\langle \frac{1}{2} - \delta, \frac{1}{2}, 0 \rangle$

Phase Pocket	Propagation Vector Stars	Type of Ground State
C, M_I	$\langle \frac{1}{2} \frac{1}{2} 0 \rangle$	multi- k
IC1, M_{II}	$\langle \frac{1}{2} \frac{1}{2} 0 \rangle, \langle \frac{1}{2} - \delta, \frac{1}{2}, 0 \rangle$	multi- k
IC2, M_{III}	$\langle \frac{1}{2} \frac{1}{2} 0 \rangle, \langle \frac{1}{2} - \delta, \frac{1}{2}, 0 \rangle$	multi- k
M_{j1}	$\langle \frac{1}{2} \frac{1}{2} 0 \rangle, \langle \frac{1}{2} - \delta, \frac{1}{2}, 0 \rangle, \langle \mathbf{q}_{I,\alpha} \rangle, \langle \mathbf{q}_{I,\beta} \rangle$	multi- k
M_{j2}	$\langle \frac{1}{2} \frac{1}{2} 0 \rangle, \langle \frac{1}{2} - \delta, \frac{1}{2}, 0 \rangle, \langle \mathbf{q}_{I,\alpha} \rangle$	multi- k
M_{k1}	$\langle \frac{1}{2} \frac{1}{2} 0 \rangle, \langle \frac{1}{2} - \delta, \frac{1}{2}, 0 \rangle, \langle \mathbf{q}_{I,\alpha} \rangle$	multi- k
M_{k2}	$\langle \frac{1}{2} \frac{1}{2} 0 \rangle, \langle \frac{1}{2} - \delta, \frac{1}{2}, 0 \rangle, \langle \mathbf{q}_{I,\alpha} \rangle$	multi- k
M_{m1}	$\langle \frac{1}{2} \frac{1}{2} 0 \rangle, \langle \frac{1}{2} - \delta, \frac{1}{2}, 0 \rangle, \langle \mathbf{q}_{I,\alpha} \rangle, \langle \mathbf{q}_{I,\beta} \rangle$	multi- k
M_{m2}	$\langle \frac{1}{2} \frac{1}{2} 0 \rangle, \langle \frac{1}{2} - \delta, \frac{1}{2}, 0 \rangle, \langle \mathbf{q}_{I,\alpha} \rangle, \langle \mathbf{q}_{I,\beta} \rangle$	multi- k
M_{n1}	$\langle \frac{1}{2} \frac{1}{2} 0 \rangle, \langle \frac{1}{2} - \delta, \frac{1}{2}, 0 \rangle, \langle \mathbf{q}_{I,\beta} \rangle$	multi- k
M_o	$\langle \frac{1}{2} \frac{1}{2} 0 \rangle$	single- k
M_p	$\langle \frac{1}{2} - \delta, \frac{1}{2}, 0 \rangle$	single- k or double- k

Table 3.7.: Ground states in the $\langle 110 \rangle$ phase diagram. For each phase in the first column (cf. Fig. 3.20) the stars of all magnetic propagation vectors, which were inferred from neutron diffraction data, are given in the second column. In the third column a comment is made, whether the structure is single- k or multi- k . The three ordered phases in zero magnetic field C, IC1, and IC2 extend to phase pockets, which are labeled M_I , M_{II} , and M_{III} , respectively.

star the sets are given by $\mathcal{S}_1^{ic} = \{A_{1,x}^{ic}, A_{1,y}^{ic}\}$, $\mathcal{S}_2^{ic} = \{A_{2,y}^{ic}, A_{3,x}^{ic}\}$, and $\mathcal{S}_3^{ic} = \{A_{2,z}^{ic}, A_{3,z}^{ic}\}$. Wave-vector arms with equivalent orientation with respect to the field direction, i.e., with preserved symmetry, typically feature the same experimental signatures due to magnetic domains. Hence, it cannot be distinguished whether k -vectors of different k -arms, for which the symmetry is preserved, form a multi- k state or whether they form a multi-domain state. Accordingly, it cannot be distinguished, whether arms, which belong to the same set \mathcal{S} , form a multi- k or a multi-domain state. In the present study temperature and field dependences were inferred for different arms of the two stars. The investigated arms include one arm of each of the five sets \mathcal{S}_1^c , \mathcal{S}_2^c , \mathcal{S}_1^{ic} , \mathcal{S}_2^{ic} , and \mathcal{S}_3^{ic} .

In detail, the main results of these experiments may be summarized as follows:

- Throughout the $\langle 110 \rangle$ phase diagram the compound displays variations of $(\pi\pi 0)$ antiferromagnetism.
- Phases C, IC1, and IC2 are part of phase pockets in the $\langle 110 \rangle$ phase diagram, which are labeled M_I , M_{II} , and M_{III} , respectively.
- In C, the magnetic ground state is multi- k . It is either double- k with propagation vectors \mathbf{k}_1^c and \mathbf{k}_2^c , or it is triple- k with propagation vectors \mathbf{k}_1^c , \mathbf{k}_2^c , and \mathbf{k}_3^c .
- In IC1, the magnetic ground state is multi- k . It is either double- k with propagation vectors \mathbf{k}_1^c and $\mathbf{k}_{2,z}^{ic}$, or it is triple- k with propagation vectors \mathbf{k}_1^c , $\mathbf{k}_{2,z}^{ic}$, and $\mathbf{k}_{3,z}^{ic}$.

- In IC2, the magnetic ground state is multi- k . It presumably represents a superposition of at least two commensurate propagation vectors, one of \mathcal{S}_1^c and one of \mathcal{S}_2^c , and at least two incommensurate propagation vectors, one of each set \mathcal{S}_1^{ic} and \mathcal{S}_2^{ic} .
- In phase pocket M_p (cf. Fig. 3.20), the magnetic ground state is either single- k or double- k with incommensurate propagation vectors of the $\langle \frac{1}{2} - \delta, \frac{1}{2}, 0 \rangle$ star.
- In phase pocket M_o , the magnetic ground state is single- k with one commensurate propagation vector of the $\langle \frac{1}{2} \frac{1}{2} 0 \rangle$ star.
- In the phase pockets M_{j1} , M_{j2} , M_{k1} , M_{m1} , M_{m2} , M_{k2} , and M_{n1} the magnetic ground state is multi- k combining propagation vectors of at least three different crystallographic stars.

The study was carried as follows. First, 14 different magnetic Bragg peaks were investigated as a function of temperature and field. These 14 Bragg peaks included the two commensurate Bragg peaks at $\mathbf{q}_{I,0} := (\overline{0.5}, 0.5, 1)$ and $\mathbf{q}_{II,0} := (\overline{1}, 0.5, \overline{0.5})$, as well as 12 incommensurate Bragg peaks in the vicinity of $\mathbf{q}_{I,0}$ and $\mathbf{q}_{II,0}$. The recorded data permitted to infer field and temperature dependences of seven different wave-vector arms. These investigated arms included one arm of each set \mathcal{S}_1^c , \mathcal{S}_2^c , \mathcal{S}_1^{ic} , \mathcal{S}_2^{ic} , and \mathcal{S}_3^{ic} , as well as arms associated with incommensurate k -vectors of the stars $\langle \mathbf{q}_{I,\alpha} \rangle$ and $\langle \mathbf{q}_{I,\beta} \rangle$, which are introduced further below. Second, propagation vectors were determined for the magnetic ground states in different pockets of the $\langle 110 \rangle$ phase diagram. Third, the discussion of the symmetry-breaking effect on k -arms by the twofold field direction permitted to specify the participating propagation vectors of the ground states in phases C, IC1, and IC2.

For the experiments at D10, neutrons of wavelength $\lambda = 1.26 \text{ \AA}$ were used. The sample was oriented such that the crystallographic (110) plane corresponded to the scattering plane. In this geometry, commensurate $(\pi\pi 0)$ peaks of only the k -arm A_1^c were located in the scattering plane. Peaks of the other two arms were accessed by means of a lifting detector.

To obtain field and temperature dependences, three field sweeps and six temperature sweeps were carried out following specific protocols as described in the following. An illustration of the trajectories of the sweeps is shown in Fig. 3.21. The field sweeps, which are labeled sweepB1, sweepB2, and sweepB3, were carried out at 2 K, 16 K, and 23 K, respectively. The three sweeps started at zero field after zero field cooling (zfc). The field first increased to a maximum field value and second decreased to zero. The temperature sweeps, which are labeled sweepT1, sweepT2, sweepT3, sweepT4, sweepT5, and sweepT6 were carried out at 0.5 T, 2.5 T, 3.5 T, 5 T, 7 T, and 9.7 T, respectively. The sweeps started in the paramagnetic state and the temperature decreased at constant field, i.e., the protocol was field cooling (fc). During the field and temperature sweeps, rocking

scans were carried out at discrete points around the two reciprocal space positions $\mathbf{q}_{I,0}$ and $\mathbf{q}_{II,0}$.

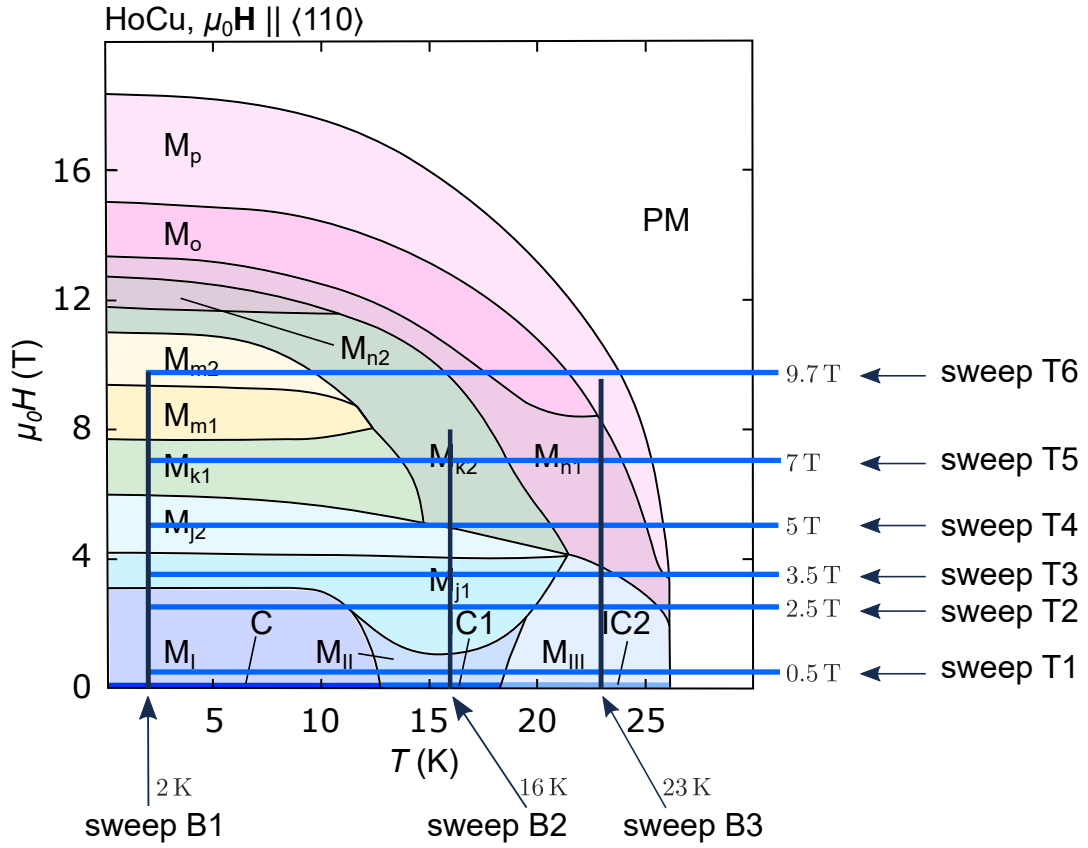


Figure 3.21.: Trajectories of the field- and temperature sweeps in the $\langle 110 \rangle$ phase diagram. The three field sweeps and six temperature sweeps, which were carried out for this study, are labeled sweepB1, sweepB2, and sweepB3, and sweepT1, sweepT2, sweepT3, sweepT4, sweepT5, and sweepT6, respectively. The illustration shows, how the field sweeps and temperature sweeps are located in the $\langle 110 \rangle$ phase diagram.

In the following a detailed account is presented of the experimental field and temperature dependences of magnetic propagation vectors. First, it is explained that magnetic Bragg peaks located at 14 different Q -positions may be investigated by means of this study, i.e., by means of the two rocking scans around $\mathbf{q}_{I,0}$ and $\mathbf{q}_{II,0}$. Note, that not all Bragg peaks are present in each phase. Two of these 14 Bragg peaks are related to commensurate magnetic propagation vectors $\left\{ \left(\frac{1}{2}, \frac{1}{2}, 0 \right) \right\}$, 8 of them to incommensurate magnetic propagation vectors $\left\{ \left(\frac{1}{2} - \delta, \frac{1}{2}, 0 \right) \right\}$, and four of them to other incommensurate propagation vectors. The 14 Bragg peaks, which are considered by this study, permit to investigate 7 different wave-vector arms of 4 crystallographic stars. Second, integrated intensities are inferred for all Bragg peaks, which were observed in one of the rocking scans. Third, field and temperature dependences were inferred for the seven different wave-vector arms, which were investigated in this study.

As explained in the following, magnetic Bragg peaks at 14 different Q -positions are considered in the present study. Ten of these 14 Bragg peaks are located at the Q -positions $\mathbf{q}_{\text{I},0}$, $\mathbf{q}_{\text{II},0}$, $\mathbf{q}_{\text{I},x}^{\pm} := (\overline{0.5} \pm \delta, 0.5, 1)$, $\mathbf{q}_{\text{I},y}^{\pm} = (\overline{0.5}, 0.5 \pm \delta, 1)$, $\mathbf{q}_{\text{II},y}^{\pm} = (\overline{1}, 0.5 \pm \delta, \overline{0.5})$, and $\mathbf{q}_{\text{II},z}^{\pm} := (\overline{1}, 0.5, \overline{0.5} \pm \delta)$. The Bragg peaks at $\mathbf{q}_{\text{I},0}$ and $\mathbf{q}_{\text{II},0}$ are indexed by propagation vectors of the $\langle \frac{1}{2} \frac{1}{2} 0 \rangle$ star. Bragg peaks at those positions may be observed, for instance, in all three zero field phases C, IC1 and IC2. Bragg peaks at the positions $\mathbf{q}_{\text{I},x}^+$, $\mathbf{q}_{\text{I},x}^-$, $\mathbf{q}_{\text{II},y}^+$, $\mathbf{q}_{\text{II},y}^-$, $\mathbf{q}_{\text{II},z}^+$, $\mathbf{q}_{\text{II},z}^-$, and $\mathbf{q}_{\text{I},\alpha}^{\pm}$ are indexed by propagation vectors of the $\{(\frac{1}{2} - \delta, \frac{1}{2}, 0)\}$ star. These vectors of the $\langle \frac{1}{2} - \delta, \frac{1}{2}, 0 \rangle$ star may be observed, for instance, in the zero field phases IC1 and IC2. As seen further below, four additional satellites, which are located at Q -positions $\mathbf{q}_{\text{I},\alpha}^+$, $\mathbf{q}_{\text{I},\alpha}^-$, $\mathbf{q}_{\text{I},\beta}^+$, and $\mathbf{q}_{\text{I},\beta}^-$, may be identified in the rocking scan around $\mathbf{q}_{\text{I},0}$.

Note, that the subscripts I and II of these Q -positions indicate, whether the Bragg peaks at these positions may be recorded in rocking scans around $\mathbf{q}_{\text{I},0}$ and $\mathbf{q}_{\text{II},0}$, respectively.

As explained before, the two commensurate peaks at $\mathbf{q}_{\text{I},0}$ and $\mathbf{q}_{\text{II},0}$ are present in phase C after zfc. To identify them experimentally, rocking scans with step width $\delta\omega = 0.05^\circ$ were carried out in phase C at $T = 2$ K after zfc. The two recorded magnetic Bragg peaks had their maxima at the rocking angles $\omega_{\text{I}} = -142.07^\circ$ and $\omega_{\text{II}} = -60.72^\circ$, respectively.

The eight incommensurate magnetic Bragg peaks, which are related to the $\langle \frac{1}{2} - \delta, \frac{1}{2}, 0 \rangle$ star, are present in phase IC1 after zfc. To identify them experimentally, rocking scans were carried out around the two positions $\mathbf{q}_{\text{I},0}$ and $\mathbf{q}_{\text{II},0}$ at $T = 16$ K after zfc. Tab. 3.8 gives an overview over the rocking angles, where the Bragg condition is fulfilled for these eight incommensurate satellites, as well as for the two commensurate Bragg peaks at $\mathbf{q}_{\text{I},0}$ and $\mathbf{q}_{\text{II},0}$, which are also present in phase IC1 after zfc.

The six Bragg peaks at $\mathbf{q}_{\text{I},0}$, $\mathbf{q}_{\text{II},0}$, $\mathbf{q}_{\text{II},y}^+$, $\mathbf{q}_{\text{II},y}^-$, $\mathbf{q}_{\text{II},z}^+$, and $\mathbf{q}_{\text{II},z}^-$ were in fact identified in the recorded data. However, the two peaks at $\mathbf{q}_{\text{I},x}^-$ and $\mathbf{q}_{\text{I},y}^-$, as well as the two peaks at $\mathbf{q}_{\text{I},x}^+$ and $\mathbf{q}_{\text{I},y}^+$ may be detected but their separation may not be resolved in these experiments. The two each are close to each other and lead to a single profile in the rocking scan. In the data presented below (cf. Fig. 3.24) they are labeled $\mathbf{q}_{\text{I},x/y}^-$ and $\mathbf{q}_{\text{I},x/y}^+$. The four additional satellites at positions $\mathbf{q}_{\text{I},\alpha}^{\pm}$ and $\mathbf{q}_{\text{I},\beta}^{\pm}$, as observed in some rocking scans around $\mathbf{q}_{\text{I},0}$, are also labeled in the figures presenting the recorded data (cf. Fig. 3.24).

Integrated intensities of the Bragg peaks at the positions listed in Tab. 3.8 were inferred from the rocking scans by means of numerical integration. For each Bragg position, an appropriate ω -range $\mathcal{I}(\mathbf{q})$ was chosen as domain of integration (cf. Tab. 3.8), and the integrated intensity was inferred using the expression

$$I(\mathbf{q}) = \frac{1}{\gamma(\mathbf{q})} \sum_{i: \omega_0 + i \cdot \delta\omega \in \mathcal{I}(\mathbf{q})} J(\omega_0 + i \cdot \delta\omega) \cdot \delta\omega, \quad (3.23)$$

where $\delta\omega$ is the step width used in the rocking scan and $J(\omega)$ the intensity that was

Q-position:	angle of peak:	integration domain: $\mathcal{I}(Q)$
$\mathbf{q}_{\text{II},0} := (\bar{1}, 0.5, \bar{0.5})$	-141.17°	$[-141.28, -141.06]$
$\mathbf{q}_{\text{II},z}^+ := (\bar{1}, 0.5, \bar{0.52})$	-142.07°	$[-142.18^\circ, -141.96^\circ]$
$\mathbf{q}_{\text{II},y}^- := (\bar{1}, 0.48, \bar{0.5})$	-141.57°	$[-141.68^\circ, -141.46^\circ]$
$\mathbf{q}_{\text{II},y}^+ := (\bar{1}, 0.52, \bar{0.5})$	-140.72°	$[-140.83^\circ, -140.61^\circ]$
$\mathbf{q}_{\text{II},z}^- := (\bar{1}, 0.5, \bar{0.48})$	-140.22°	$[-140.38^\circ, -140.16^\circ]$
$\mathbf{q}_{\text{I},0} := (\bar{0.5}, 0.5, 1)$	-60.72°	$[-60.96^\circ, -60.50^\circ]$
$\mathbf{q}_{\text{I},x}^- := (\bar{0.52}, 0.5, 1)$	-61.19°	$[-61.46^\circ, -61.00^\circ]$
$\mathbf{q}_{\text{I},y}^+ := (\bar{0.5}, 0.52, 1)$	-61.15°	
$\mathbf{q}_{\text{I},x}^- := (\bar{0.48}, 0.5, 1)$	-60.24°	$[-60.50^\circ, -60.00^\circ]$
$\mathbf{q}_{\text{I},y}^- := (\bar{0.5}, 0.48, 1)$	-60.29°	
$\mathbf{q}_{\text{I},\alpha}^+$	-	$[-62.71^\circ, -62.25^\circ]$
$\mathbf{q}_{\text{I},\beta}^+$	-	$[-62.70^\circ, -61.16^\circ]$
$\mathbf{q}_{\text{I},\beta}^-$	-	$[-59.81^\circ, -59.35^\circ]$
$\mathbf{q}_{\text{I},\alpha}^-$	-	$[-58.75^\circ, -59.21^\circ]$

Table 3.8.: Magnetic peaks, which were investigated in this study by means of rocking scans around $\mathbf{q}_{\text{I},0} = (\bar{0.5}, 0.5, 1)$ and around $\mathbf{q}_{\text{II},0} = (\bar{1}, 0.5, \bar{0.5})$. For each Bragg peak position, which is listed in the first column, the rocking angle, where the Bragg condition is fulfilled, is given in the second column. The subscripts of the Q-positions in the first column indicate, whether the Bragg peaks at those positions may be observed in rocking scans around $\mathbf{q}_{\text{I},0}$ and $\mathbf{q}_{\text{II},0}$, respectively. In the third column, the ω -intervals are given, which were used as domain of numerical integration. For the peaks labeled $\mathbf{q}_{\text{I},\alpha/\beta}$ only integration domains but no rocking angles are given.

recorded at the rocking angle ω . No background was subtracted. Each integrated intensity was normalized with a \mathbf{q} -specific scaling parameter γ that is specified below. The separation of magnetic peaks in the vicinity of $\mathbf{q}_{\text{II},0}$ is relatively small. Hence, residual integrated intensities may arise due to overlap of magnetic satellites. In particular, the intensities of peaks located at $\mathbf{q}_{\text{II},y}^\pm$ may cause residual integrated intensity in $I(\mathbf{q}_{\text{II},z}^\pm)$ and vice versa. Similarly, the intensities of peaks located at $\mathbf{q}_{\text{II},x}^\pm$ may cause residual integrated intensity in $I(\mathbf{q}_{\text{II},0})$ and vice versa. Note, that for the numerical integration the pairs consisting of $\mathbf{q}_{\text{I},x}^+$ and $\mathbf{q}_{\text{I},y}^+$, as well as $\mathbf{q}_{\text{I},x}^-$ and $\mathbf{q}_{\text{I},y}^-$, which may not be separated due to resolution, are considered as one peak each.

Temperature and field dependences of k -arms of the $\langle \frac{1}{2} \frac{1}{2} 0 \rangle$ star were determined as follows. The temperature and field dependences of the two commensurate Bragg peaks at $\mathbf{q}_{\text{I},0}$ and $\mathbf{q}_{\text{II},0}$ directly reflect temperature and field dependences of the k -arms A_1^c and A_2^c , respectively.

Temperature and field dependences of arms of the $\langle \frac{1}{2} - \delta, \frac{1}{2}, 0 \rangle$ star were obtained as follows. Incommensurate satellites in the vicinity of $(\pi\pi 0)$ reflections always appear in pairs denoted by \mathbf{q}^\pm . The two constituents of a pair belong to conjugated k -arms, i.e.,

they belong to the same Ω -arm. They are indexed as satellites around different structural peak positions, such as:

$$\mathbf{q}_{\text{I},x}^- = \left(-\frac{1}{2} - \delta, \frac{1}{2}, 1\right) = (-1, 0, 1) + \mathbf{k}_{1,x}^{ic} \quad (3.24)$$

$$\mathbf{q}_{\text{I},x}^+ = \left(-\frac{1}{2} + \delta, \frac{1}{2}, 1\right) = (0, 1, 1) - \mathbf{k}_{1,x}^{ic}. \quad (3.25)$$

As seen further below, the two satellites of such a conjugated pair always feature similar temperature and field dependences, which reflects that the magnetic structure factor is roughly the same at the two positions $\mathbf{q}_{\text{I},x}^+$ and $\mathbf{q}_{\text{I},x}^-$ due to the relatively small splitting δ . To obtain temperature and field dependences of the incommensurate wave-vector arms, the average of integrated intensities was considered for each pair of incommensurate satellites \mathbf{q}^\pm , i.e., $I(\mathbf{q}^\pm) := \frac{1}{2}[I(\mathbf{q}^+) + I(\mathbf{q}^-)]$. Accordingly, in the following, the integrated intensity of the average of a pair \mathbf{q}^\pm is referred to as integrated intensity of a pair \mathbf{q}^\pm . In particular, temperature and field dependences were obtained for the pairs $\mathbf{q}_{\text{II},y}^\pm$ and $\mathbf{q}_{\text{II},z}^\pm$, reflecting the temperature and field dependences of the arms $A_{2,y}^{ic}$ and $A_{2,z}^{ic}$, as well as for the pairs $\mathbf{q}_{\text{I},\alpha}^\pm$ and $\mathbf{q}_{\text{I},\beta}^\pm$. Further temperature and field dependences were determined for the average of $\mathbf{q}_{\text{I},x}^+$, $\mathbf{q}_{\text{I},x}^-$, $\mathbf{q}_{\text{I},y}^+$, and $\mathbf{q}_{\text{I},y}^-$, which may not be separated due to the resolution of the instrument. This average reflects the temperature and field dependences of both arms $A_{1,x}^{ic}$ and $A_{1,y}^{ic}$. As the two arms have the same orientation with respect to the field they should feature similar temperature and field dependences. Accordingly, these arms are not distinguished further in this study and they are referred to as $A_{1,x/y}^{ic}$. The corresponding Q -positions are referred to as $\mathbf{q}_{\text{I},x/y}^\pm$. In this text, the integrated intensity of averages \mathbf{q}^\pm is sometimes referred to as integrated intensity at \mathbf{q}^\pm .

The parameters γ were chosen such that in zero magnetic field after zfc the integrated intensities, which are associated with k -arms of the same crystallographic star, feature the same value. This reflects that the magnetic domains are in equilibrium. For the integrated intensities of $\mathbf{q}_{\text{I},0}$ and $\mathbf{q}_{\text{II},0}$, which are associated with the k -arms A_1^c and A_2^c , respectively, the parameters γ were chosen such that the integrated intensities are the same in phase C, at $T = 2$ K after zfc, i.e., $I(\mathbf{q}_{\text{I},0}) = I(\mathbf{q}_{\text{II},0})$. This reflects, that the domains of the commensurate $(\pi\pi 0)$ structure in phase C are equally populated after zfc. For the averages over incommensurate satellites $\mathbf{q}_{\text{II},y}^\pm$, $\mathbf{q}_{\text{II},z}^\pm$, and $\mathbf{q}_{\text{I},x/y}^\pm$, which are associated with the arms $A_{2,y}^{ic}$, $A_{2,z}^{ic}$, and $A_{1,x/y}^{ic}$, respectively, the parameters γ were chosen such that the integrated intensities are the same in phase IC1, at $T = 16$ K after zfc, i.e., $I(\mathbf{q}_{\text{I},x/y}^\pm) = I(\mathbf{q}_{\text{II},y}^\pm) = I(\mathbf{q}_{\text{II},z}^\pm)$. This reflects, that the domains of the ground state in IC1 are equally populated in zero field after zfc. For the pairs $\mathbf{q}_{\text{I},\alpha}^\pm$ and $\mathbf{q}_{\text{I},\beta}^\pm$ an independent but constant parameter was chosen.

In the following, the data are presented, which were recorded by means of the three field

sweeps sweepB1, sweepB2, and sweepB3. Diffraction data $J(\omega)$ as a function of field, as recorded by means of rocking scans around $\mathbf{q}_{\text{I},0}$ and $\mathbf{q}_{\text{II},0}$, are presented in terms of color plots. The inferred integrated intensities as a function of field are first discussed for peaks of the stars $\langle \frac{1}{2} \frac{1}{2} 0 \rangle$ and $\langle \frac{1}{2} - \delta, \frac{1}{2}, 0 \rangle$ only. The evolution as a function of field of the peaks located at $\mathbf{q}_{\alpha}^{\pm}$ and \mathbf{q}_{β}^{\pm} is discussed further below. Temperature dependences that were determined at different magnetic fields by means of temperature sweeps are presented in the appendix (cf. Sec. A.4).

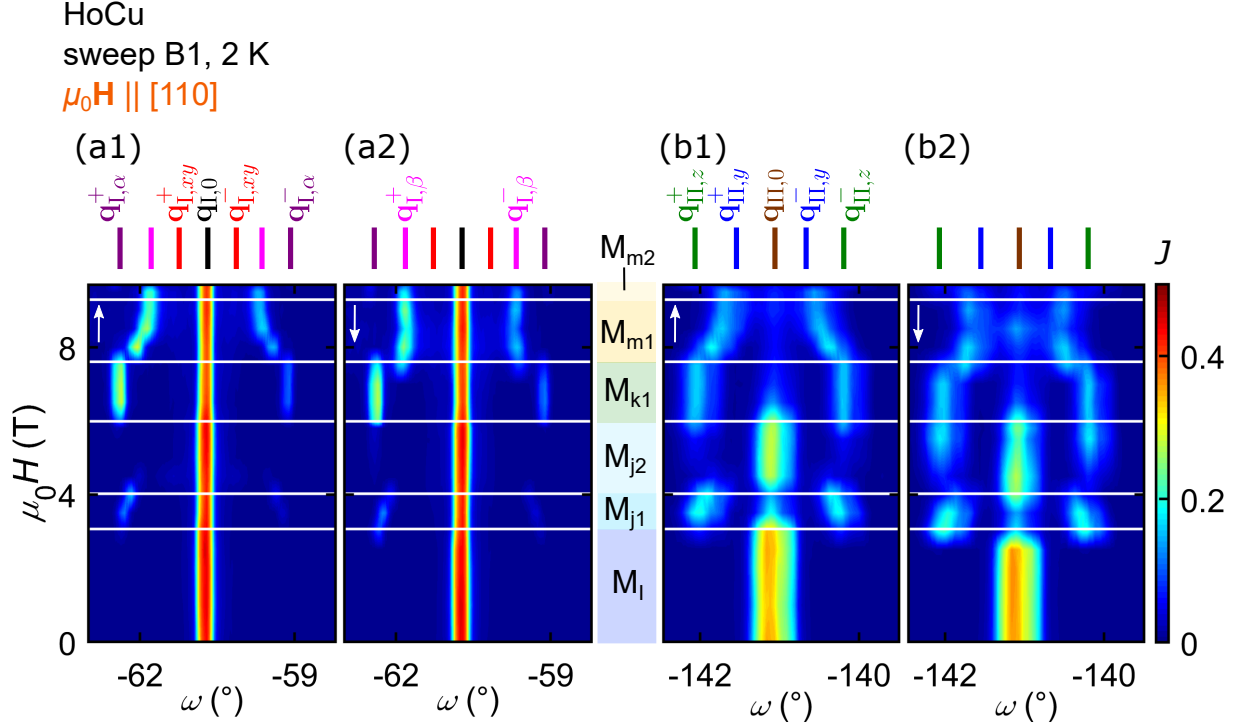


Figure 3.22.: Field sweep sweepB1, which started in phase C, at $T = 2$ K after zfc. Shown is the field dependence of diffraction data $J(\omega)$ recorded by means of rocking scans. (a1) and (a2) show the scattering intensity in the vicinity of $\mathbf{q}_{\text{I},0}$ for increasing and decreasing fields, respectively. (b1) and (b2) show the scattering intensity in the vicinity of $\mathbf{q}_{\text{II},0}$ for increasing and decreasing fields, respectively. The field was first increased from 0 T to 9.7 T and then decreased to 0 T. Colored stripes at the top indicate the positions of the Bragg peaks listed in Tab. 3.8. Colored bars in the middle indicate the phases of the $\langle 110 \rangle$ phase diagram, which were traversed.

Fig. 3.22 presents the data, recorded by means of rocking scans as a function of field, as determined from sweepB1. Shown in Fig. 3.22 (a) are the data $J(\omega)$ recorded by means of rocking scans around $\mathbf{q}_{\text{I},0}$ for (a1) increasing field and for (a2) decreasing field. Fig. 3.22 (b) shows the data $J(\omega)$ recorded by means of rocking scans around $\mathbf{q}_{\text{II},0}$ for (b1) increasing field and for (b2) decreasing field. The positions of all magnetic Bragg peaks in Tab. 3.8 are tagged at the top of the figure by colored stripes. The phase pockets of

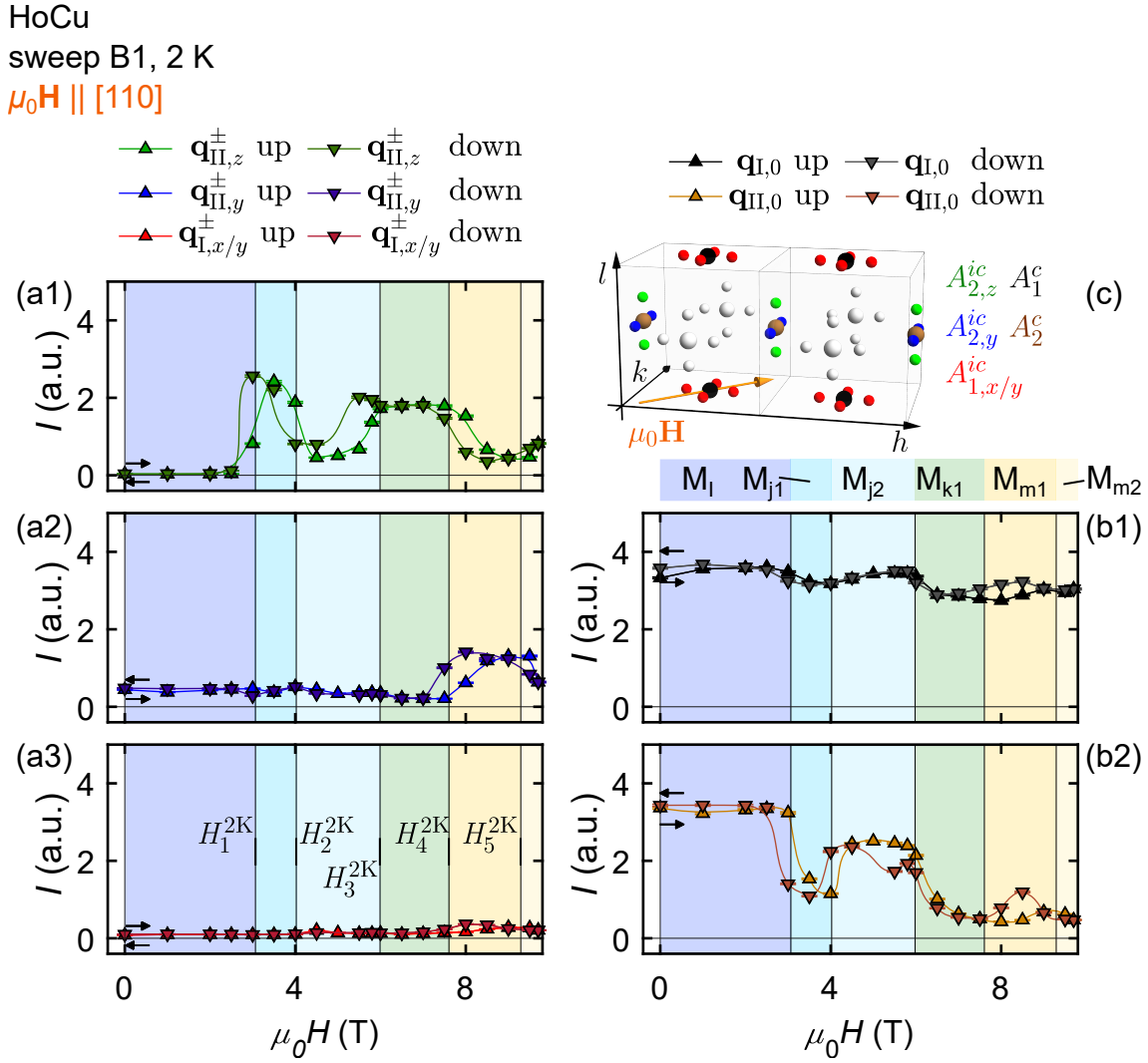


Figure 3.23.: Integrated intensities as a function of field as inferred from sweepB1 of Bragg peaks, which are associated with the stars $\langle \frac{1}{2} \frac{1}{2} 0 \rangle$ and $\langle \frac{1}{2} - \delta, \frac{1}{2}, 0 \rangle$, respectively. The integrated intensities at (a1) $\mathbf{q}_{\text{II},z}^{\pm}$, (a2) $\mathbf{q}_{\text{II},y}^{\pm}$, and (a3) $\mathbf{q}_{\text{I},x/y}^{\pm}$ reflect the field dependences of the arms $A_{2,z}^{ic}$, $A_{2,y}^{ic}$, and $A_{1,x/y}^{ic}$, respectively. These three arms belong to the $\langle \frac{1}{2} - \delta, \frac{1}{2}, 0 \rangle$ star. The integrated intensities at (b1) $\mathbf{q}_{\text{I},0}$ and (b2) $\mathbf{q}_{\text{II},0}$ reflect the field dependences of the k -arms A_1^c and A_2^c , respectively. These two arms belong to the $\langle \frac{1}{2} \frac{1}{2} 0 \rangle$ star. Vertical lines represent the transition fields as inferred from the $\langle 110 \rangle$ phase diagrams presented in Ref. [18]. (c) Schematic illustration of the orientation of the investigated k -arms with respect to the magnetic field direction. The phase pockets in the $\langle 110 \rangle$ phase diagram, which are traversed during the sweep, are indicated by colored bars.

the $\langle 110 \rangle$ phase diagram, which are traversed during the sweep, are indicated by colored bars in the middle

The comparison of scattering intensities at $\mathbf{q}_{\text{I},0}$ and $\mathbf{q}_{\text{II},0}$ reveals the distinctively different field dependences of the two commensurate wave-vector arms A_1^c and A_2^c , for which the symmetry is broken in the field. While the commensurate peak at $\mathbf{q}_{\text{I},0}$ exhibits finite intensity throughout the whole field range, the intensity of the peak at $\mathbf{q}_{\text{II},0}$ disappears

twice during the sweep. Several changes of incommensurate propagation vectors indicate transitions between several magnetic phases featuring different magnetic ground states.

Shown in Fig. 3.23 are the integrated intensities at the positions (a1) $\mathbf{q}_{\text{II},z}^{\pm}$, (a2) $\mathbf{q}_{\text{II},y}^{\pm}$, (a3) $\mathbf{q}_{\text{I},x/y}^{\pm}$, (b1) $\mathbf{q}_{\text{I},0}$, and (b2) $\mathbf{q}_{\text{II},0}$ as a function of field. Triangles pointing upwards represent data points for increasing field, triangles pointing downwards represent data points for decreasing field. The phase pockets of the $\langle 110 \rangle$ phase diagram, which are traversed during the sweep, are indicated by colored bars. The transition fields, as inferred from the magnetic phase diagram, are represented by vertical lines. These transition fields are clearly related to anomalies in the integrated intensities as a function of field. The five field dependences reflect the evolution of the three arms (a1) $A_{2,z}^{ic}$, (a2) $A_{2,y}^{ic}$, and (a3) $A_{1,x/y}^{ic}$ of the $\langle \frac{1}{2} - \delta, \frac{1}{2}, 0 \rangle$ star and of the two k -arms (b1) A_1^c and (b2) A_2^c of the $\langle \frac{1}{2} \frac{1}{2} 0 \rangle$ star. Fig. 3.23 (c) illustrates schematically the orientation of the five arms with respect to the field direction. The two arms $A_{1,x/y}^{ic}$, which have the same orientation in the field, are depicted in the same color.

Further, qualitative differences of the field dependences of k -arms, which belong to the same star, reflect their different orientation with respect to the twofold magnetic field direction. When the field increases up to 9.7 T, the integrated intensity of the commensurate peak at $\mathbf{q}_{\text{I},0}$ exhibits only slight variations with at least two broad dips. The integrated intensity of the commensurate peak at $\mathbf{q}_{\text{II},0}$ displays a distinctively different behavior. In phase M_{I} it displays a plateau. At $H_1^{2\text{K}} = 3.07$ T, the integrated intensity drops sharply featuring distinctively smaller values in phase M_{j1} , i.e., between $H_1^{2\text{K}}$ and $H_2^{2\text{K}} = 4$ T. Above $H_2^{2\text{K}}$ it increases again to a plateau in phase M_{j2} . Above $H_3^{2\text{K}} = 5.99$ T it decreases again and remains small for fields up to 9.7 T, featuring a weak dip at $H_5^{2\text{K}} = 9.30$ T.

The integrated intensity of $\mathbf{q}_{\text{I},x/y}^{\pm}$ is vanishingly small during the whole sweep, apart from a shallow maximum slightly above 8 T. The integrated intensity at $\mathbf{q}_{\text{II},z}^{\pm}$ is vanishingly small for fields below $H_1^{2\text{K}}$, i.e., in phase M_{I} . At roughly $H_1^{2\text{K}}$ it increases sharply featuring finite values in phase M_{j1} . It decreases again sharply slightly above $H_2^{2\text{K}}$ and is clearly weaker in phase M_{j2} . At roughly $H_3^{2\text{K}}$ it again starts to increase and displays a plateau in phase M_{k1} ranging to $H_4^{2\text{K}} = 7.61$ T. Between $H_4^{2\text{K}}$ and 9.7 T, i.e., in phase M_{m1} and beyond, it slowly decreases. The integrated intensity at $\mathbf{q}_{\text{II},y}^{\pm}$ is small for fields below $H_4^{2\text{K}}$. Residual integrated intensities are presumably due to a finite overlap with peaks located at $\mathbf{q}_{\text{II},0}^{\pm}$. Above $H_4^{2\text{K}}$ it starts to increase, has a local maximum in phase M_{m1} , and decreases again between $H_5^{2\text{K}}$ and 9.7 T. For decreasing field the curves of all integrated intensities are shifted to lower field values, reflecting a weak hysteresis. Between $H_5^{2\text{K}}$ and $H_4^{2\text{K}}$, i.e., in phase M_{m1} , the integrated intensities at $\mathbf{q}_{\text{II},0}$ and $\mathbf{q}_{\text{I},0}$ are stronger for decreasing field than for increasing field. Notably, in zero magnetic field after the field

sweep, the integrated intensities at both $\mathbf{q}_{\text{II},0}$ and $\mathbf{q}_{\text{I},0}$ feature roughly the same value as in zero magnetic field after zfc, although the symmetry between the two wave vectors is broken by the twofold field direction reflecting the multi- k nature of the ground state in phase C.

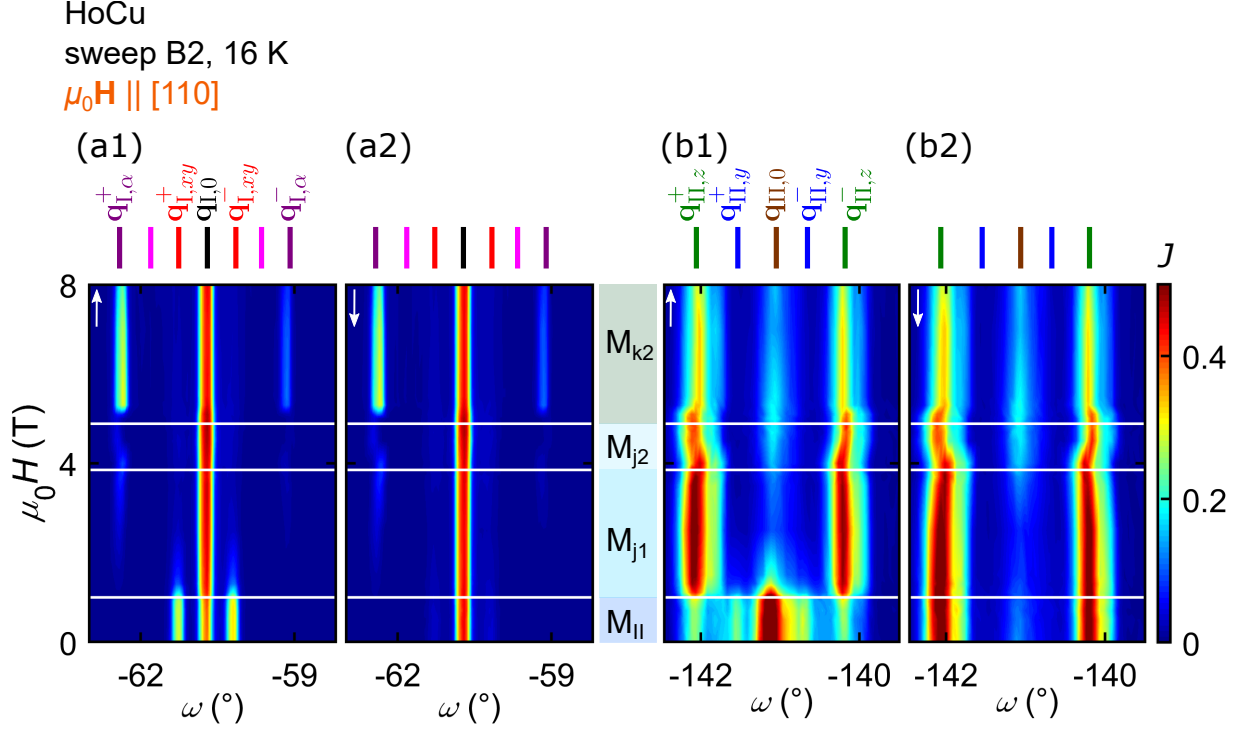


Figure 3.24.: Field sweep sweepB2, which started in phase IC1, at $T = 16$ K after zfc. Shown is the field dependence of diffraction data $J(\omega)$ recorded by means of rocking scans. (a1) and (a2) show the scattering intensity in the vicinity of $\mathbf{q}_{\text{I},0}$ for increasing and decreasing fields, respectively. (b1) and (b2) show the scattering intensity in the vicinity of $\mathbf{q}_{\text{II},0}$ for increasing and decreasing fields, respectively. The field was first increased from 0 T to 9.7 T and then decreased to 0 T. Colored stripes at the top indicate the positions of the Bragg peaks listed in Tab. 3.8. Colored bars in the middle indicate the phases of the $\langle 110 \rangle$ phase diagram, which were traversed.

Fig. 3.24 presents data recorded by means of the rocking scans as a function of field, as determined by means of sweepB2. Fig. 3.24 (a) shows the data $J(\omega)$ recorded in the vicinity of $\mathbf{q}_{\text{I},0}$ and Fig. 3.24 (b) the data $J(\omega)$ recorded in the vicinity of $\mathbf{q}_{\text{II},0}$.

Shown in Fig. 3.25 are the integrated intensities at (a1) $\mathbf{q}_{\text{II},z}^{\pm}$, at (a2) $\mathbf{q}_{\text{II},y}^{\pm}$, at (a3) $\mathbf{q}_{\text{I},x/y}^{\pm}$, at (b1) $\mathbf{q}_{\text{I},0}$, and at (b2) $\mathbf{q}_{\text{II},0}$ as a function of field. In zero magnetic field after zfc, the commensurate peaks feature almost the same integrated intensities $I(\mathbf{q}_{\text{I},0}) \approx I(\mathbf{q}_{\text{II},0})$, reflecting equilibrium of the magnetic domains in phase IC1. The integrated intensities of the incommensurate satellites display the same value by definition of the parameters γ . When the field increases, the integrated intensities at $\mathbf{q}_{\text{I},0}$, $\mathbf{q}_{\text{II},0}$, $\mathbf{q}_{\text{I},x/y}^{\pm}$, $\mathbf{q}_{\text{II},y}^{\pm}$, and $\mathbf{q}_{\text{II},z}^{\pm}$ are constant in phase M_{II} . At $H_1^{16\text{K}} = 1.0$ T, the integrated intensities at $\mathbf{q}_{\text{I},0}$ and $\mathbf{q}_{\text{II},z}^{\pm}$ start to

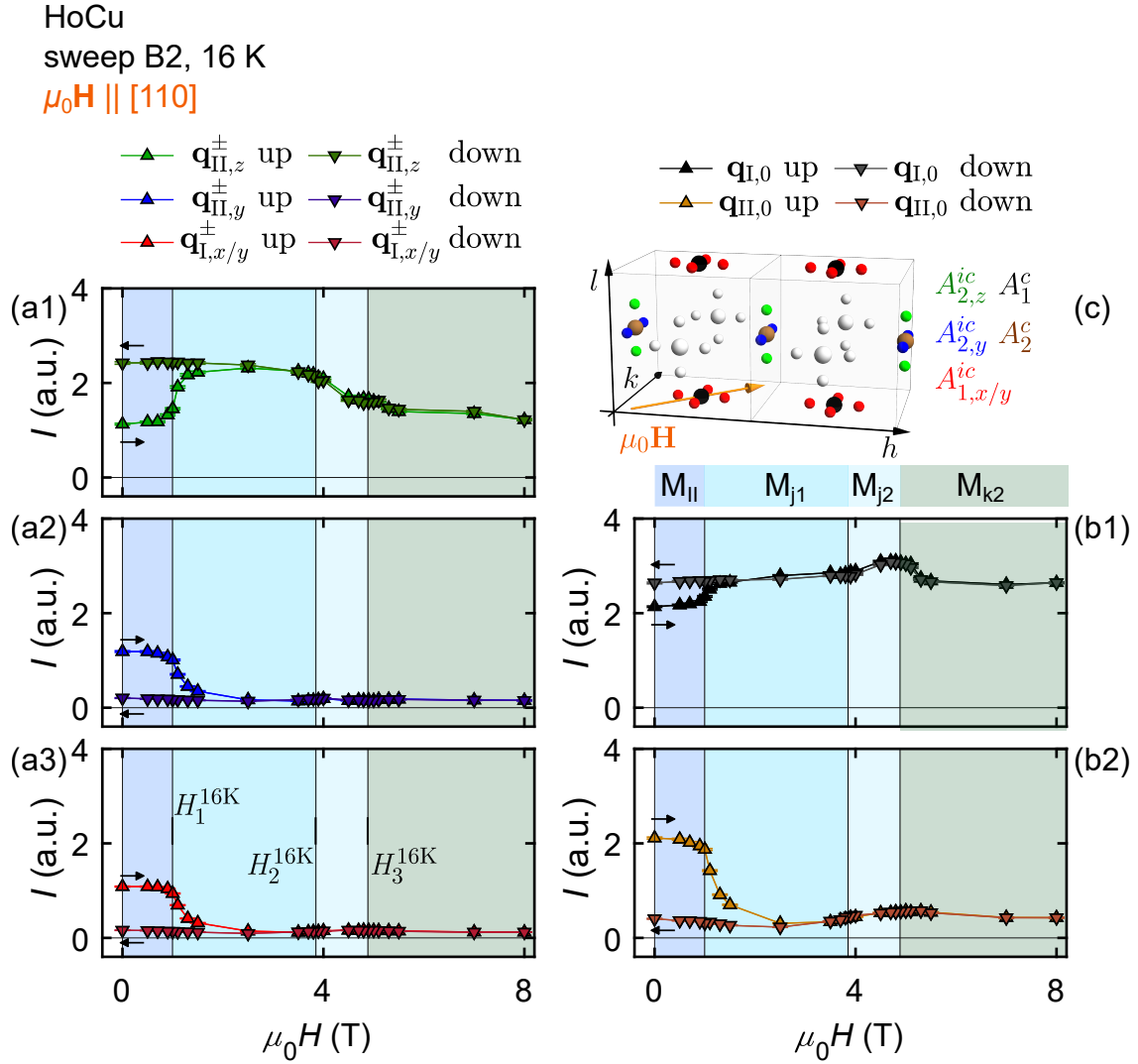


Figure 3.25.: Integrated intensities as a function of field as inferred from sweepB2 of Bragg peaks, which are associated with the stars $\langle \frac{1}{2} \frac{1}{2} 0 \rangle$ and $\langle \frac{1}{2} - \delta, \frac{1}{2}, 0 \rangle$, respectively. The integrated intensities at (a1) $\mathbf{q}_{\text{II},z}^{\pm}$, (a2) $\mathbf{q}_{\text{II},y}^{\pm}$, and (a3) $\mathbf{q}_{\text{I},x/y}^{\pm}$ reflect the field dependences of the arms $A_{2,z}^{ic}$, $A_{2,y}^{ic}$, and $A_{1,x/y}^{ic}$, respectively. These three arms belong to the star $\langle \frac{1}{2} - \delta, \frac{1}{2}, 0 \rangle$. The integrated intensities at (b1) $\mathbf{q}_{\text{I},0}$ and (b2) $\mathbf{q}_{\text{II},0}$ reflect the field dependences of the k -arms A_1^c and A_2^c , respectively. These two arms belong to the $\langle \frac{1}{2} \frac{1}{2} 0 \rangle$ star. Vertical lines represent the transition fields as inferred from the $\langle 110 \rangle$ phase diagrams presented in Ref. [18]. (c) Schematic illustration of the orientation of the investigated arms with respect to the magnetic field direction. The phase pockets in the $\langle 110 \rangle$ phase diagram, which are traversed, are indicated by colored bars.

increase, whereas the integrated intensities at $\mathbf{q}_{\text{II},0}$, $\mathbf{q}_{\text{I},x/y}^{\pm}$, and $\mathbf{q}_{\text{II},y}^{\pm}$ decrease to vanishingly small values. The integrated intensities of $\mathbf{q}_{\text{I},x/y}^{\pm}$ and $\mathbf{q}_{\text{II},y}^{\pm}$ remain vanishingly small for fields up to 8 T. The integrated intensity of $\mathbf{q}_{\text{II},0}$ increases slightly between $H_2^{16\text{K}} \approx 3.85$ T and $H_3^{16\text{K}} = 4.89$ T, i.e., in phase M_{j2} , displays a weak maximum at $\approx H_3^{16\text{K}}$, and decreases between $H_3^{16\text{K}}$ and 8 T, i.e., in phase M_{k2} . The integrated intensity at $\mathbf{q}_{\text{II},z}^{\pm}$ displays essentially a plateau between $H_1^{16\text{K}}$ and $H_2^{16\text{K}}$ in phase M_{j1} , decreases between $H_2^{16\text{K}}$ and

H_3^{16K} in phase M_{j2} , and displays a plateau in phase M_{k2} between H_3^{16K} and 8 T that starts to decrease weakly at a field slightly below 8 T. No differences between decreasing and increasing fields are visible for fields above H_1^{16K} , i.e., no hysteresis may be observed. In phase M_{II} the integrated intensities at $\mathbf{q}_{I,0}$ and $\mathbf{q}_{II,z}^\pm$ remain on the value of the plateaus observed in phase M_{j1} between H_1^{16K} and H_2^{16K} . In contrast, the integrated intensities at $\mathbf{q}_{II,0}$, $\mathbf{q}_{I,x/y}^\pm$, and $\mathbf{q}_{II,y}^\pm$ remain vanishingly small. This reflects that the domain populations before and after the field sweep are different.

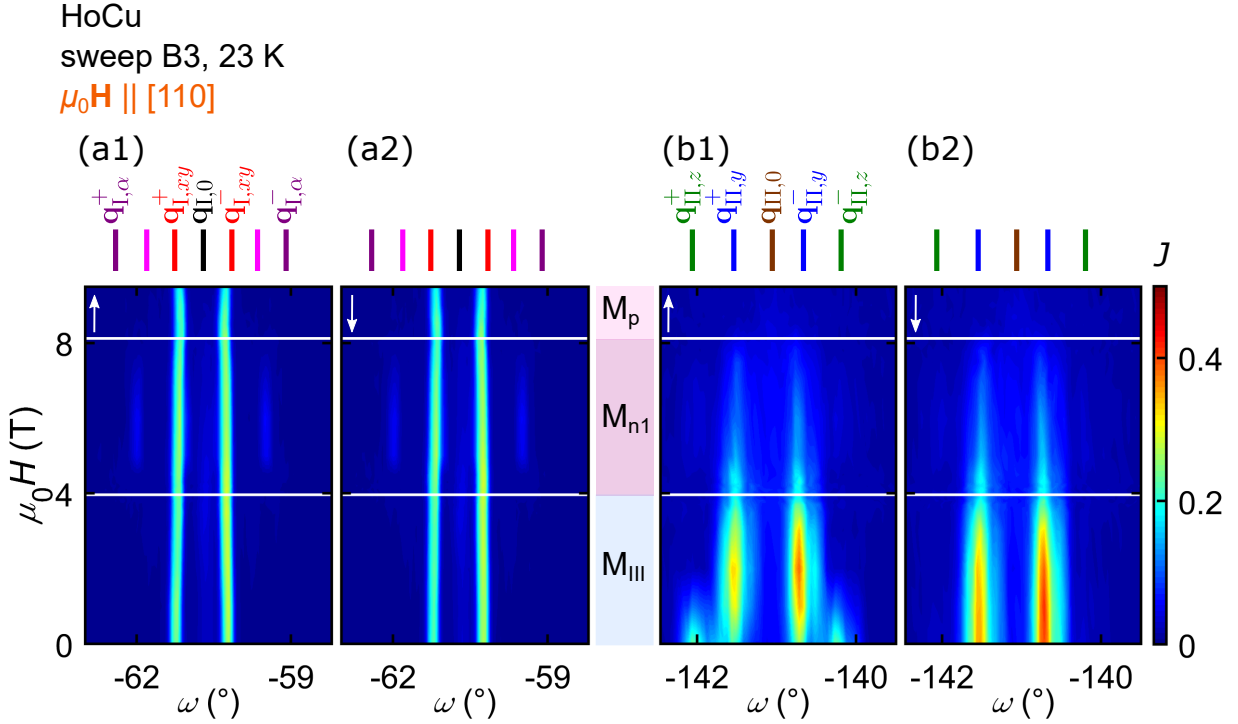


Figure 3.26.: Field sweep sweepB3, which started in phase IC2, at $T = 23$ K after zfc. Shown is the field dependence of diffraction data $J(\omega)$ recorded by means of rocking scans. (a1) and (a2) show the scattering intensity in the vicinity of $\mathbf{q}_{I,0}$ for increasing and decreasing fields, respectively. (b1) and (b2) show the scattering intensity in the vicinity of $\mathbf{q}_{II,0}$ for increasing and decreasing fields, respectively. The field was first increased from 0 T to 9.7 T and then decreased to 0 T. Colored stripes at the top indicate the positions of the Bragg peaks listed in Tab. 3.8. Colored bars in the middle indicate the phases of the $\langle 110 \rangle$ phase diagram, which were traversed.

Fig. 3.26 presents the data recorded by means of rocking scans as a function of field, as determined by means of sweepB3. Fig. 3.26 (a) shows the data $J(\omega)$ recorded in the vicinity of $\mathbf{q}_{I,0}$ and Fig. 3.26 (b) the data $J(\omega)$ recorded in the vicinity of $\mathbf{q}_{II,0}$.

Shown in Fig. 3.27 are the integrated intensities at (a1) $\mathbf{q}_{II,z}^\pm$, at (a2) $\mathbf{q}_{II,y}^\pm$, at (a3) $\mathbf{q}_{I,x/y}^\pm$, at (b1) $\mathbf{q}_{I,0}$, and at (b2) $\mathbf{q}_{II,0}$ as a function of field. In zero magnetic field after zfc, the two commensurate Bragg peaks display roughly the same integrated intensities. The same is true for the incommensurate Bragg peaks, reflecting that magnetic domains in phase IC2

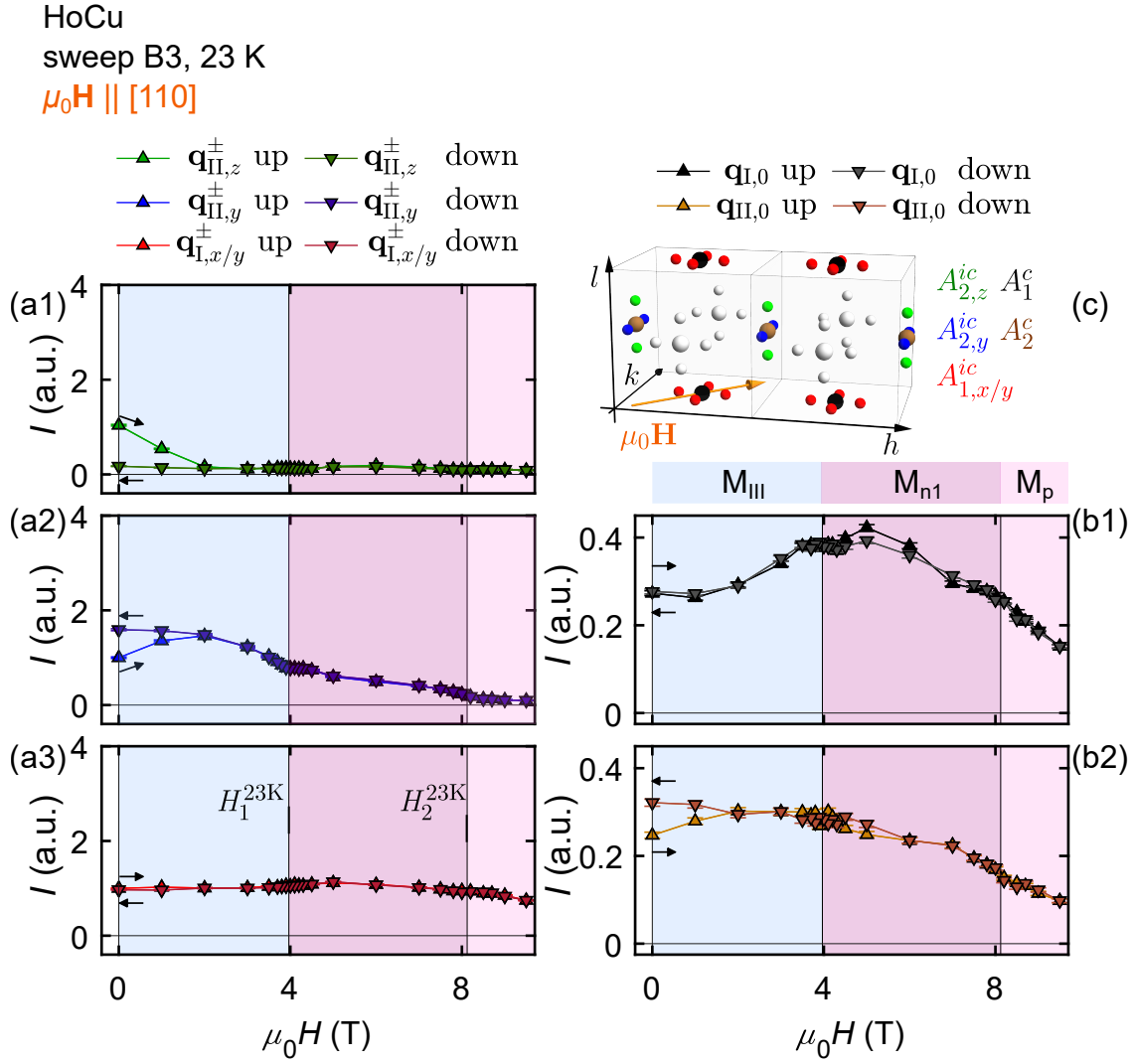


Figure 3.27.: Integrated intensities as a function of field as inferred from sweepB3 of Bragg peaks, which are associated with the stars $\langle \frac{1}{2} \frac{1}{2} 0 \rangle$ and $\langle \frac{1}{2} - \delta, \frac{1}{2}, 0 \rangle$, respectively. The integrated intensities of (a1) $\mathbf{q}_{\text{II},z}^{\pm}$, (a2) $\mathbf{q}_{\text{II},y}^{\pm}$, and (a3) $\mathbf{q}_{\text{I},x/y}^{\pm}$ reflect the field dependences of the arms $A_{2,z}^{ic}$, $A_{2,y}^{ic}$, and $A_{1,x/y}^{ic}$, respectively. These three arms belong to the $\langle \frac{1}{2} - \delta, \frac{1}{2}, 0 \rangle$ star. The integrated intensities of (b1) $\mathbf{q}_{\text{I},0}$ and (b2) $\mathbf{q}_{\text{II},0}$ reflect the field dependences of the k -arms A_1^c and A_2^c , respectively. These two arms belong to the $\langle \frac{1}{2} \frac{1}{2} 0 \rangle$ star. Vertical lines represent the transition fields as inferred from the $\langle 110 \rangle$ phase diagrams presented in Ref. [18]. (c) Schematic illustration of the orientation of the investigated k -arms with respect to the magnetic field direction. The phase pockets in the $\langle 110 \rangle$ phase diagram, which are traversed, are indicated by colored bars.

are equally populated. When the field increases, the integrated intensity at $\mathbf{q}_{\text{II},z}^{\pm}$ decreases and vanishes around 2 T in phase M_{III} . The intensity remains vanishingly small for fields up to 8 T. The integrated intensity of $\mathbf{q}_{\text{II},y}^{\pm}$ first increases, displays a local maximum in phase M_{III} at 1 T, and decreases for fields larger than 1 T. At $H_1^{23\text{K}}$ the slope changes and in phase M_p above $H_2^{23\text{K}}$ the intensity is vanishingly small. The integrated intensity at $\mathbf{q}_{\text{I},x/y}^{\pm}$ is almost constant and exhibits only slight variations featuring a shallow maximum

at 5 T in phase M_{n1} . The integrated intensity at $\mathbf{q}_{I,0}$ first increases in phase M_{III} , exhibits a local maximum at a field slightly larger than H_1^{23K} , and decreases in the field range between H_1^{23K} and 8 T, i.e., in phases M_{n1} and M_p . The integrated intensity at $\mathbf{q}_{II,0}$ increases at low fields, displays a local maximum at roughly H_1^{23K} , and decreases up to 8 T, i.e. in phases M_{n1} and M_p . When the field decreases, no differences may be observed in the integrated intensities at $\mathbf{q}_{I,x/y}^\pm$. No differences are visible in the integrated intensities at $\mathbf{q}_{II,y}^\pm$ and $\mathbf{q}_{II,z}^\pm$ for fields between 8 T and 1 T. In phase M_{III} for fields below 1 T, the integrated intensity at $\mathbf{q}_{II,y}^\pm$ is larger than for increasing fields, whereas the integrated intensity at $\mathbf{q}_{II,z}^\pm$ remains vanishingly small. The integrated intensities at $\mathbf{q}_{I,0}$ do not exhibit strong differences for increasing and decreasing field between 8 T and 0 T. In the vicinity of 5 T in phase M_{n1} only, the intensity is slightly weaker for decreasing field than for increasing field. No differences are visible in the integrated intensity at $\mathbf{q}_{I,0}$ for increasing and decreasing field between 8 T to 6 T. Between 6 T and 3 T in phase M_{n1} the integrated intensity at $\mathbf{q}_{I,0}$ is slightly larger for decreasing field than for increasing field. Below 2 T in phase M_{III} the intensity of $\mathbf{q}_{II,0}$ is larger for decreasing field than for increasing field. The difference in integrated intensities before and after the field sweep reflects that the population of magnetic domains changed during the field sweep.

Presented in Fig. 3.28 are the integrated intensities of $\mathbf{q}_{I,\alpha}^\pm$ and $\mathbf{q}_{I,\beta}^\pm$, as inferred from the field sweeps sweepB1, sweepB2, and sweepB3. The field dependences, which are presented in Fig. 3.28 (a), (b), and (c), were inferred from the data presented in Fig. 3.22, Fig. 3.24, and Fig. 3.26, respectively.

When the field increases in sweepB1, the integrated intensity at $\mathbf{q}_{I,\alpha}^\pm$ remains vanishingly small in phase M_I . At H_1^{2K} the integrated intensity starts to increase, displays a local maximum in phase M_{j1} , and decreases steeply just above H_2^{2K} . Above H_3^{2K} it exhibits a steep increase, displays a local maximum in phase M_{k1} , decreased sharply above H_4^{2K} and displays a plateau at relatively small intensity in phase M_{m1} . At the highest field values, above H_5^{2K} , the intensity increases again. The integrated intensity at $\mathbf{q}_{I,\beta}^\pm$ remains vanishingly small in phase M_I . In phase M_{j1} it starts to increase and displays a local maximum at H_2^{2K} . Above H_2^{2K} in phase M_{j2} it decreases steeply. In phase M_{k1} it increases with a small slope. At H_4^{2K} the intensity increases sharply, displays a local maximum in phase M_{m1} and decreases sharply at approximately H_5^{2K} . When the field decreases, the curves are slightly shifted, reflecting a weak hysteresis.

When the field increases in sweepB2, the integrated intensity at $\mathbf{q}_{I,\alpha}^\pm$ remains vanishingly small in phase M_{II} . In phase M_{j1} it increases slowly. At H_2^{16K} it has a kink and a local maximum. In phase M_{j2} , i.e., between H_2^{16K} and H_3^{16K} , it decreases. At H_3^{16K} it has a kink, slightly above H_3^{16K} it first displays a sharp step-like increase to a local maximum, followed by a slow decrease when approaching 8 T, the highest field measured. The integrated

intensity of $\mathbf{q}_{\mathbf{l},\beta}^{\pm}$ remained vanishingly small for fields below H_3^{2K} . Slightly above H_3^{16K} it increases to a weak plateau in phase M_{k2} between H_3^{16K} and 8 T. No difference is visible between increasing and decreasing fields.

When the field increases in sweepB3, the integrated intensity at $\mathbf{q}_{\mathbf{l},\alpha}^{\pm}$ is vanishingly small for fields up to 9.5 T, apart from a weak maximum slightly above H_1^{23K} in phase M_{n1} . The integrated intensity at $\mathbf{q}_{\mathbf{l},\beta}^{\pm}$ starts to slowly increase at 2 T. Above H_1^{23K} it first increased with larger slope, displays a local maximum in phase M_{n1} , and decreases again. For fields larger than H_2^{23K} in phase M_p , the integrated intensity displays a tail while still decreasing. When the field decreases, no hysteresis is observed.

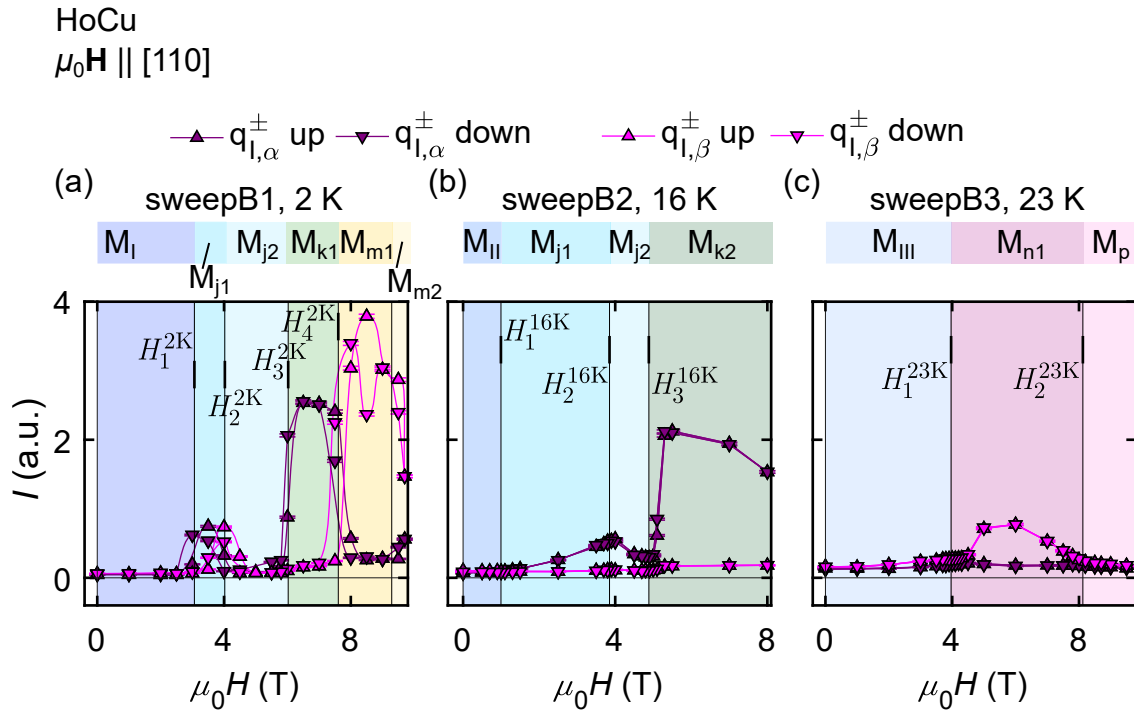


Figure 3.28.: Field dependences of the magnetic satellites $\mathbf{q}_{\mathbf{l},\alpha}^{\pm}$ and $\mathbf{q}_{\mathbf{l},\beta}^{\pm}$. Shown in (a), (b), and (c) are integrated intensities as a function of field, as determined at $T = 2$ K (sweepB1), at $T = 16$ K (sweepB2), and at $T = 23$ K (sweepB3), respectively. Data points for increasing fields are represented by squares, for decreasing fields by triangles. The transitions, as inferred from bulk phase diagrams [18], are represented by vertical lines.

The field- and temperature dependences allow to specify the magnetic propagation vectors in the phase pockets of the $\langle 110 \rangle$ phase diagram. Stars of magnetic propagation vectors of the ground states in each phase pocket were determined as follows. For each phase pocket all those stars were identified, for which integrated intensities at related Bragg peak positions feature finite values in the majority of the corresponding field- or temperature region. The resulting stars of the corresponding wave vectors, which were identified, are summarized in Tab. 3.7.

All ground states with propagation vectors of at least two different stars are multi- k . This holds true for the ground states in the phase pockets M_{II} (and phase IC1), M_{III} (and phase IC2), M_{j1} , M_{j2} , M_{k1} , M_{k2} , M_{m1} , M_{m2} , and M_{n1} . In phase M_o , the ground state has only propagation vectors of the star $\langle \frac{1}{2} \frac{1}{2} 0 \rangle$. As argued in the following, the ground state in M_o is single- k . During field cooling in a field of 9.7 T, i.e., during sweepT6, in phase M_o the integrated intensity at $\mathbf{q}_{\text{I}}^c \in A_1^c \in \mathcal{S}_1^c$ is strongly enhanced whereas $\mathbf{q}_{\text{II}}^c \in A_2^c \in \mathcal{S}_2^c$ remains relatively weak. Hence, only the single k -arm with orientation S_1^c is participating and the ground state has propagation vectors of only $A_1^c \in \mathcal{S}_1^c$ implying that the structure is single- k .

In phase M_p , the ground state has only propagation vectors of the $\langle \frac{1}{2} - \delta, \frac{1}{2}, 0 \rangle$ star. As argued in the following, the ground state is either single- k or double- k . During field-cooling in a field of 9.7 T, i.e., during sweepT6, in phase M_p the integrated intensity at $\mathbf{q}_{\text{I},x/y}^{ic} \in A_{\text{I},x/y}^{ic}$ is strongly enhanced, whereas $\mathbf{q}_{\text{II},z}^{ic}$ and $\mathbf{q}_{\text{II},y}^{ic}$ are vanishingly small. Hence, the ground state has propagation vectors of only k -arms with orientation S_1^{ic} . As S_1^{ic} contains only two k -arms, the magnetic structure in phase M_p has either one or two participating k -arms. Accordingly, the magnetic structure is either single- k or double- k . Note that a multi- k ground state combining incommensurate propagation vectors that lie in the vicinity of the same commensurate $(\pi\pi 0)$ wave-vector arm may be relatively unconventional.

In the following, the number of commensurate and incommensurate propagation vectors of the ground states in M_{I} , which comprises C, in M_{II} , which comprises IC1, and in M_{III} , which comprises IC2, are specified further. In principle, the ground state in phase C may represent a single- k , double- k , or triple- k structure as established in Sec. 3.3.3.2. The experimental study above allows now to infer, that the ground state in phase C is either double- k or triple- k . In particular, the ground state is not single- k , as established in the following. In phase M_{I} , which comprises phase C, the Bragg peaks located at $\mathbf{q}_{\text{I}}^c \in A_1^c \in \mathcal{S}_1^c$ and $\mathbf{q}_{\text{II}}^c \in A_2^c \in \mathcal{S}_2^c$ always display the same integrated intensities. This was confirmed for the following field histories: (i) In zero magnetic field after zfc. Here, the integrated intensities at \mathbf{q}_{I}^c and \mathbf{q}_{II}^c feature the same value by definition of the parameters γ . This definition accounts for equal distribution of magnetic domains in zero field after zfc. (ii) after the field sweep sweepB1, which was presented in Fig. 3.23, (iii) after the temperature sweep sweepT1, i.e., after fc in a finite field of 0.5 T, and (iv) after the temperature sweep sweepT2, i.e., after fc in a finite field of 2.5 T (cf. Sec. A.4 for further information).

If the magnetic structure in phase M_{I} , and hence in C, would be single- k , a distinctively different behavior of the two Bragg peaks at \mathbf{q}_{I}^c and \mathbf{q}_{II}^c would be expected for the three protocols (ii), (iii), and (iv). Hence, it may be concluded that the ground state in phase C combines propagation vectors of k -arms of the sets \mathcal{S}_1^c and \mathcal{S}_2^c . In particular, the ground

state represents either a double- k structure with propagation vectors \mathbf{k}_1^c and \mathbf{k}_2^c or a triple- k structure with propagation vectors \mathbf{k}_1^c , \mathbf{k}_2^c , and \mathbf{k}_3^c .

In principle, the ground state in phase IC1 may represent any superposition of up to three commensurate and up to six incommensurate propagation vectors, which was established in Sec. 3.3.3.2. From the experimental study reported here, it may be established that the ground state in IC1 either represents a double- k or a triple- k state.

In phase M_{II} , which comprises IC1, after sweepB2 presented in Fig. 3.25 only the Bragg peaks located at $\mathbf{q}_I^c \in A_1^c \in \mathcal{S}_1^c$ and $\mathbf{q}_{II,z}^{ic} \in A_{2,z}^{ic} \in \mathcal{S}_3^{ic}$ feature finite integrated intensities. In contrast, the integrated intensities at $\mathbf{q}_{II}^c \in A_2^c \in \mathcal{S}_2^c$, $\mathbf{q}_{I,x/y}^{ic} \in A_{1,x/y}^{ic} \in \mathcal{S}_1^{ic}$, and $\mathbf{q}_{II,y}^{ic} \in A_{2,y}^{ic} \in \mathcal{S}_2^{ic}$ are vanishingly small. This suggests that the ground state in phase IC1 combines propagation vectors of k -arms of the sets \mathcal{S}_1^c and \mathcal{S}_3^{ic} . Hence the ground state in IC1 either represents a double- k structure with propagation vectors \mathbf{k}_1^c and $\mathbf{k}_{2,z}^{ic}$, or a triple- k structure with propagation vectors \mathbf{k}_1^c , $\mathbf{k}_{2,z}^{ic}$, and $\mathbf{k}_{3,z}^{ic}$.

Note, that the combination of the two propagation vectors $\mathbf{k}_{2,z}^{ic}$, and $\mathbf{k}_{3,z}^{ic}$ of the $\langle \frac{1}{2} - \delta, \frac{1}{2}, 0 \rangle$ star having collinear incommensurability may lead to mixed higher orders at positions such as $(\frac{1}{2} \pm 3\delta, \frac{1}{2}, 0)$, where scattering intensity was observed in phase IC1 as reported in Sec. 3.3.3.7.

In principle, the ground state in phase IC2 may represent any superposition of up to three commensurate and up to six incommensurate propagation vectors, which was established in Sec. 3.3.3.2. From the experimental study reported here, it may be inferred that the ground state in phase IC2 represents a multi- k state with at least four propagation vectors.

In phase M_{III} , which comprises IC2, after the field sweep sweepB3 presented in Fig. 3.27 only the Bragg peaks located at $\mathbf{q}_I^c \in A_1^c \in \mathcal{S}_1^c$, $\mathbf{q}_{II}^c \in A_2^c \in \mathcal{S}_2^c$, $\mathbf{q}_{I,x/y}^{ic} \in A_{1,x/y}^{ic} \in \mathcal{S}_1^{ic}$, and $\mathbf{q}_{II,y}^{ic} \in A_{2,y}^{ic} \in \mathcal{S}_2^{ic}$ have finite integrated intensities. In contrast the integrated intensity at $\mathbf{q}_{II,z}^{ic} \in A_{2,z}^{ic} \in \mathcal{S}_3^{ic}$ is vanishingly small. The same is observed in phase M_{III} during temperature sweep sweepT2, i.e., during field cooling in a field of 2.5 T (cf. Sec. A.4 for further information).

This observation suggests that the ground state in M_{III} , and hence in IC2, combines wave vectors of k -arms of the sets $\in \mathcal{S}_1^c$, \mathcal{S}_2^c , \mathcal{S}_1^{ic} , and \mathcal{S}_2^{ic} . In particular, the ground state represents a superposition of at least four propagation vectors. The combination of propagation vectors of the $\langle \frac{1}{2} - \delta, \frac{1}{2}, 0 \rangle$ star with noncollinear incommensurability may lead to mixed higher harmonics at positions such as $(\frac{1}{2} + \delta, \frac{1}{2} \pm 2\delta, 0)$, where scattering intensity was observed in phase IC2 as reported in Sec. 3.3.3.7.

3.3.4.2. Fields Along Fourfold Directions

To investigate the evolution of magnetic order for fields along fourfold $\langle 100 \rangle$ directions, neutron diffraction of the single crystal OFZ95-3-3-h was carried out at MIRA [138]. Fields were applied along the crystallographic [001] direction. However, the setup of the experiments provided fields of only 2.2 T. The objective of these experiments was on one hand to study magnetic ground states for fields along $\langle 100 \rangle$. On the other hand this field direction in principle qualifies to specify the number of propagation vectors of the ground states in zero field, as the field may break symmetries between propagation-vectors of these ground states.

All magnetic propagation vectors of the ground states in phases C, IC1, and IC2 belong to one of the stars $\langle \frac{1}{2} \frac{1}{2} 0 \rangle$ and $\langle \frac{1}{2} - \delta, \frac{1}{2}, 0 \rangle$. There are two possible orientations of commensurate $(\pi\pi 0)$ arms and three possible orientations of $(\pi - \delta, \pi, 0)$ arms in a field directed along a fourfold $\langle 100 \rangle$ axis. The [001] field direction breaks the symmetry between the commensurate k -arms A_1^c and A_2^c , and it breaks the symmetry between A_1^c and A_3^c . Between A_2^c and A_3^c it preserves the symmetry. The field direction preserves the symmetry between the incommensurate arms $A_{1,x}^{ic}$ and $A_{1,y}^{ic}$, between $A_{2,y}^{ic}$ and $A_{3,x}^{ic}$, as well as between $A_{2,z}^{ic}$ and $A_{3,z}^{ic}$. Between each of the three pairs it breaks the symmetry. In these experiments only the commensurate k -arm A_1^c and the incommensurate arm $A_{1,x}^{ic}$ were investigated as a function of temperature and field.

The main results of these experiments may be summarized as follows:

- In phase C, the magnetic Bragg peak, which is located at $\mathbf{q}_0 := (\frac{1}{2}, \frac{1}{2}, 0)$, vanishes in relatively small fields of 2 T. This was observed independent of the field history.
- This field dependence of the integrated intensity at \mathbf{q}_0 may be related either to a change of magnetic domains of the ground state of phase C implying that the ground state is single- k or double- k , or to a magnetic phase transition where the magnetic ground state changes. In the latter case, the ground state may be either single- k , double- k , or triple- k .
- Temperature dependences of the magnetic Bragg peaks \mathbf{q}_0 and $\mathbf{q}_{1,2} := (\frac{1}{2} \pm \delta, \frac{1}{2}, 0)$ are distinctively different under zero magnetic field and under a field of 2.2 T along [001].

The study was organized as follows. First, the integrated intensity of the Bragg peak located at \mathbf{q}_0 in phase C was studied as a function of field. Therefore, a field sweep starting in phase C at 5 K, was carried out. The field dependence of the commensurate Bragg peak $\mathbf{q}_0 = (\frac{1}{2}, \frac{1}{2}, 0)$ may reflect the field dependence of the k -arm A_1^c . Second, temperature dependences were determined for the peaks located at \mathbf{q}_0 and $\mathbf{q}_{1,2}$ at zero magnetic field (i.e. zfc) and at a finite field of 2.2 T (i.e. fc). Therefore, integrated intensities of \mathbf{q}_0 and

$\mathbf{q}_{1,2}$, respectively, were studied as a function of temperature. As a function of temperature, \mathbf{q}_0 reflects the temperature dependence of the k -arm A_1^c , whereas the average of \mathbf{q}_1 and \mathbf{q}_2 reflects the temperature dependence of the arm $A_{1,x}^{ic}$. Third, implications of these experiments on the ground states in the zero field phases are discussed.

For the experiments at MIRA, neutrons with a wavelength $\lambda \approx 4.52 \text{ \AA}$ were used. The sample was oriented such that the crystallographic (001) plane corresponded to the scattering plane. In this study, we investigated Bragg peaks, which are related to the $\langle \frac{1}{2} \frac{1}{2} 0 \rangle$ star, as present, for instance, in phase C, and Bragg peaks, which are related to the $\langle \frac{1}{2} - \delta, \frac{1}{2}, 0 \rangle$ star, as present, for instance, in phase IC1. The commensurate magnetic peak at $\mathbf{q}_0 \in A_1^c$ and the incommensurate peaks at $\mathbf{q}_{1,2} \in A_{1,x}^{ic}$ were, apart from equivalent peaks, the only reflections associated with the stars $\langle \frac{1}{2} \frac{1}{2} 0 \rangle$ and $\langle \frac{1}{2} - \delta, \frac{1}{2}, 0 \rangle$, respectively, located in the scattering plane and accessible in these experiments. Reflections of other k -arms (apart from $A_{1,y}^{ic}$) were far outside the horizontal plane, the exact angles depending on the incoming neutron wavelength. Temperature and field dependences of Bragg peaks were inferred from the temperature and field sweeps as follows. During the temperature and field sweeps rocking scans were carried out at a discrete set of field values and temperature values, respectively. From the rocking scans, integrated intensities of the three Bragg peaks located at \mathbf{q}_0 , \mathbf{q}_1 , and \mathbf{q}_2 were inferred.

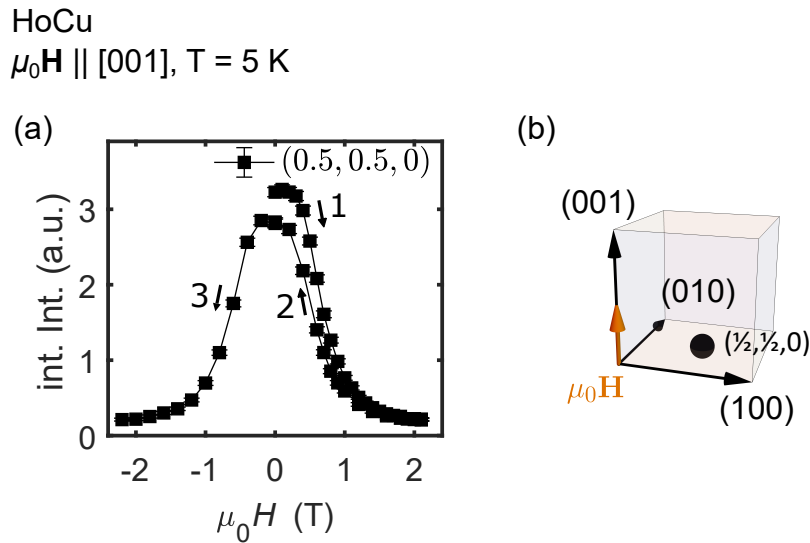


Figure 3.29.: Field dependence of the Bragg peak, located at \mathbf{q}_0 in phase C. (a) Integrated intensity of the Bragg peak located at \mathbf{q}_0 as a function of field. This field dependence may reflect the field dependence of the k -arm A_1^c . The field sweep started at $T = 5 \text{ K}$ in phase C after zfc. The field first increased to 2.2 T , second decreased to 0 T , and third decreased to -2.2 T . (b) Schematic picture, illustrating the orientation of the Bragg peak at \mathbf{q}_0 in the field, directed along $[001]$.

For the field sweep, which started in phase C at $T = 5 \text{ K}$ after zfc the field first increased to 2.2 T , second decreased to 0 T , and third decreased to negative values up to -2.2 T .

Shown in Fig. 3.29 is the integrated intensity of the Bragg peak at $\mathbf{q}_0 \sim \mathbf{k}_1^c$ as a function of field. As a function of increasing field, the integrated intensity decreases monotonically and vanishes at roughly 2 T. When the field decreases further, the integrated intensity increases monotonically and displays a local maximum at $\mu_0 H = 0$ T, being $\approx 12\%$ smaller than the integrated intensity after zfc. For inverted fields the integrated intensity decreases monotonically and vanishes at roughly -2 T.

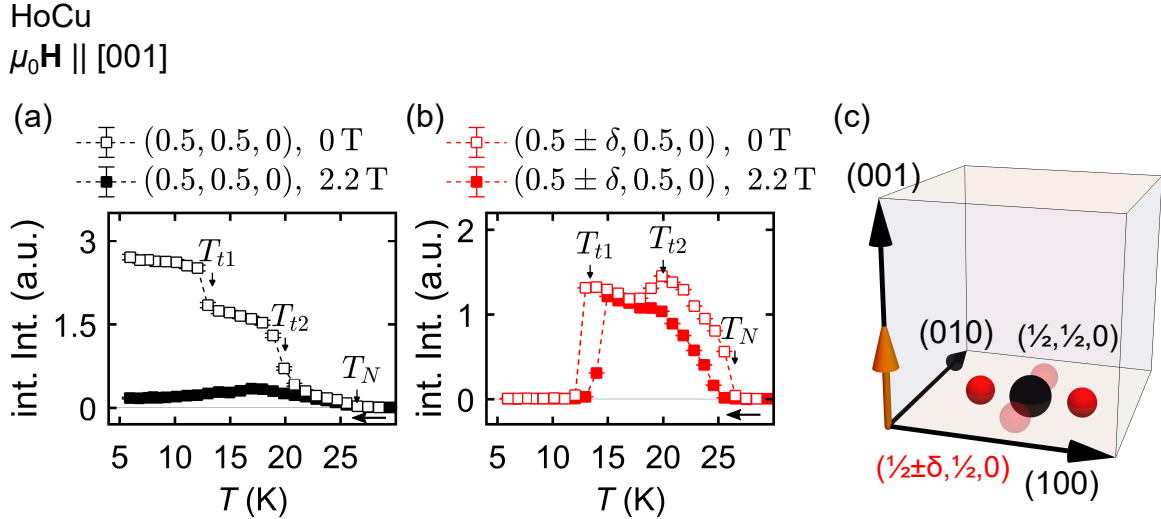


Figure 3.30: Temperature dependences of the Bragg peaks, located at \mathbf{q}_0 , \mathbf{q}_1 , and \mathbf{q}_2 . (a) Integrated intensities of the Bragg peak at \mathbf{q}_0 as a function of temperature. Shown are the temperature dependences, as inferred from the temperature sweep in in zero field (white squares) and from the temperature sweep in a field of 2.2 T (black squares). (b) Average of integrated intensities of the Bragg peaks at \mathbf{q}_1 and at \mathbf{q}_2 as a function of temperature. Shown are the temperature dependences, as inferred from the temperature sweep in in zero field (white squares) and from the temperature sweep in a field of 2.2 T (black squares). (c) Schematic picture, illustrating the orientation of the Bragg peaks at \mathbf{q}_0 , \mathbf{q}_1 , and \mathbf{q}_2 in a field along (001). The Bragg peaks located at $(\frac{1}{2}, \frac{1}{2} \pm \delta, 0)$ are illustrated by spheres with lower opacity.

Shown in Fig. 3.30 are the integrated intensities of \mathbf{q}_0 and of the average of \mathbf{q}_1 and \mathbf{q}_2 as a function of temperature at zero magnetic field (zfc) and at a finite field of 2.2 T (fc).

The temperature dependences of the peak at \mathbf{q}_0 are shown in Fig. 3.30 (a). In zero magnetic field, the integrated intensity of the peak at \mathbf{q}_0 increases as a function of decreasing temperatures exhibiting step steps at T_{t2} and at T_{t1} , respectively. At a finite field of 2.2 T the integrated intensity of the peak at \mathbf{q}_0 exhibits a distinctively different temperature dependence. Maximum values of the integrated intensity are almost one order of magnitude weaker than at zero magnetic field. The intensity starts to increase at roughly T_N and displays a shallow, relatively broad maximum slightly below T_{t2} .

The temperature dependences of the average of integrated intensities of peaks at \mathbf{q}_1 and \mathbf{q}_2 are shown in Fig. 3.30 (b). At zero magnetic field, the integrated intensity of the incommensurate peaks starts to increase at T_N . At T_{t2} and T_{t1} it displays kinks and

between T_{t_1} and T_{t_2} it features a local minimum. At T_{t_1} it decreases rapidly to vanishingly small values. At the finite field of 2.2 T, the integrated intensity of the incommensurate satellites starts to increase slightly below T_N . Between T_N and a temperature slightly larger than T_{t_1} it increases monotonically as a function of decreasing temperature with a kink at T_{t_2} , where the slope changes. Slightly above T_{t_1} the intensity exhibits a kink and decreases to vanishingly small values.

The qualitatively different temperature dependences at zero magnetic field and at a field reflect that symmetries between k -arms are broken in the field along [001]. However, these experiments do not permit to infer the number of propagation vectors of the ground states in C, IC1, and IC2. The suppression of the commensurate peak \mathbf{q}_0 at temperatures below T_{t_1} by fields of ± 2 T was observed for different field protocols and may arise either due to a transition from phase C to another phase, or due to a change of population of the magnetic domains. In the latter case, the peak suppression indicates that the ground state of phase C is either single- k or double- k , but not triple- k . As the other two k -arms A_2^c and A_3^c were not investigated as a function of field, these experiments do not permit to distinguish between these two scenarios.

3.3.4.3. Fields Along Threefold Directions

In order to study the evolution of magnetic order for fields along threefold $\langle 111 \rangle$ directions, neutron diffraction of the single crystal OFZ95-3-3-h was carried out at the time-of-flight diffractometer Wish [140]. Magnetic fields were applied along the cubic $[111]$ direction. The main objective of these experiments was to study magnetic ground states at different points in the $\langle 111 \rangle$ phase diagram.

These experiments do not permit to specify the number of propagation vectors of the ground states in the phases C, IC1, and IC2. There is only one possible orientation of $(\pi\pi 0)$ arms and of $(\pi - \delta, \pi, 0)$ arms, respectively, in a field directed along a threefold $\langle 111 \rangle$ axis (cf. Sec. 3.2 for further information). In particular, the threefold field direction preserves the symmetry between all commensurate k -arms of the $\langle \frac{1}{2}\frac{1}{2}0 \rangle$ star and between all incommensurate k -arms of the $\langle \frac{1}{2} - \delta, \frac{1}{2}, 0 \rangle$ star, respectively. Hence, these experiments do not permit to determine the number of propagation vectors of one of the ground state at zero magnetic field.

The $\langle 111 \rangle$ phase diagram, which was determined by Rahn (cf. Refs. [18, 118]), is shown in Fig. 3.31. The regions in this phase diagram were assigned colors and labels. The capital letters R shall indicate, that magnetic fields are applied along a cubic space diagonal. As for the $\langle 110 \rangle$ phase diagram, the regions in the $\langle 111 \rangle$ phase diagram will be referred to as "phases" or "phase pockets". Note, however, that these "phases" are not necessarily phases in a thermodynamic sense, i.e., they are not necessarily separated by phase transitions [139].

The main results of these experiments may be summarized as follows:

- Throughout the $\langle 111 \rangle$ phase diagram HoCu displays variations of $(\pi\pi 0)$ antiferromagnetism.
- In phases R_I , R_{a1} , R_{a2} , R_{a3} , R_{a4} , and R_{a5} the magnetic ground state represents a commensurate $(\pi\pi 0)$ antiferromagnet. Accordingly, these ground states are superpositions of propagation vectors of the $\langle \frac{1}{2}\frac{1}{2}0 \rangle$ star. They may be single- k , double- k , or triple- k . Fields along $\langle 111 \rangle$ do not permit to distinguish the three cases.
- In phases R_{II} , R_{b4} , R_{b2} , R_{b3} , R_{b5} , R_{III} , and R_{b1} the ground states are superpositions of propagation vectors of the stars $\langle \frac{1}{2}\frac{1}{2}0 \rangle$ and $\langle \frac{1}{2} - \delta, \frac{1}{2}, 0 \rangle$. Accordingly, these ground states are multi- k and have a long-wavelength modulation.
- In phases R_{c3} , R_{c4} , R_{c5} , and R_{c2} the ground states are superpositions of propagation vectors of the stars $\langle \frac{1}{2}\frac{1}{2}0 \rangle$, $\langle \frac{1}{2} - \delta, \frac{1}{2}, 0 \rangle$, and $\langle \frac{1}{2} - \delta, \frac{1}{2}, \delta \rangle$. Accordingly, these ground states are multi- k and have a long-wavelength modulation.

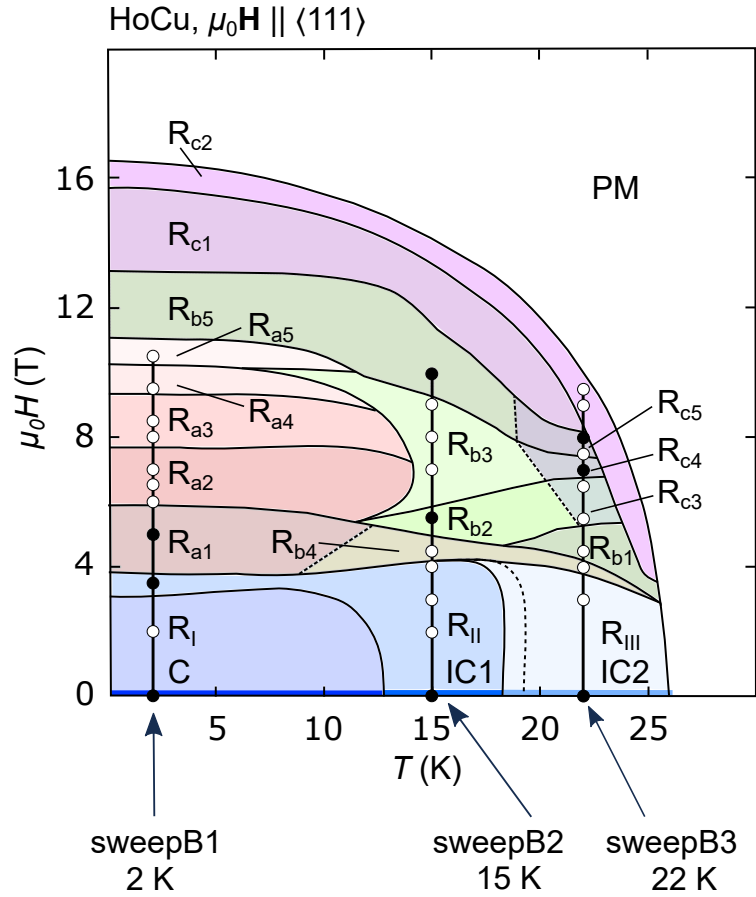


Figure 3.31.: The $\langle 111 \rangle$ phase diagram of HoCu. The phase diagram was determined by Rahn in Refs. [18, 118]. For this study the phase pockets were labeled and assigned colors. The dotted lines may represent phase boundaries, as inferred from the present study. The trajectories of these three field sweeps, which were carried out for this study, are represented by vertical lines. The positions in the phase diagram, where time-of-flight data were recorded, are represented by circles. The circles, which are filled, are the positions, where data is further below presented in Figs. 3.32, 3.34, and 3.36.

To study the $\langle 111 \rangle$ phase diagram, field sweeps were carried out at three different temperatures. For each of these sweeps, changes of magnetic propagation vectors as a function of field were investigated. Further, integrated intensities of magnetic Bragg peaks as a function of field were inferred from the sweeps. This permitted to specify the ground states in different phases of the $\langle 111 \rangle$ phase diagram.

For the experiments, the sample was oriented such that the crystallographic (111) plane corresponded to the horizontal scattering plane. Field sweeps started in phase C at $T = 2$ K after zfc (sweepB1), in phase IC1 at $T = 15$ K after zfc (sweepB2), and in phase IC2 at $T = 22$ K after zfc (sweepB3). Therefore, fields increased from 0 T to roughly 10 T and time-of-flight diffraction data were recorded at discrete field values. The trajectories of the three sweeps in the $\langle 111 \rangle$ phase diagram are represented by vertical lines in Fig. 3.31.

The positions in the phase diagram, where diffraction data were recorded, are represented by circles.

At each position, where time-of-flight data were recorded, a large volume of the reciprocal space was measured, containing roughly 20 ($\pi\pi 0$) positions. Data were treated by means of the data reduction software Mantid [141]. In particular, magnetic Bragg peaks were indexed with propagation vectors and integrated intensities $I_{\mathbf{q}=\mathbf{G}_{hkl}}(B) = F_o^2(h, k, l)$ of Bragg peaks were inferred.

The presentation of the data is organized as follows. For each field sweep, first changes of magnetic propagation vectors as a function of field are discussed. Therefore, an indexation of all magnetic Bragg peaks, which were observed in the time-of-flight data, was carried out for each data set. In this presentation, the indexation of magnetic peaks is illustrated for some of the recorded data sets in terms of the peaks in the vicinity of $\mathbf{q}_I := (0.5, \overline{0.5}, 0)$. The positions of these data sets in the $\langle 111 \rangle$ phase diagram are indicated by circles, which are filled black. Second, field dependences of integrated intensities are presented for specific magnetic Bragg peaks, which are related to the propagation-vector stars $\langle \frac{1}{2} \frac{1}{2} 0 \rangle$, $\langle \frac{1}{2} - \delta, \frac{1}{2}, 0 \rangle$, and $\langle \frac{1}{2} - \delta, \frac{1}{2}, \delta \rangle$, respectively.

For the first field sweep, sweepB1 at $T = 2$ K, time-of-flight diffraction data were recorded in phase R_I at the field values 0 T and 2 T, in phase R_{II} at 3.5 T, in phase R_{a1} at 5 T, in phase R_{a2} at 6 T, 6.5 T, and 7 T, in phase R_{a3} at 8 T and 8.5 T, in phase R_{a4} at 9.5 T, and in phase R_{a5} at 10.5 T.

As explained further, the magnetic ground state represents a commensurate ($\pi\pi 0$) antiferromagnet in phases R_I , R_{a1} , R_{a2} , R_{a3} , R_{a4} , and R_{a5} . As no qualitative differences of the diffraction data were observed in R_{a1} , R_{a2} , R_{a3} , R_{a4} , and R_{a5} , it may be concluded, that these regions of the $\langle 111 \rangle$ phase diagram belong to a single thermodynamic magnetic phase. In phase R_{II} , which comprises the zero-field phase IC1, the data confirmed that the ground state is a superposition of propagation vectors of the stars $\langle \frac{1}{2} \frac{1}{2} 0 \rangle$ and $\langle \frac{1}{2} - \delta, \frac{1}{2}, 0 \rangle$. In particular, this indicates, that the ground state in phase R_{II} has a long-wavelength modulation and that it is multi- k . Higher-order peaks were present in phase R_{II} . They may reflect the multi- k character of the ground state in phase R_{II} .

Fig. 3.32 illustrates distinctive changes of magnetic propagation vectors during sweepB1. Shown in the figure are diffraction data as recorded in the vicinity of \mathbf{q}_I at three different fields. The corresponding positions in the phase diagram (cf. Fig. 3.31) are represented by filled circles.

In phase R_I the single Bragg peak at \mathbf{q}_I reflects commensurate ($\pi\pi 0$) antiferromagnetism with propagation vector $(\frac{1}{2}, \frac{1}{2}, 0)$ (Fig. 3.32 (a)). In phase R_{II} (cf. Fig. 3.32 (b)) a commensurate propagation vector $(\frac{1}{2}, \frac{1}{2}, 0)$ and incommensurate propagation vectors

$(\frac{1}{2} - \delta, \frac{1}{2}, 0)$ and $(\frac{1}{2}, \frac{1}{2} - \delta, 0)$ are required to index the magnetic Bragg peaks, which were observed at \mathbf{q}_I and at $\mathbf{q}_{1,2} := (\frac{1}{2} \pm \delta, -\frac{1}{2}, 0)$ and $\mathbf{q}_{3,4} := (\frac{1}{2}, -\frac{1}{2} \pm \delta, 0)$, respectively. The splitting parameter in phase R_{II} is given by $\delta \approx 0.02$. This value is in agreement with the splitting parameter observed in phase IC1, which was reported in Sec. 3.3.3. In phases R_{a1} , R_{a2} , R_{a3} , R_{a4} , and R_{a5} a single Bragg peak at \mathbf{q}_I reflects commensurate $(\pi\pi 0)$ antiferromagnetism with propagation vector $(\frac{1}{2}, \frac{1}{2}, 0)$. For instance, Fig. 3.32 (c) shows the scattering data of the Bragg peak, which was recorded in phase R_{a1} .

In the diffraction data, recorded in phase R_{II} at 3.5 T, peaks are present at positions $\mathbf{q}_{5,6} = (\frac{1}{2}, -\frac{1}{2}, \pm 2\delta)$, at $\mathbf{q}_{7,8} := (\frac{1}{2} \pm 3\delta, -\frac{1}{2}, 0)$, and at $\mathbf{q}_{9,10} := (\frac{1}{2}, -\frac{1}{2} \pm 3\delta, 0)$. Scattering intensity at the positions $\mathbf{q}_{5,6}$ may be related to higher-order peaks, which arise due to a multi- k structure with propagation vectors $\mathbf{k}_a = (\frac{1}{2}, 0, \frac{1}{2} - \delta)$, and $\mathbf{k}_b = (\frac{1}{2}, \frac{1}{2}, 0)$. For instance, the term $2\mathbf{k}_a + \mathbf{k}_b - (1, 1, 1) = (\frac{1}{2}, -\frac{1}{2}, -2\delta)$ may explain higher-order intensity at \mathbf{q}_6 . It was established in Sec. 3.3.3.7, that higher-order peaks at positions $\mathbf{q}_{7,8,9,10}$ may either reflect the anharmonicity of the ground state, or they may represent mixed higher-harmonics due to a multi- k structure with several propagation vectors of the $\langle \frac{1}{2} - \delta, \frac{1}{2}, 0 \rangle$ star.

HoCu, $\mu_0\mathbf{H} \parallel [111]$
sweepB1, T = 2 K

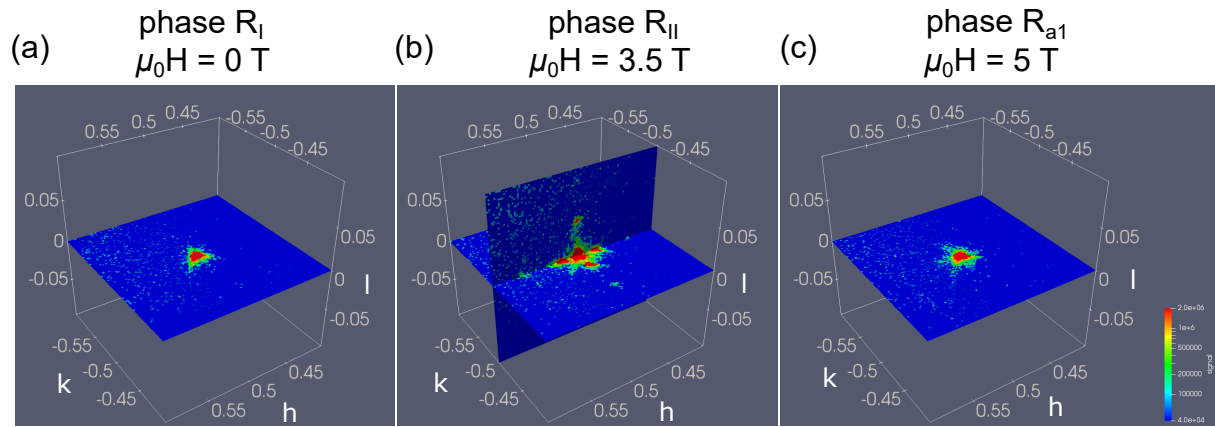


Figure 3.32.: Distinctive changes of magnetic propagation vectors during sweepB1. Magnetic propagation vectors may be inferred from the time-of-flight scattering data by means of indexing of magnetic Bragg peaks. Shown are the magnetic Bragg peaks in the vicinity of $(\frac{1}{2}, -\frac{1}{2}, 0)$ at three different magnetic fields. (a) In phase R_I , a single Bragg peak at \mathbf{q}_I reflects commensurate $(\pi\pi 0)$ antiferromagnetism with propagation vectors of the $\langle \frac{1}{2} \frac{1}{2} 0 \rangle$ star. (b) In phase R_{II} , relatively strong Bragg peaks, which were observed at \mathbf{q}_I and at \mathbf{q}_1 , \mathbf{q}_2 , \mathbf{q}_3 , and \mathbf{q}_4 , reflect, that the ground state is a superposition of propagation vectors of the stars $\langle \frac{1}{2} \frac{1}{2} 0 \rangle$ and $\langle \frac{1}{2} - \delta, \frac{1}{2}, 0 \rangle$. Higher-orders are present at \mathbf{q}_5 , \mathbf{q}_6 , \mathbf{q}_7 , \mathbf{q}_8 , \mathbf{q}_9 , and \mathbf{q}_{10} . (c) In phase R_{a1} a single Bragg peak at \mathbf{q}_I reflects commensurate $(\pi\pi 0)$ antiferromagnetism with propagation vectors of the $\langle \frac{1}{2} \frac{1}{2} 0 \rangle$ star.

In the following integrated intensities of Bragg peaks, as recorded by means of sweepB1, are presented. In phase R_I at 0 T the integrated intensity at the commensurate peak position is given by $I_{\mathbf{q}_I} = 8.47 \pm 0.04$. In phase R_{II} at 3.5 T the integrated intensity of the commensurate peak is given by $I(\mathbf{q}_I) = 10.59 \pm 0.04$ and the integrated intensities of the incommensurate peaks at \mathbf{q}_1 , \mathbf{q}_2 , \mathbf{q}_3 , and \mathbf{q}_4 are ranging from 2.60 ± 0.02 to 3.77 ± 0.02 . Further, the peaks at the incommensurate positions $\mathbf{q}_{5,6}$ have much smaller integrated intensities given by 0.26 ± 0.01 and 0.20 ± 0.01 , respectively. Peaks at positions $\mathbf{q}_{7,8,9,10}$ have almost vanishing integrated intensities but are clearly visible. In phase R_{a1} at 5 T the integrated intensity of the commensurate peak is given by $I_{\mathbf{q}_I} = 11.47 \pm 0.04$.

In the following, field dependences, as inferred from sweepB1, are presented of peaks, which are related to different arms of the $\langle \frac{1}{2} \frac{1}{2} 0 \rangle$ star. In particular, the integrated intensities as a function of field of the two commensurate magnetic Bragg peaks at $\mathbf{q}_I = (\overline{0.5}, 0.5, 0)$ and $\mathbf{q}_{III} = (\overline{0.5}, 0, 0.5)$ are presented. The peaks at \mathbf{q}_I and \mathbf{q}_{III} are indexed with propagation vectors of the k -arms A_1^c and A_3^c , respectively. As the two k -arms A_1^c and A_3^c have the same orientation in the magnetic field, they feature qualitatively the same field dependence, as presented in the following.

Fig. 3.33 (a) shows the integrated intensities of the two Bragg peaks at \mathbf{q}_I and \mathbf{q}_{III} as a function of field, as inferred from sweepB1. The integrated intensities, which are shown, are normalized to the integrated intensity at zero magnetic field, i.e., $i_{\mathbf{q}}(B) := I_{\mathbf{q}}(B)/I_{\mathbf{q}}(B=0)$. The qualitatively same field dependence of these normalized integrated intensities reflects the preserved symmetry between the k -arms A_1^c and A_3^c . The orientation of the three k -arms of the $\langle \frac{1}{2} \frac{1}{2} 0 \rangle$ star with respect to the field is schematically illustrated in Fig. 3.33 (b). Deviations $(i_{\mathbf{q}_{III}} - i_{\mathbf{q}_I})/i_{\mathbf{q}_{III}}$ are smaller than 13% and may be caused by misalignment of the sample.

For the second field sweep, i.e., sweepB2 at $T = 15$ K, time-of-flight data were recorded in phase R_{II} at the fields 0 T, 2 T, 3 T, and 4 T, in phase R_{b4} at the field 4.5 T, in phase R_{b2} at the field 5.5 T, in phase R_{b3} at the fields 7 T, 8 T, and 9 T, and in phase R_{b5} at the field 10 T.

No distinctive changes of magnetic propagation vectors were observed during sweepB2. In the entire field range, the magnetic ground state was found to represent a superposition of commensurate propagation vectors of the $\langle \frac{1}{2} \frac{1}{2} 0 \rangle$ star and incommensurate propagation vectors of the $\langle \frac{1}{2} - \delta, \frac{1}{2}, 0 \rangle$ star. In particular, the ground states in phases R_{II} , R_{b6} , R_{b2} , R_{b3} , and R_{b5} are multi- k with propagation vectors of the stars $\langle \frac{1}{2} \frac{1}{2} 0 \rangle$ and $\langle \frac{1}{2} - \delta, \frac{1}{2}, 0 \rangle$. As no qualitative difference between these phases was observed, they may belong to a single thermodynamic phase.

Fig. 3.34 illustrates the presence of these magnetic propagation vectors showing diffraction data recorded at three different fields during sweepB2. Shown are diffraction data

HoCu, $\mu_0\mathbf{H} \parallel \langle 111 \rangle$
sweepB1, $T = 2$ K

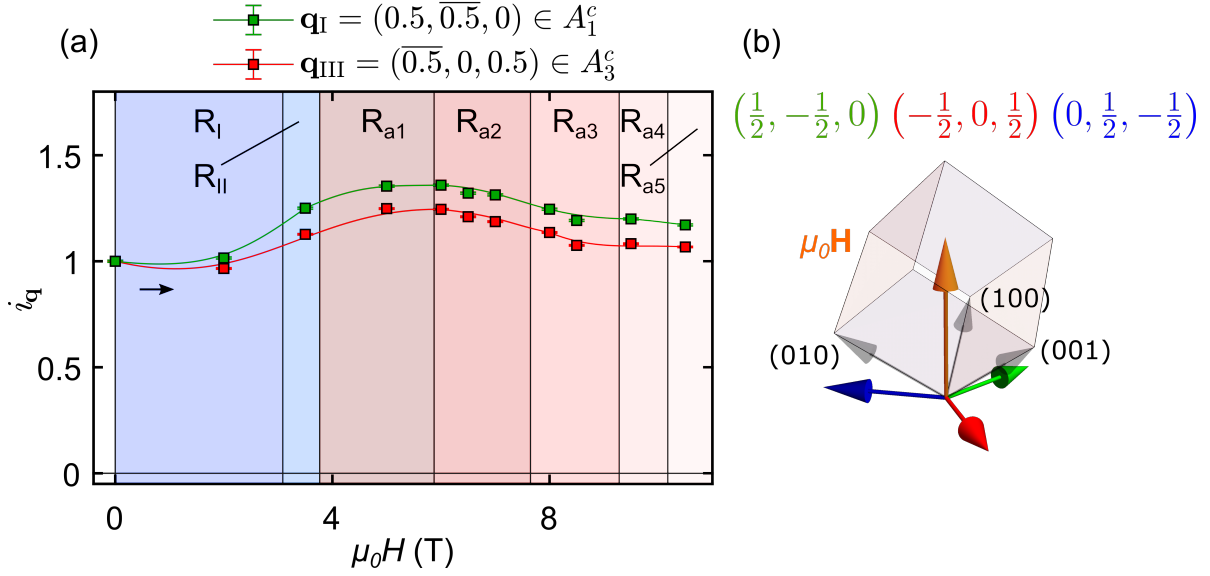


Figure 3.33.: Field dependences, as inferred from sweepB1, of different k -arms of the $\langle \frac{1}{2} \frac{1}{2} 0 \rangle$ star. (a) Integrated intensities of the commensurate Bragg peaks $\mathbf{q}_I = (0.5, \overline{0.5}, 0) \in A_1^c$ and $\mathbf{q}_{III} = (\overline{0.5}, 0, 0.5) \in A_3^c$, which are related to the k -arms A_1^c and A_3^c , respectively. The integrated intensities, which are shown, are normalized to the integrated intensity in zero magnetic field, i.e., $i_q(B) := I_q(B) / I_q(B = 0)$. The qualitatively same field dependences of the two peak intensities reflect the preserved symmetry between the k -arms A_1^c and A_3^c . (c) Orientation of the three k -arms A_1^c , A_2^c , and A_3^c in a field along $[111]$.

in the vicinity of the Q -position \mathbf{q}_I recorded at 0 T in phase R_{II} (Fig. 3.34 (a)), at 5.5 T in phase R_{b2} (Fig. 3.34 (b)), and at 10 T in phase R_{b5} (Fig. 3.34 (c)). The corresponding positions in the phase diagram, where data were recorded, are represented by filled circles in Fig. 3.31.

In all three phases, R_{II} , R_{b2} , and R_{b5} , relatively strong Bragg peaks are present at the position \mathbf{q}_I , which may be indexed by means of the propagation vector $(\frac{1}{2}, \frac{1}{2}, 0)$, and at the positions \mathbf{q}_1 , \mathbf{q}_2 , \mathbf{q}_3 , and \mathbf{q}_4 , which may be indexed by means of propagation vectors $(\frac{1}{2} - \delta, \frac{1}{2}, 0)$ and $(\frac{1}{2}, \frac{1}{2} - \delta, 0)$.

Peaks at higher-order positions change slightly during sweepB2. In phase R_{II} at zero magnetic field peaks at the higher-order positions \mathbf{q}_5 , \mathbf{q}_6 , \mathbf{q}_7 , \mathbf{q}_8 , \mathbf{q}_9 , and \mathbf{q}_{10} are relatively weak but visible. In phases R_{b2} and R_{b5} peaks at higher-order positions \mathbf{q}_5 , \mathbf{q}_6 , \mathbf{q}_7 , \mathbf{q}_8 , \mathbf{q}_9 , and \mathbf{q}_{10} are distinctively stronger than in phase R_{II} . Further, peaks, which are presumably also higher-order, were observed at the positions $\mathbf{q}_{11} = (\frac{1}{2}, -\frac{1}{2}, 4\delta)$ and $\mathbf{q}_{12} = (\frac{1}{2}, -\frac{1}{2}, -4\delta)$.

In the following, integrated intensities of magnetic Bragg peaks, as inferred from sweepB2, are presented. In phase R_{II} at zero magnetic field the integrated intensity

of the commensurate peak is given by $I_{\mathbf{q}_I} = 7.22 \pm 0.03$ and the integrated intensities of the four incommensurate satellites $\mathbf{q}_{1,2,3,4}$ range from 3.83 ± 0.02 to 4.83 ± 0.03 . Peaks at higher-order positions have almost vanishing integrated intensities. In phase R_{b2} at the field 5.5 T the integrated intensity of the commensurate peak is given by $I_{\mathbf{q}_I} = 7.73 \pm 0.02$, the integrated intensities $I_{\mathbf{q}_{1,2,3,4}}$ are ranging from 3.02 ± 0.02 to 4.55 ± 0.03 , and the integrated intensities $I_{\mathbf{q}_{5,6}}$ are given by 0.28 ± 0.01 and 0.35 ± 0.01 . In phase R_{b5} at 10 T the integrated intensity of the commensurate peak is given by $I_{\mathbf{q}_I} = 4.74 \pm 0.03$, $I_{\mathbf{q}_{1,2,3,4}}$ are ranging from 2.27 ± 0.02 to 2.86 ± 0.02 , and the integrated intensities $I_{\mathbf{q}_{5,6}}$ are given by 0.48 ± 0.01 and 0.60 ± 0.01 .

In the following, integrated intensities as a function of field, as inferred from sweepB2, are presented first of peaks, which are related to the $\langle \frac{1}{2} \frac{1}{2} 0 \rangle$ star, and second of peaks, which are related to the $\langle \frac{1}{2} - \delta, \frac{1}{2}, 0 \rangle$ star. In particular, this presentation illustrates, that k -arms of the stars $\langle \frac{1}{2} \frac{1}{2} 0 \rangle$ and $\langle \frac{1}{2} - \delta, \frac{1}{2}, 0 \rangle$, respectively, always feature similar field dependences for fields directed along a threefold $\langle 111 \rangle$ direction. This reflects that the field does not break the symmetry between different arms of the stars $\langle \frac{1}{2} \frac{1}{2} 0 \rangle$ and $\langle \frac{1}{2} - \delta, \frac{1}{2}, 0 \rangle$, respectively.

Fig. 3.35 (a) shows the normalized integrated intensities $i_{\mathbf{q}}(B)$ of the two commensurate peaks at \mathbf{q}_I and \mathbf{q}_{III} as a function of field, as inferred from sweepB2. The peaks at \mathbf{q}_I and at \mathbf{q}_{III} are related to the k -arms A_1^c and A_3^c , respectively, which have the same orientation in the field. The integrated intensities as a function of field exhibit qualitatively similar field dependences. Maximum deviation was observed at 8 T, where $i_{\mathbf{q}_{III}}(B)$ is roughly 38 % larger than $i_{\mathbf{q}_I}(B)$. This deviation may be caused by misalignment of the sample.

Fig. 3.35 (b) shows the normalized integrated intensities $i_{\mathbf{q}}(B)$ as a function of field of the four incommensurate peaks $\mathbf{q}_3 \in A_{1,y}^{ic}$, $\mathbf{q}_2 \in A_{1,x}^{ic}$, $(-\frac{1}{2} + \delta, 0, \frac{1}{2}) \in A_{3,x}^{ic}$, and $(-\frac{1}{2}, 0, \frac{1}{2} - \delta) \in A_{3,z}^{ic}$, as inferred from sweepB2. In the whole field range, no huge differences were visible between the integrated intensities at the four incommensurate positions. This reflects, that the arms $A_{1,y}^{ic}$, $A_{1,x}^{ic}$, $A_{3,x}^{ic}$, and $A_{3,z}^{ic}$ have the same orientation in the magnetic field.

For the third field sweep, i.e., sweepB3 at $T = 22$ K, time-of-flight data were recorded in phase R_{III} at the fields 0 T and 3 T, in phase R_{b4} at 4 T, in phase R_{b1} at 4.5 T, in phase R_{c3} at 5.5 T and 6.5 T, in phase R_{c4} at 7 T, in phase R_{c5} at 7.5 T and 8 T, and in phase R_{c2} at 9 T and 9.5 T.

In phases R_{III} , R_{b4} , and R_{b1} the ground state represents a superposition of propagation vectors of the stars $\langle \frac{1}{2} \frac{1}{2} 0 \rangle$ and $\langle \frac{1}{2} - \delta, \frac{1}{2}, 0 \rangle$. In phases R_{c3} , R_{c4} , R_{c5} , and R_{c2} the ground state represents a superposition of propagation vectors of the stars $\langle \frac{1}{2} \frac{1}{2} 0 \rangle$, $\langle \frac{1}{2} - \delta, \frac{1}{2}, 0 \rangle$,

HoCu, $\mu_0\mathbf{H} \parallel [111]$
sweepB2, T = 15 K

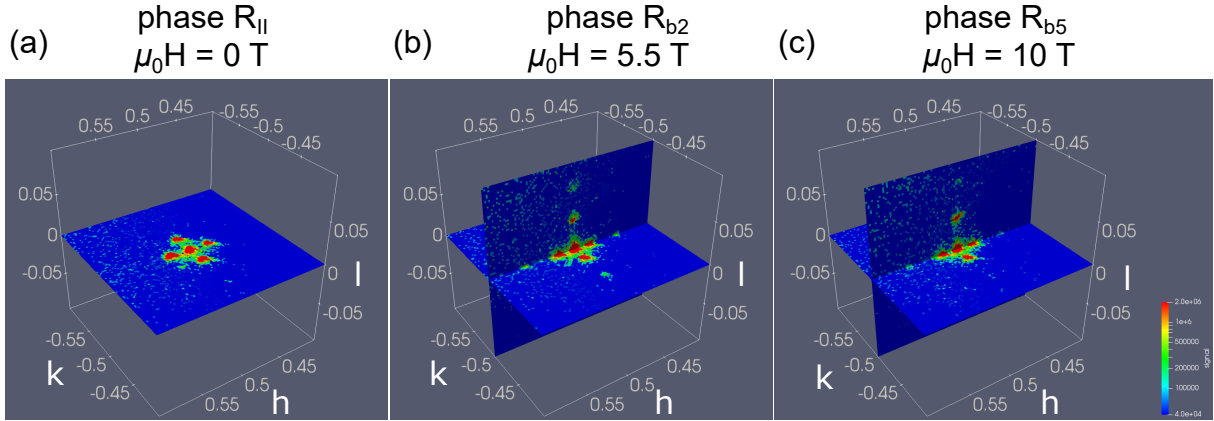


Figure 3.34.: Evolution of magnetic propagation vectors during sweepB2. Magnetic propagation vectors may be inferred from the time-of-flight scattering data by means of indexing of magnetic Bragg peaks. Shown are magnetic peaks in the vicinity of $(\bar{0}.5, 0.5, 0)$ at three different fields. In the whole field range, Bragg peaks appear at \mathbf{q}_I , as well as at \mathbf{q}_1 , \mathbf{q}_2 , \mathbf{q}_3 , and \mathbf{q}_4 , reflecting that the ground states are superpositions of propagation vectors of the stars $\langle \frac{1}{2} \frac{1}{2} 0 \rangle$ and $\langle \frac{1}{2} - \delta, \frac{1}{2}, 0 \rangle$. Mixed higher orders at \mathbf{q}_5 and \mathbf{q}_6 may reflect the multi- k character of the ground states.

and $\langle \frac{1}{2} - \delta, \frac{1}{2}, \delta \rangle$, as established in the following. Accordingly, the ground state is at least triple- k and has a long-wavelength modulation.

Fig. 3.36 shows the diffraction data in the vicinity of the Q -position \mathbf{q}_I recorded at three different fields, illustrating qualitative changes of magnetic propagation vectors as a function of field during sweepB3.

In phases R_{III} , R_{b4} , and R_{b1} , relatively strong Bragg peaks are present at \mathbf{q}_I , which is indexed by $(\frac{1}{2}, \frac{1}{2}, 0)$, and at \mathbf{q}_1 , \mathbf{q}_2 , \mathbf{q}_3 , and \mathbf{q}_4 , which may be indexed by propagation vectors $(\frac{1}{2} - \delta, \frac{1}{2}, 0)$ and $(\frac{1}{2}, \frac{1}{2} - \delta, 0)$, respectively. For instance, Fig. 3.36 (a) shows these Bragg peaks, as recorded in phase R_{III} . Intensities at \mathbf{q}_5 , \mathbf{q}_6 , \mathbf{q}_7 , \mathbf{q}_8 , \mathbf{q}_9 , and \mathbf{q}_{10} may be related to higher-order peaks. In phases R_{c3} , R_{c4} , R_{c5} , and R_{c2} relatively strong Bragg peaks appear at positions \mathbf{q}_I and at \mathbf{q}_1 , \mathbf{q}_2 , \mathbf{q}_3 , \mathbf{q}_4 , $(\frac{1}{2}, -\frac{1}{2} \pm \delta, \delta)$, $(\frac{1}{2}, -\frac{1}{2} \pm \delta, -\delta)$, $(\frac{1}{2} \pm \delta, -\frac{1}{2}, \delta)$, and $(\frac{1}{2} \pm \delta, -\frac{1}{2}, -\delta)$. For instance, the scattering data, recorded in phases R_{c4} and R_{c5} are shown in Fig. 3.36 (b) and (c), respectively.

A multitude of peaks at higher-order positions was observed in phases R_{c4} and R_{c5} , as explained in the following.

Fig. 3.39 (a) and (b1) show scattering data in the $(\frac{1}{2}, k, l)$ -plane, as recorded by means of sweepB3 in phases R_{c4} and R_{c5} , respectively. In both phases, relatively strong peaks are present at the positions \mathbf{q}_I , \mathbf{q}_3 , \mathbf{q}_4 .

HoCu, $\mu_0\mathbf{H} \parallel \langle 111 \rangle$
sweepB2, T = 15 K

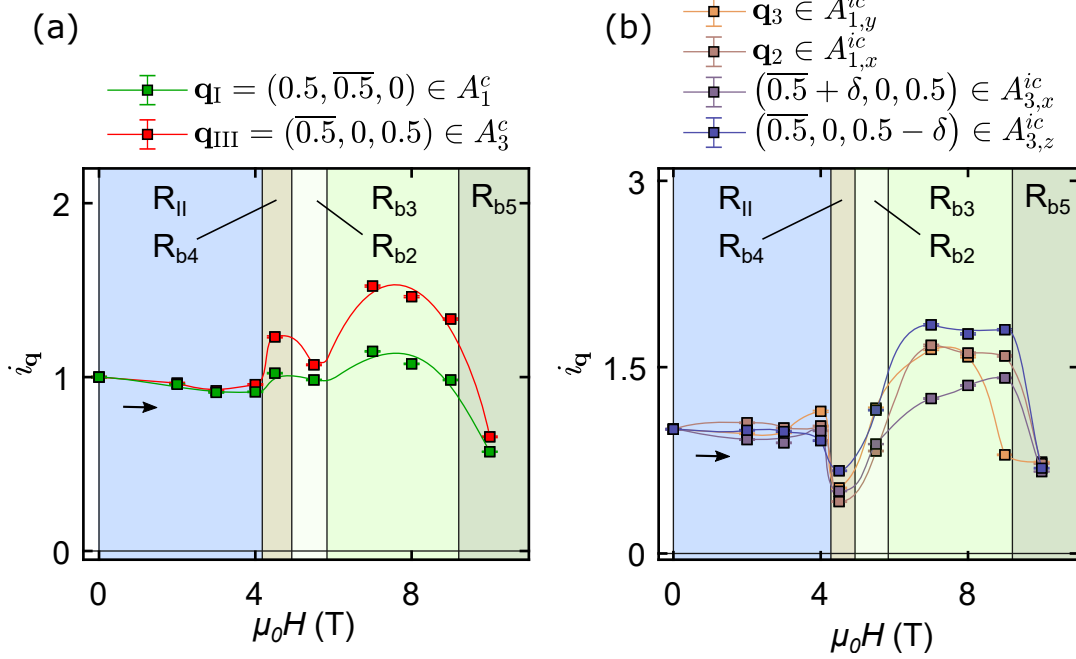


Figure 3.35.: Field dependences of peaks of the stars $\langle \frac{1}{2} \frac{1}{2} 0 \rangle$ and $\langle \frac{1}{2} - \delta, \frac{1}{2}, 0 \rangle$, as inferred from sweep sweepB2. (a) Normalized integrated intensities i_q as a function of field of the Bragg peaks at \mathbf{q}_I and \mathbf{q}_{III} . The two peaks are associated with the k -arms A_1^c and A_3^c , respectively. The qualitatively same field dependences reflect that the symmetry between the k -arms A_1^c and A_3^c is preserved in the magnetic field. (b) Normalized integrated intensities i_q of the incommensurate peaks at $\mathbf{q}_3 \in A_{1,y}^{ic}$, $\mathbf{q}_2 \in A_{1,x}^{ic}$, $(-\frac{1}{2} + \delta, 0, \frac{1}{2}) \in A_{3,x}^{ic}$, and $(-\frac{1}{2}, 0, \frac{1}{2} - \delta) \in A_{3,z}^{ic}$ as a function of field. The qualitatively same field dependences reflect that the symmetry between the arms $A_{1,y}^{ic}$, $A_{1,x}^{ic}$, $A_{3,x}^{ic}$, and $A_{3,z}^{ic}$ is preserved in the magnetic field.

Peaks at \mathbf{q}_5 and \mathbf{q}_6 , which may be higher order, are visible in R_{c4} and in R_{c5} . Peaks at positions $(\frac{1}{2}, \frac{1}{2}, \pm\delta)$ are visible in R_{c5} but not in R_{c4} .

Higher orders, which were observed in phase R_{c4} , but not in R_{c5} , are at the positions $(\frac{1}{2}, -\frac{1}{2} \pm \delta, \pm 2\delta)$ and $(\frac{1}{2}, -\frac{1}{2} \pm \delta, \mp 2\delta)$.

Higher orders, which were observed in phase R_{c5} , but not in phase R_{c4} , are at the positions $(\frac{1}{2}, -\frac{1}{2} \pm \frac{3}{2} \cdot \delta, 0)$. Further, higher orders, which were observed in phase R_{c5} , but not in phase R_{c4} , are at the positions $(\frac{1}{2}, k + 0.15, -2\delta)$ and $(\frac{1}{2}, k - 0.15, +2\delta)$.

Fig. 3.39 (b2) shows scattering data in the $(hk0)$ plane, as recorded in phase R_{c5} by means of sweepB3. Higher orders were observed at the positions $(\frac{1}{2} + \delta, -\frac{1}{2} + 2\delta, 0)$, $(\frac{1}{2} + 2\delta, -\frac{1}{2} + \delta, 0)$, $(\frac{1}{2} - \delta, -\frac{1}{2} - 2\delta, 0)$, and $(\frac{1}{2} - 2\delta, -\frac{1}{2} - \delta, 0)$. Peaks at those positions were not observed in phase R_{c4} .

In the following, integrated intensities as a function of field, as inferred from sweepB3

HoCu, $\mu_0\mathbf{H} \parallel [111]$
sweepB3, T = 22 K

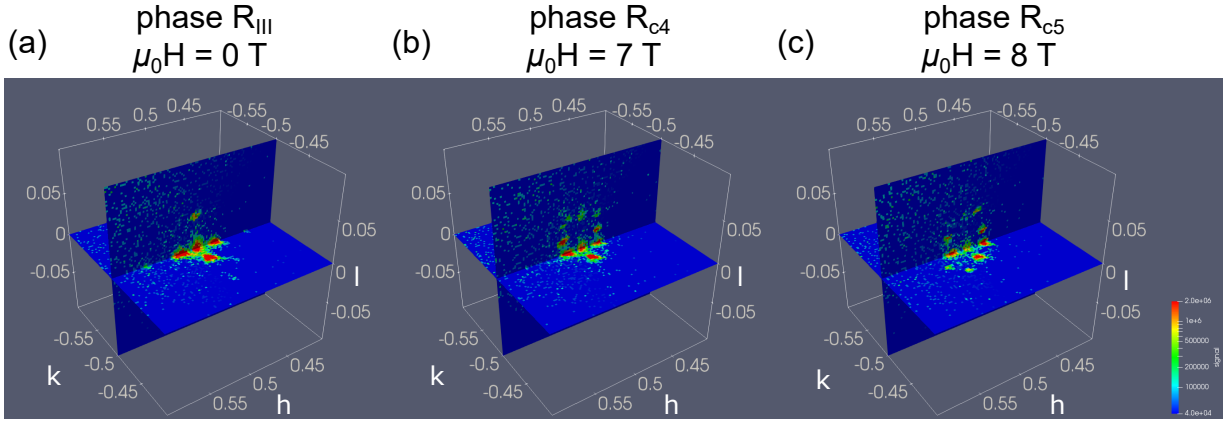


Figure 3.36.: Distinctive changes of magnetic propagation vectors during sweepB3. Magnetic propagation vectors may be inferred from the time-of-flight scattering data by means of indexation of magnetic Bragg peaks. Shown are the magnetic Bragg peaks in the vicinity of $(\frac{1}{2}, -\frac{1}{2}, 0)$ at three different magnetic fields. (a) In phase R_{III} , Bragg peaks at \mathbf{q}_{I} , \mathbf{q}_1 , \mathbf{q}_2 , \mathbf{q}_3 , and \mathbf{q}_4 reflecting that the ground state is a superposition of propagation vectors of the stars $\langle \frac{1}{2} \frac{1}{2} 0 \rangle$ and $\langle \frac{1}{2} - \delta, \frac{1}{2}, 0 \rangle$. (b) In phase R_{c4} and (c) in phase R_{c5} , relatively strong Bragg peaks are present at \mathbf{q}_{I} , \mathbf{q}_1 , \mathbf{q}_2 , \mathbf{q}_3 , \mathbf{q}_4 , $(\frac{1}{2} \pm \delta, -\frac{1}{2}, \delta)$, $(\frac{1}{2} \pm \delta, -\frac{1}{2}, -\delta)$, $(\frac{1}{2}, -\frac{1}{2} \pm \delta, \delta)$, $(\frac{1}{2}, -\frac{1}{2} \pm \delta, -\delta)$ reflect that the ground states in phases R_{c4} and R_{c5} , respectively, are superpositions of propagation vectors of the stars $\langle \frac{1}{2} \frac{1}{2} 0 \rangle$, $\langle \frac{1}{2} - \delta, \frac{1}{2}, 0 \rangle$, and $\langle \frac{1}{2} - \delta \frac{1}{2}, \delta \rangle$.

are presented for peaks, which are associated with the stars $\langle \frac{1}{2} \frac{1}{2} 0 \rangle$ and $\langle \frac{1}{2} - \delta, \frac{1}{2}, 0 \rangle$, respectively.

Fig. 3.37 (a) shows the normalized integrated intensities $i_{\mathbf{q}}(B)$ of the two commensurate peaks at \mathbf{q}_{I} and \mathbf{q}_{III} as a function of field, as inferred from sweepB3. The peaks at \mathbf{q}_{I} and at \mathbf{q}_{III} are related to the k -arms A_1^c and A_3^c , respectively, which have the same orientation in the magnetic field. Maximum deviation between the two commensurate peaks $(i_{\mathbf{q}_{\text{III}}} - i_{\mathbf{q}_{\text{I}}})/i_{\mathbf{q}_{\text{III}}}$ was 13%. This reflects that the symmetry between the k -arms is preserved in the field.

Fig. 3.37 (b) shows the normalized integrated intensities $i_{\mathbf{q}}(B)$ of the four incommensurate peaks $\mathbf{q}_3 \in A_{1,y}^{ic}$, $\mathbf{q}_2 \in A_{1,x}^{ic}$, $(-\frac{1}{2} + \delta, 0, \frac{1}{2}) \in A_{3,x}^{ic}$, and $(-\frac{1}{2}, 0, \frac{1}{2} - \delta) \in A_{3,z}^{ic}$ as a function of field, as inferred from sweepB3. The qualitatively same field dependences reflect that the arms $A_{1,y}^{ic}$, $A_{1,x}^{ic}$, $A_{3,x}^{ic}$, and $A_{3,z}^{ic}$ have the same orientation in the field. The deviation between the curves may be caused by misalignment of the sample.

In the following, field dependences of k -arms, which are associated with the $\langle \frac{1}{2} - \delta, \frac{1}{2}, \delta \rangle$ star, are investigated. The $\langle \frac{1}{2} - \delta, \frac{1}{2}, \delta \rangle$ star has 24 different arms or 12 pairs of conjugated

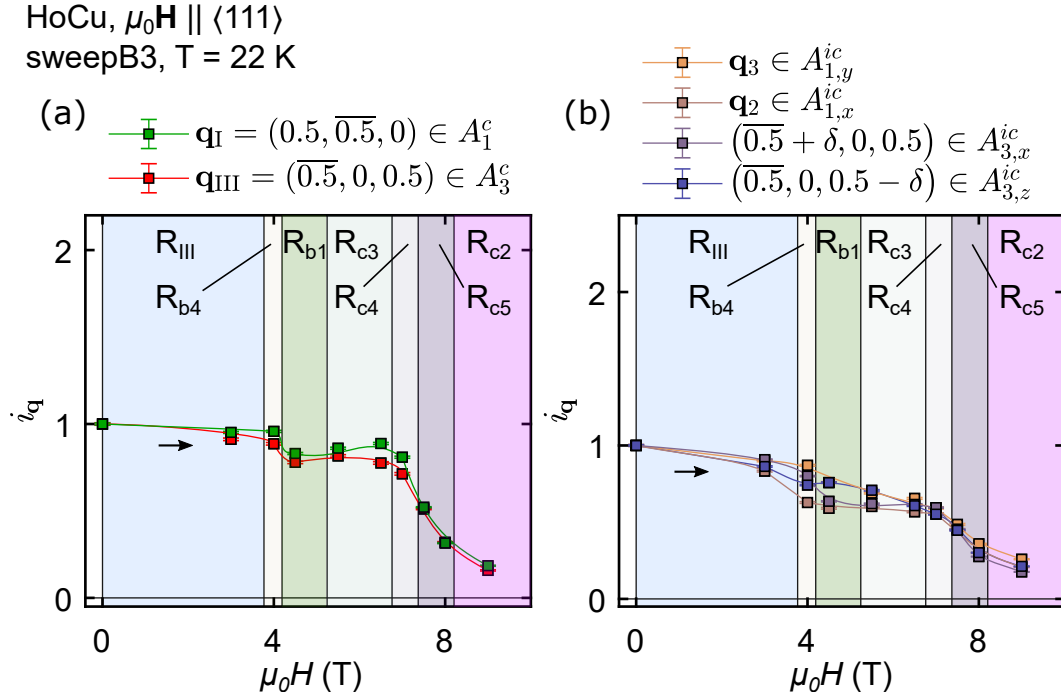


Figure 3.37.: Field dependences, as inferred from sweepB3, of different k -arms of the stars $\langle \frac{1}{2} \frac{1}{2} 0 \rangle$ and $\langle \frac{1}{2} - \delta, \frac{1}{2}, 0 \rangle$, respectively. (a) Normalized integrated intensities $i_{\mathbf{q}}$ as a function of field of the Bragg peaks at \mathbf{q}_I and \mathbf{q}_{III} . The two peaks are associated with the k -arms A_1^c and A_3^c , respectively. The qualitatively same field dependences reflect that the symmetry between the k -arms A_1^c and A_3^c is preserved in the magnetic field. (b) Normalized integrated intensities $i_{\mathbf{q}}$ of the incommensurate peaks at $\mathbf{q}_3 \in A_{1,y}^{ic}$, $\mathbf{q}_2 \in A_{1,x}^{ic}$, $(-\frac{1}{2} + \delta, 0, \frac{1}{2}) \in A_{3,x}^{ic}$, and $(-\frac{1}{2}, 0, \frac{1}{2} - \delta) \in A_{3,z}^{ic}$ as a function of field. The qualitatively same field dependences reflect that the symmetry between the arms $A_{1,y}^{ic}$, $A_{1,x}^{ic}$, $A_{3,x}^{ic}$, and $A_{3,z}^{ic}$ is preserved in the magnetic field.

k -arms. As explained in Sec. 2.2, one may identify conjugated k -arms in terms of Ω -arms. Accordingly, the $\langle \frac{1}{2} - \delta, \frac{1}{2}, \delta \rangle$ star has 12 different Ω -arms.

There are only two possible orientations of k -arms in a field along [111]. Accordingly, the k -arms may be assigned to two sets as follows:

$$\mathcal{S}_a = \left\{ \left[\frac{1}{2} + \delta, \frac{1}{2}, \delta \right]_{\sim}, \left[\frac{1}{2}, \frac{1}{2} + \delta, \delta \right]_{\sim}, \left[\delta, \frac{1}{2} + \delta, \frac{1}{2} \right]_{\sim}, \right. \quad (3.26)$$

$$\left. \left[\delta, \frac{1}{2}, \frac{1}{2} + \delta \right]_{\sim}, \left[\frac{1}{2} + \delta, \delta, \frac{1}{2} \right]_{\sim}, \left[\frac{1}{2}, \delta, \frac{1}{2} + \delta \right]_{\sim}, cc. \right\} \quad (3.27)$$

and:

$$\mathcal{S}_b = \left\{ \left[\frac{1}{2} + \delta, \frac{1}{2}, -\delta \right]_{\sim}, \left[\frac{1}{2}, \frac{1}{2} + \delta, -\delta \right]_{\sim}, \left[-\delta, \frac{1}{2} + \delta, \frac{1}{2} \right]_{\sim}, \right. \quad (3.28)$$

$$\left. \left[-\delta, \frac{1}{2}, \frac{1}{2} + \delta \right]_{\sim}, \left[\frac{1}{2} + \delta, -\delta, \frac{1}{2} \right]_{\sim}, \left[\frac{1}{2}, -\delta, \frac{1}{2} + \delta \right]_{\sim}, cc. \right\} \quad (3.29)$$

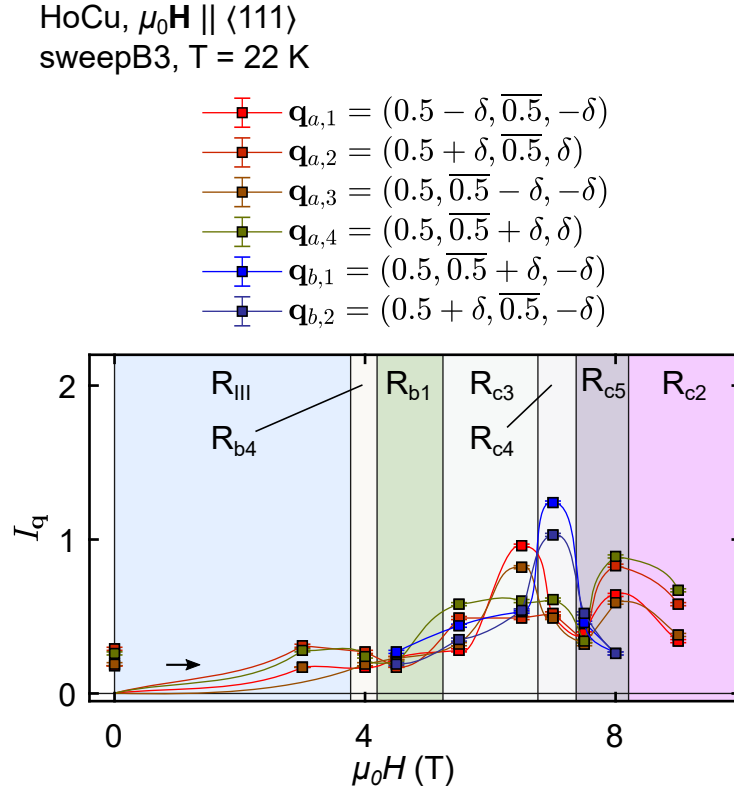


Figure 3.38.: Field dependences, as inferred from sweepB3, of different k -arms of the $\langle \frac{1}{2} - \delta, \frac{1}{2}, \delta \rangle$ star. Shown are integrated intensities as a function of field of Bragg peaks located at $\mathbf{q}_{a,1}$, $\mathbf{q}_{a,2}$, $\mathbf{q}_{a,3}$, $\mathbf{q}_{a,4}$, $\mathbf{q}_{b,1}$, and $\mathbf{q}_{b,2}$. The Bragg peaks at $\mathbf{q}_{a,1}$, $\mathbf{q}_{a,2}$, $\mathbf{q}_{a,3}$, and $\mathbf{q}_{a,4}$ are associated with k -arms, which have the orientation \mathcal{S}_a in the magnetic field along $[111]$. They display similar field dependences reflecting this same orientation. In contrast, the Bragg peaks at $\mathbf{q}_{b,1}$ and $\mathbf{q}_{b,2}$ display distinctively different field dependences. They are associated with k -arms, which have the orientation \mathcal{S}_b in the magnetic field along $[111]$.

Each set comprises also the conjugation of each k -arm, as indicated by $cc..$

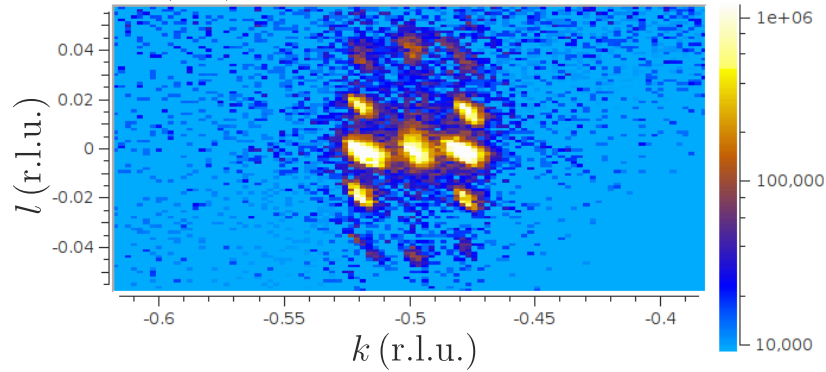
The two sets \mathcal{S}_a and \mathcal{S}_b represent the two possible orientations of k -arms of the $\langle \frac{1}{2} - \delta, \frac{1}{2}, \delta \rangle$ star in a field along $[111]$. Accordingly, we may expect that k -arms, which have the same orientation, feature the same field dependences.

In the following, integrated intensities as a function of field, as inferred from sweepB3, are presented of Bragg peaks, which are related to different k -arms of the $\langle \frac{1}{2} - \delta, \frac{1}{2}, \delta \rangle$ star. Fig. 3.38 shows integrated intensities as a function of field of the peaks $\mathbf{q}_{a,1}$, $\mathbf{q}_{a,2}$, $\mathbf{q}_{a,3}$, and $\mathbf{q}_{a,4}$, which are associated with k -arms that have orientation \mathcal{S}_a , as well as integrated intensities of the peaks $\mathbf{q}_{b,1}$ and $\mathbf{q}_{b,2}$, which are associated with k -arms that have orientation \mathcal{S}_b . The integrated intensities of these six Bragg peaks as a function of field reflect the two possible orientations of k -arms in a field along $[111]$. The peaks, which are related to \mathcal{S}_a have a maximum in phase R_{c3} and a second maximum, which extends over the two phases R_{c5} and R_{c2} . In contrast, the peaks, which are related to \mathcal{S}_b display a distinctively different behavior featuring a single maximum in phase R_{c4} .

HoCu, $\mu_0\mathbf{H} \parallel [111]$
sweepB3, T = 22 K

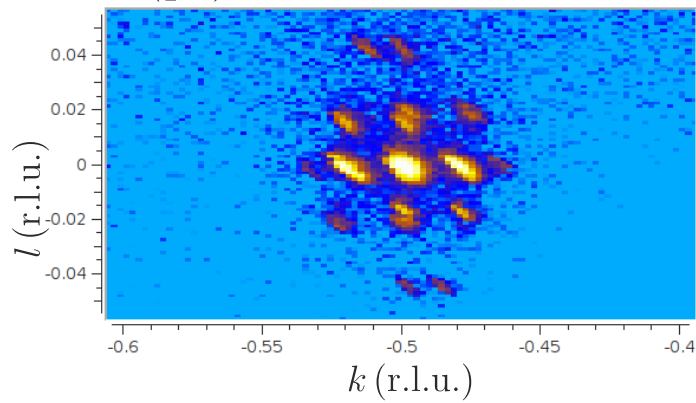
(a) phase R_{c4}
 $\mu_0H = 7 \text{ T}$

$(\frac{1}{2}kl)$ – plane



(b) phase R_{c5}
 $\mu_0H = 8 \text{ T}$

(b1) $(\frac{1}{2}kl)$ – plane



(b2) $(hk0)$ – plane

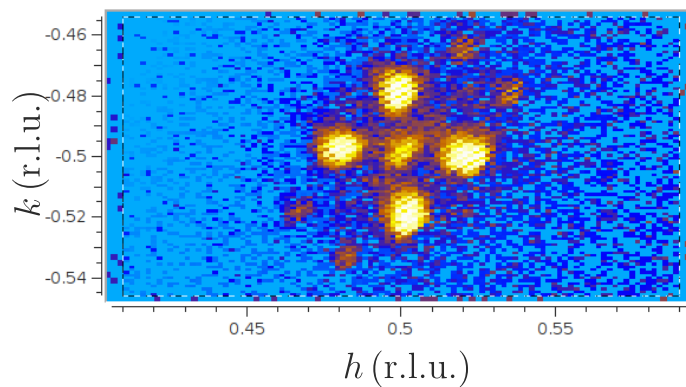


Figure 3.39.: Multitude of higher harmonics in phases R_{c4} and R_{c5} . (a) Scattering intensity in the $(\frac{1}{2}, k, l)$ plane, as recorded in phase R_{c4} . (b1) Scattering intensity in the $(\frac{1}{2}, k, l)$ plane, as recorded in phase R_{c5} . (b2) Scattering intensity in the $(h, k, 0)$ plane, as recorded in phase R_{c5} .

3.3.5. Magnetic Structures in Zero Magnetic Field

In the following, magnetic structure determinations are presented for the three phases C, IC1, and IC2. While specific magnetic structures are determined for C and IC1, an educated guess with intriguing properties is suggested for IC2.

The study is mainly based on the results from neutron experiments presented in Secs. 3.3.3 and 3.3.4. These experiments provided the following prerequisites for the magnetic structure determinations. (i) The propagation vector stars of magnetic ground states were determined for the three phases in Sec. 3.3.3.2. As a result, only the "propagation vector types" were obtained, but not the number of propagation vectors in the Fourier series. (ii) For each propagation vector \mathbf{k}_0 all pre-factors in the Fourier series that are allowed by symmetry were established in Sec. 3.3.3.4 by representational analysis. (iii) From all pre-factors allowed by symmetry the ones that in fact occur in the Fourier-description of the ground states were determined in Sec. 3.3.3.5 by a polarization analysis. The findings were further confirmed in Sec. 3.3.3.6 by Rietveld refinements. (iv) The number of propagation vectors of each ground state was specified in Sec. 3.3.4.1.

3.3.5.1. Ground State in Phase C

The main results of the structure determination in phase C may be summarized as follows:

- The magnetic ground state in phase C represents the commensurate $(\pi\pi 0)$ structure t2 (Tab. 3.1).
- This ground state is triple- k , highly noncollinear, and noncoplanar. Magnetic moments are directed along $\langle 111 \rangle$ directions.
- The magnetic unit cell has the size $2a \times 2a \times 2a$.
- The stabilization of this multi- k ground state cannot be explained by only bilinear Heisenberg interactions and crystal electric fields. Presumably quadrupolar interactions stabilize the ground state.

It is known from the experimental study in Sec. 3.3.3.2 (cf. Ref. [68]), that phase C displays commensurate $(\pi\pi 0)$ antiferromagnetism without any ferromagnetic component in the magnetic ground state. We assumed that the magnetic ground state represents one of the 21 structures fulfilling the two conditions, that all moments (i) have equal modulus and (ii) are directed along directions from a unique crystallographic star, which is either $\langle 100 \rangle$, $\langle 110 \rangle$, or $\langle 111 \rangle$ (cf. Ref. [106]). Among these 21 structures, which are summarized in Tab. 3.1, only the five structures s2, s4, d2, d5, and t2 were found to be consistent with the experimental observations in Secs. 3.3.3.5 and 3.3.3.6. Further, only three among the five structures, namely d2, d5, and t2, were consistent with the field study in Sec. 3.3.4.1, which required that the ground state is multi- k .

The presentation of the structure determination is organized as follows. First, real-space pictures are presented for the five structures, which are in agreement with the neutron experiments in zero magnetic field. The easy axis and crystal electric fields of the structures are discussed. Second, symmetry arguments establish that only one magnetic structure, the $(\pi\pi 0)$ antiferromagnet t2, is in agreement with the experimental observations in Sec. 3.3.4.1. Third, mechanisms stabilizing the multi- k ground state in phase C are discussed.

Fig. 3.40 shows the five commensurate $(\pi\pi 0)$ structures in agreement with the experimental observations in Sec. 3.3.4. The magnetic moments in s2 are directed along fourfold $\langle 100 \rangle$ directions, in s4 and d2 along twofold $\langle 110 \rangle$ directions, and in d5 and t2 along threefold $\langle 111 \rangle$ directions. Although knowledge about crystal electric fields often proves useful for an unambiguous determination of magnetic ground states [68, 69, 106], it does not permit to distinguish the three structures d2, d5, and t2, as all three are in well agreement with previous studies on crystal electric fields reporting that the fourfold $\langle 100 \rangle$ axes are the hard directions, whereas twofold $\langle 110 \rangle$ and threefold $\langle 111 \rangle$ directions have similar energies, suggesting a binary easy plane [113]. The energies of $(\pi\pi 0)$ structures may be compared by a model, which is often used for rare-earth systems [30], accounting for isotropic bilinear Heisenberg exchange between moments \mathbf{J}_i and for crystal electric fields:

$$\hat{H} = \sum_{\langle i,j \rangle} \mathbf{J}_i \mathbf{J}_j + \sum_i H_{cf}(\mathbf{J}_i) . \quad (3.30)$$

The 21 $(\pi\pi 0)$ structures in Tab. 3.1 feature the same isotropic bilinear Heisenberg energies (cf. Ref. [106]) implying that the first term in Eq. (3.30) is equal for all $(\pi\pi 0)$ structures. Accordingly, with regard to Eq. (3.30) the structures s4, d2, d5, and t2 in Fig. 3.40 should be energetically preferred to s1 due to crystal electric fields. However, the three structures in question, d2, d5, and t2, cannot be distinguished further by the Hamiltonian in Eq. (3.30).

In the following, it is established that the symmetry properties of only t2 (among the five structures in Fig. 3.40) are in agreement with the experimental observations presented in Sec. 3.3.4.1. In these experiments, magnetic fields broke the symmetry between the two k -arms A_1^c and A_2^c . This broken symmetry should have a vast impact on magnetic domains. However, in phase C it was found that independent of the field history the integrated intensities of Bragg peaks located at $\mathbf{q}_{I,0} \in A_1^c$ and at $\mathbf{q}_{II,0} \in A_2^c$ always feature the zero-field value, i.e., when magnetic domains were equally populated. In particular, the magnetic structure factor does not depend on the field history. This can be explained with the structure t2 but not with the other structures in Fig. 3.40. There are namely only

two different magnetic domains of the structure $t2$, D_1^{t2} and D_2^{t2} . As both domains feature the same structure factors $F_{D_1^{t2}}^2(h, k, l) = F_{D_2^{t2}}^2(h, k, l)$ (cf. Sec. A.1), a magnetic ground state representing $t2$ would imply that integrated intensities of Bragg peaks located at $\mathbf{q}_{I,0} \in A_1^c$ and $\mathbf{q}_{II,0} \in A_2^c$ do not depend on the field history in agreement with the experimental observations in Sec. 3.3.4.1. In contrast, for each of the structures $s2$, $s4$, $d2$, and $d5$ there exist at least two domains that (i) feature different structure factors and (ii) may have different energies in the field as there is no symmetry operation mapping one of the domains on the other while leaving \mathbf{B} invariant. In particular, the properties (i) and (ii) would imply that the integrated intensities of Bragg peaks located at $\mathbf{q}_{I,0} \in A_1^c$ and $\mathbf{q}_{II,0} \in A_2^c$ strongly depend on the field history.

It should be noted that there are some discrepancies between a ground state representing the structure $t2$ and the experiments in Sec. 3.3.4.1. The integrated intensity of the Bragg peak located at $(\frac{1}{2}, \frac{1}{2}, 0)$ in phase C is not entirely independent of the field history, when fields are applied along the fourfold $[001]$ direction. After a field sweep the integrated intensity of the Bragg peak was $\approx 12\%$ smaller than after zfc. In principle, this is at odds with the structure $t2$. However, for the structures $s2$, $s4$, $d2$, and $d5$ a difference much larger than 12% may be expected due to the strong symmetry breaking effect of the field. Hence, the ground state in phase C represents most likely the structure $t2$.

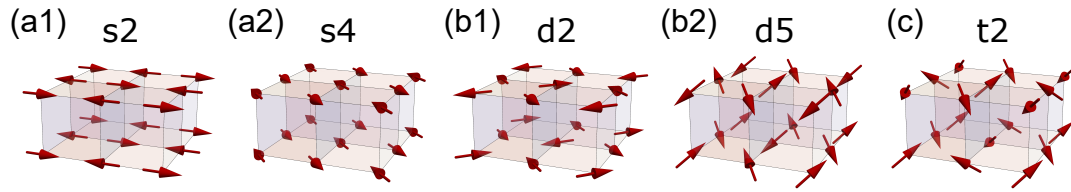


Figure 3.40.: Magnetic ground state candidates in phase C. Among the 21 commensurate $(\pi\pi 0)$ antiferromagnets in Tab. 3.1 regarded for the structure determination only 5 are compatible with the neutron diffraction data in zero magnetic field (Sec. 3.3.3). These structures are shown in the figure. The structures (a1) $s2$ and (a2) $s4$ are single- k . The structures (b1) $d2$ and (b2) $d5$ are double- k . The structure (c) $t2$ is triple- k . Among them, only the three multi- k structures $d2$, $d5$, and $t2$ are in agreement with the field study in Sec. 3.3.4.1. As concluded by means of symmetry arguments in the text, only the structure $t2$ may represent the ground state in phase C.

3.3.5.2. Ground State in Phase IC1

The main results of the magnetic structure determination in phase IC1 may be summarized as follows:

- The magnetic ground state in phase IC1 represents the triple- k structure \mathcal{T}_2 (cf. Fig. 3.45), which is a superposition of one commensurate and two incommensurate propagation vectors.
- Locally, the structure resembles commensurate $(\pi\pi 0)$ antiferromagnets.
- Due to the incommensurate superstructure this local $(\pi\pi 0)$ antiferromagnet changes as a function of real-space coordinates. It is oscillating between coplanar and non-coplanar arrangements.
- The magnetic unit cell has the size $\approx 2a \times 2a \times 25a$.

From neutron experiments in Sec. 3.3.3.2 it is known, that the magnetic ground state in phase IC1 is a superposition of propagation vectors of the stars $\langle \frac{1}{2}, \frac{1}{2}, 0 \rangle$ and $\langle \frac{1}{2} - \delta, \frac{1}{2}, 0 \rangle$. The Fourier decomposition of the ground state was specified in Sec. 3.3.3.5. In particular, the pre-factors of the sinusoidal terms were determined. As established in Sec. 3.3.4.1, the structure may either represent a double- k structure with propagation vectors \mathbf{k}_1^c and $\mathbf{k}_{2,z}^{ic}$ or a triple- k structure with propagation vectors \mathbf{k}_1^c , $\mathbf{k}_{2,z}^{ic}$, and $\mathbf{k}_{3,z}^{ic}$.

The structure determination is organized as follows. First, it is argued that there are three specific structures in agreement with the experimental observations in Secs. 3.3.3.5 and 3.3.4.1 that may potentially describe the ground state in phase IC1, namely the double- k structure \mathcal{D}_1 and the triple- k structures \mathcal{T}_1 and \mathcal{T}_2 . Second, an intuitive picture is established, how the commensurate and incommensurate terms in the Fourier series of the magnetic ground state geometrically look like. Further, it is discussed how these components may be superposed to double- k and triple- k structures. Third, a real-space picture for the three magnetic structures \mathcal{D}_1 , \mathcal{T}_1 , and \mathcal{T}_2 is established. Fourth, it is argued that only \mathcal{T}_2 may represent the ground state in phase IC1.

There is only one double- k structure, \mathcal{D}_1 , which is in agreement with the neutron study in 3.3.4.1. It may be written as follows:

$$\mathbf{m}_{\mathcal{D}_1}(\mathbf{R}) = m_0 \cdot (001)^T \exp(\mathbf{k}_1^c \cdot \mathbf{R}) + m_1 \cdot (100)^T \cos(\mathbf{k}_{2,z}^{ic} \cdot \mathbf{R} + \phi_1) \quad (3.31)$$

As the phase shift ϕ_1 can be eliminated by a translation $\mathbf{R}' = \mathbf{R} + \tau$ of the origin such that $\tau \cdot \mathbf{k}_{2,z}^{ic} = \phi_1$ and hence $\mathbf{k}_{2,z}^{ic} \cdot \mathbf{R} + \phi_1 = \mathbf{k}_{2,z}^{ic} \cdot \mathbf{R}'$, it may be omitted, i.e., $\phi_1 = 0$. The size of the moments is not constant, but varies as a function of real-space coordinates $\mathbf{R} = a \cdot (x, y, z)$, as $|\mathbf{m}_{\mathcal{D}_1}(\mathbf{R})| = |\cos(2\pi\delta \cdot z)|$.

The triple- k structures that are in agreement with the neutron study in 3.3.4.1 may be expressed in terms of:

$$\mathbf{m}_{3k}(\mathbf{R}) = m_0 \cdot (001)^T \exp(\mathbf{k}_1^c \cdot \mathbf{R}) + m_1 (100)^T \cos(\mathbf{k}_{2,z}^{ic} \cdot \mathbf{R} + \phi_1) + m_1 (010)^T \cos(\mathbf{k}_{3,z}^{ic} \cdot \mathbf{R} + \phi_2). \quad (3.32)$$

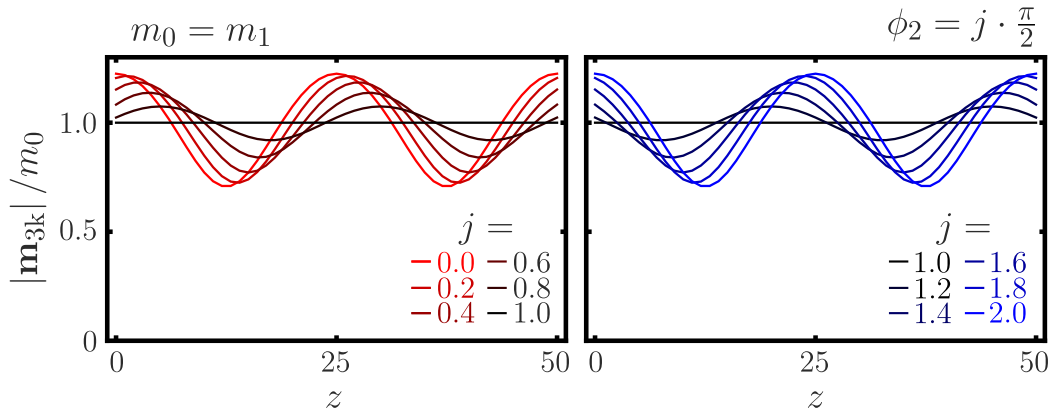


Figure 3.41.: Spatial dependence of the modulus $|\mathbf{m}_{3k}|$ of the triple- k structures \mathbf{m}_{3k} , which are defined in the text, as a function of the phase-shift ϕ_2 . Shown are z -dependences of the modulus for triple- k structures \mathbf{m}_{3k} with different phase-shifts ϕ_2 . This function is well defined, as the modulus does not depend on x and y . For $\phi_0 = \frac{\pi}{2}$ only, the modulus is spatially constant. The spatial dependence is shown for the specific case $m_0 = m_1$. For $m_0 \neq m_1$ spatial dependences are qualitatively identical.

One of the two phase-shifts may be omitted, e.g., $\phi_1 = 0$, corresponding to a translation of the origin. However, the second phase shift ϕ_2 represents the relative phase of the two incommensurate propagations and is crucial for the shape of the magnetic structure. This is indicated by the spatial dependence of the modulus as a function of ϕ_2 . Fig. 3.41 shows the modulus $|\mathbf{m}_{3k}|$ as a function of z for different phase shifts between 0 and π . The function of z is well defined, as the modulus does not depend on the spatial coordinates x and y . The z -dependence is shown for the specific case $m_0 = m_1$, but it is qualitatively identical for $m_0 \neq m_1$. The spatial dependence of the modulus is pronounced for $\phi_0 = 0$ and $\phi_0 = \pi$. For $\phi_0 = \frac{\pi}{2}$ only, the modulus of \mathbf{m}_{3k} is spatially constant. The relative phase ϕ_2 cannot be inferred from first-order neutron scattering [8] and it may be extremely difficult to unambiguously determine relative phases in a multi- k structure (cf. Refs. [105, 142]).

For the present study we investigated the following two cases: (i) the triple- k structure \mathcal{T}_1 representing \mathbf{m}_{3k} with phase shift $\phi_2 = 0$ and (ii) the triple- k structure \mathcal{T}_2 representing \mathbf{m}_{3k} with phase shift $\phi_2 = \frac{\pi}{2}$. Structures with phase shifts $0 < \phi_0 < \frac{\pi}{2}$ may be seen as a mixture of the two magnetic structures \mathcal{T}_1 and \mathcal{T}_2 .

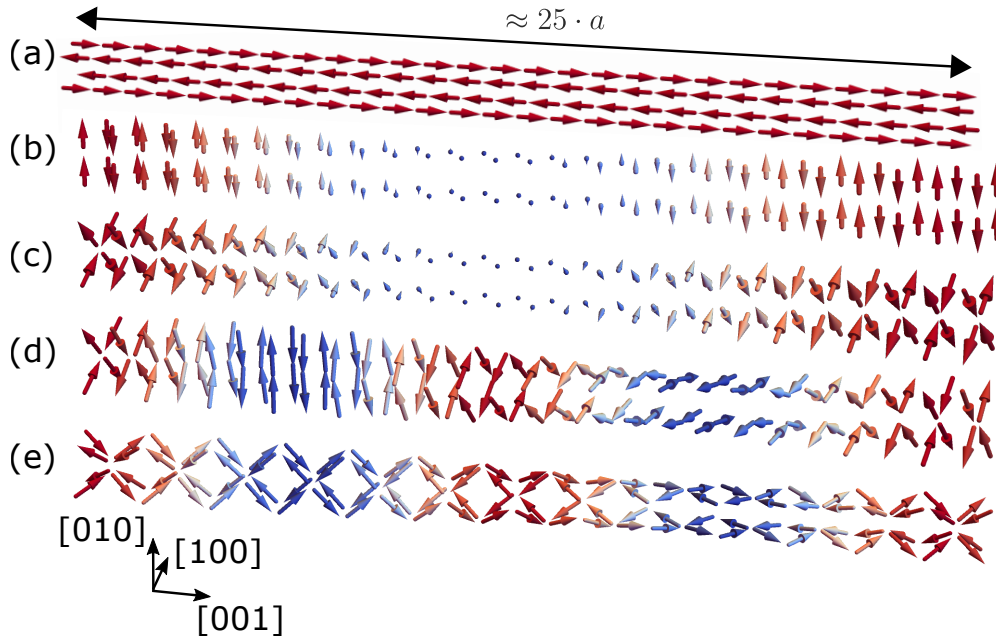


Figure 3.42.: Real-space pictures of the components in the Fourier series of the ground state in phase IC1. (a) Commensurate antiferromagnetic component $\sim \hat{e}_z \cdot \cos(\mathbf{k}_1^c \cdot \mathbf{R})$. (b) Incommensurate antiferromagnetic component $\sim \hat{e}_y \cdot \cos(\mathbf{k}_{3,z}^{ic} \cdot \mathbf{R})$ representing an amplitude-modulated antiferromagnet. (c) Superposition of two amplitude modulations $\hat{e}_x \cos(\mathbf{k}_{2,z}^{ic}) + \hat{e}_y \cos(\mathbf{k}_{3,z}^{ic} + \phi)$ with phase $\phi = 0$, and (d) with phase $\phi = \frac{\pi}{2}$. (e) Triple- k structure representing a superposition of (d) and (a).

Before discussing the three structures in detail, it is instructive to establish an intuitive real-space picture of the single components that appear in the Fourier decomposition of the magnetic structures:

- Fig. 3.42 (a) illustrates the commensurate antiferromagnetic component $\sim \hat{e}_z \cdot \cos(\mathbf{k}_1^c \cdot \mathbf{R})$ representing a collinear texture, for which all moments are directed along $\pm [001]$. The modulus of the moments is constant. Along $[001]$ bonds nearest neighbours are coupled ferromagnetically, along $[100]$ and $[010]$ antiferromagnetically.
- Fig. 3.42 (b) illustrates the incommensurate antiferromagnetic component $\hat{e}_y \mathbf{k}_{3,z}^{ic}$ representing an antiferromagnetic amplitude modulation. The structure is akin to the antiferromagnetic spin-density wave, which was reported in chromium [143]. The structure is collinear and all moments are directed along $\pm [010]$. As a function of x and y , the modulus of the moments is constant. As a function of z , the modulus of the moments oscillates sinusoidally with a pitch length of $\sim \frac{1}{2\delta} \cdot a \approx 25 \cdot a$. Along $[100]$ and $[001]$ bonds nearest neighbours are coupled antiferromagnetically, along $[010]$ bonds ferromagnetically.

The superposition of two or more amplitude modulations may lead to complex magnetic

textures. In this section our emphasis is on superpositions of incommensurate wave vectors that lie in the vicinity of different commensurate $(\pi\pi 0)$ wave vectors and that have an incommensurate splitting with respect to the same fourfold $\langle 100 \rangle$ direction, i.e., a collinear splitting. Figs. 3.42 (c) and (d) show such superpositions of amplitude modulations:

$$\hat{e}_x \cos(\mathbf{k}_{2,z}^{ic}) + \hat{e}_y \cos(\mathbf{k}_{3,z}^{ic} + \phi). \quad (3.33)$$

In Fig. 3.42 (c) a structure is shown, for which they are superposed with the same phase, i.e., $\phi = 0$. The result is a noncollinear but coplanar antiferromagnet with modulated amplitude. In Fig. 3.42 (d) a structure is shown, for which the two amplitude modulations are superposed with a shifted phase of $\phi = \frac{\pi}{2}$. The result is a complex magnetic structure with constant modulus of magnetic moments. Along the z direction the moments together form an antiferromagnetic helix with periodicity of ≈ 25 lattice parameters. Fig. 3.42 (e) shows a structure, which represents a superposition of Fig. 3.42 (d) and Fig. 3.42 (a).

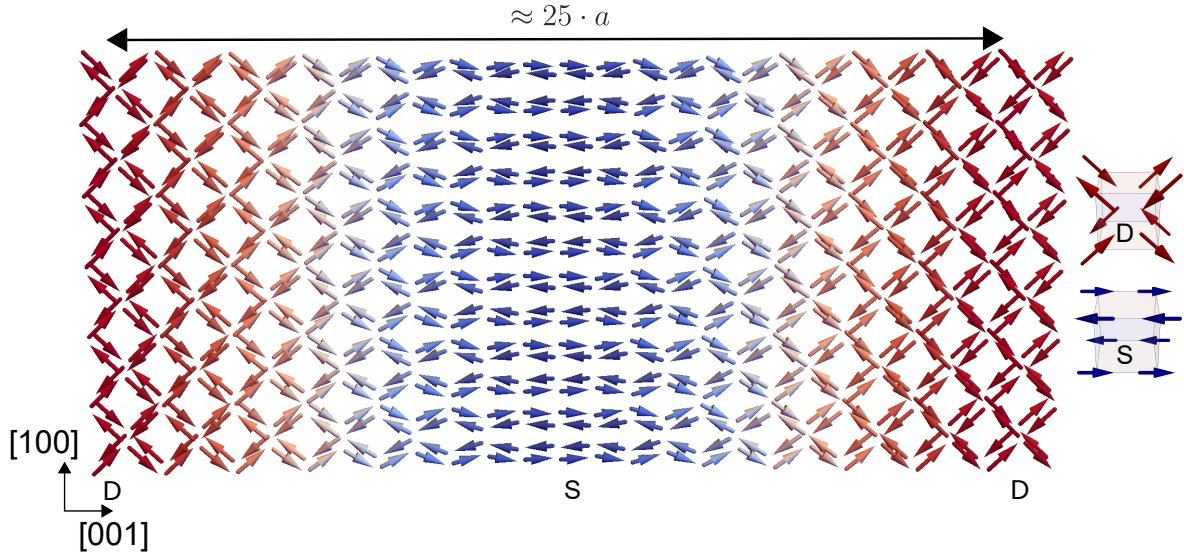


Figure 3.43.: Double- k structure \mathcal{D}_1 that was considered as possible candidate for the ground state in phase IC1. The structure is a superposition of one commensurate and one incommensurate propagation vector. Locally the structure is akin to commensurate $(\pi\pi 0)$ antiferromagnets. The magnetic superstructure cell is one-dimensional with the following characteristic z -regions. In z -region D the local antiferromagnet represents the structure d1 (cf. Tab. 3.1), in z -region S it represents the antiferromagnet s1.

In the following, real-space pictures for the three structures \mathcal{D}_1 , \mathcal{T}_1 , and \mathcal{T}_2 are established. In the presentation, real-space pictures are shown for the specific case, where $m_0 = m_1 = m_2$, representing archetypes for all other structures with parameters $m_0 \neq m_1$. Realistic values m_0 and $m_1 = m_2$ are inferred from experiments and commented on.

Fig. 3.43 shows the double- k structure \mathcal{D}_1 . Locally, i.e., within a local magnetic cell of size $(2a)^3$, the structure \mathcal{D}_1 is akin to commensurate $(\pi\pi 0)$ antiferromagnets listed

in Tab. 3.1. The magnetic superstructure cell is onedimensional along the z direction. The local $(\pi\pi 0)$ antiferromagnets change as a function of z with a periodicity of ≈ 25 lattice parameters due to the magnetic superstructure. As a function of x and y the local $(\pi\pi 0)$ antiferromagnet does not change. This leads to distinct characteristic z -regions. In the z -region D, the structure is coplanar and the local antiferromagnet is akin to the commensurate antiferromagnet d1 (cf. Tab. 3.1). In the z -region S, the structure is collinear and the local antiferromagnet is akin to s1. In the z -region D, all magnetic moments are parallel to $\langle 110 \rangle$ directions. In the z -region S, the moments are directed essentially along $\langle 100 \rangle$ axes, which is at odds with previous studies on the crystal electric fields [113]. The modulus of the magnetic moments is strictly finite but not constant. The magnetic ground state, if representing the structure \mathcal{D}_1 , presumably has a ratio $m_1/m_0 \neq 1$. The exact value may be inferred from experimental data in Sec. 3.3.3.7. Therefore, integrated intensities $I(\mathbf{q})$ in Tab. 3.6, which may represent measured structure factors, may be compared with the magnetic structure factor $\sigma_{\mathcal{D}_1}(\sigma)$ as calculated for the magnetic structure \mathcal{D}_1 . For the calculation of the structure factor via Eq. (2.4), all domains of \mathcal{D}_1 have to be taken into account. The measured and calculated structure factors were compared for the following positions $\mathbf{q}_0 = (\frac{1}{2}, \frac{1}{2}, 0)$, $\mathbf{q}_{1,2} = (\frac{1}{2} \pm \delta, \frac{1}{2}, 0)$, and $\mathbf{q}_{3,4} = (\frac{1}{2}, \frac{1}{2} \pm \delta, 0)$. It is obtained:

$$\frac{\sigma_{\mathcal{D}_1}(\mathbf{q}_1) + \sigma_{\mathcal{D}_1}(\mathbf{q}_2) + \sigma_{\mathcal{D}_1}(\mathbf{q}_3) + \sigma_{\mathcal{D}_1}(\mathbf{q}_4)}{\sigma_{\mathcal{D}_1}(\mathbf{q}_0)} = \frac{I(\mathbf{q}_1) + I(\mathbf{q}_2) + I(\mathbf{q}_3) + I(\mathbf{q}_4)}{I(\mathbf{q}_0)} \quad (3.34)$$

$$\Rightarrow m_1/m_0 \approx 2.50 \quad (3.35)$$

Qualitatively, the structure \mathcal{D}_1 with a ratio $m_1 \approx 2.50 \cdot m_0$ is akin to the archetype structure \mathcal{D}_1 with values $m_1 = m_0$. Only, the local antiferromagnet in z -region D is slightly distorted and the moments are tilted towards the hard fourfold directions. For $m_1/m_0 = 1$ the moments are parallel to $\langle 110 \rangle$ directions, enclosing angles $\pm 45^\circ$ with $\pm [100]$. In contrast, for $m_1/m_0 = 2.5$ the moments are tilted away from these $\langle 110 \rangle$ directions towards $\langle 100 \rangle$ directions, enclosing angles 21.8° with $\pm [100]$. In z -region S the local antiferromagnet is unaffected.

Fig. 3.44 shows the triple- k structure \mathcal{T}_1 . The local $(\pi\pi 0)$ character is again preserved. The superstructure cell is again onedimensional along the z -direction. The local antiferromagnet changes as a function of z with a periodicity of ≈ 25 lattice parameters due to the incommensurate superstructure. As a function of x and y the local antiferromagnet does not change. This leads to distinct characteristic z -regions. In z -region T the structure is noncoplanar and the local antiferromagnet is akin to t1. In z -region S the local antiferromagnet is collinear and akin to s1. In the z -regions, where the local antiferromagnets are noncoplanar, all magnetic moments are directed along $\langle 111 \rangle$ axes, whereas in

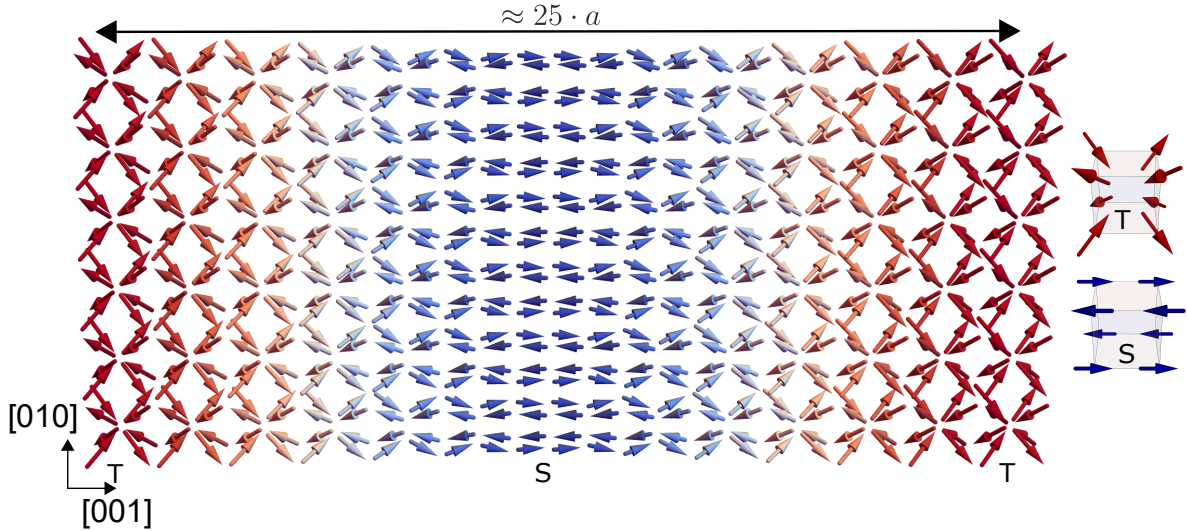


Figure 3.44.: Triple- k structure \mathcal{T}_1 that was considered as possible candidate for the ground state in phase IC1. The structure is a superposition one commensurate and two incommensurate propagation vectors. Locally the structure is akin to commensurate $(\pi\pi 0)$ antiferromagnets. The magnetic superstructure cell is onedimensional with the following characteristic z -regions. In z -region T the local antiferromagnet represents the structure t1, in z -region S it represents the antiferromagnet s1.

the z -regions, where the local antiferromagnets are collinear, they are directed along $\langle 100 \rangle$ axes, which are assumed to be the hard axes. The modulus of the magnetic moments is always finite but not constant.

Fig. 3.45 shows the triple- k structure \mathcal{T}_2 . The structure displays local $(\pi\pi 0)$ character and the local antiferromagnet changes as a function of z with a periodicity of 25 lattice parameters due to the incommensurate superstructure. As a function of x and y the local antiferromagnet does not change. This leads to the following distinct z -regions in one unit cell. In z -region T_1 the structure is noncoplanar and the local antiferromagnet is akin to the structure t1. In z -region T_2 the structure is also noncoplanar. The local antiferromagnets in T_1 and T_2 correspond to the two chiral domains of the structure t1. The two domains are related to each other, for instance, (i) by time reversal, which inverses the direction of each magnetic moment, i.e. $\mathbf{M} \rightarrow -\mathbf{M}$, or (ii) by a reflection at one of the planes (100), (010), or (001). In the two z -regions D_1 and D_2 the magnetic structure is coplanar corresponding to two different (orientational) domains of the antiferromagnet d1. In the z -regions D_1 and D_2 the moments are directed along twofold directions and in the z -regions T_1 and T_2 they are directed along threefold directions. The magnetic moments possess equal modulus on each site. A realistic value m_1/m_0 of the ground state in IC1 representing \mathcal{T}_2 may again be determined from experimental data. The calculation

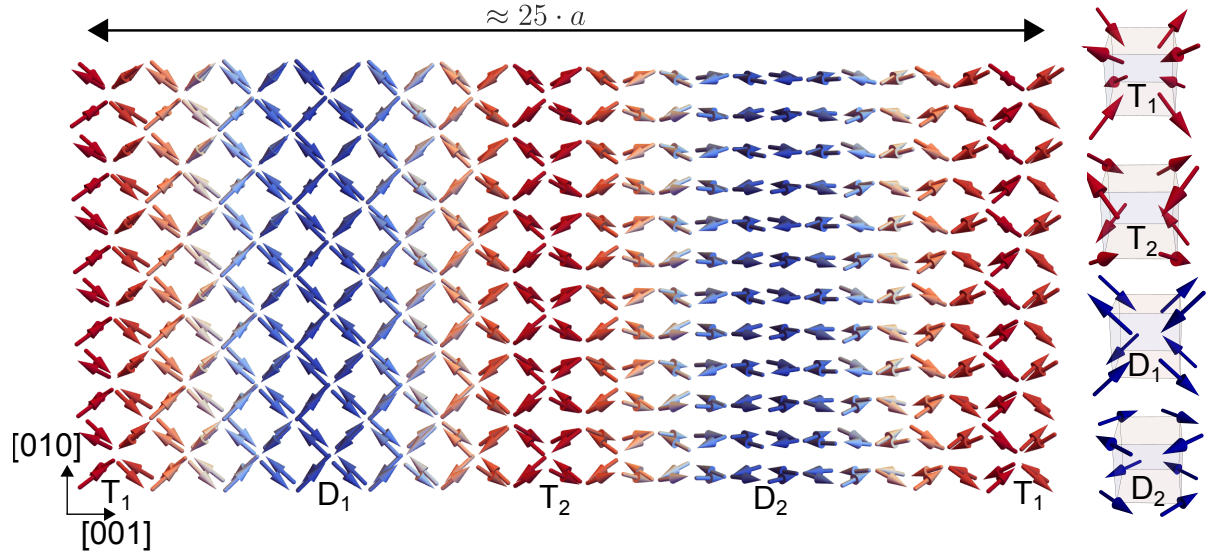


Figure 3.45.: Triple- k structure \mathcal{T}_2 representing the ground state in phase IC1. The structure is a superposition one commensurate and two incommensurate propagation vectors. The incommensurate modulations are phase shifted by $\frac{\pi}{2}$. Locally the structure is akin to commensurate $(\pi\pi 0)$ antiferromagnets. The magnetic superstructure cell is onedimensional with the following characteristic z -regions. The local antiferromagnets in the z -regions T_1 and T_2 represent two different domains of the structure t1, in the z -regions D_1 and D_2 they represent two different orientation domains of the antiferromagnet d1. The figure shows the structure \mathcal{T}_2 for $m_0 = m_1$. The case $m_1/m_0 \approx 1.77$, which may describe the experimental data, is discussed in the text.

is analogous to that for \mathcal{D}_1 , except for the number of possible domains. It is obtained by comparison of calculated and measured structure factors:

$$\frac{\sigma\mathcal{T}_2(\mathbf{q}_1) + \sigma\mathcal{T}_2(\mathbf{q}_2) + \sigma\mathcal{T}_3(\mathbf{q}_3) + \sigma\mathcal{T}_2(\mathbf{q}_4)}{\sigma\mathcal{T}_2(\mathbf{q}_0)} = \frac{I(\mathbf{q}_1) + I(\mathbf{q}_2) + I(\mathbf{q}_3) + I(\mathbf{q}_4)}{I(\mathbf{q}_0)} \quad (3.36)$$

$$\Rightarrow m_1/m_0 \approx 1.77 \quad (3.37)$$

There are no qualitative differences between the archetype structure \mathcal{T}_2 with $m_0 = m_1$ and the structure \mathcal{T}_2 with $m_0 \neq m_1$. Only, the local antiferromagnets are distorted as explained in the following. For $m_1/m_0 = 1$, in the z -regions T_1 and T_2 the moments are directed along $\langle 111 \rangle$ axes, enclosing angles $\pm 35.26^\circ$ with one of the face diagonals $\pm [110]$ or $\pm [1\bar{1}0]$, respectively. In contrast, for $m_1/m_0 = 1.77$ the moments are tilted towards the face-diagonals away from $[001]$, enclosing angles $\pm 21.78^\circ$ with these face diagonals. For $m_1/m_0 = 1$, in the z -regions D_1 and D_2 the moments are perfectly directed along $\langle 110 \rangle$ axes, enclosing angles $\pm 45^\circ$ with one of the two directions $+ [001]$ and $- [001]$, respectively. For $m_1/m_0 = 1.77$, the moments are tilted towards $[010]$ enclosing angles $\pm 60.53^\circ$ with $\pm [001]$. In particular, in both cases the moments enclose large angles with the hard fourfold directions.

In the following, it is established that only the triple- k state \mathcal{T}_2 may represent the

magnetic ground state in phase IC1. The reasons are as follows. From the three structures that are in agreement with the neutron data, \mathcal{T}_2 is the only one in agreement with studies on crystal electric fields [113], as all moments enclose large angles with fourfold axes, which were reported to be clearly the hard directions. In contrast, for both \mathcal{D}_1 and \mathcal{T}_1 there are regions in real space, where the moments are parallel to the energetically unfavorable fourfold directions. Furthermore, the triple- k structure \mathcal{T}_2 , combining incommensurate propagation vectors with collinear incommensurability, gives an explanation for peaks at higher-harmonic positions $(\frac{1}{2} \pm 3\delta, \frac{1}{2}, 0)$ that were discussed in Sec. 3.3.3.7 (cf. Ref. [30]). For \mathcal{D}_1 no such mixed higher-harmonics would exist.

3.3.5.3. Ground State in Phase IC2

The main results of the magnetic structure determination in phase IC2 may be summarized as follows:

- The magnetic ground state in phase IC2 represents a complex multi- k antiferromagnet, which is modulated with an incommensurate superstructure.
- As an educated guess for the magnetic ground state, the structure \mathcal{M}_1 is suggested.
- Locally, \mathcal{M}_1 is akin to commensurate $(\pi\pi 0)$ antiferromagnets. Due to the superstructure this local antiferromagnet spatially varies between collinear, coplanar, and noncoplanar arrangements.
- The magnetic unit cell has a size of $\approx 50a \times 50a \times 2a$.

From neutron experiments in Sec. 3.3.3.2 it is known, that the magnetic ground state in phase IC2 is a superposition of propagation vectors of the stars $\langle \frac{1}{2} \frac{1}{2} 0 \rangle$ and $\langle \frac{1}{2} - \delta, \frac{1}{2}, 0 \rangle$. The pre-factors to the sinusoidal terms in the Fourier decomposition of the ground state were specified in Sec. 3.3.3.5. It was further established in Sec. 3.3.4.1, that the structure is a superposition of propagation vectors of k -arms $\in \mathcal{S}_1^c, \mathcal{S}_2^c, \mathcal{S}_1^{ic},$ and \mathcal{S}_2^{ic} . In particular, the structure combines propagation vectors with noncollinear incommensurability, such as $(\frac{1}{2} - \delta, 0, \frac{1}{2})$ and $(0, \frac{1}{2} - \delta, \frac{1}{2})$. This is reflected by higher harmonics that were observed at positions such as $(\frac{1}{2} + \delta, \frac{1}{2} \pm 2\delta, 0)$, as reported in Sec. 3.3.3.7.

In the following, a structure \mathcal{M}_1 is presented as educated guess for the magnetic structure in phase IC2. The structure \mathcal{M}_1 is chosen such that it resembles the structure in phase IC1 and is in agreement with all experimental observations. We propose a structure \mathcal{M}_1 , which arises due to a superposition of two antiferromagnetic helices and commensurate antiferromagnetic components. In particular, the structure \mathcal{M}_1 shall represent the directorfield of the following vectorfield:

$$\begin{aligned} \mathbf{m}_{\mathcal{M}_1}(\mathbf{R}) &= m_0 \cdot [\hat{e}_z \exp(i\mathbf{k}_1^c \cdot \mathbf{R}) + \hat{e}_x \exp(i\mathbf{k}_2^c \cdot \mathbf{R}) + \hat{e}_y \exp(i\mathbf{k}_3^c \cdot \mathbf{R})] + \\ &+ m_1 \cdot \left[(100)^T \cos(\mathbf{k}_{2,y}^{ic} \cdot \mathbf{R}) + (001)^T \cos\left(\mathbf{k}_{1,y}^{ic} \cdot \mathbf{R} + \frac{\pi}{2}\right) + \right. \\ &+ (010)^T \cos(\mathbf{k}_{3,x}^{ic} \cdot \mathbf{R}) + (001)^T \cos\left(\mathbf{k}_{1,x}^{ic} \cdot \mathbf{R} + \frac{\pi}{2}\right) \left. \right] \end{aligned} \quad (3.38)$$

$$= c_{\mathcal{M}_1}(\mathbf{R}) + ic_{\mathcal{M}_1}(\mathbf{R}) . \quad (3.39)$$

The directorfield of the structure may be defined in terms of $n_{\mathcal{M}_1} = \mathbf{m}_{\mathcal{M}_1}(\mathbf{R}) / |\mathbf{m}_{\mathcal{M}_1}(\mathbf{R})|$. The structure was split into its commensurate and incommensurate components.

The pre-factors of the commensurate contributions could not be successfully determined in the polarization analysis. However, we assume, that they are related to one irreducible representation only, namely $\Gamma_3(\mathbf{k}_c)$, as is case in phase IC1. The experimental

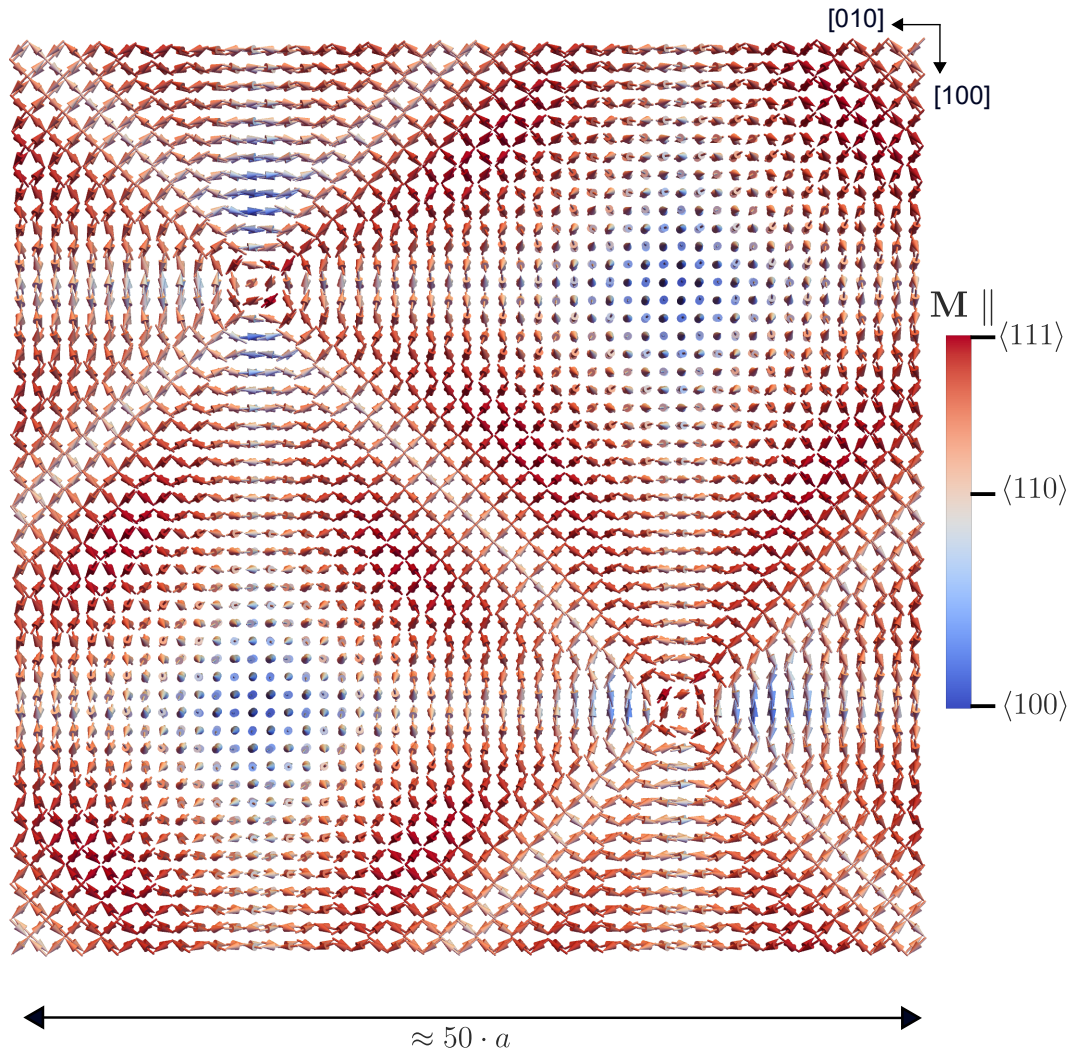


Figure 3.46.: Magnetic structure \mathcal{M}_1 , which was suggested as educated guess for the magnetic ground state in phase IC2. Locally the structure is akin to various commensurate $(\pi\pi 0)$ antiferromagnets. Local antiferromagnets represent t1, the moments pointing along $\langle 111 \rangle$ directions, or they represent d1, the moments pointing along $\langle 110 \rangle$, or s1, the moments pointing along $\langle 100 \rangle$.

study suggests that the incommensurate components are much larger than commensurate components. In the following, the ratio is arbitrarily set to $\frac{m_0}{m_1} = 0.1$.

Fig. 3.46 shows a real-space picture of the structure \mathcal{M}_1 . The unit cell has a long wavelength along two spatial directions and has the size $50a \times 50a \times 2a$. Locally, within a crystallographic unit cell, the structure is akin to commensurate $(\pi\pi 0)$ antiferromagnets. As a function of x and y , the local antiferromagnet changes. The local antiferromagnets are akin to the commensurate structures s1, d1, and t1, respectively. In large parts of the magnetic unit cell, the moments point either along threefold directions, i.e., $\mathbf{M} \parallel \langle 111 \rangle$, and the local antiferromagnet is akin to the structure t1, or they point along twofold directions, i.e., $\mathbf{M} \parallel \langle 110 \rangle$, and the local antiferromagnet is akin the structure d1. Notably,

very few moments are directed along fourfold directions, i.e., $\mathbf{M} \parallel \langle 100 \rangle$ (blue regions). At these points the local antiferromagnet is akin to the structure s1. Hence, the structure \mathcal{M}_1 is in agreement with studies on crystal electric fields [113] that showed that the $\langle 100 \rangle$ directions are clearly the hard axes.

3.3.6. Topological and Geometric Properties

The magnetic structures that were determined in Sec. 3.3.5 exhibit intriguing geometric and topological properties that are discussed in this section. The presentation starts with an introduction to the properties, which were addressed in this section. These properties are then discussed for the ground states in phases C (Sec. 3.3.6.1), IC1 (Sec. 3.3.6.2), and IC2 (Sec. 3.3.6.3). Finally, we investigated, whether superpositions of $(\pi\pi 0)$ propagation vectors may form knots with finite Hopf index, which is presented in Sec. 3.3.6.4.

In the following, an overview over the properties considered in this section is provided. It is addressed, how noncoplanar the magnetic ground states are. Noncoplanar magnetic structures characteristically feature **(scalar) spin chiralities** [144]. For a set of three magnetic moments \mathbf{m}_i , \mathbf{m}_j , and \mathbf{m}_k the scalar spin chirality is defined in terms of $\mathbf{m}_i \cdot (\mathbf{m}_j \times \mathbf{m}_k)$. As this cross product vanishes for a set of coplanar vectors, the scalar spin chirality measures how noncoplanar a magnetic structure is. Noncoplanar magnetic structures are often discussed in connection with the anomalous Hall effect, as Berry phases may be related to scalar spin chiralities, which may represent a fictitious magnetic field for the conduction electrons [145].

Another aspect addressed in the study, is how well the **120° relationship** (cf. Ref. [146]) is fulfilled for three magnetic moments. Therefore, the following vector may be calculated:

$$\boldsymbol{\kappa} = \frac{2}{3\sqrt{3}} (\mathbf{m}_i \times \mathbf{m}_j + \mathbf{m}_j \times \mathbf{m}_k + \mathbf{m}_k \times \mathbf{m}_i) \quad (3.40)$$

The closer the modulus $|\boldsymbol{\kappa}|$ is to 1, the better the 120° relationship is fulfilled [147, 148].

It is furthermore addressed, whether the ground states in phases C, IC1, and IC2 are **topologically protected against unwinding**. To investigate the topology of magnetic ground states it is of major importance to find the correct **order-parameter space** [23, 149], as the topology of the order-parameter space \mathcal{P} also reflects the topological properties of the magnetic ground state. In particular, we investigate the homotopy groups of the order-parameter space, as they provide a mathematical tool to determine whether maps are protected against unwinding (cf. Ref. [150] for further information). In particular, a ground state, which is associated with a nontrivial element in a homotopy group, may be protected against unwinding.

In the following, some examples of order-parameter spaces are given. For a ferromagnetic system of spins that can rotate on a circle (as in the ferromagnetic XY model), the order-parameter space may be given by S^1 , for spins that can point in any direction on a sphere, the order-parameter space may be given by S^2 . In contrast, for antiferromagnets, which are highly discontinuous, it is more complicated to find the right order-parameter

space. For collinear antiferromagnets, an order-parameter space may be identified as follows. Conventional collinear antiferromagnets are typically described in terms of a staggered magnetization [23]. As the staggered magnetization is equivalent for antipodal points on a sphere $\pm \hat{n} \in S^2$, the order-parameter space of a collinear antiferromagnet may be related to real projective spaces $\mathbb{R}P^n$, which are in fact constructed by identification of antipodal points on a sphere. Accordingly, an antiferromagnetic cycloid [151], which represents a modulated variation of a collinear antiferromagnet, may be naturally described in a $\mathbb{R}P^1$ order-parameter space. For the highly noncollinear antiferromagnets discussed in this thesis this description in terms of a staggered magnetization fails. Hence, concepts were established, as presented further below, to identify appropriate order-parameter spaces.

In order to investigate the topology of the order-parameter space, the homotopy groups $\pi_n(\mathcal{P})$ may be calculated [150]. The properties of homotopy groups are nonlocal properties of \mathcal{P} and may be linked to specific physical phenomena [152]. Of particular interest in this thesis are the fundamental group $\pi_1(\mathcal{P})$, as well as the group $\pi_2(\mathcal{P})$ (cf. Ref. [153]). The fundamental group $\pi_1(\mathcal{P})$ describes the homotopy types of closed curves in the order-parameter space \mathcal{P} . Curves that are associated with the same element in $\pi_1(\mathcal{P})$ may be continuously transformed into each other. In particular, curves, which are not associated with $0 \in \pi_1(\mathcal{P})$, cannot be contracted to a single point in \mathcal{P} . The group $\pi_2(\mathcal{P})$ describes the homotopy type of maps $S^2 \rightarrow \mathcal{P}$ (cf. Ref. [154]). Again, two maps that are associated with the same element in $\pi_2(\mathcal{P})$ can be continuously transformed into each other. A map, which is not associated with $0 \in \pi_2(\mathcal{P})$ cannot be transformed into a constant map and is protected against unwinding.

There are prominent examples for the application of the homotopy concept:

- The order-parameter space of the ferromagnetic XY model is given by $\text{SO}(2) \simeq S^1$. The fundamental group of this order-parameter space is non-trivial, as $\pi_1(\text{SO}(2)) = \mathbb{Z}$. Two curves on a circle can be continuously transformed into each other, if they have the same winding number $\in \mathbb{Z}$. The non-trivial elements in $\pi_1(\text{SO}(2))$ may be associated with point defects in the ferromagnetic XY model [147].
- The order-parameter space of the ferromagnetic Heisenberg model is given by S^2 [149]. The homotopy group $\pi_2(S^2) = \mathbb{Z}$ is non-trivial. The non-trivial elements in $\pi_2(S^2)$ have a non-trivial winding number and may be related to instantons in the ferromagnetic Heisenberg model [147]. In fact, Skyrmions, as detected in MnSi [6] or FeCoSi [11], may be described by maps, which are associated with a non-trivial element in the homotopy group $\pi_2(S^2)$. Accordingly, they may not be continuously transformed into a collinear ferromagnet, which has the winding number 0. Hence, they may be topologically protected against unwinding.

- Around 1960 Tony Skyrme introduced the concepts of Skyrmions for the description of nuclear particles in terms of a continuous field theory [155–157]. These particle-like excitations may be related to elements of the homotopy group $\pi_3(S^3) = \mathbb{Z}$.
- Hopfions are knots with a non-trivial Hopf index representing non-trivial elements in the group $\pi_3(S^2) = \mathbb{Z}$.

The calculation of homotopy groups can be extremely difficult even for simple order-parameter spaces. Luckily, for many physical order-parameter spaces, homotopy groups can be deduced from spherical homotopy groups $\pi_n(S^m)$, which were calculated up to high values of $m, n \in \mathbb{N}$ (cf. Ref. [154]). Note, that even if the homotopy group $\pi_{n_0}(\mathcal{P})$ is known, it may still be difficult to determine the homotopy type of a specific map $\gamma : S^{n_0} \rightarrow \mathcal{P}$ in the group $\pi_{n_0}(\mathcal{P})$. In the specific case $S^n \rightarrow S^n$, i.e., $\mathcal{P} = S^n$, the determination of the homotopy type is simple, as the homotopy type of $\gamma : S^n \rightarrow S^n$ within $\pi_n(S^n)$ is related to the Brouwer degree of the map γ [158], which may easily be calculated. In contrast, for a map $\gamma : S^3 \rightarrow S^2$, where the homotopy type is related to the Hopf index of γ , the calculation is not straightforward. In physical cases, i.e., when the map is not too unconventional, the Hopf index equals the linking number of two different preimages $\gamma^{-1}(y_1)$ and $\gamma^{-1}(y_2)$ of $y_1, y_2 \in S^2$ [159]. Hence, in practice, the Hopf index may often be determined graphically [160].

It is further addressed, how time reversal \mathcal{T} acts on the magnetic ground states. The impact of time reversal is important for the prerequisites of numerous theorems and phenomena. If time reversal is preserved, i.e., $[H, \mathcal{T}] = 0$, Kramers theorem [161] implies that energy eigenstates are doubly degenerate, if the total spin in the system is odd. The time reversal operator \mathcal{T} reverses the direction of each magnetic moment in a system, i.e., $\mathcal{T}\mathbf{S} = -\mathbf{S}$. Hence, a magnetic structure by definition breaks the time reversal symmetry, as $\mathcal{T}\mathbf{m}(\mathbf{R}) = -\mathbf{m}(\mathbf{R})$. However, weaker conditions often ensure for a broad range of interactions, that Kramers theorem is still applicable although time reversal symmetry is broken [162]. In particular, if time-reversal in combination with another operator \mathcal{O} , for which $\mathcal{T}\mathcal{O}$ is antiunitary and $(\mathcal{T}\mathcal{O})^2 = -1$, represents a good symmetry, an analogue of Kramers theorem still implies that eigenstates are doubly degenerate [163]. A collinear antiferromagnet may, e.g., be split into two sublattices that are shifted by a translation vector τ such that the structure is ferromagnetic on each sublattice. The translation operator T_τ then makes time-reversal to a good symmetry, as:

$$T_\tau \mathcal{T} \mathbf{m}(\mathbf{R}) = -T_\tau \mathbf{m}(\mathbf{R}) = -\mathbf{m}(\mathbf{R} + \tau) = \mathbf{m}(\mathbf{R}) . \quad (3.41)$$

Hence, collinear antiferromagnets have doubly degenerate bands.

The impact of time reversal is also important for topological properties of the electronic

structure. Namely, if spatial inversion and time reversal are good symmetries, the Berry curvature Ω of the electronic structure is forced to vanish (cf. Ref. [117]). In particular, the intrinsic anomalous Hall effect as well as Chern numbers, which are obtained by integration of the Berry curvature [163, 164], vanish. As magnetic long-range order breaks time reversal symmetry, the Berry curvature Ω may possibly become finite in the presence of magnetic long-range order. For an ordinary collinear antiferromagnet, the Berry curvature vanishes nevertheless in the presence of spatial inversion symmetry. Here, the combination of a translation and time reversal represents a good symmetry forcing the Berry curvature to vanish. For noncollinear and especially noncoplanar ground states, the Berry curvature may possibly be finite. However, each system has to be considered separately. The Berry curvature Ω in the presence of noncollinear $(\pi\pi 0)$ order was investigated in detail in the scope of this thesis, as reported in Secs. 3.3.7.2 and 3.3.7.3

3.3.6.1. Ground State in Phase C

As reported in the following, topological and geometric properties of commensurate $(\pi\pi 0)$ antiferromagnets were investigated. The focus lies on the structure t2, which represents the ground state in phase C, but also the other four $(\pi\pi 0)$ antiferromagnets, which were in agreement with the experiments reported in 3.3.3, are commented on.

The results of the considerations may be summarized as follows:

- The magnetic ground state in phase C (structure t2) is noncoplanar. This is reflected by finite scalar spin chiralities.
- In the presence of the ground state t2, time reversal in combination with a translation is not a good symmetry, suggesting that Kramers theorem is possibly not applicable. Note, that the Berry curvature may possibly be finite.
- The other four structures that were in agreement with the experimental results in Sec. 3.3.3, namely the collinear single- k structures s2 and s4, as well as the double- k structures d2 and d5, are coplanar. This is reflected by the lack of scalar spin chiralities. Further, time reversal in combination with a translation is a good symmetry implying that an analogue of Kramers theorem is applicable.
- In magnetic fields, the coplanar structures d2 and d5 may become noncoplanar. This is reflected by finite scalar spin chiralities in the presence of ferromagnetic components. Further, time reversal in combination with a translation is not a good symmetry. The Berry curvature may possibly be finite.
- In magnetic fields, the collinear structures s2 and s4 may become noncollinear. There are no finite scalar spin chiralities. However, time reversal in combination

with a translation is not a good symmetry. Again, the Berry curvature may possibly be finite.

The discussion in this section is organized as follows. First, the topological properties of the single- k structures s2 and s4 as well as of the double- k structures d2 and d5 in zero magnetic field and in magnetic field are discussed. Second, the topological properties of the triple- k structure t2, which represents the magnetic ground state in phase C, are discussed. Here, scalar spin chiralities, the 120° relationship, and the effect of time reversal symmetry were considered.

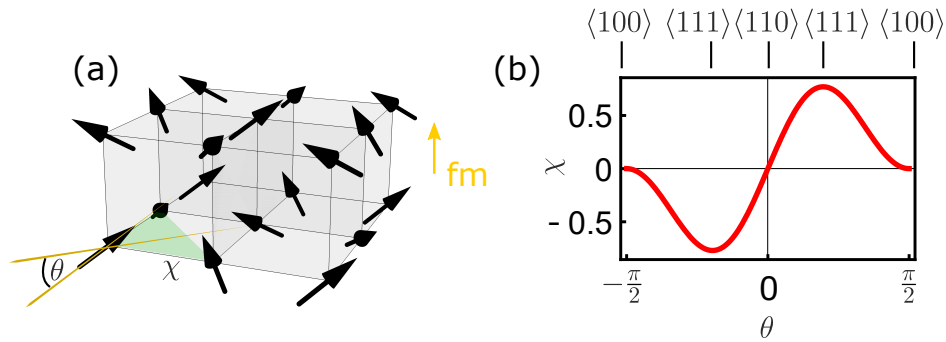


Figure 3.47.: Finite scalar spin chirality in coplanar $(\pi\pi 0)$ textures induced by ferromagnetic components. Considered was the structure d2, which is coplanar in zero magnetic field. Accordingly, spin chiralities are zero at zero magnetic field. (a) A ferromagnetic component $\mathbf{fm} \parallel [001]$ induced by, e.g., a magnetic field inclines the moments effectively out of the basal plane by an angle θ . (b) Finite scalar spin chiralities are induced by the field, as shown in the green triangle as a function of tilting angle θ .

All single- k and double- k $(\pi\pi 0)$ structures are coplanar in zero magnetic field, which is reflected by vanishing scalar spin chiralities. For the coplanar but noncollinear structures d2 and d5, however, finite scalar spin chiralities may be caused by magnetic fields, as demonstrated in the following. Consider therefore, e.g., the structure d2 and a magnetic field that is applied along the $[001]$ direction. The effect of the magnetic field on the magnetic ground state strongly depends on magnetocrystalline anisotropies [165]. However, in a simple picture, it may be assumed that the moments of d2 are inclined out of the basal plane by an angle θ due to a ferromagnetic component caused by the magnetic field. The magnetic structure becomes noncoplanar due to the ferromagnetic component. Fig. 3.47 shows the scalar spin chirality of the moments on the sites of a triangle as a function of θ . In zero magnetic field, when $\theta = 0$, the scalar spin chirality vanishes reflecting that the structure is coplanar. For increasing θ , the scalar spin chirality increases until it displays a maximum for $\theta \approx 54^\circ$. At this angle, all moments are directed along $\langle 111 \rangle$ directions and the structure is maximally noncoplanar. For angles larger than 54° the scalar spin chirality decreases and vanishes at $\theta = 90^\circ$, where the structure is collinear with all moments directed along $\langle 100 \rangle$ directions.

In the following, it is discussed, how time reversal acts on the single- k and double- k ground states in zero field and in magnetic fields. Furthermore it is discussed, whether the prerequisites of Kramers theorem are fulfilled for the single- k and double- k structures. In zero magnetic field, an analogous version of Kramers theorem is applicable for the single- k and double- k structures. The single- k structures are bipartite, the two sublattices being shifted by τ . As a consequence, the operator $T_\tau \mathcal{T}$ represents a good symmetry for the single- k textures s2 and s4 fulfilling the prerequisites of an analogue of Kramers theorem (cf. Ref. [162]). The double- k antiferromagnets d2 and d5 are not bipartite. However, in zero magnetic field there is still a vector τ , such that time reversal in combination with the translation T_τ is a good symmetry, i.e., $T_\tau \mathcal{T} \mathbf{m} = \mathbf{m}$. Hence, the analogue of Kramers theorem is still applicable. In the presence of a tiny ferromagnetic component caused by a magnetic field, however, for both single- k and double- k structures the combined symmetry $T_\tau \mathcal{T}$ may be broken. Whether there is another operator, which in combination with time reversal is a good symmetry, strongly depends on the interactions in the system. However, the prerequisites for Kramers theorem may possibly not be fulfilled in magnetic fields.

The triple- k structure t2 is noncoplanar and scalar spin chiralities are finite even in zero magnetic field. There are in total $\binom{8}{3} = 56$ triangles within the unit cell $2a \cdot 2a \cdot 2a$. For 32 of these triangles the scalar spin chirality is finite. For the same triangles the $\boldsymbol{\kappa}$ vector, gauging how good the 120° relationship is fulfilled, is finite and amounts $|\boldsymbol{\kappa}| = \frac{8}{9}$. An analogue of Kramers theorem is not as easily applicable as for the single- k and double- k structures. There is namely no translation operator for the structure t2 such that $T_\tau \mathcal{T}$ is a good symmetry. More complex operators representing in combination with time reversal a good symmetry might exist. Note, however, that the types of interactions in the system determine, whether the prerequisites for an analogue of Kramers theorem are still fulfilled for such a putative operator.

The geometry of the structure t2 may be illustrated in terms of layers comprising crystallographic (111) planes. Fig. 3.48 (a) shows three (111) planes of the structure t2. The moments located in the same layer are depicted in the same color. Figs. 3.48 (b) show the layers separately. Each of the layers represents a two-dimensional triangular lattice. The magnetic structure on each layer is identical, but the layers are shifted with respect to each other perpendicular to the [111] direction. On a two-dimensional sublattice of each triangular lattice, the moments are directed along [111]. The remaining moments form a honeycomb lattice.

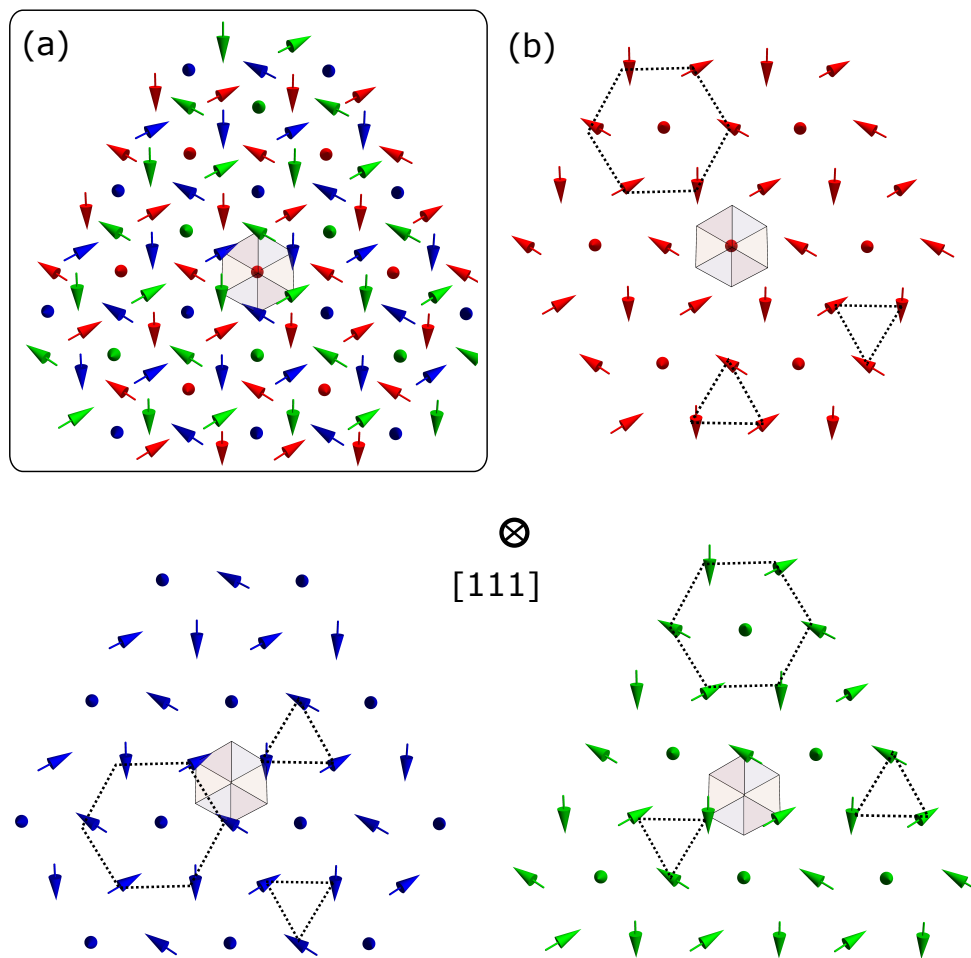


Figure 3.48.: The ground state in phase C, which is represented by the structure t2, viewed along a threefold direction. (a) The structure may be decomposed into staggered layers comprising crystallographic (111) planes. (b) Each of the layers represents a two-dimensional triangular lattice.

3.3.6.2. Ground State in Phase IC1

In the following, the topological and geometric properties of the magnetic ground state in phase IC1 are presented. Comments are also made on the structures \mathcal{T}_1 and \mathcal{D}_1 , which were considered in Sec. 3.3.5.2.

The main results of these considerations may be summarized as follows:

- The magnetic ground state in IC1 (structure \mathcal{T}_2) may be described in a $\mathbb{R}P^1$ order-parameter space.
- The structure \mathcal{T}_2 is topologically non-trivial. It represents a non-trivial element in $\pi_1(\mathbb{R}P^1)$, which is related to a non-trivial winding number. Accordingly, \mathcal{T}_2 is topologically protected against unwinding. In particular, it cannot be continuously transformed into a collinear antiferromagnet.
- The structure \mathcal{T}_2 may be portrayed as a lattice of monopoles and antimonopoles.
- The magnetic structures \mathcal{D}_1 and \mathcal{T}_1 are topologically trivial. They can be continuously transformed into a collinear antiferromagnet.

The discussion is organized as follows. First, it is established for the structure \mathcal{T}_2 that the spatial dependence of the local $(\pi\pi 0)$ order may be described in a $\mathbb{R}P^1$ order-parameter space. Second, it is shown that \mathcal{T}_2 is topologically non-trivial and that this topology is related to a non-trivial winding number. Third, it is established that \mathcal{T}_2 consists of four cones with a periodicity of 50 lattice parameters, which is twice as much as the periodicity of \mathcal{T}_2 . Fourth, it is shown that in the z -regions, where local antiferromagnets are non-coplanar, the structure \mathcal{T}_2 may be portrayed as a lattice of hedgehogs and antihedgehogs carrying magnetic charges. Fifth, the topology of the magnetic structures \mathcal{D}_1 and \mathcal{T}_1 is investigated.

As noted earlier (cf. Sec. 3.3.5.2), the structure \mathcal{T}_2 is locally akin to commensurate $(\pi\pi 0)$ antiferromagnets. As a function of z the local $(\pi\pi 0)$ antiferromagnet changes, whereas it is independent of x and y . In the following, it is established that this z dependence of the local $(\pi\pi 0)$ structure may be described in a $\mathbb{R}P^1$ order-parameter space. These considerations generalize the concept of a staggered magnetization, which is typically used for the description of ordinary antiferromagnets.

The structure \mathcal{T}_2 , which was described by means of Eq. (3.32) with $\phi = \frac{\pi}{2}$, may be expressed as follows:

$$\mathbf{m}_{\mathcal{T}_2}(\mathbf{R}) = m_0 \hat{e}_z \cdot (-1)^{x+y} + m_1 \left[\hat{e}_x \cdot (-1)^{y+z} \cdot \cos(2\pi\delta z) + \hat{e}_y \cdot (-1)^{x+z} \cdot \sin(2\pi\delta z) \right].$$

Introducing a function $\mathbf{f} : \mathbb{R} \rightarrow S^1$, $\mathbf{f}(z) := (\cos(2\pi\delta z), \sin(2\pi\delta z))^T$ allows to rewrite \mathcal{T}_2 :

$$\mathbf{m}_{\mathcal{T}_2}(\mathbf{R}) = m_0 \cdot \hat{e}_z \cdot (-1)^{x+y} + m_1 \cdot \left(\hat{e}_x \cdot (-1)^{y+z}, \hat{e}_y \cdot (-1)^{x+z} \right)^T \cdot \mathbf{f}(z). \quad (3.42)$$

The local $(\pi\pi 0)$ antiferromagnets are unambiguously determined by the values $\mathbf{f}(z) \in S^1$. But as it turns out, the same local antiferromagnet is obtained for antipodal points on the circle $\mathbf{f} = \pm \hat{n} \in S^1$. Hence, the natural image set of the function \mathbf{f} is the real projective line, i.e., $\mathbf{f} : \mathbb{R} \rightarrow \mathbb{R}P^1$. The periodicity of the ground state \mathcal{T}_2 in z direction amounts to 25 lattice constants. As one unit cell $[0; 25[$ may be identified with S^1 , the parameter \mathbf{f} may also be understood as function $\mu : S^1 \rightarrow \mathbb{R}P^1$. Fig. 3.49 illustrates the description of the ground state \mathcal{T}_2 in terms of the function μ in the $\mathbb{R}P^1$ order-parameter space. Each element $f = (\cos(\phi), \sin(\phi)) \in \mathbb{R}P^1$ unambiguously represents a local commensurate $(\pi\pi 0)$ antiferromagnet. One half of the circle in the figure represents the space $\mathbb{R}P^1$. In this scheme, the function μ represents a path on the circle that is oriented anticlockwise. As seen further below, this path is associated with a nontrivial element in the fundamental group implying that the structure \mathcal{T}_2 is protected against unwinding.

In order to investigate the topological properties of the order-parameter space $\mathbb{R}P^1$, the spherical homotopy groups $\pi_n(\mathbb{R}P^1)$ were calculated. Since $\mathbb{R}P^1$ is homeomorphic to S^1 [166], the topological properties of $\mathbb{R}P^1$ are the same as of S^1 . In particular, the fundamental group is non-trivial, $\pi_1(\mathbb{R}P^1) = \pi_1(S^1) = \mathbb{Z}$, whereas all higher spherical homotopy groups vanish, $\pi_n(\mathbb{R}P^1) = 0$, $n \geq 2$ [154]. Due to this mathematical equivalency between S^1 and $\mathbb{R}P^1$, the spatial dependence of the local $(\pi\pi 0)$ structure may also be described in a S^1 order-parameter space.

The topology of \mathcal{T}_2 is non-trivial, which can be shown easily as follows. A homeomorphism between the real projective line and a circle is given by $h : \mathbb{R}P^1 \rightarrow S^1$, $h([z]_{\mathbb{R}P^1}) = z^2$. As the S^1 order parameter $h(\mu)$ makes a full winding with winding number +1 over a distance of 25 lattice constants, $h(\mu)$ represents the non-trivial element +1 in $\pi_1(S^1)$. In particular, μ represents the non-trivial element +1 in the group $\pi_1(\mathbb{R}P^1)$ and the structure \mathcal{T}_2 is associated with a non-trivial winding number.

As the structure \mathcal{T}_2 , i.e., the function μ , is represented by a non-trivial element in the group $\pi_1(\mathbb{R}P^1)$, it cannot be continuously transformed into the collinear antiferromagnet $s1$ (cf. Tab. 3.1), which is represented by the trivial element 0 in the group $\pi_1(\mathbb{R}P^1)$. Accordingly, the structure \mathcal{T}_2 is protected against unwinding.

As shown in the following, the ground state \mathcal{T}_2 consists of four cones. Two of the cones are propagating in positive \hat{z} direction with mathematically positive winding sense (counterclockwise). The other cones are propagating in negative direction. The winding sense

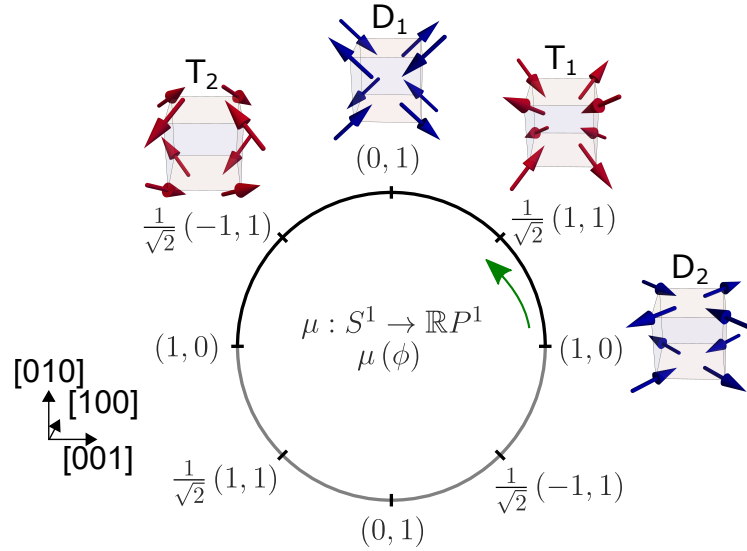


Figure 3.49.: Magnetic ground state in phase IC1, representing the structure \mathcal{T}_2 , as described in a $\mathbb{R}P^1$ order-parameter space. The spatial dependence of the local $(\pi\pi 0)$ order in phase IC1 may be described in the parameter space $\mathbb{R}P^1$, which is obtained by identifying antipodal points on a circle. Accordingly, each local $(\pi\pi 0)$ antiferromagnet of the structure \mathcal{T}_2 is unambiguously represented by a specific value of $f = (x, y) \in \mathbb{R}P^1$. In the illustration, the upper semicircle represents the space $\mathbb{R}P^1$. Each of the local antiferromagnets of the ground state \mathcal{T}_2 is represented by a point on the semicircle. In this scheme, the structure \mathcal{T}_2 is represented by a path μ on the circle, which is oriented anticlockwise.

is also mathematically positive (counterclockwise), but with respect to the negative \hat{z} direction. Hence, the cone chiralities are opposite. Note that the sign of these chiralities was random due to the random definition of the structure \mathcal{T}_2 . Due to the achiral space group, there is also a second domain of the structure \mathcal{T}_2 , where all chiralities are opposite. The pitch length of each cone is given by $\sim \frac{1}{8} \approx 50$ lattice constants, which is twice as large as the pitch length of the composite magnetic structure \mathcal{T}_2 . What seems like a contradiction reflects the $\mathbb{R}P^1$ nature of the magnetic ground state. For a better understanding of the structure \mathcal{T}_2 it is instructive to first discuss its local symmetry relations and the relations between moments in a local unit cell. Therefore, the eight moments at the corners of the unit cell $U_0 = [0, a] \times [0, a] \times [z_0, z_0 + a]$ are considered. Fig. 3.50 shows the cell U_0 , which comprises the moments $\mathbf{S}_1, \dots, \mathbf{S}_8$. Once $\mathbf{S}_1 := \mathbf{m}_{\mathcal{T}_2}(0, 0, z_0)$ is given, the directions of the other moments may be calculated from \mathbf{S}_1 by means of simple operators. Tab. 3.50 gives an overview over these operators, which are defined via $\mathbf{S}_i = \mathcal{O}\mathbf{S}_1$. The moments $\mathbf{S}_2, \mathbf{S}_3$, and \mathbf{S}_4 at $z = z_0$ are related to \mathbf{S}_1 by operators \hat{P}_x, \hat{P}_y , and \hat{P}_z , which change the sign of the x -, y -, and z -spin-component, respectively. The moments at $z = z_0 + 1$, i.e., $\mathbf{S}_5, \mathbf{S}_6$,

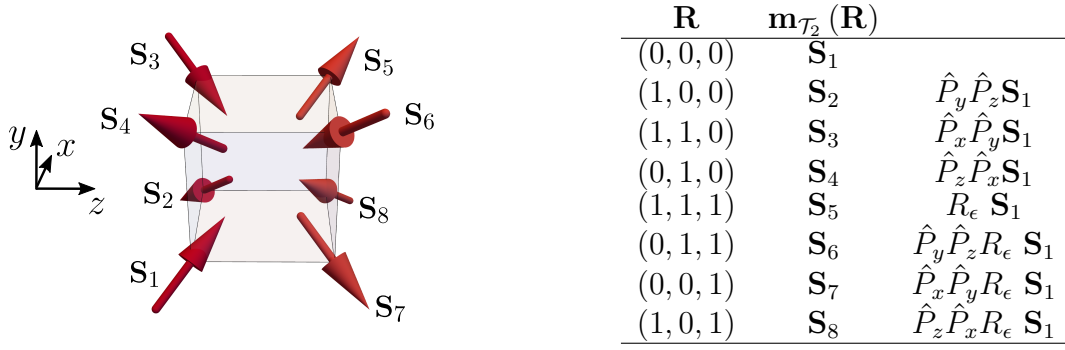


Figure 3.50.: Relation between magnetic moments within a crystallographic unit cell of the structure \mathcal{T}_2 . The four moments at a fixed z coordinate are related to the spin \mathbf{S}_1 through operators \hat{P}_x , \hat{P}_y , and \hat{P}_z , changing the sign of x -, y -, and z -spin-component, respectively. The moments at $z+1$ are related to \mathbf{S}_1 through a combination of operators \hat{P}_x , \hat{P}_y , \hat{P}_z and a helical rotation R_ϵ .

\mathbf{S}_7 , and \mathbf{S}_8 , are related to \mathbf{S}_1 by a combination of \hat{P}_x , \hat{P}_y , \hat{P}_z and a small helical rotation by an angle $\epsilon = 2\pi\delta \approx 7.2^\circ$, which is given by:

$$R_\epsilon = \begin{pmatrix} \cos(\epsilon) & -\sin(\epsilon) & 0 \\ \sin(\epsilon) & \cos(\epsilon) & 0 \\ 0 & 0 & 1 \end{pmatrix}. \quad (3.43)$$

The relations in Fig. 3.50 suggest a decomposition of the the ground state \mathcal{T}_2 into four sublattices, such that the structure \mathcal{T}_2 is continuous on each sublattice. Each sublattice represents a bbc lattice. The first sublattice contains \mathbf{S}_1 and \mathbf{S}_5 , the second one \mathbf{S}_2 and \mathbf{S}_6 , the third one \mathbf{S}_3 and \mathbf{S}_8 , and the fourth one \mathbf{S}_4 and \mathbf{S}_7 . For the mathematical definition of these sublattices, we define a cubic lattice with lattice constants $2a$, i.e., $C_{2a} = \{2a \cdot (i, j, k)\}$. The four bbc lattices may then be described as follows:

$$L_1 = (\mathbf{R}_{\mathbf{S}_1} + C_{2a}) \cup (\mathbf{R}_{\mathbf{S}_5} + C_{2a}) \quad (3.44)$$

$$L_2 = (\mathbf{R}_{\mathbf{S}_2} + C_{2a}) \cup (\mathbf{R}_{\mathbf{S}_6} + C_{2a}) \quad (3.45)$$

$$L_3 = (\mathbf{R}_{\mathbf{S}_3} + C_{2a}) \cup (\mathbf{R}_{\mathbf{S}_7} + C_{2a}) \quad (3.46)$$

$$L_4 = (\mathbf{R}_{\mathbf{S}_4} + C_{2a}) \cup (\mathbf{R}_{\mathbf{S}_8} + C_{2a}) \quad (3.47)$$

On each sublattice the structure \mathcal{T}_2 is continuous and represents a cone. On, e.g., L_1 Eq. (3.42) reduces to:

$$\mathbf{m}_{\mathcal{T}_1}(\mathbf{R})|_{\mathbf{R} \in L_1} = \mathbf{m}_{\mathcal{T}_1}(0, 0, 2 \cdot z) = m_0 \cdot \hat{e}_z + m_1 \hat{e}_y \cos(4\pi\delta \cdot z) + m_1 \hat{e}_x \sin(4\pi\delta \cdot z) \quad z \in \mathbb{Z}.$$

The periodicity of the cone $\sim \frac{1}{\delta} \approx 50$ is inferred directly from this formula. Fig. 3.51 (a) shows the cone on sublattice L_1 within one superstructure cell. Most notably, the cone makes only half of a winding within a full superstructure cell. Fig. 3.51 (b) illustrates the signs of the cone chiralities on the sublattices. The cones on sublattices L_1 and L_3 propagate in positive z direction and have positive chirality $\chi = +1$. On sublattices L_2 and L_4 the cone chirality is opposite $\chi = -1$.

With respect to time reversal symmetry, we note that there is no simple operator that makes time reversal to a good symmetry in the presence of the ground state \mathcal{T}_2 . Accordingly, the Berry curvature may potentially be finite for the ground state \mathcal{T}_2 .

It was illustrated in Sec. 3.3.5.2 that the local $(\pi\pi 0)$ antiferromagnets vary between coplanar and noncoplanar arrangements. As a measure of how coplanar the structure \mathcal{T}_2 is, scalar spin chiralities may be calculated. In z -regions D_1 and D_2 all scalar spin chiralities vanish reflecting the coplanar arrangement of the magnetic moments. In contrast, triangles with finite scalar spin chiralities are found everywhere else, and they are particularly large in the z -regions T_1 and T_2 , reflecting the noncoplanar arrangement of the moments.

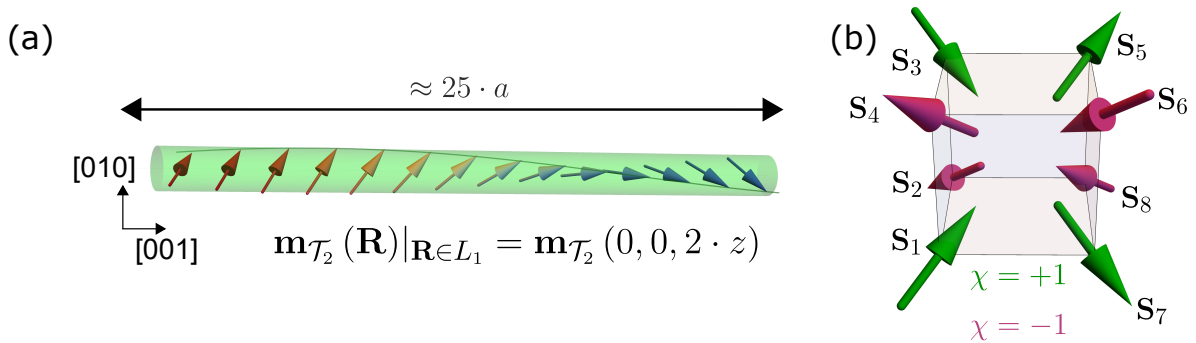


Figure 3.51.: Decomposition of the ground state of phase IC1, represented by \mathcal{T}_2 , into cones. (a) The magnetic structure \mathcal{T}_2 may be decomposed into four bbc-lattices. On each sublattice the structure \mathcal{T}_2 is continuous and represents a cone. Shown in (a) is the structure \mathcal{T}_2 on the sublattice L_1 . The cone has a periodicity of 50 lattice parameters. (b) On sublattice L_1 , which comprises \mathbf{S}_1 and \mathbf{S}_5 , and on sublattice L_3 , which comprises \mathbf{S}_3 , and \mathbf{S}_7 , the cone propagates along $[001]$ with positive chirality (green). On sublattice L_2 , which comprises \mathbf{S}_2 and \mathbf{S}_6 , and on sublattice L_4 , which comprises \mathbf{S}_4 and \mathbf{S}_8 , the cones have opposite chirality (purple).

In the following it is shown, that the local $(\pi\pi 0)$ antiferromagnets in the spatial regions T_1 and T_2 may be portrayed as hedgehog-antihedgehog lattices. Accordingly, the structure \mathcal{T}_2 may be viewed as layers comprising monopoles and layers comprising anti-monopoles. The commensurate $(\pi\pi 0)$ antiferromagnets in z -regions T_1 and T_2 represent two different chiral domains of the same commensurate $(\pi\pi 0)$ structure t1. Fig. 3.52 illustrates the decomposition into hedgehogs and antihedgehogs. The positions of hedgehogs and antihedgehogs are reversed for the two domains. This decomposition may sug-

gest the existence of tiny monopole-antimonopole strings, which may be reminiscent of monopoles in spin ice [167]. The question is pressing, whether the monopole-antimonopole strings may be pulled apart by means of magnetic fields or whether a diffusive motion of monopoles is possible (cf. Ref. [168]).

The decomposition into monopoles and antimonopoles may be established as follows. The structure in z -regions T_1 and T_2 may be described by the following vectorfields that are obtained in interatomic interpolation of the commensurate antiferromagnets:

$$\mathbf{m}_{T_1} = \hat{e}_z \cos(\pi(x+y)) + \hat{e}_x \cos(\pi(y+z)) + \hat{e}_y \cos(\pi(x+z)) \quad (3.48)$$

$$\mathbf{m}_{T_2} = \hat{e}_z \cos(\pi(x+y)) - \hat{e}_x \cos(\pi(y+z)) + \hat{e}_y \cos(\pi(x+z)) \quad (3.49)$$

It can easily be checked that both interpolated vectorfields vanish at $\mathbf{x}_1 = (a, a, a) \cdot \frac{1}{4}$ and at $\mathbf{x}_2 = (a, a, a) \cdot \frac{3}{4}$. The continuous interpolation of T_1 has a hedgehog at $\frac{a}{4}(1, 1, 1)$ and an anti-hedgehog at $\frac{3a}{4}(1, 1, 1)$. The singularities are spatially separated by $\frac{1}{2}a\sqrt{3}$. For T_2 the positions of hedgehog and antihedgehog are exchanged.

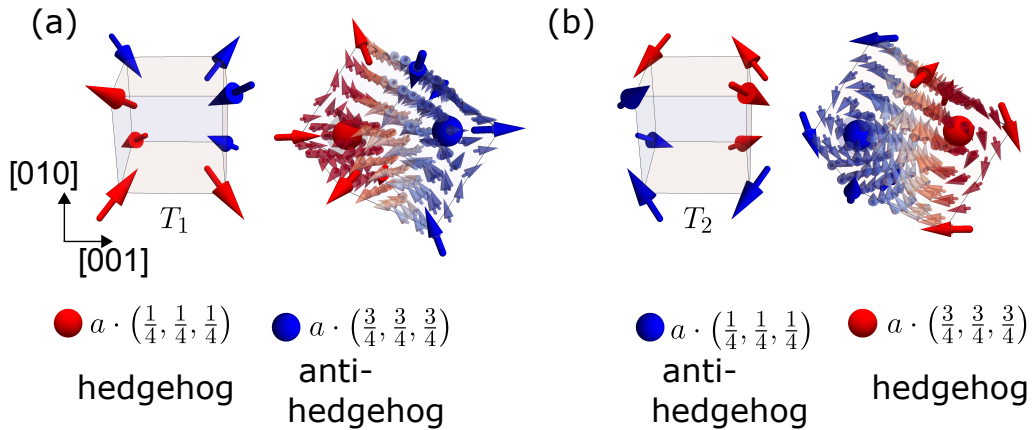


Figure 3.52.: Decomposition of the ground state in phase IC1, represented by T_2 , into hedgehogs and antihedgehogs. In the regions, where the structure T_2 is noncoplanar, the local antiferromagnets represent the commensurate structure $t1$, which may be viewed as hedgehog-, antihedgehog-pair. In the spatial regions T_1 and T_2 of T_2 , the local antiferromagnets represents different chiral domains of the commensurate antiferromagnet $t1$. (a) In region T_1 the structure may be portrayed as a composition of a hedgehog at $\frac{a}{4}(1, 1, 1)$ and an anti-hedgehog at $\frac{3a}{4}(1, 1, 1)$. (b) In region T_2 the positions of hedgehog and anti-hedgehog are reversed.

We establish further that the hedgehogs and antihedgehogs are the origin of a positive and a negative magnetic charge, respectively. This may be seen as follows. The directorfield of the magnetization is defined in terms of:

$$\mathbf{n} : [0, a]^3 \setminus \{\mathbf{x}_1, \mathbf{x}_2\} \rightarrow \mathbb{R}^3, \quad \mathbf{n}(\mathbf{x}) = \frac{\mathbf{m}}{|\mathbf{m}|} \quad (3.50)$$

Following the study in Ref. [169], a Berry curvature field may be defined in terms of $b_k = \frac{1}{2}\epsilon^{ijk}\mathbf{n}(\mathbf{x})\cdot[\partial_i\mathbf{n}(\mathbf{x})\times\partial_j\mathbf{n}(\mathbf{x})]$. The integration of the Berry curvature on tiny spheres K around the singularities \mathbf{x}_1 and \mathbf{x}_2 reveals (cf. [169]):

$$Q_{T_1}(\mathbf{x}) = \frac{1}{4\pi} \int_{\partial K(\mathbf{x})} dS \cdot b_{T_1} = \begin{cases} +1, & \mathbf{x} = \mathbf{x}_1 \\ -1, & \mathbf{x} = \mathbf{x}_2 \end{cases}, \quad Q_{T_2}(\mathbf{x}) = -Q_{T_1}(\mathbf{x}) \quad (3.51)$$

Hence, the singularities have non-trivial winding numbers, which are related to magnetic charges of emergent monopoles and antimonopoles [169].

It is now shown that the topology of the magnetic structures \mathcal{D}_1 and \mathcal{T}_1 is trivial. The order-parameter spaces of \mathcal{D}_1 and \mathcal{T}_1 may be established in analogy to the study on \mathcal{T}_2 . It is found that the structure \mathcal{D}_1 may be described in the order-parameter space $\mathcal{P}_{\mathcal{D}_1} = D^1$, i.e., an interval (representing a disk in one dimension), whereas the structure \mathcal{D}_2 may be described in the order-parameter space $\mathcal{P}_{\mathcal{D}_2} = D^2$, i.e., a disc in two dimensions. The order-parameter space $\mathcal{P}_{\mathcal{D}_1} = D^1$, as well as $\mathcal{P}_{\mathcal{D}_2} = D^2$ are both homotopic to a single point [154]. In particular, all homotopy groups vanish, i.e., $\pi_{n \geq 1}(D^2) = \pi_{n \geq 1}(D^1) = 0$ implying that the structures \mathcal{D}_1 and \mathcal{T}_1 are topologically trivial. Accordingly, the structures \mathcal{D}_1 and \mathcal{T}_1 may be continuously transformed to collinear antiferromagnets and they are not protected against unwinding.

3.3.6.3. Ground State in Phase IC2

The topological properties of the structure \mathcal{M}_1 , which was suggested as educated guess for the ground state in phase IC2, are now investigated.

The main results of these investigations may be summarized as follows:

- The magnetic structure \mathcal{M}_1 may be described in a $\mathbb{R}P^2$ order-parameter space.
- The structure \mathcal{M}_1 is topologically non-trivial. It represents a non-trivial element in the homotopy group $\pi_2(\mathbb{R}P^2)$. Accordingly, the structure cannot be continuously transformed into a collinear antiferromagnet and it is protected against unwinding. However, this topology is not related to an ordinary winding number.
- The structure \mathcal{M}_1 consists of square Skyrmion-sublattices.

The presentation of these considerations is organized as follows. First, the order-parameter space that allows to describe the spatial dependence of the local $(\pi\pi 0)$ antiferromagnet is established. Second, it is shown that the structure consists of four Skyrmion lattices, two with positive and two with negative winding number.

It was explained before that the structure \mathcal{M}_1 locally looks like commensurate $(\pi\pi 0)$ antiferromagnets. The spatial dependence of the local antiferromagnet can be described in a $\mathbb{R}P^2$ order-parameter space. This can be established in analogy to the previous section. Fig. 3.53 illustrates the description of \mathcal{M}_1 in the order-parameter space $\mathbb{R}P^2$. Each element in $\mathbb{R}P^2$ corresponds to a pair of antipodal points $\hat{n} \in S^2$ and unambiguously represents a local $(\pi\pi 0)$ antiferromagnet. In the figure, the space $\mathbb{R}P^2$ is represented by the northern hemisphere. The points on the sphere are described in terms of spherical coordinates (θ, ϕ) . The local $(\pi\pi 0)$ antiferromagnets of \mathcal{M}_1 represent the $(\pi\pi 0)$ structures t1, d1, and s1. For t1, there are two domains, i.e., orientations with respect to the lattice, for d1 and s1 there are three domains.

To investigate the topological properties of \mathcal{M}_1 , the homotopy groups $\pi_n(\mathbb{R}P^2)$ were calculated. The fundamental group is given by $\pi_1(\mathbb{R}P^2) = \mathbb{Z}_2$. Further the second homotopy group is given by $\pi_2(\mathbb{R}P^2) = \pi_2(S^2) = \mathbb{Z}$. To determine the topological properties of \mathcal{M}_1 , the element in $\pi_n(\mathbb{R}P^2)$ the structure \mathcal{M}_1 is associated with has to be determined. By a tedious calculation using covering spaces [154] it may be established that \mathcal{M}_1 is associated with a non-trivial element in the order-parameter space $\pi_2(\mathbb{R}P^2)$ (however, these considerations are beyond the scope of this thesis). Accordingly, the structure has a non-trivial topology. \mathcal{M}_1 cannot be continuously transformed into a collinear antiferromagnet such as s1, which is associated with the trivial element 0 in the group $\pi_2(\mathbb{R}P^2)$. Note, that the non-trivial topology of the structure \mathcal{M}_1 is not related to an ordinary winding number. Winding numbers which are typically defined for maps such

as $S^1 \rightarrow S^1$ or $S^2 \rightarrow S^2$ are related to a Brouwer degree [158]. However, a Brouwer degree does not exist for maps $S^2 \rightarrow \mathbb{R}P^2$, as the space $\mathbb{R}P^2$ does not possess an orientation.

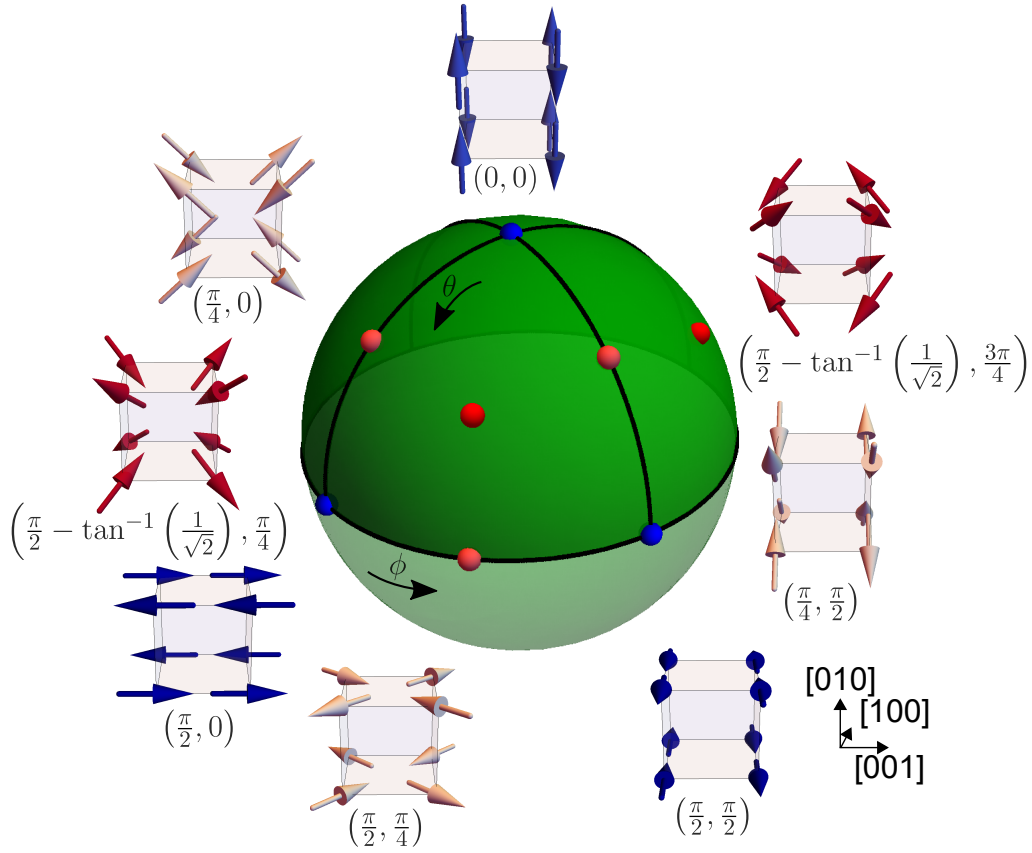


Figure 3.53.: Ground state candidate \mathcal{M}_1 of phase IC2 as described in a $\mathbb{R}P^2$ order-parameter space. The spatial dependence of the local $(\pi\pi 0)$ order may be described in the $\mathbb{R}P^2$ parameter space, which is obtained by identifying antipodal points on a sphere. Accordingly, each local $(\pi\pi 0)$ antiferromagnet of the structure \mathcal{M}_1 may be represented by an element in $\mathbb{R}P^2$, i.e., by an element on a hemisphere. In the picture, the space $\mathbb{R}P^2$ is represented by the northern hemisphere. The points on the sphere are described by spherical coordinates (θ, ϕ) .

It is shown in the following, that the magnetic structure \mathcal{M}_1 consists of four bbc Skyrmin lattices, each with a magnetic unit cell of size $50a \times 50a$. Therefore, the structure \mathcal{M}_1 may be written as follows:

$$\begin{aligned} \mathbf{m}_{\mathcal{M}_1}(\mathbf{R}) = & m_0 \hat{e}_z \cdot (-1)^{x+y} + m_0 \hat{e}_x \cdot (-1)^{y+z} + m_0 \hat{e}_y \cdot (-1)^{z+x} + \\ & + m_1 \hat{e}_x \cdot (-1)^{y+z} \cos(2\pi\delta y) + m_1 \hat{e}_z \cdot (-1)^{x+z} \sin(2\pi\delta y) + \\ & + m_1 \hat{e}_y \cdot (-1)^{x+z} \cos(2\pi\delta x) + m_1 \hat{e}_z \cdot (-1)^{x+y} \sin(2\pi\delta x). \end{aligned} \quad (3.52)$$

Analogously to the approach in Sec. 3.3.6.2, the cubic lattice may be decomposed into four bbc lattices L_1 , L_2 , L_3 , and L_4 . On each of the four sublattices, the structure \mathcal{M}_1 represents a square Skyrmin lattice. Fig. 3.54 (a) shows one layer of the structure \mathcal{M}_1 ,

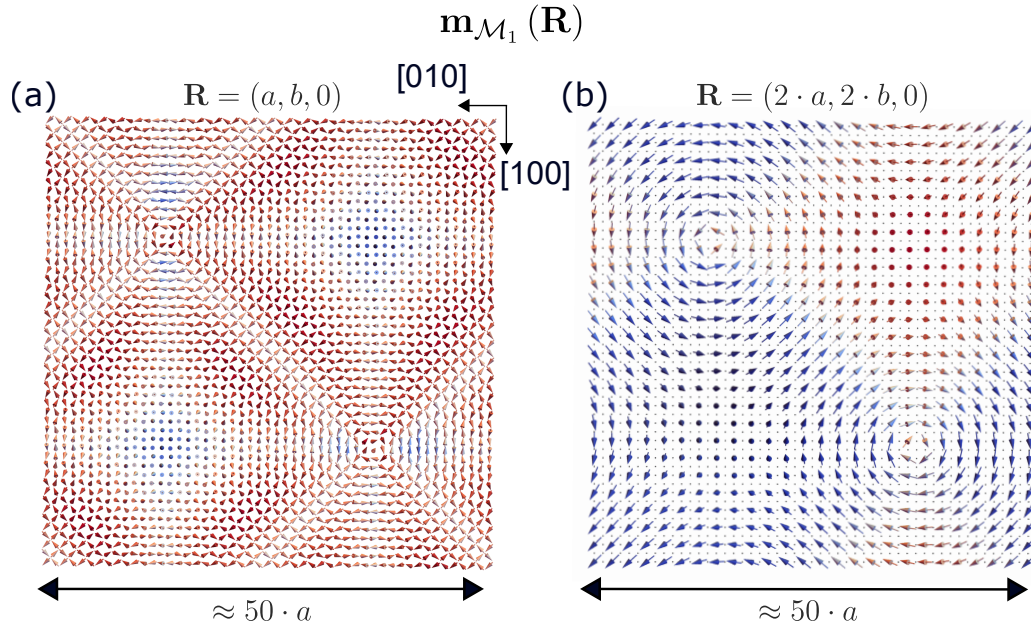


Figure 3.54.: Decomposition of the structure \mathcal{M}_1 into square Skyrmin lattices. The structure \mathcal{M}_1 may be decomposed into four bcc-sublattices. On each sublattice, the structure \mathcal{M}_1 represents a square Skyrmin lattice. (a) Structure \mathcal{M}_1 in the $z = 0$ plane. Shown is the structure on lattice sites from all four sublattices L_1 , L_2 , L_3 , and L_4 in the $z = 0$ plane. (b) Structure \mathcal{M}_1 on sublattice L_1 . Shown is the structure \mathcal{M}_1 in the $z = 0$ plane on sublattice L_1 . The structure represents a square Skyrmin with finite winding number.

namely $z = 0$, in a $50a \times 50a$ cell. Fig. 3.54 (b) shows the same layer but depicted are only lattice points of the sublattice L_1 . The shape of the structure on L_1 clearly resembles that of a Skyrmin.

To establish the Skyrmin nature on each sublattice, the winding number [6] may be calculated for a unit cell $U_0(L)$ of extent $50a \times 50a$ that contains only sites of one sublattice L by integration of the Skyrmin density (cf. Ref. [170]):

$$\int_{U_0(L)} \frac{1}{4\pi} \mathbf{n} (\partial_x \mathbf{n} \times \partial_y \mathbf{n}) dx dy = \begin{cases} +1, & L = L_1, L_3 \\ -1, & L = L_2, L_4 \end{cases} \quad (3.53)$$

The finite winding numbers ± 1 , which were obtained by numerical integration, reflect the Skyrmin nature of the structure \mathcal{M}_1 on each sublattice.

3.3.6.4. Knots in Three Dimensions

For the following presentation, we investigated, whether the superposition of three non-coplanar sine-wave modulations may lead to a knot with finite Hopf index [159].

The superposition of three ferromagnetic helices, e.g., along the cubic directions [100], [010] and [001], may represent a three dimensional lattice of hedgehogs and antihedgehogs [169]. In ferromagnets the study of such superpositions is more straight forward than in antiferromagnets, as the order-parameter spaces are typically more intuitive (cf. Secs. 3.3.6.2 and 3.3.6.3). For this study, we assume that an order-parameter space has been identified, such that the magnetic structure can be described by a continuous function $\mathbf{M} : \mathbb{R}^3 \rightarrow \mathbb{R}^3$. While it has been established that the superposition of helices may lead to a lattice of hedgehogs and antihedgehogs, we want to investigate whether such a superposition may also possess a non-trivial Hopf index [159]. The Hopf index reflects, whether a structure $S^3 \rightarrow S^2$ is protected against unwinding. The corresponding homotopy group is given by $\pi_3(S^2) = \mathbb{Z}$ [154]. So far no static magnetic structures featuring a non-trivial Hopf number have been observed experimentally. It is often argued that a static magnetic structure cannot have a non-trivial Hopf index following Derrick's theorem [171]. Note, that the boundary conditions are crucial for the stability of solitons [172]. There are many works that discuss the stability of Hopfions or which address, how to overcome Derrick's theorem [173–175]. The topological concept of Hopfions may be important in many areas like hydrodynamics [176], electrodynamics [177, 178] or Bose-Einstein-Condensates, where vortex knots [179] with finite Hopf index may also exist.

The main results of these considerations may be summarized as follows:

- The superposition of three noncollinear sine waves may lead to topologically non-trivial vectorfields like a lattice of monopoles and antimonopoles.
- This knot-like superposition cannot be interpreted as Hopfion.

To investigate, whether the superposition of three noncollinear sine waves may result in a Hopfion, the following vectorfield was considered:

$$\mathbf{M}(x, y, z) = \hat{e}_z \cdot \cos[\pi(x + y)] + \hat{e}_x \cdot \cos[\pi(y + z)] + \hat{e}_y \cdot \cos[\pi(x + z)] + \mathbf{fm}, \quad (3.54)$$

where the constant vector \mathbf{fm} represents a uniform magnetization.

The study is organized as follows. First, it is established under which conditions \mathbf{M} may be interpreted as a map $S^3 \rightarrow S^2$. Second, the Hopf index, which describes the topology of maps $S^3 \rightarrow S^2$, is determined graphically for two different uniform magnetizations.

In the following it is explained under which conditions \mathbf{M} may be interpreted as a map $S^3 \rightarrow S^2$. The periodicity of the vectorfield \mathbf{M} amounts to 2 in all three spatial dimensions.

Hence the map goes from a 3-torus to three-dimensional space, i.e. $\mathbf{M} : [-1, 1]^3 \rightarrow \mathbb{R}^3$ [180]. Whether the map \mathbf{M} has singularities or not depends strongly on the modulus of the uniform magnetization. In the following, singularities are neglected for a moment and it is assumed that the directorfield is well defined on the torus:

$$\mathbf{n} : [-1, 1]^3 \rightarrow S^2, \quad \mathbf{n} := \frac{\mathbf{M}(x, y, z)}{|\mathbf{M}(x, y, z)|}. \quad (3.55)$$

Next, it is assumed that the unit cell, i.e., the box $[-1, 1]^3$, may be identified with S^3 . Mathematically this is typically done with a stereographic projection [181]. The prerequisites mainly consist of boundary conditions such that \mathbf{n} is constant at the border of the box.

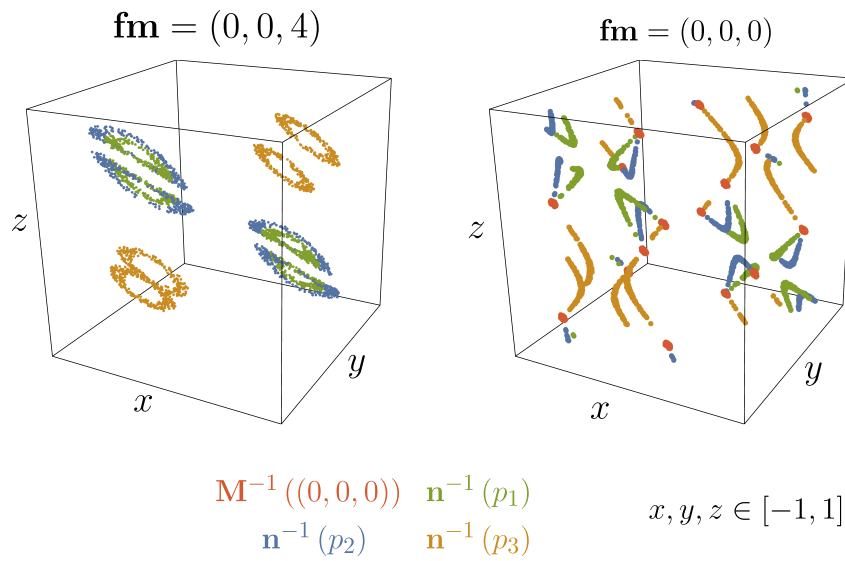


Figure 3.55.: Preimages of several image points under the directorfield \mathbf{n} of \mathbf{M} , as determined by a graphical Monte Carlo method. (a) In the case of a large ferromagnetic component the preimages of p_1 , p_2 , and p_3 represent closed curves that are not linked with respect to each other. Accordingly, the Hopf index of the directorfield vanishes. (b) If the ferromagnetic component is zero, singularities are present, at which \mathbf{M} is zero and the directorfield is not well defined (red points). The preimages represent stripes between the singularities. Accordingly, the Hopf index cannot be calculated, as \mathbf{n} cannot be interpreted as map $S^3 \rightarrow S^2$.

The graphical determination of the Hopf index of \mathbf{n} was done as follows. We used the property that the Hopf index of a map $S^3 \rightarrow S^2$ is equal to the linking number of preimages $\mathbf{n}^{-1}(p_1)$ and $\mathbf{n}^{-1}(p_2)$ for given points $p_1, p_2 \in S^2$ in the image set [174, 182]. The Hopf index of \mathbf{M} turns out to be zero, if the uniform magnetization is large. In contrast, for vanishing uniform magnetization, the Hopf index cannot be determined, as the map is not defined on the whole three-sphere S^3 . For the numerical study, three points $\in S^2$ were defined such that $p_1 = \mathbf{n}(-0.23, -0.54, 0.34)$, $p_2 = \mathbf{n}(0.43, 0.14, -0.43)$, and $p_3 = \mathbf{n}(0.23, 0.54, 0.34)$. Furthermore, it was set $p_0 = (0, 0, 0)$. The preimages $\mathbf{n}^{-1}(p_1)$,

$\mathbf{n}^{-1}(p_2)$, and $\mathbf{n}^{-1}(p_3)$, as well as $\mathbf{M}^{-1}(p_0)$ were drawn with a computer program by means of the following Monte-Carlo approach. A small radius $\epsilon = 0.02$ was defined and random points x in a box were created, i.e., $x \in [-1, 1]^3$. Each point x was drawn, only if the image $\mathbf{n}(x)$ lay in a sphere around p with radius ϵ , i.e., $\mathbf{n}(x) \in K_\epsilon(p)$. The procedure stopped, when 1000 points were drawn. This provided a graphical illustration of the preimage of p .

Fig. 3.55 shows the preimages of the three points p_1 , p_2 , and p_3 under the map \mathbf{n} . If the uniform contribution \mathbf{fm} is large, the preimages represent circles and the linking numbers are zero. Accordingly, the map \mathbf{n} has Hopf index zero and represents the trivial element 0 in the group $\pi_3(S^2)$. Accordingly, the vectorfield \mathbf{n} is topologically trivial. In contrast, for vanishing uniform magnetization, the preimages do not represent closed curves but stripes between singularities. At specific points in the preimage set S^3 the vectorfield \mathbf{M} is zero (red points). The banana-like shape of the preimages may be understood as follows. At the points where $\mathbf{M} = 0$, the directorfield \mathbf{n} is not well defined. In particular, the directorfield is not defined on the whole set S^3 . Accordingly, the Hopf index is not the correct framework to classify the topology of the vectorfield \mathbf{n} , as the map \mathbf{n} does not map the whole three-sphere S^3 on S^2 . However, the stripe-like preimages, even though not carrying a Hopf charge, strongly indicate that the topology of \mathbf{n} may be non-trivial. They are akin to preimages of torons, which were discussed in related studies in Ref. [174].

3.3.7. The Conduction Electrons

In a theoretical study, we investigated the impact of $(\pi\pi 0)$ ground states on conduction electrons and their electronic structure. We therefore considered the Berry curvature of the band structure and the anomalous Hall effect in the presence of noncoplanar structures, noncollinear structures, and long-wavelength modulations.

The presentation is organized as follows. First, a short introduction to the Hall effect is given in Sec. 3.3.7.1. Second, it was established in Sec. 3.3.7.2, that a finite Berry curvature may be caused by noncoplanar $(\pi\pi 0)$ structures. Third, it was discussed in Sec. 3.3.7.3 that the Berry curvature may become finite in all commensurate $(\pi\pi 0)$ structures, when a ferromagnetic component, as caused by a magnetic field, is added. Fourth, it was found in Sec. 3.3.7.4 that a topological Hall effect may be caused by specific $(\pi\pi 0)$ magnets with an incommensurate superstructure.

3.3.7.1. Introduction on the Hall effect

In conventional conductors, the Hall resistivity ρ_{xy} typically depends linearly on external magnetic fields [183] if magnetic order is absent. In ferromagnetic conductors, the Hall signal is often strongly enhanced by an additional contribution, which is commonly referred to as anomalous Hall effect [184]. Pugh and Lippert [185] established an empirical relation, which accounts for the two effects and applies to a broad range of materials:

$$\rho_{xy} \sim R_0 \cdot H_z + R_s M_z \quad (3.56)$$

This additional contribution depending linearly on the net magnetization may be referred to as ordinary anomalous Hall effect. Accordingly, in conventional antiferromagnets with zero net magnetization, no such ordinary anomalous Hall effect is expected. An ordinary anomalous Hall effect in antiferromagnets may arise, when a magnetic field induces a net magnetization.

For a long time, it was assumed, that additional Hall signals arising due to magnetic order may only be caused by a finite net magnetization. Recently, several cases were reported, where an anomalous Hall effect may arise, which does not scale linearly with the net magnetization. A prominent example is the topological Hall effect ρ_{xy}^{top} [9], which was observed in the Skyrmion lattice phase of MnSi [6]. This additional contribution to the Hall effect arises due to the emergent electrodynamics [10], which is related to the nontrivial topology of the Skyrmion lattice.

Furthermore, it has been noticed that an anomalous Hall effect may especially be hosted in antiferromagnets, which are noncoplanar [145]. Here, additional contributions

to the Hall effect may arise due to Berry phases, which are related to the tilting of spins [145, 186, 187]. As pointed out in Ref. [163], this effect occurs in antiferromagnets, when symmetries, which typically force the Berry curvature of the electronic structure (cf. Ref. [117]) and hence the intrinsic anomalous Hall effect to vanish, are absent. Predicted was an anomalous Hall effect, which is related to this absence of symmetries, in the noncollinear magnetic phase of Mn_3Ir [163]. Experimentally, this type of anomalous Hall effect was observed recently in the related compounds Mn_3Sn [188] and Mn_3Ge [189].

3.3.7.2. Anomalous Hall Effect in the Presence of Noncoplanar ($\pi\pi 0$) Antiferromagnetism

To simulate the transport properties of HoCu or isomorphous compounds in the presence of noncoplanar ($\pi\pi 0$) order, a simple theoretical model was considered. In this model, the localized rare-earth moments form a static magnetic ground state representing the commensurate structure $t1$ (cf. Tab. 3.1). The conduction electrons are described in terms of a s -band tight-binding model. They can hop on a sc lattice and the interaction with the localized f -electron spins are described in terms of a local field.

The model, which is introduced further below, was solved (i) without any distortion and (ii) with an anisotropic lattice distortion. The distortion turned out to be crucial for the topological properties of the electronic structure. Our study on a sc lattice is relevant for a variety of materials. In particular, we claim that DyCu and HoCu are physical realizations of this model. DyCu namely was reported to host the magnetic ground state $t1$ in one of its ordered phases [93]. Further, anisotropic magnetostriction, which may represent the anisotropic distortions in our model, was observed experimentally in DyCu [119]. The model may also be realized in phase IC1 of HoCu , as one of the local ($\pi\pi 0$) antiferromagnets of the ground state in phase IC1 represents the magnetic structure $t1$ (cf. Sec. 3.3.5.2). Anisotropic magnetostriction in HoCu was reported in Ref. [119]. Note that our study is reminiscent of the study in Ref. [190], which considered noncoplanar magnetic order on a distorted fcc lattice.

The results for the undistorted model (i) may be summarized as follows:

- In the presence of noncoplanar magnetic ($\pi\pi 0$) order the Berry curvature of the electronic structure becomes finite.
- A complex arrangement of magnetic monopoles emerges in the electronic structure. These singularities appear in pairs carrying opposite magnetic charges.
- Integrals over the Berry curvature vanish, which is reflected by vanishing Chern numbers. In particular, the intrinsic anomalous Hall effect vanishes.

The implications of a distortion along the cubic [111] direction (ii) may be summarized as follows:

- The arrangement of singularities in the electronic structure is distorted. Integrals over the Berry curvature become finite, which is reflected by finite Chern numbers. In particular, an anomalous Hall effect arises due to the finite Berry curvature. However, if magnetic domains are equally distributed, the anomalous Hall effect is zero in average.
- An orbital magnetization of the conduction electrons is induced by the distortion. Due to the orbital magnetization the two magnetic domains have different energy in magnetic fields, even if the net magnetization of rare-earth moments vanishes. Accordingly, the magnetic domain population is changed by a field and the anomalous Hall effect, which may be measured, becomes finite.

The presentation of our study is organized as follows. First, the specific Hamiltonian our model is based on is introduced. Second, the model is solved in the undistorted case. Therefore, the band structure and the Berry curvature are calculated. A complex arrangement of monopoles and antimonopoles is found. It is shown that Chern numbers as well as the orbital magnetization of conduction electrons vanish. Third, the effect of an anisotropic distortion arising in a field along [111] are discussed. The positions of monopoles and antimonopoles are investigated. Implications on Chern numbers, orbital magnetization, and transport properties are discussed in detail.

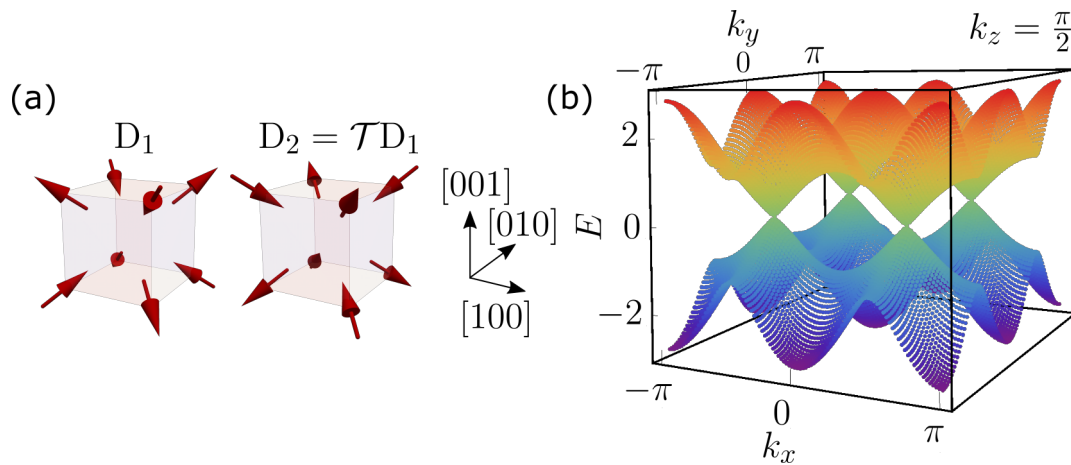


Figure 3.56.: Dirac cones in the electronic structure in the presence of a noncoplanar $(\pi\pi 0)$ ground state. (a) Noncoplanar magnetic ground state t1. There are two possible magnetic domains D_1 and D_2 that are mapped on each other by the time reversal operator \mathcal{T} . (b) The calculated dispersion relation, as shown in the plane $k_z = \frac{\pi}{2}$, features cones at singularities of the electronic structure.

The localized rare-earth moments in our model represent the static magnetic structure t1. Fig. 3.56 (a) shows a real-space picture of the ground state t1. There are two possibil-

ities, how t1 can be oriented on a sc lattice, representing the two domains D_1 and D_2 of the structure t1. The time reversal operator, which reverses the sign of each spin, maps one domain on the other, i.e., $D_2 = \mathcal{T}D_1$. Further, reflections at the planes $x = 0$, $y = 0$, or $z = 0$, respectively, map the domain D_1 on D_2 and vice versa. Accordingly, the two domains represent two different chiral domains of the structure t1.

As f -electrons in a rare-earth system are relatively localized and not primarily involved in conduction [191], the magnetic structure t1 is assumed to be static for this study. The itinerant electrons in our model participating in conduction are described by the following Hamiltonian [145]:

$$H = - \sum_{i,j} d_{ij} t_{ij} a_i^\dagger a_j - J_h \sum_i \mathbf{S}_i \cdot (a_i^\dagger \boldsymbol{\sigma} a_i). \quad (3.57)$$

The first term accounts for hopping between neighboring sites. The operators \hat{a}_i^\dagger and \hat{a}_i represent the two-component creation and annihilation operators for an electron on site i , and t_{ij} is the hopping transfer from site i to j . In the present study, hopping processes along $\langle 100 \rangle$ and $\langle 110 \rangle$ directions are considered. The second term, which describes the interaction between conduction electrons with the structure t1, is akin to the double exchange term introduced by Anderson [192]. $\boldsymbol{\sigma}$ represents the Pauli vector and J_h is the strength of the coupling between the conduction electrons and the rare-earth moments \mathbf{S} [186, 192, 193]. The parameters d_{ij} allow to introduce lattice distortions into the model further below (cf. Ref. [190]).

The Hamiltonian was solved by exact calculations that were carried out with Mathematica. The hopping parameters were therefore set to $t_{\langle 110 \rangle} = t_{\langle 100 \rangle} = 1$. These specific values were chosen arbitrarily. However, qualitatively similar results are obtained as long as $t_{\langle 110 \rangle}/t_{\langle 100 \rangle} > 0.6$. In contrast, for values $t_{\langle 110 \rangle}/t_{\langle 100 \rangle} < 0.6$ the topological properties of the electronic structure turn out to be much simpler. The specific case $t_{\langle 110 \rangle} = 0$, i.e., where hopping processes are considered only along fourfold directions, was discussed in Ref. [194] for the same static ground state t1.

In order to study the undistorted model, it was set $d_{ij} = 1$. Following previous studies [186, 190, 193], we assume that the coupling between conduction electrons and core electrons is relatively strong, i.e., $J_H \gg t_{ij}$. The magnetic ground state then acts as a local magnetic field on the conduction electrons and forces the spins of conduction electrons on site i parallel to the static field \mathbf{S}_i . Accordingly, the wave function for the electron spin on site i may be defined in terms of $|\chi_i\rangle = \left(\cos \frac{\theta_i}{2}, \sin \frac{\theta_i}{2} \cdot e^{i\Phi_i} \right)^T$, where θ_i and Φ_i are the

polar angles of the spin \mathbf{S}_i . In the limit $J_H \gg t_{ij}$ the Hamiltonian may be reduced to a single-component spin-less version with effective hopping transfer t_{ij}^{eff} [190]:

$$H = - \sum_{\langle i,j \rangle} t_{ij}^{\text{eff}} c_i^\dagger c_j. \quad (3.58)$$

The creation and annihilation operators c_i^\dagger and c_j are scalar and the effective transfer is given by [192]:

$$\begin{aligned} t_{ij}^{\text{eff}} &= d_{ij} t_{ij} \cdot \langle \chi_i | \chi_j \rangle = \\ &= d_{ij} t_{ij} \left(\cos \frac{\theta_i}{2} \cos \frac{\theta_j}{2} + \sin \frac{\theta_i}{2} \sin \frac{\theta_j}{2} \exp[-i(\Phi_i - \Phi_j)] \right). \end{aligned} \quad (3.59)$$

The Hamiltonian can be transformed into momentum space by setting [150, 190]:

$$\begin{aligned} c_i^\dagger &= \frac{1}{\sqrt{N}} \sum_{\mathbf{k}}^{\text{B.Z.}} \exp(-i\mathbf{k} \cdot \mathbf{R}_i) c_{\mathbf{k}}^\dagger \\ \Rightarrow H &= \sum_{\alpha, \beta} c_{\alpha, \mathbf{k}}^\dagger c_{\beta, \mathbf{k}} H_{\alpha\beta}(\mathbf{k}), \end{aligned} \quad (3.60)$$

where the indices $\alpha, \beta = 1, \dots, 4$ represent the four spin sub-lattices of t1. $H_{\alpha, \beta}$ is a Hermitean 4×4 matrix and has the shape:

$$H(\mathbf{k}) = \begin{pmatrix} 0 & f_{12}(\mathbf{k}) & f_{13}(\mathbf{k}) & f_{14}(\mathbf{k}) \\ \overline{f_{12}}(\mathbf{k}) & 0 & f_{23}(\mathbf{k}) & f_{24}(\mathbf{k}) \\ \overline{f_{24}} & \overline{f_{23}} & 0 & f_{34}(\mathbf{k}) \\ \overline{f_{14}} & \overline{f_{13}} & \overline{f_{12}} & 0 \end{pmatrix}. \quad (3.61)$$

The entries are given by:

$$\begin{aligned} f_{ij}(\mathbf{k}) &= \left[\left(\exp(i\mathbf{k} \cdot \boldsymbol{\lambda}_{ij}^a) + \exp(-i\mathbf{k} \cdot \boldsymbol{\lambda}_{ij}^a) \right) + \right. \\ &\quad \left. + \sum_{\lambda} \left(\exp(i\mathbf{k} \cdot \boldsymbol{\lambda}_{ij}^b) + \exp(-i\mathbf{k} \cdot \boldsymbol{\lambda}_{ij}^b) \right) \right] \cdot t_{ij}^{\text{eff}}, \end{aligned} \quad (3.62)$$

with the exchange paths $\boldsymbol{\lambda}_{12}^a = \boldsymbol{\lambda}_{34}^a = \hat{e}_1$, $\boldsymbol{\lambda}_{14}^a = \boldsymbol{\lambda}_{23}^a = \hat{e}_2$, $\boldsymbol{\lambda}_{13}^a = \boldsymbol{\lambda}_{24}^a = \hat{e}_3$, $\boldsymbol{\lambda}_{12}^{b1} = \boldsymbol{\lambda}_{34}^{b1} = \hat{e}_2 + \hat{e}_3$, $\boldsymbol{\lambda}_{12}^{b2} = \boldsymbol{\lambda}_{34}^{b2} = \hat{e}_2 - \hat{e}_3$, $\boldsymbol{\lambda}_{13}^{b1} = \boldsymbol{\lambda}_{24}^{b1} = \hat{e}_1 + \hat{e}_2$, $\boldsymbol{\lambda}_{12}^{b2} = \boldsymbol{\lambda}_{34}^{b2} = \hat{e}_1 - \hat{e}_2$, $\boldsymbol{\lambda}_{14}^{b1} = \boldsymbol{\lambda}_{23}^{b1} = \hat{e}_1 + \hat{e}_3$, and $\boldsymbol{\lambda}_{14}^{b2} = \boldsymbol{\lambda}_{23}^{b2} = \hat{e}_1 - \hat{e}_3$.

The eigenvalue problem $H(k_x, k_y, k_z)$ was solved with Mathematica. As the matrix is Hermitean, the eigenvalues are real. Two energy bands $E_l(\mathbf{k}) = E_{1/2}(\mathbf{k})$ and $E_u(\mathbf{k}) = E_{3/4}(\mathbf{k})$ were found, both of which are doubly degenerate. Mathematica provided continuous bands $|v_{n, \alpha}\rangle := v_{n, \alpha}(\mathbf{k})$ ($1 \leq n, \alpha \leq 4$) as the solutions of the eigenvalue problem. An

orthonormal basis $|u_{n,\alpha}\rangle$ ($1 \leq n, \alpha \leq 4$) was constructed by the Gram-Schmidt process. There are singularities in the band structure, as expected for a Hermitian matrix with three variables [164].

As explained in the following, the band $|v_1\rangle$ features a complex arrangement of singularities carrying magnetic charges. In contrast, the band $|v_2\rangle$ is presumably topologically trivial, as no numerical evidence for a finite Berry curvature of the second band was found. In the following, the topological properties of $|v_1\rangle$ are discussed for the magnetic domain D_1 . Impacts of domain effects are discussed further below.

The band $|v_1\rangle$ has in total 40 singularities in the first Brillouin zone. Fig. 3.57 (a) shows the distribution of these singularities. In the first octant of the first Brillouin zone, i.e., $\{(k_x, k_y, k_z) : k_x, k_y, k_z > 0\}$, there are five singularities. Four of them are at the positions $\mathbf{p}_i \in \left\{ \left(\frac{\pi}{2}, \frac{\pi}{2}, \frac{\pi}{2} \right) + \frac{\pi}{6} \cdot \delta_i, 1 \leq i \leq 4 \right\}$, with $\delta_1 = (1, 1, 1)$, $\delta_2 = (-1, -1, 1)$, $\delta_3 = (1, -1, -1)$, and $\delta_4 = (-1, 1, -1)$, representing the corner sites of a tetrahedron. They are sources of positive magnetic charges as seen further below. In the center of the tetrahedron, at the position $\mathbf{p}_5 = \left(\frac{\pi}{2}, \frac{\pi}{2}, \frac{\pi}{2} \right)$, there is a singularity carrying a negative charge. The positions of the other 35 singularities in the first Brillouin zone are obtained from $\mathbf{p}_1, \dots, \mathbf{p}_5$ via reflections M_x, M_y , and M_z , at the planes $x = 0, y = 0$, and $z = 0$. Each reflection maps monopoles on antimonopoles and vice versa. Thus, in total there are 20 monopoles and 20 antimonopoles in the first Brillouin zone. At each singularity, the two energy bands E_u and E_o touch at a single point featuring a cone like shape. Fig. 3.56 (b) illustrates this, showing the dispersion relation in the plane $k_z = \frac{\pi}{2}$ containing four singularities.

In order to investigate the topology of the band structure, the vector potential $\mathbf{A}_1(\mathbf{k}) := \sum_{\alpha} \langle u_{1,\alpha} | \nabla | u_{1,\alpha} \rangle$ and the Berry curvature $\Omega_1(\mathbf{k}) := \nabla_{\mathbf{k}} \times \mathbf{A}_1(\mathbf{k})$ [117, 186, 190] were calculated by means of Mathematica.

The magnetic charges of the singularities were determined by numerical integration with a radius $\rho = 0.15$. In the first octant it was obtained:

$$Q(\mathbf{q}) = \frac{1}{4\pi i} \int_{\partial K_{\rho}(\mathbf{q})} d\mathbf{S} \cdot \Omega = \begin{cases} +1, & \mathbf{q} = \mathbf{p}_1, \mathbf{p}_2, \mathbf{p}_3, \mathbf{p}_4 \\ -1, & \mathbf{q} = \mathbf{p}_5 \end{cases} . \quad (3.63)$$

Further, numerical integration with $\rho = 0.1$ showed that the magnetic charges are related to finite winding numbers:

$$W(\mathbf{q}) = \frac{1}{4\pi i} \int_{\partial K_{\rho}(\mathbf{q})} d\mathbf{S} \cdot \mathbf{b} = \begin{cases} +1, & \mathbf{q} = \mathbf{p}_1, \mathbf{p}_2, \mathbf{p}_3, \mathbf{p}_4 \\ -1, & \mathbf{q} = \mathbf{p}_5 \end{cases} , \quad (3.64)$$

where $b^i = \sum_{i,j,k} \frac{1}{|\Omega|^3} \epsilon_{ijk} \Omega \cdot (\partial_j \Omega \times \partial_k \Omega)$.

Chern numbers were calculated by integration over two-dimensional slices through the Brioullin zone [3, 164]:

$$\gamma(k_z) := \frac{1}{2\pi i} \int_{[-\pi, \pi]^2} d^2\mathbf{k} \Omega(\mathbf{k}) \cdot \hat{e}_z \quad (3.65)$$

Fig. 3.57 (b) shows the results of the numerical integration. The vanishing Chern numbers in the absence of a distortion ($d = 1$) reflect the high symmetry of the monopole-antimonopole distribution. As the arrangement is symmetric under reflections M_x , M_y , and M_z , the magnetic flux penetrating a slice through the Brioullin zone vanishes implying vanishing Chern numbers. This absence of any finite Chern numbers also implies that three-dimensional integrals over the Berry curvature vanish. We confirmed this by numerical integration. In particular, no anomalous Hall effect due to Berry phases is expected. It was confirmed further by numerical integration, that the orbital magnetization [117] vanishes, if distortions are absent.

In the following, the implications of a lattice distortion along [111] are discussed. The distortion may arise due to uniaxial stress, or anisotropic magnetostriction caused by a field along [111]. Experimental evidence for this type of distortion was reported in Ref. [119]. The distortion does not have large effects on hopping processes along fourfold directions, as a distortion along [111] affects all $\langle 100 \rangle$ directions in the same way. In contrast, there are two possibilities how $\langle 110 \rangle$ bonds may be oriented with respect to the [111] direction. Three $\langle 110 \rangle$ directions are perpendicular to [111], the other ones are not perpendicular. An anisotropic distortion should have a different effect on the two types of $\langle 110 \rangle$ bonds. Hence, for the first set of (perpendicular) directions it is set $d_{\langle 110 \rangle, \perp} = 0.9$, for the other $\langle 110 \rangle$ bonds it is set $d = 1$, in order to account for the distortion (cf. Ref. [190]).

Due to this distortion, the positions of the monopoles and antimonopoles are shifted, as explained in the following. The positions of the 40 singularities in the first Brillouin zone without any distortion, i.e., $d = 1$ may be summarized as follows:

$$q_0(ijk) = \left((-1)^i \frac{\pi}{2}, (-1)^j \frac{\pi}{2}, (-1)^k \frac{\pi}{2} \right) \quad (3.66)$$

$$p_0(ijk, n) = q_0(ijk) - \text{sgn}(Q_{q_0(ijk)}) \delta_n \cdot \frac{\pi}{6} \quad (3.67)$$

with $i, j, k \in \{0, 1\}$, $n \in \{1, 2, \dots, 4\}$. The triplets q_0 represent the positions of the center-positions of the tetrahedrons and the triplets p_0 represent the positions of the edges of the tetrahedron.

In the presence of the distortion $d = 0.9$, the singularities were shifted to the positions:

$$q_1(ijk) = q_0(ijk) - \text{sgn}(Q_{q_0(ijk)}) \cdot \xi_1 \cdot (1, 1, 1) \quad (3.68)$$

$$p_1(ijk, n) = p_0(ijk, n) + \text{sgn}(Q_{q_0(ijk)}) \sigma_n \quad (3.69)$$

where $\sigma_1 = \xi_2 \cdot (1, 1, 1)$, $\sigma_2 = \xi_3 \cdot (\frac{1}{4}, \frac{1}{4}, -1)$, $\sigma_3 = \xi_3 \cdot (-1, \frac{1}{4}, \frac{1}{4})$, and $\sigma_4 = \xi_3 \cdot (\frac{1}{4}, -1, \frac{1}{4})$ with $\xi_1 \approx 0.131$, $\xi_2 \approx 0.085$, and $\xi_3 \approx 0.114$. Due to this distortion the parity symmetries are broken, i.e., monopoles and antimonopoles are not mapped on each other any more by reflections M_x , M_y and M_z . Hence, the monopole-antimonopole pairs are split up. This is also reflected by finite Chern numbers. Fig. 3.57 (b) shows the Chern numbers in the distorted case ($d = 0.9$) as obtained from numerical integration. The schematic picture shows the z -coordinates of the distorted singularities and the Chern numbers are clearly related to this distortion.

The Chern numbers $\gamma(k_z)$ may also be inferred directly from the z -coordinate distribution of the singularities by means of the following variation of Stoke's law:

$$\gamma(k_z) = \sum_{k < k_z} Q(k) - \sum_{k > k_z} Q(k). \quad (3.70)$$

Hence, the Chern number $\gamma(k_z)$ represents the sum of all charges in the first Brillouin zone at positions $k < k_z$ minus the sum of all charges at positions $k > k_z$. This variation of Stoke's law was derived by basic vector analysis calculations in Sec. A.3.

This breakup of monopole antimonopole pairs has a vast impact on the topological properties of the system. The finite Chern numbers in the presence of anisotropic distortions suggest that three dimensional integrals over the Berry curvature may possibly be finite. As shown in the following, the transverse conductivity for field along [111], which is related to an integral over the Berry curvature [195], is finite:

$$\sigma_{xy} = -\frac{e^2}{\hbar \cdot (2\pi)^2} \int_{\text{BZ}} d^3\mathbf{k} f(E(\mathbf{k})) \cdot \Omega^{(111)}(\mathbf{k}). \quad (3.71)$$

In the zero temperature limit the Fermi-Dirac distribution is given by a step function:

$$W(E) = \frac{1}{\exp\left(\frac{E-\mu}{k_B T}\right) + 1} \sim \theta(E_F - E). \quad (3.72)$$

The integral Eq. (3.71) was calculated numerically for a Fermi level $E_F \approx -2.6$, which approximately corresponds to the case of half band filling. Therefore, we neglected the second band entirely, which is topologically trivial. The case of quarter filling, which corresponds to equal filling of both bands, would give qualitatively similar results. Nu-

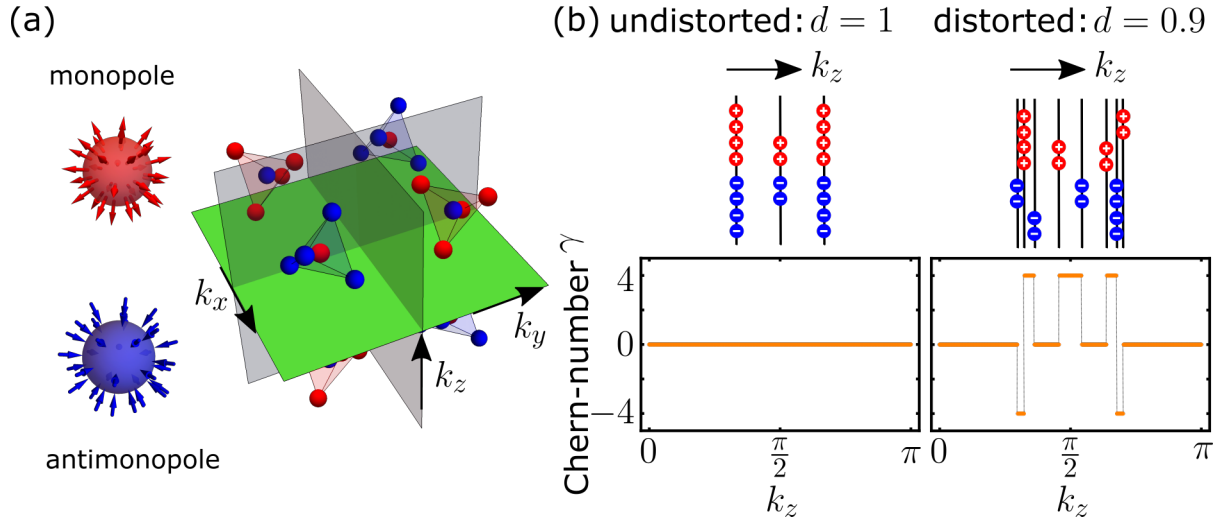


Figure 3.57.: Non-trivial Chern numbers arising due to the distortion of monopoles and anti-monopoles. (a) There are 40 singularities in the first Brillouin zone, 20 of them with positive, 20 with negative magnetic charge. In each octant, four singularities form a tetrahedron. In the center of the tetrahedron there is a singularity with opposite magnetic charge. (b) In the undistorted model ($d = 1$) all Chern numbers $\gamma(k_z)$ vanish, as shown by numerical integration. In the distorted model ($d = 0.9$) the monopole and antimonopole pairs break up. Accordingly, finite Chern numbers $\gamma(k_z)$ were obtained by numerical integration. The finite Chern numbers $\gamma(k_z)$ reflect the distribution of z coordinates of the distorted singularities and follow a variation of Stoke's law for Chern numbers, as explained in the text.

merical integration in the distorted case ($d = 0.9$) yields $\sigma_{xy}^{D_1} \approx (-0.11 \pm 0.02) \cdot e^2/4h\pi^2$ for the magnetic domain D_1 . For the second domain, the sign is opposite, i.e., $\sigma_{xy}^{D_2} \approx (+0.11 \pm 0.02) \cdot e^2/4h\pi^2$. Hence, in a situation where magnetic domains are equally populated, no anomalous Hall effect is obtained.

However, as shown in the following, the two magnetic domains have different energies due to an orbital magnetization of the conduction electrons. The orbital magnetization caused by the band structure may be calculated as follows [117]:

$$\begin{aligned} \mathbf{M}_{\text{orb}} = & -\frac{ie}{2\hbar} \sum_{n,\alpha} \int d^3k [\langle \partial_{\mathbf{k}} u_{n,\alpha} | \times (H - E_n) | \partial_{\mathbf{k}} u_{n,\alpha} \rangle + \\ & + 2(E_n - E_F) \langle \partial_{\mathbf{k}} u_{n,\alpha} | \times | \partial_{\mathbf{k}} u_{n,\alpha} \rangle]. \end{aligned} \quad (3.73)$$

Numerical integration revealed $\mathbf{M}_{\text{orb}}^{D_1} \approx -\frac{e}{2\hbar} \cdot 0.236 \cdot (1, 1, 1)$ in the first domain and $\mathbf{M}_{\text{orb}}^{D_2} = -\mathbf{M}_{\text{orb}}^{D_1}$ in the second domain. Hence, the two domains have different energies in a magnetic field $\parallel (1, 1, 1)$. Accordingly, the magnetic domains may be manipulated by magnetic fields, even though the net magnetization of the rare-earth moments vanishes (cf. Ref. [165]). In particular, an anomalous Hall effect due to the Berry curvature emerges.

The prediction of an orbital magnetization arising due to the band structure is of

particular interest. A proper theoretical treatment of orbital magnetization has long been a riddle [117] and was solved only recently [196–198].

To probe our study, we suggest to measure the anomalous Hall effect of the compounds DyCu and HoCu in the magnetically ordered regime. We further predict a dependence of the Hall effect on uniaxial pressure. In particular, we suggest to apply a tiny magnetic field along a threefold direction, in order to remove one of the two chiral magnetic domains. By means of uniaxial pressure along the same threefold axis the size of the anomalous Hall effect may be tuned.

3.3.7.3. Anomalous Hall Effect in the Presence of Noncollinear ($\pi\pi 0$) Antiferromagnetism

In the following, it is established that also noncollinear ($\pi\pi 0$) structures may display a finite Berry curvature and an anomalous Hall effect, which is not ordinary. The Berry curvature may namely become finite, when a ferromagnetic component, as caused by a magnetic field, is added. The mechanism we describe may possibly arise in each of the four antiferromagnets s2, s4, d2, and d5, once small fields are applied. In t2 the Berry curvature may be finite even at zero magnetic field. The impact of a small magnetic field on the magnetic ground states may be complicated and depends strongly on the magnetocrystalline anisotropies [165]. In the following, it is assumed that an applied magnetic field simply adds a tiny ferromagnetic component to the ground states leading to a tiny rotation of the magnetic moments towards the field direction. The discussion is closely related to the study in Ref. [163].

In the presence of collinear antiferromagnetic order in a centrosymmetric crystal, the Berry curvature Ω and hence the intrinsic anomalous Hall effect vanish (cf. Ref. [163]). The centrosymmetry namely implies that $\Omega(\mathbf{k}) = \Omega(-\mathbf{k})$. As a collinear antiferromagnet is bipartite, the combination of time reversal \mathcal{T} and a translation $T_{\mathbf{d}}$ represents a good symmetry implying that $\Omega(\mathbf{k}) = -\Omega(-\mathbf{k})$. Taken together the Berry curvature vanishes in collinear antiferromagnets with centrosymmetry. However, when the $\mathcal{T}T_{\mathbf{d}}$ symmetry is broken the Berry curvature may possibly become finite, as explained in the following.

In the noncoplanar antiferromagnet t2 the operator $\mathcal{T}T_{\mathbf{d}}$ does not describe a good symmetry (cf. Sec. 3.3.6.1). The argument above, which showed that the Berry curvature vanishes for collinear antiferromagnets, does not hold true for t2, as $\mathcal{T}T_{\mathbf{d}}$ is not a good symmetry. Hence, the Berry curvature may possibly be finite for the structure t2 even at zero magnetic field. There are other symmetry operators, which may, when acting on t2, represent in combination with time reversal good symmetries and which may possibly imply that the Berry curvature vanishes at zero magnetic field. However, the type of

interactions determine, whether such putative combined operators represent good symmetries. Hence, if other interactions such as spin-orbit coupling are not invariant under these operators, the Berry curvature Ω may possibly become finite (cf. Ref. [163]). A proper treatment of spin-orbit coupling would require a detailed description of the orbitals, which is beyond the scope of this thesis. However, we point out that the Berry curvature and possibly also the intrinsic anomalous Hall effect may be finite for the structure t2 at zero magnetic field.

In the bipartite, collinear antiferromagnets s2 and s4, $\mathcal{T}T_{\mathbf{d}}$ is a good symmetry at zero magnetic field forcing the Berry curvature to vanish. However, once a magnetic field is applied and a ferromagnetic component is added, the structures become noncollinear and the combined symmetry $\mathcal{T}T_{\mathbf{d}}$ is broken. Accordingly, the Berry curvature may possibly be finite in magnetic fields. Again, the type of interactions determine, whether other putative combined operators represent good symmetries, which may force the Berry curvature to vanish.

In the coplanar antiferromagnets d2 and d5, $\mathcal{T}T_{\mathbf{d}}$ is a good symmetry in zero magnetic field, even though the structures are noncollinear. Once a ferromagnetic component is added, the combined symmetry $\mathcal{T}T_{\mathbf{d}}$ is again broken. Accordingly, the Berry curvature may possibly be finite in magnetic fields. Again, the type of interactions determine, whether putative combined operators represent good symmetries, which may force the Berry curvature to vanish.

3.3.7.4. Topological Hall Effect

In this section it is established that $(\pi\pi 0)$ structures with an incommensurate superstructure may possibly lead to a topological Hall effect in magnetic fields. As the main result it is found that a variation of the magnetic structure \mathcal{M}_1 can cause a topological Hall effect.

In the following, a specific $(\pi\pi 0)$ ground state with incommensurate superstructure is proposed. It is then argued that in the presence of a field this ground state may cause a topological Hall effect via specific intra-sublattice hopping processes. As specific magnetic ground state we consider the directorfield of the following vectorfield:

$$\begin{aligned} \mathbf{m}_{\mathcal{M}_2}(\mathbf{R}) &= m_0 \cdot \hat{e}_z + m_1 \cdot \left[(100)^T \cos(\mathbf{k}_{2,y}^{ic} \cdot \mathbf{R}) + (001)^T \cos\left(\mathbf{k}_{1,y}^{ic} \cdot \mathbf{R} + \frac{\pi}{2}\right) + \right. \\ &\quad \left. + (010)^T \cos(\mathbf{k}_{3,x}^{ic} \cdot \mathbf{R}) + (001)^T \cos\left(\mathbf{k}_{1,x}^{ic} \cdot \mathbf{R} + \frac{\pi}{2}\right) \right] \end{aligned} \quad (3.74)$$

$$= m_0 \cdot \hat{e}_z + ic_{\mathcal{M}_1}(\mathbf{R}) . \quad (3.75)$$

This structure \mathcal{M}_2 represents a variation of the ground state \mathcal{M}_1 (cf. Sec. 3.3.6.3). The major difference between the two structures is that \mathcal{M}_2 contains ferromagnetic commensurate components, whereas \mathcal{M}_1 contains an antiferromagnetic commensurate component. A ferromagnetic component may, for instance, be caused by a magnetic field.

The structure \mathcal{M}_2 still consists of four sublattices, on which the structure represents Skyrmions, as is the case for \mathcal{M}_1 . However, the winding number (cf. Ref. [6, 170]) has the same sign now on each sublattice:

$$\int_{U_0(L)} \frac{1}{4\pi} \mathbf{n} (\partial_x \mathbf{n} \times \partial_y \mathbf{n}) dx dy = +1. \quad (3.76)$$

It is hard to theoretically treat the transport properties for such complex ground states having a large unit cell. For the structure \mathcal{M}_2 , there are inter-sublattice and intra-sublattice hopping processes of the conduction electrons that have to be taken into account. The inter-sublattice processes are highly discontinuous. They cannot be treated in this thesis, as they lead to eigenvalue problems with matrices containing $\approx 50^2$ entries.

However, intra-sublattice hopping-processes may give rise to a topological Hall effect, as argued in the following. In a situation where all hopping processes are directed along threefold directions all electrons stay on the same sublattice L_1 , L_2 , L_3 , or L_4 , respectively. It may be assumed that the spins of conduction electrons, when moving through the sample, adiabatically follow the Skyrmion spin-textures on the sublattices [9]. Due to the finite winding density of the Skyrmion lattice, an effective field B_{eff} is acting on the conduction electrons [9].

The effective field leads to a transverse conductivity (cf. Ref. [9]):

$$\Delta\rho_{xy} = PR_0 B_{\text{eff}}. \quad (3.77)$$

The effective field B_{eff} can be estimated by means of $B_{\text{eff}} = \Phi_0 \Phi$, where $\Phi_0 = \frac{h}{e}$ is the flux quantum, Φ the Skyrmion density, P the local spin polarization of the conduction electrons, and R_0 the normal Hall coefficient [9]. Hence, intra-sublattice hopping may lead to a topological Hall effect. Note, that there may be magnetic domains with different chirality of the magnetic ground state. However, the direction of the magnetic field determines the sign of the winding number. Accordingly, the winding number is equal for other domains of the magnetic structure \mathcal{M}_2 .

3.4. The Compound TmCu

In the following, a microscopic study on the cubic antiferromagnet TmCu, the second of three RCu compounds, is presented. The compound features complex rare-earth magnetism and may possibly host magnetic ground states possessing non-trivial topology. Our study was inspired by the observation of a complex phase diagram and unconventional contributions to the Hall effect [118], which may possess topological origin (cf. Refs. [9, 109, 110]). Previous magnetic structure determinations were using neutron diffraction from polycrystalline samples [68]. As the main results of single crystal neutron diffraction we identified a variety of magnetic ground states, including multi- k structures and structures with a long wavelength in real-space exceeding 50 Å.

The presentation is organized as follows. First, an introduction to the literature on the compound is provided in Sec. 3.4.1. Second, magnetic ground states were investigated in zero magnetic field, which is presented in Sec. 3.4.2. Third, magnetic ground states were studied for fields along the three major cubic directions, which is presented in Sec. 3.4.2.

3.4.1. Introduction to TmCu

The compound TmCu may, similarly to HoCu, be a candidate material for hosting antiferromagnetic structures with non-trivial topology, even though the space group is centrosymmetric. The reasons are as follows. Complex magnetic phase diagrams suggest a multitude of competing interactions. The unconventional Hall effect, which was reported in Ref. [118], is clearly related to magnetic long-range order, but does not arise due to an ordinary anomalous Hall effect. When related to real-space Berry phases, the Hall effect may be indication of antiferromagnetic ground states with non-trivial topology (cf. Refs. [9, 109, 110]).

The compound TmCu crystallizes in the cubic CsCl structure with lattice constant 3.415 Å [71]. The tripositive rare-earth ions carry magnetic long-range order at temperatures below ≈ 8 K. The Tm^{3+} ions may be portrayed as localized magnetic moments, carrying the moment $\approx g_J \cdot \sqrt{J \cdot (J + 1)} = 7.57 \mu_B$, as inferred from Hund's rules ($L = 5$, $S = 1$, $J = 6$, and $g_J = \frac{7}{6}$ [30]). Complex magnetic phase diagrams evolve, as shown in Fig. 3.58 for the three major cubic directions and inferred from magnetization, ac susceptibility, and transport measured on single crystals (cf. Ref. [118]). The qualitative differences between the phase diagrams reflect the importance of cubic anisotropies. Critical fields are considerably smaller for fourfold directions than for twofold and threefold directions, suggesting a fourfold easy axis, which is in agreement with neutron spectroscopy studies (cf. Refs. [68, 84]).

In zero magnetic field, two magnetically ordered phases are established with transition temperatures $T_t = 6.7$ K and $T_N = 7.7$ K. Specific heat features signatures characteristic of first-order phase transitions at both temperatures T_t and T_N [68]. Susceptibility in zero magnetic field displays Curie-Weiss behavior with $\Theta \approx -8$ K [70], a value characteristic of a non-frustrated antiferromagnet. The inferred fluctuating moment amounts to $7.56 \mu_B$, which is close to the free-ion value of Tm^{3+} . Note, that the transition temperature T_N , which was reported in Ref. [70], had a too large value of 11 K.

Typical magnetization as a function of field features multiple steps and is akin to multi-step metamagnetism. Most notable is the unconventional behavior of the Hall effect, which was reported in Ref. [118]. In the magnetically ordered regime, the Hall resistivity ρ_{xy} as a function of field exhibits additional contributions, which are clearly related to magnetic long-range order, but do not depend linearly on the net magnetization, as characteristic of an ordinary anomalous Hall effect. The Hall effect may be related to Berry phases, caused by a magnetic ground state possessing non-trivial topology.

Magnetic structure determinations were carried out in the two ordered phases in zero field using neutron diffraction on polycrystalline samples [68]. At $T = 1.5$ K, in the lower-temperature phase, which is further below labeled phase C, a commensurate $(\pi\pi 0)$ structure with an ordered moment of $\approx 4.7 \mu_B$ was reported. The ground state was reported to be either a single- k structure, with magnetic moments pointing along the c -axis, i.e., $\theta = 0^\circ$, or a multi- k structure with the same structure factor featuring also the same diffraction pattern. The asymmetric broadening of a nuclear Bragg peak in this commensurate magnetic phase, which was confirmed by single crystal neutron measurements [199], was of the order of 0.7%. This may be indication that the magnetic structure is single- k , the moments being directed along a fourfold direction. In the second ordered phase just below the ordering temperature, which is further below labeled phase IC, incommensurate magnetic propagation vectors $(0.56, 0.5, 0)$, as well as commensurate propagation vectors $(0.5, 0.5, 0)$ were reported in Ref. [68]. As ground state a superposition of an antiferromagnetic amplitude modulation with a periodicity of ≈ 16 lattice parameters, as well as a commensurate contribution was suggested. The tetragonal distortion, as inferred from the asymmetric broadening of a nuclear Bragg peak, was smaller than in the commensurate phase, but still present. Studies using single-crystalline material confirmed the propagation vector $(0.56, 0.5, 0)$ [199], even though this description is insufficient, as explained in our study further below. Magnetic excitations in TmCu were studied using single crystal neutron spectroscopy, as reported in Ref. [199]. The quadrupolar interactions, which were thoroughly studied in TmCu by means of parastriction, magnetization, and neutron spectroscopy [84], are presumably of major importance for the understanding of magnetic order in TmCu [68, 84] and may possibly even be strong enough to compete with bilinear

exchange interactions [84]. In particular, the comparison with related isomorphous compounds may prove fruitful, such as TmZn [85, 87], where quadrupolar order was observed in combination with magnetic order, or TmCd [78, 83], where quadrupolar order was observed, but no magnetic order.

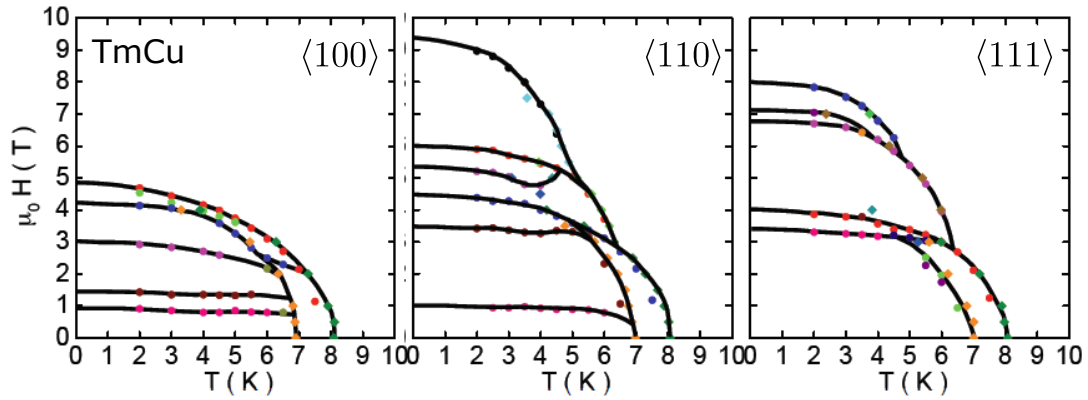


Figure 3.58.: Magnetic phase diagrams of TmCu for fields along the major cubic directions $\langle 100 \rangle$, $\langle 110 \rangle$, and $\langle 111 \rangle$. Data were inferred from field and temperature dependences of magnetization, ac susceptibility, and transport. The figure was taken from [118].

3.4.2. Magnetic Propagation Vectors in Zero Magnetic Field

To determine propagation vectors of the magnetic ground states at zero magnetic field, neutron diffraction of sample OFZ107-2-a was carried out at the time-of-flight diffractometer Wish [140].

The main results of these experiments may be summarized as follows:

- The magnetically ordered phases in zero magnetic field display variations of $(\pi\pi 0)$ antiferromagnetism.
- In phase C ($T < T_t \approx 6.7$ K [68]), the ground state represents a superposition of commensurate propagation vectors of the star $\langle \frac{1}{2} \frac{1}{2} 0 \rangle$. The ground state may be single- k , double- k , or triple- k .
- In phase IC ($T_t < T < T_N \approx 7.7$ K [68]), the ground state represents a superposition of incommensurate propagation vectors of the star $\langle \frac{1}{2} + \tau_1, \frac{1}{2}, \tau_2 \rangle$, where $\tau_1 = 0.06$ and $\tau_2 = 0.03$, and commensurate propagation vectors of the star $\langle \frac{1}{2} \frac{1}{2} 0 \rangle$. Note, however, that contributions due to commensurate propagation vectors are tiny.

For the experiments the sample was oriented such that the (111) plane corresponded to the scattering plane. Time-of-flight diffraction data were recorded in phase C at $T = 2$ K and in phase IC at 7.25 K. The data analysis followed the same procedure as in Sec. 3.3.4.3. Propagation vectors were inferred from the diffraction data by indexation of magnetic Bragg peaks. In the following, the indexation of magnetic peaks is illustrated in terms of the Bragg peaks that were detected in the vicinity of $(\frac{1}{2}, -\frac{1}{2}, 0)$ in the reciprocal space.

In phase C the recorded data feature commensurate Bragg peaks of the $\langle \frac{1}{2} \frac{1}{2} 0 \rangle$ star. Fig. 3.59 (a) shows the diffraction data in the vicinity of $(\frac{1}{2}, -\frac{1}{2}, 0)$ as recorded in phase C. The single magnetic Bragg peak at the commensurate position $(\frac{1}{2}, -\frac{1}{2}, 0)$ reflects $(\pi\pi 0)$ antiferromagnetism. Accordingly, the magnetic ground state represents a superposition of propagation vectors of the star $\langle \frac{1}{2} \frac{1}{2} 0 \rangle$, which is in excellent agreement with previous studies [68]. The integrated intensity of this commensurate magnetic Bragg peak is given by 5.85 ± 0.03 . As the $\langle \frac{1}{2} \frac{1}{2} 0 \rangle$ star possesses three different k -arms, the ground state in phase C may be single- k , double- k , or triple- k .

In phase IC the recorded data feature commensurate $(\pi\pi 0)$ reflections, as well as incommensurate satellites in the vicinity of $(\pi\pi 0)$ positions. As explained in the following, the data indicate, that the ground state in IC is a superposition of commensurate and incommensurate propagation vectors.

Fig. 3.59 (b) shows 9 Bragg peaks, which were observed in the vicinity of $(\frac{1}{2}, -\frac{1}{2}, 0)$. The Bragg peaks are located at the positions $(\frac{1}{2}, -\frac{1}{2}, 0)$, $(\frac{1}{2} \pm \tau_1, -\frac{1}{2}, \tau_2)$, $(\frac{1}{2} \pm \tau_1, -\frac{1}{2}, -\tau_2)$, $(\frac{1}{2}, -\frac{1}{2} \pm \tau_1, \tau_2)$, and $(\frac{1}{2}, -\frac{1}{2} \pm \tau_1, -\tau_2)$ with $\tau_1 = 0.06$ and $\tau_2 = 0.03$. The Bragg peak lo-

cated at the commensurate position may be indexed with the propagation vector $(\frac{1}{2}, \frac{1}{2}, 0)$. The Bragg peaks located at incommensurate positions may be indexed with propagation vectors of the star $\langle \frac{1}{2} - \tau_1, \frac{1}{2}, \tau_2 \rangle$.

Accordingly, the ground state in phase IC is a superposition of propagation vectors of the stars $\langle \frac{1}{2}, \frac{1}{2}, 0 \rangle$ and $\langle \frac{1}{2} - \tau_1, \frac{1}{2}, \tau_2 \rangle$. In particular, the ground state has a long-wavelength modulation of the order of $a/\tau_1 \approx 16 \cdot a$ in x -direction and of the order of $a/\tau_2 \approx 33 \cdot a$ in z -direction.

The eight Bragg peaks at incommensurate positions in IC have integrated intensities ranging from 0.43 ± 0.01 to 0.79 ± 0.01 . The integrated intensity of the commensurate peak is relatively weak and given by 0.04 ± 0.01 . Note, that the size of the incommensurate modulation is in agreement with the study by Morin [68], which reported propagation vectors $(\frac{1}{2} - 0.06, \frac{1}{2}, 0)$ as inferred from neutron powder diffraction. However, the direction of the incommensurate modulation is different.

The wave-vector star $\langle \frac{1}{2} - \tau_1, \frac{1}{2}, \tau_2 \rangle$ of the incommensurate propagation vector in phase IC has 12·2 different k -arms. Conjugated k -arms may be identified in terms of pairs, which we call Ω -arms. Accordingly, the $\langle \frac{1}{2} - \tau_1, \frac{1}{2}, \tau_2 \rangle$ star has 12 different Ω -arms, i.e., pairs of conjugated k -arms [56]. Note, that for the multi- k structures studied in this thesis, we do not distinguish between conjugated arms, as explained in Sec. 2.2. Four of the Ω -arms have a pair of Bragg peaks in the vicinity of the $(\frac{1}{2}, -\frac{1}{2}, 0)$ position. Accordingly, eight Q -positions associated with the $\langle \frac{1}{2} - \tau_1, \frac{1}{2}, \tau_2 \rangle$ star are located in the vicinity of $(\frac{1}{2}, -\frac{1}{2}, 0)$, all of which were observed in our experiments.

TmCu

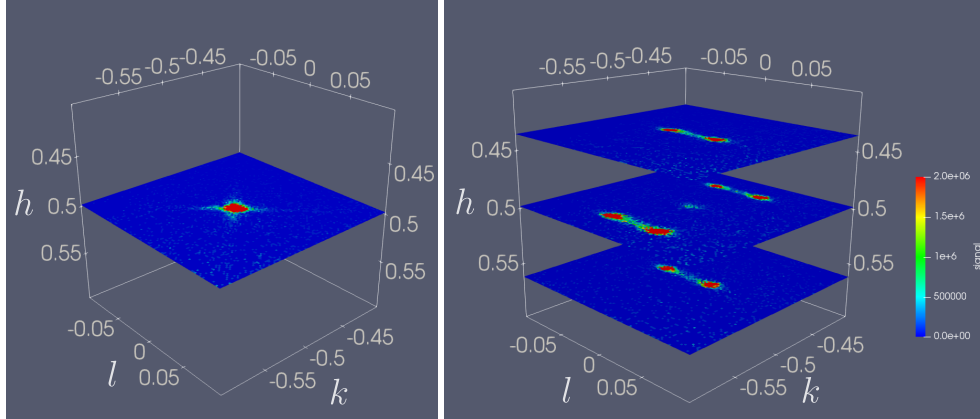
 $\mu_0 H = 0$ T(a) phase C
T = 2 K(b) phase IC
T = 7.25 K

Figure 3.59. Magnetic propagation vectors in the two ordered phases at zero magnetic field. The propagation vectors may be inferred by indexation of magnetic Bragg peaks. Shown are diffraction data as recorded in the vicinity of $(\frac{1}{2}, -\frac{1}{2}, 0)$. (a) Commensurate Bragg peak at $(\frac{1}{2}, -\frac{1}{2}, 0)$ reflecting commensurate $(\pi\pi 0)$ antiferromagnetism in phase C. The ground state in phase C has propagation vectors of the star $\langle \frac{1}{2}, \frac{1}{2}, 0 \rangle$. (b) Commensurate Bragg peak at $(\frac{1}{2}, -\frac{1}{2}, 0)$ as well as 8 incommensurate satellites, as observed in phase IC. The indexation of the magnetic Bragg peaks requires propagation vectors of the stars $\langle \frac{1}{2}, \frac{1}{2}, 0 \rangle$ and $\langle \frac{1}{2} - \tau_1, \frac{1}{2}, \tau_2 \rangle$, where $\tau_1 = 0.06$ and $\tau_2 = 0.03$. The ground state in IC is multi- k and has a long-wavelength modulation.

3.4.3. Neutron Diffraction in Magnetic Fields

Neutron diffraction in magnetic fields on sample OFZ107-2-a was carried out at the time-of-flight diffractometer Wish [140].

The main results of these experiments may be summarized as follows:

- In the $\langle 100 \rangle$ phase diagram (Fig. 3.60) the magnetic ground states may be characterized as follows. The magnetic ground state in X_I , X_{a1} , and X_{a2} represents a single- k ($\pi\pi 0$) antiferromagnet.
- The magnetic ground state in X_{c1} represents an antiferromagnet with propagation vectors of the star $\langle \frac{1}{2} - \delta, \frac{1}{2}, 0 \rangle$, where $\delta = 0.07$. Accordingly, the ground state has a long-wavelength modulation.
- In the $\langle 110 \rangle$ phase diagram (Fig. 3.63) the magnetic ground states may be characterized as follows. The magnetic ground state in M_I , M_{a1} , and M_{a2} represents a single- k ($\pi\pi 0$) antiferromagnet. The magnetic ground state in phase M_{b1} represents a superposition of propagation vectors of the stars $\langle \frac{1}{2}, \frac{1}{2}, 0 \rangle$, $\langle \frac{1}{2}, \frac{1}{2}, \frac{1}{7} \rangle$, $\langle \frac{1}{2}, \frac{1}{2}, \frac{2}{7} \rangle$, and $\langle \frac{1}{2}, \frac{1}{2}, \frac{3}{7} \rangle$. Accordingly, phase M_{b1} does not display a variation of ($\pi\pi 0$) antiferromagnetism.
- In the $\langle 111 \rangle$ phase diagram (Fig. 3.66) the magnetic ground states may be characterized as follows. The magnetic ground state in R_I and R_{a1} represents a single- k ($\pi\pi 0$) antiferromagnet. The magnetic ground state in R_{b1} , R_{b2} , and R_{b3} represents a superposition of propagation vectors of the stars $\langle \frac{1}{2}, \frac{1}{2}, 0 \rangle$ and $\langle \frac{1}{2} - \delta, \frac{1}{2}, 0 \rangle$, where $\delta = 0.07$. Accordingly, the magnetic ground state is multi- k and has a long-wavelength modulation.
- The regions X_I , X_{a1} , X_{a2} , M_I , M_{a1} , M_{a2} , R_I , and R_{a1} may belong to a single thermodynamic phase. The ground state in this phase is a single- k ($\pi\pi 0$) antiferromagnet. In particular, the ground state in phase C is a single- k ($\pi\pi 0$) antiferromagnet

Experiments were carried out with three different sample orientations. The three orientations were such that the scattering plane corresponded to the (001) plane (orientation O1), to the (0 $\bar{1}$ 1) plane (orientation O2), and to the (111) plane (orientation O3). In each orientation, magnetic fields were applied vertically. Accordingly, in orientation O1, O2, and O3 the magnetic field was directed along [001], [0 $\bar{1}$ 1], and [111], respectively. In each orientation, a field sweep was carried out, starting in phase C at 2 K after zfc. The three field sweeps may be labeled sweepO1, sweepO2, and sweepO3, respectively.

The $\langle 100 \rangle$, $\langle 110 \rangle$, and $\langle 111 \rangle$ phase diagrams, which were determined by Rahn (cf. Ref. [118]), are shown in Figs. 3.60, 3.63, and 3.66, respectively. The regions in this phase diagram were assigned colors and labels. The capital letters X , M , and R shall indicate, that magnetic fields are applied along a cubic edge, a cubic face diagonal, and a cubic

space diagonal, respectively. The regions in the $\langle 111 \rangle$ phase diagram will be referred to as "phases" or "phase pockets". Note, however, that these "phases" are not necessarily phases in a thermodynamic sense, i.e., they are not necessarily thermodynamically separated by phase transitions [139].

To determine field dependences of magnetic propagation vectors, time-of-flight diffraction data sets were recorded at discrete field values during the three sweeps sweepO1, sweepO2, and sweepO3, respectively. Each recorded data set contained diffraction intensities of a large number of Q -positions, which are related to the star $\langle \frac{1}{2} \frac{1}{2} 0 \rangle$. From each time-of-flight data set, magnetic propagation vectors were inferred by indexation of the magnetic Bragg peaks in the data set. In the following presentation, the determination of magnetic propagation vectors in orientation O1, in orientation O2, and in orientation O3 is illustrated by means of indexation of the Bragg peaks in the vicinity of $(\frac{1}{2}, \frac{1}{2}, 0)$, $(0, \frac{1}{2}, \frac{1}{2})$, and $(\frac{1}{2}, -\frac{1}{2}, 0)$, respectively. Integrated intensities and field dependences were inferred from the data sets by the same procedure, which was described in Sec. 3.3.4.3.

In orientation O1 time-of-flight data sets were recorded in phase X_I at the fields 0 T and 0.5 T, in phase X_{a1} at 1 T, 1.2 T, and 1.4 T, in phase X_{a2} at 2 T, in phase X_{b1} at 3.2 T and 4 T, in phase X_{c1} at 4.5 T, and in the field polarized state at 6 T.

In this orientation O1, the diffraction data permitted to study Bragg peak positions, which are related to the k -arm A_1^c of the $\langle \frac{1}{2} \frac{1}{2} 0 \rangle$ star, or positions, which are in the close vicinity of these Q -positions. Peak positions, which are related to the arms A_2^c and A_3^c , were not accessible in this orientation.

In the following, magnetic propagation vectors as a function of field, as inferred from sweepO1, are discussed. As established in the following, the magnetic ground state represents a commensurate $(\pi\pi 0)$ antiferromagnet in the regions X_I , X_{a1} , and X_{a2} . Note, that region X_I comprises phase C. As shown in this study, the regions X_I , X_{a1} , and X_{a2} presumably belong to a single thermodynamic phase. In this phase, the ground state is given by a single- k $(\pi\pi 0)$ antiferromagnet. In phase X_{c1} , the ground state has propagation vectors of the star $\langle \frac{1}{2} - \delta, \frac{1}{2}, 0 \rangle$, where $\delta \approx 0.07$. Accordingly, the ground state has a long-wavelength modulation. The ground state in X_{c1} may also have tiny contributions due to propagation vectors of the star $\langle \frac{1}{2}, \frac{1}{2}, 0 \rangle$. In phase X_{b1} magnetic scattering was vanishingly small at positions, which are related to the k -arm A_1^c , and at positions, which are close to this k -arm. Presumably, all magnetic intensities were at positions, which are related to the k -arms A_2^c and A_3^c , or at positions, which are located far away from the scattering plane.

In the following, the indexation of Bragg peaks is illustrated for some data sets, which were recorded by means of sweepO1. The corresponding positions in the phase diagram are represented by filled circles in Fig. 3.60. Fig. 3.61 illustrates distinctive changes of

magnetic propagation vectors during sweepO1. Shown are magnetic Bragg peaks, which were observed in the vicinity of $(\frac{1}{2}, \frac{1}{2}, 0)$. In phase X_I , the single Bragg peak at $(\frac{1}{2}, \frac{1}{2}, 0)$ reflects commensurate $(\pi\pi 0)$ antiferromagnetism (Fig. 3.61 (a)). The integrated intensity of the commensurate peak at $(\frac{1}{2}, \frac{1}{2}, 0)$ is given by 5.81 ± 0.03 . Similar diffraction patterns in phases X_{a1} and X_{a2} reflect commensurate $(\pi\pi 0)$ antiferromagnetism.

As shown in Fig. 3.61 (b), in phase X_{c1} at a field of 4.5 T Bragg peaks were observed at the incommensurate positions $(\frac{1}{2} \pm \delta, \frac{1}{2}, 0)$ and $(\frac{1}{2}, \frac{1}{2} \pm \delta, 0)$ with $\delta \approx 0.07$. The incommensurate splitting is suggestive of a long-wavelength modulation of the order of $a/\delta \approx 14 \cdot a$. Bragg peaks at those positions may be indexed by propagation vectors of the star $\langle \frac{1}{2} - \delta, \frac{1}{2}, 0 \rangle$. Weak intensity was observed at the commensurate peak position $(\frac{1}{2}, \frac{1}{2}, 0)$. The integrated intensities of the incommensurate satellites are ranging from 0.63 ± 0.01 to 1.18 ± 0.01 and the integrated intensity of the commensurate peak is given by 0.03 ± 0.01 .

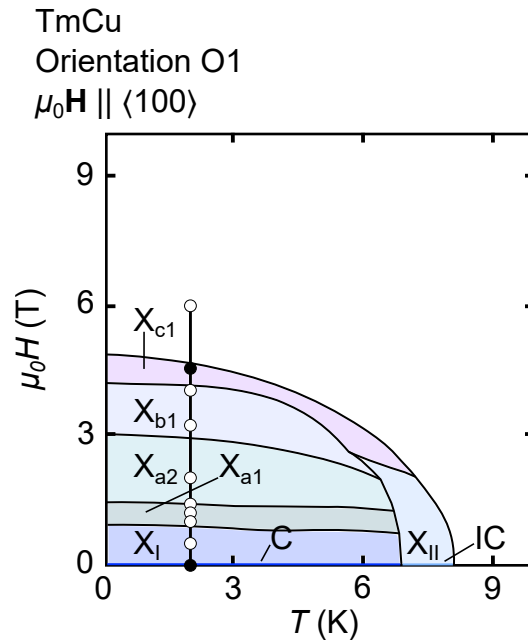


Figure 3.60.: Regions of the $\langle 100 \rangle$ phase diagram of TmCu. The phase diagram was determined by Rahn (cf. Ref. [118]). For this study the regions, which may possibly represent phase pockets, were labeled and filled with colors. The vertical line represents the field sweep, which was carried out for this study. Diffraction data were recorded at the points, which are indicated by circles. The filled circles indicate the data sets, for which diffraction data are presented further below.

In the following, integrated intensities as a function of field, as inferred from sweepO1, of Bragg peaks of the star $\langle \frac{1}{2} \frac{1}{2} 0 \rangle$ are presented. Fig. 3.62 shows field dependences of commensurate Bragg peaks, which are related to the k -arm A_1^c , as inferred from the field sweep in orientation O1. Shown are the normalized integrated intensities $i_q(B) = I_q(B)/I_q(0)$. As a function of field, the integrated intensities of all peaks decrease steeply

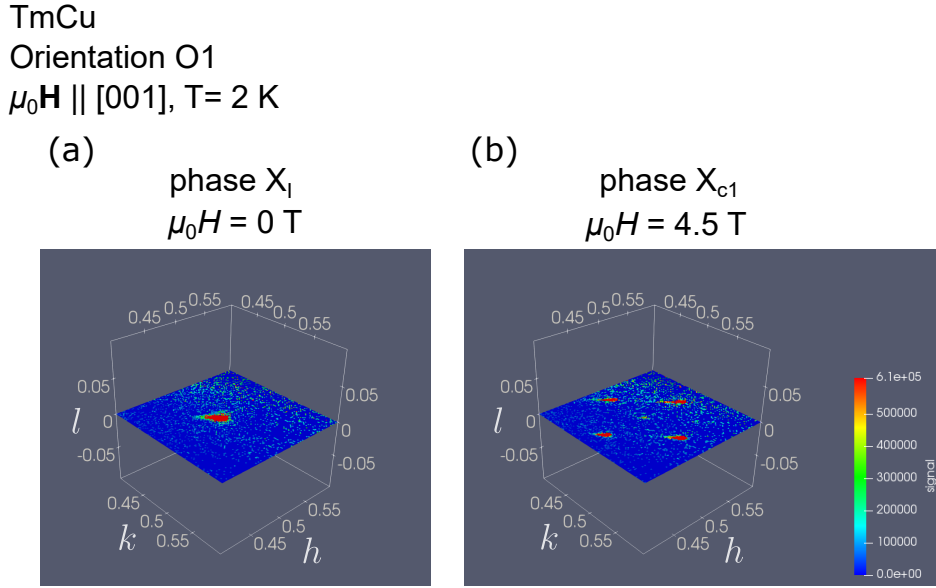


Figure 3.61.: Evolution of magnetic propagation vectors during sweep O1 in orientation O1. The indexation of magnetic Bragg peaks may be illustrated in terms of the Bragg peaks, which were observed in the vicinity of $(\frac{1}{2}, \frac{1}{2}, 0)$. Shown are the recorded data in the vicinity of $(\frac{1}{2}, \frac{1}{2}, 0)$. (a) Scattering intensity in phase X_I at 0 T. The single Bragg peak at $(\frac{1}{2}, \frac{1}{2}, 0)$ reflects commensurate $(\pi\pi 0)$ antiferromagnetism. (b) Scattering intensity intensity in X_{c1} at 4.5 T. The Bragg peaks at $(\frac{1}{2}, \frac{1}{2}, 0)$, at $(\frac{1}{2} \pm \delta, \frac{1}{2}, 0)$, and at $(\frac{1}{2}, \frac{1}{2} \pm \delta, 0)$ indicate that the ground state is a superposition of propagation vectors of the stars $\langle \frac{1}{2} \frac{1}{2} 0 \rangle$ and $\langle \frac{1}{2} - \delta, \frac{1}{2}, 0 \rangle$.

and vanish in the field range < 2 T. If the regions X_I , X_{a1} , and X_{a2} share the same ground state, the decrease of integrated intensities is due to a change of the magnetic domain populations. In particular, this decrease indicates, that either one or two k -arms of the star $\langle \frac{1}{2} \frac{1}{2} 0 \rangle$ may participate in phases X_I , X_{a1} , and X_{a2} . Accordingly, the ground state is either single- k or double- k , but not triple- k . Further below it is argued, that the ground state is most likely single- k .

Note, that in principle, this decrease of magnetic intensities might also arise due to a phase transition related to a change of the magnetic ground state. Note, however, that in this case phases X_I , X_{a1} , and X_{a2} would be thermodynamically separated.

In orientation O2 time-of-flight data sets were recorded in phase M_I at 0.5 T, in phase R_{a1} at 1 T, 2 T, and 3 T, in phase M_{a2} at 3.5 T and 4 T, in phase M_{b1} at 4 T, 5 T and 5.5 T, in phase M_{c1} at 6 T, in phase M_{c2} at 6.5 T, 8 T, and 10 T, and in the field polarized state at 12 T.

As explained in the following, the ground state represents a commensurate $(\pi\pi 0)$ antiferromagnet in M_I , M_{a1} , and M_{a2} . Note that M_I comprises the zero-field phase C. We assume, that the three regions M_I , M_{a1} , and M_{a2} belong to a single thermodynamic phase. The ground state in this phase is a single- k $(\pi\pi 0)$ structure. The ground state

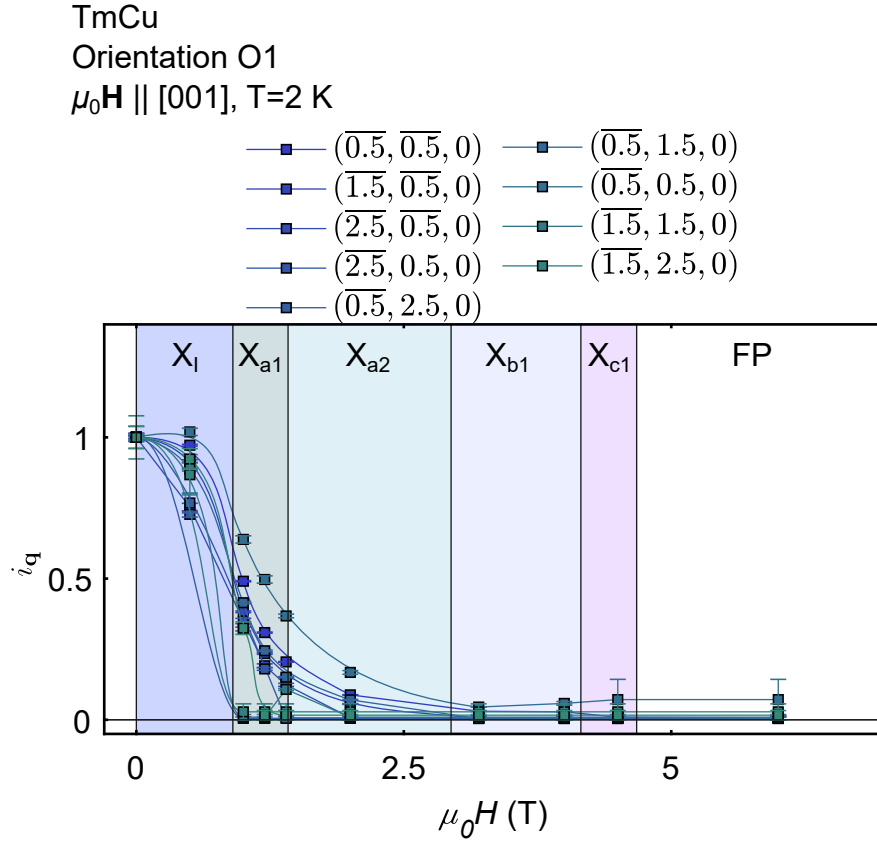


Figure 3.62.: Integrated intensities as a function of field of commensurate Bragg peaks, as inferred from sweepO1 in orientation O1. Integrated intensities of peaks, which are related to the k -arm A_1^c , are shown as a function of field along [001]. Field dependences of integrated intensities were divided by the integrated intensity in zero magnetic field $i_{\mathbf{q}}(B) = I_{\mathbf{q}}(B) / I_{\mathbf{q}}(0)$.

in M_{b1} represents a superposition of wave-vectors, which are distinctively different from the propagation vectors of the $\langle \frac{1}{2} \frac{1}{2} 0 \rangle$ star. In particular, the ground state in M_{b1} does not represent a $(\pi\pi 0)$ antiferromagnet or a variation of it. In M_{c1} and M_{c2} only relatively weak Bragg intensities were observed.

In the following, the indexation of Bragg peaks is illustrated for three different data sets, which were recorded by means of sweepO2. The corresponding positions in the phase diagram are represented by filled circles in Fig. 3.63. Fig. 3.64 shows magnetic Bragg peaks in the vicinity of $(0, \frac{1}{2}, \frac{1}{2})$ as inferred from the three data sets. Note, that data are shown on a logarithmic color scale.

In phase M_I at 0.5 T a single Bragg peak is present at the position $(0, \frac{1}{2}, \frac{1}{2})$ reflecting commensurate $(\pi\pi 0)$ antiferromagnetism (Fig. 3.64 (a)). Similar diffraction patterns were observed in M_{a1} and M_{a2} reflecting commensurate $(\pi\pi 0)$ antiferromagnetism.

Figs. 3.64 (b) and (c) show the scattering intensities in the vicinity of the position $(0, \frac{1}{2}, \frac{1}{2})$, as observed in phase M_{b1} at the fields 4.5 T and 5 T, respectively. A Bragg peak is present at the commensurate position $(0, \frac{1}{2}, \frac{1}{2})$. Further, relatively weak peaks

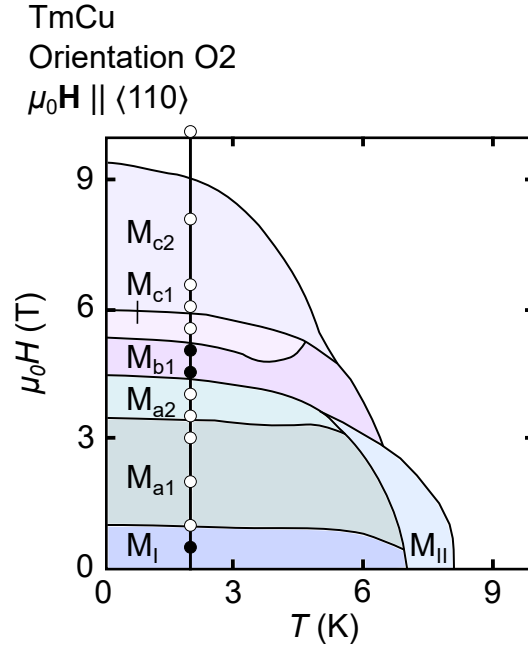


Figure 3.63.: Regions of the $\langle 110 \rangle$ phase diagram of TmCu. The phase diagram was determined by Rahn (cf. Ref. [118]). For this study the regions, which may possibly represent phase pockets, were labeled and filled with colors. The vertical line represents the field sweep, which was carried out for this study. Diffraction data were recorded at the points, which are indicated by circles. The filled circles indicate the data sets, for which diffraction data are presented further below.

were detected at the positions $(0, \frac{1}{2} \pm \delta, \frac{1}{2})$ and $(0, \frac{1}{2}, \frac{1}{2} \pm \delta)$ with $\delta \approx 0.07$. However, the ground state is not a variation of a $(\pi\pi 0)$ antiferromagnet, as magnetic Bragg peaks are present also at positions, located far away from $(\pi\pi 0)$ positions.

Fig. 3.65 shows a two dimensional slice through the diffraction data, which were recorded in phase M_{b1} at a field of 5 T. Magnetic Bragg peaks are present at commensurate positions $(h_j, -0.5, -0.5)$, where $h_j = j \cdot \frac{1}{7}$ and $j = \{4, 5, 6, 7, \dots, 22\}$. A similar pattern of magnetic Bragg peaks was observed in the $(h, k, 1.5)$ plane, as presented in Sec. A.5.

The Bragg peaks may be indexed by means of propagation vectors of the stars $\langle \frac{1}{2}, \frac{1}{2}, 0 \rangle$, $\langle \frac{1}{2}, \frac{1}{2}, \frac{1}{7} \rangle$, $\langle \frac{1}{2}, \frac{1}{2}, \frac{2}{7} \rangle$, and $\langle \frac{1}{2}, \frac{1}{2}, \frac{3}{7} \rangle$. Accordingly, the ground state is multi- k with at least four different propagation vectors.

The magnetic Bragg peaks, as observed in phase M_{b1} , are reminiscent of diffraction data, which may be observed for spin-slip states. Spin-slip structures are hosted in numerous rare-earth systems, as reported in Refs. [100, 200, 201]. The breakup of $(\pi\pi 0)$ antiferromagnetism in phase R_{b1} is in stark contrast to all other ground states detected in TmCu, HoCu, and ErCu, which are all variations of $(\pi\pi 0)$ antiferromagnets.

In the following, integrated intensities as a function of field of Bragg peaks of the $\langle \frac{1}{2}, \frac{1}{2}, 0 \rangle$ star, as inferred from sweepO2, are presented. Shown in Fig. 3.68 (a), (b), and (c) are the integrated intensities as a function of field, of the Bragg peaks, which are associated with

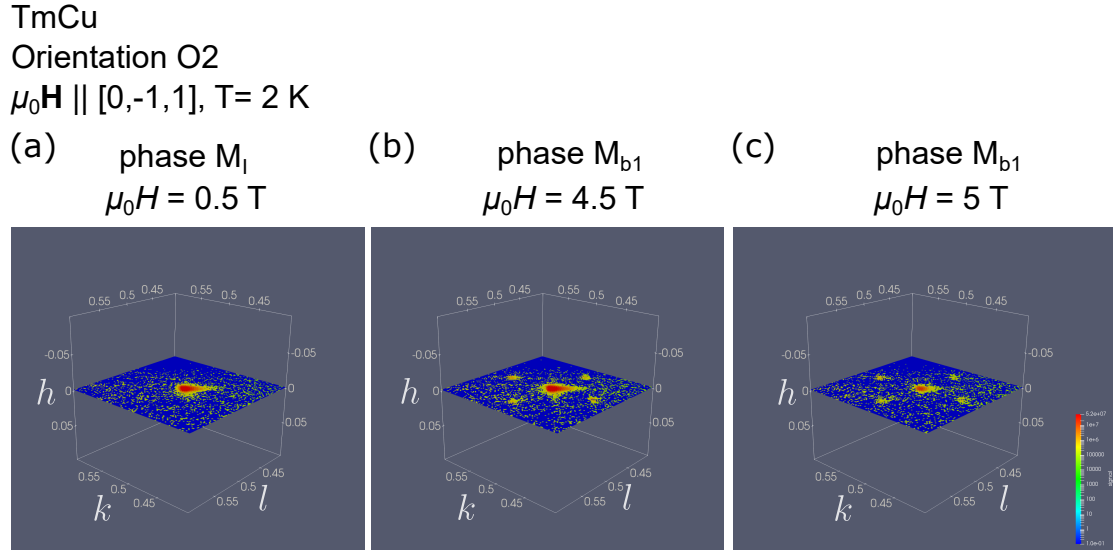


Figure 3.64.: Evolution of magnetic propagation vectors in orientation O2. The indexing of magnetic Bragg peaks may be illustrated in terms of the Bragg peaks, which were observed in the vicinity of $(0, \frac{1}{2}, \frac{1}{2})$. Shown are diffraction data recorded in the vicinity of $(0, \frac{1}{2}, \frac{1}{2})$. (a) Scattering intensity in phase M_I at 0.5 T. The single Bragg peak at $(0, \frac{1}{2}, \frac{1}{2})$ reflects commensurate $(\pi\pi 0)$ antiferromagnetism. (b),(c) Scattering intensity intensity in X_{b1} at 4.5 T and in X_{b1} at 5 T. The Bragg peaks at $(0, \frac{1}{2}, \frac{1}{2})$, at $(0, \frac{1}{2} \pm \delta, \frac{1}{2})$, and at $(0, \frac{1}{2}, \frac{1}{2} \pm \delta)$ may be indexed with propagation vectors of the stars $\langle \frac{1}{2} \frac{1}{2} 0 \rangle$ and $\langle \frac{1}{2} - \delta, \frac{1}{2}, 0 \rangle$. However, as explained in the text, Bragg peaks, located far away from $(\pi\pi 0)$ positions, are present in X_{b1} . Accordingly, the ground state is not a variation of a $(\pi\pi 0)$ antiferromagnet.

the k -arms A_1^c , A_2^c , and A_3^c , respectively. In this orientation O2, where the magnetic field was directed along $[0\bar{1}1]$, the k -arms A_1^c and A_3^c have the same orientation. In contrast, A_2^c has a different orientation with respect to the field. The integrated intensities in Fig. 3.68 reflect these two different orientations of k -arms. In relatively low fields, the integrated intensities of Bragg peaks, which are related to A_1^c and A_3^c , respectively, drop to vanishingly small values. In contrast, the integrated intensities of Bragg peaks, which are related to A_2^c , increase to a plateau. Accordingly, only a single k -arm is participating in M_{a1} and M_{a2} . Further, we assume that the regions M_I , M_{a1} , and M_{a2} belong to a single thermodynamic phase. It may be concluded that the ground state in these phases is single- k , as only one k -arm is participating. Accordingly, also the ground state in phase C is single- k .

Note, that in principle, this decrease of magnetic intensities might also arise due to a phase transition related to a change of the magnetic ground state. In this case, however, M_I and M_{a1} do not belong to the same phase.

In orientation O3, time-of-flight data sets were recorded in phase R_I at the fields 0 T, 1 T, 2 T, and 3 T, in phase R_{a1} at 3.2 T, 3.4 T, and 3.6 T, in phase R_{b1} at 3.8 T, 4 T, 4.2 T,

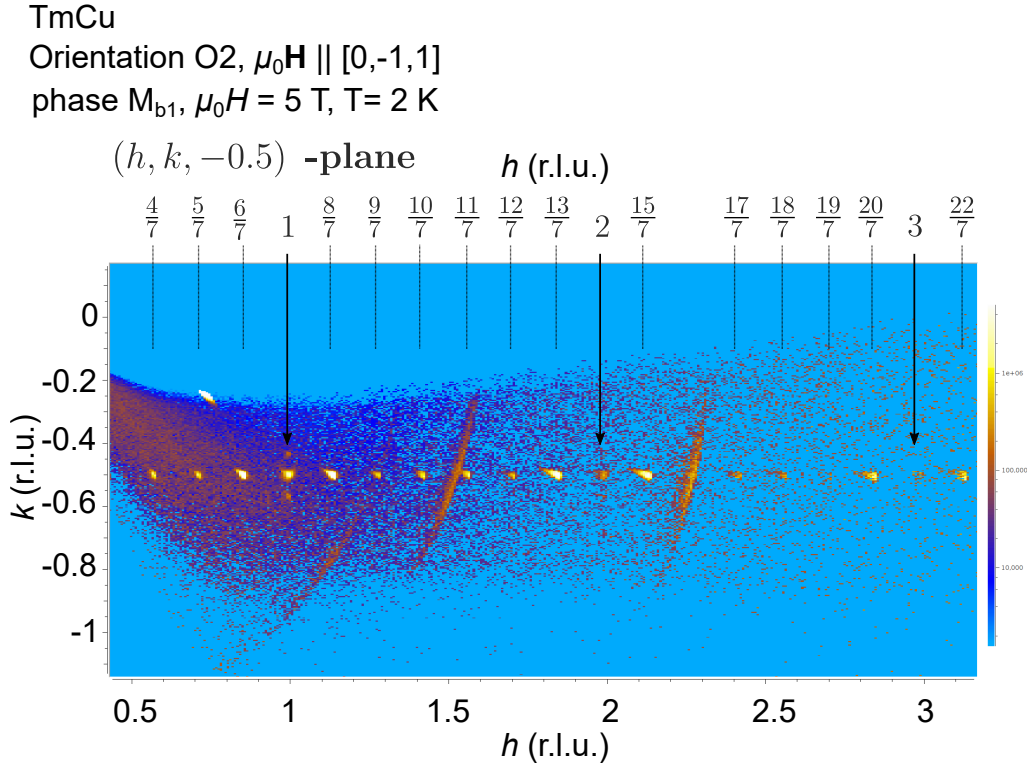


Figure 3.65.: Propagation vectors of the ground state in X_{b1} in orientation O2. Shown are diffraction data in the $(h, k, -0.5)$ plane, as recorded in X_{b1} at 5 T. Along the line $(h, -0.5, -0.5)$ Bragg peaks were observed at the positions $h = j \cdot \frac{1}{7}$ with $j = \{4, 5, 6, 7, \dots, 22\}$. Accordingly, the magnetic ground state is multi- k . Propagation vectors of the stars $\langle \frac{1}{2}, \frac{1}{2}, 0 \rangle$, $\langle \frac{1}{2}, \frac{1}{2}, \frac{1}{7} \rangle$, $\langle \frac{1}{2}, \frac{1}{2}, \frac{2}{7} \rangle$, and $\langle \frac{1}{2}, \frac{1}{2}, \frac{3}{7} \rangle$ are required to index the magnetic Bragg peaks.

5 T, 6 T, 6.2 T, and 6.4 T, in phase R_{b2} at 6.6 T and 6.8 T, in phase R_{b3} at 7 T, 7.2 T, 7.4 T, 7.6 T, 7.8 T, and 8 T.

As explained in the following, the ground state was found to represent a commensurate $(\pi\pi 0)$ antiferromagnet in R_I and R_{a1} . In R_{b1} , R_{b2} , and R_{b3} , the ground state was found to represent a superposition of propagation vectors of the stars $\langle \frac{1}{2}, \frac{1}{2}, 0 \rangle$ and $\langle \frac{1}{2} - \delta, \frac{1}{2}, 0 \rangle$, where $\delta = 0.07$. We believe that R_I and R_{a1} belong to a single thermodynamic phase. Further, we believe that R_{b1} , R_{b2} , and R_{b3} belong to a single thermodynamic phase.

In the following, the indexation of Bragg peaks is illustrated for some data-sets, recorded by means of sweepO3. The corresponding positions in the phase diagram are represented by filled circles in Fig. 3.66. Fig. 3.67 shows diffraction data in the vicinity of $(\frac{1}{2}, -\frac{1}{2}, 0)$ as inferred from the three data sets.

In phases R_I and R_{a1} a single Bragg peak is present at $(\frac{1}{2}, -\frac{1}{2}, 0)$ reflecting commensurate $(\pi\pi 0)$ antiferromagnetism. For instance, Fig. 3.67 (a) shows the Bragg peak, which was recorded in phase R_I at 0 T. The integrated intensity of the commensurate peak is given by 8.21 ± 0.04 .

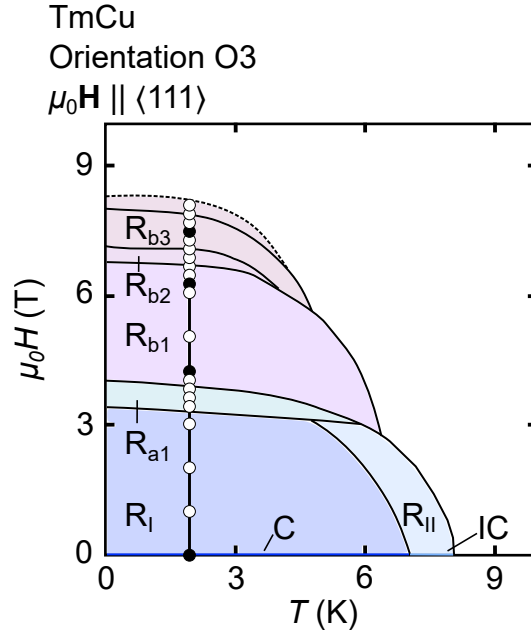


Figure 3.66.: Regions of the $\langle 111 \rangle$ phase diagram of TmCu. The phase diagram was determined by Rahn (cf. Ref. [118]). For this study the regions, which may possibly represent phase pockets, were labeled and filled with colors. The vertical line represents the field sweep, which was carried out for this study. Diffraction data were recorded at the points, which are indicated by circles. The filled circles indicate the data sets, for which diffraction data is presented further below.

In R_{b1} , R_{b2} , and R_{b3} Bragg peaks are present, which may be indexed by propagation vectors of the stars $\langle \frac{1}{2} \frac{1}{2} 0 \rangle$ and $\langle \frac{1}{2} - \delta, \frac{1}{2}, 0 \rangle$. In particular, the ground state in these regions is multi- k and has a long-wavelength modulation. For instance, Fig. 3.67 (b), (c), and (d) show the scattering intensity, as recorded in phases R_I at 0 T, R_{b1} at 4 T, R_{b1} at 6 T, and in R_{b3} at 7.2 T, respectively. In all three phases R_{b1} , R_{b2} , and R_{b3} Bragg peaks are present at $(\frac{1}{2}, -\frac{1}{2}, 0)$, at $(\frac{1}{2} \pm \delta, -\frac{1}{2}, 0)$, and at $(\frac{1}{2}, -\frac{1}{2} \pm \delta, 0)$, where $\delta \approx 0.07$. Accordingly, the magnetic ground state represents a superposition of commensurate and incommensurate propagation vectors of the stars $\langle \frac{1}{2}, \frac{1}{2}, 0 \rangle$ and $\langle \frac{1}{2} - \delta, \frac{1}{2}, 0 \rangle$, respectively. The ground state is multi- k and has a long-wavelength modulation of the order of $a/\delta \approx 14 \cdot a$. In phase R_{b1} at 4 T the integrated intensities of the incommensurate satellites are ranging from 0.18 ± 0.01 to 0.58 ± 0.01 , the integrated intensity of the commensurate peak is given by 0.86 ± 0.01 .

We believe that the regions X_I , X_{a1} , X_{a2} , M_I , M_{a1} , M_{a2} , R_I , and R_{a1} belong to a single thermodynamic phase, which has a single- k ($\pi\pi 0$) antiferromagnet as the magnetic ground state. In particular, the ground state in phase C is single- k .

This finding of a single- k ground state is notable. At zero magnetic field, the ground state is collinear, having only a single ($\pi\pi 0$) propagation vector. When a magnetic field is applied, this ground state may possibly become noncollinear due to a ferromagnetic component. Recently, an unconventional Hall effect was reported in Ref. [118], which

TmCu

Orientation O3

 $\mu_0\mathbf{H} \parallel [1,1,1]$, $T = 2$ K

(a) phase R_I $\mu_0H = 0$ T (b) phase R_{b1} $\mu_0H = 4$ T (c) phase R_{b1} $\mu_0H = 6$ T (d) phase R_{b3} $\mu_0H = 7.2$ T

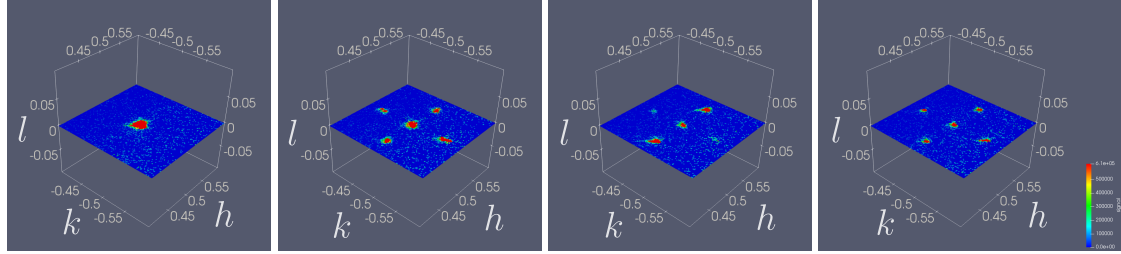


Figure 3.67.: Evolution of magnetic propagation vectors in orientation O3. The indexing of magnetic Bragg peaks may be illustrated in terms of the Bragg peaks, which were observed in the vicinity of $(\frac{1}{2}, -\frac{1}{2}, 0)$. Shown are the recorded data in the vicinity of $(\frac{1}{2}, -\frac{1}{2}, 0)$. (a) Scattering intensity in phase R_I at 0 T. The single Bragg peak at $(\frac{1}{2}, -\frac{1}{2}, 0)$ reflects commensurate $(\pi\pi 0)$ antiferromagnetism. (b), (c), and (d) Scattering intensity in R_{b1} at 4 T, in R_{b1} at 6 T, and in R_{b3} at 7.2 T, respectively. The Bragg peaks at $(\frac{1}{2}, -\frac{1}{2}, 0)$, at $(\frac{1}{2} \pm \delta, -\frac{1}{2}, 0)$, and at $(\frac{1}{2}, -\frac{1}{2} \pm \delta, 0)$ require propagation vectors of the stars $\langle \frac{1}{2} \frac{1}{2} 0 \rangle$ and $\langle \frac{1}{2} - \delta, \frac{1}{2}, 0 \rangle$, respectively.

is not accounted for by an ordinary anomalous Hall effect, scaling linearly with the net magnetization. Accordingly, the ground state in phases X_I , X_{a1} , X_{a2} , M_I , M_{a1} , M_{a2} , R_I , and R_{a1} may represent a noncollinear antiferromagnet causing an anomalous Hall effect, which is not ordinary. This finding may suggest the presence of a finite Berry curvature of the electronic structure (cf. Sec. 3.3.7.3 for further information).

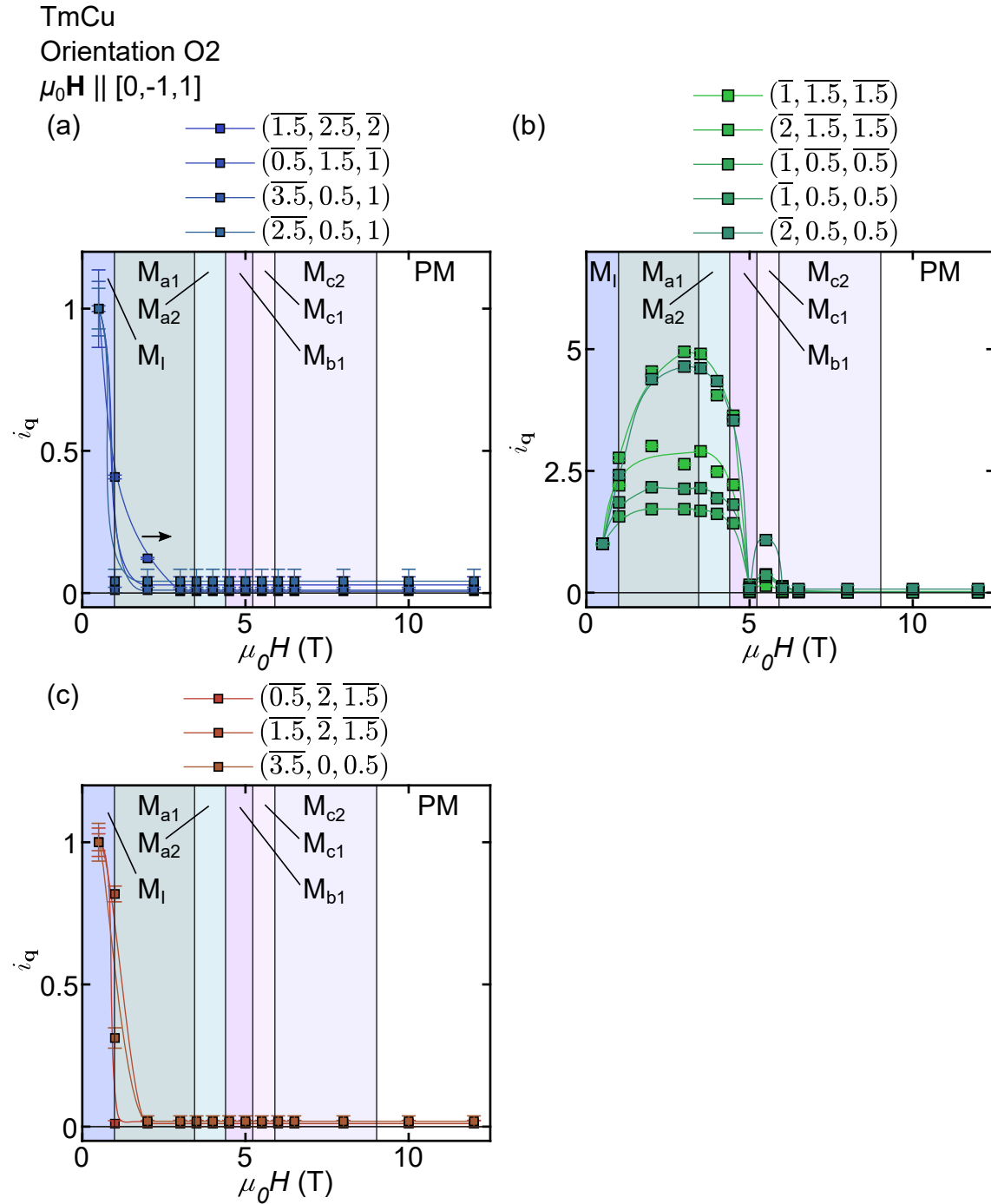


Figure 3.68.: Integrated intensities as a function of field of commensurate Bragg peaks, as inferred from sweepO2 in orientation O2. Integrated intensities of peaks, which are related to the k -arms (a) A_1^c , (b) A_2^c , and (c) A_3^c are shown as a function of field along $[001]$. Field dependences of integrated intensities were divided by the integrated intensity in zero magnetic field $i_q(B) = I_q(B)/I_q(0)$.

3.5. The Compound ErCu

In the following section, we present a microscopic study on the antiferromagnet ErCu, the third of three RCu compounds studied in this thesis, which may host complex magnet ground states with non-trivial topology. Previous magnetic structure determinations in zero magnetic field were based on polycrystalline samples and did not consider all ordered phases. As our main results of single crystal neutron diffraction we identified several magnetic ground states including multi- k structures and modulations with large wavelengths of the order of 170 Å.

The presentation is organized as follows. First, an introduction to the compound is provided in Sec. 3.5.1. Second, a study by means of neutrons is presented in Sec. 3.5.2. Magnetic propagation vectors were determined in the three magnetically ordered phases at zero magnetic field (Sec. 3.5.2.1) and the ground states were specified by representational analysis (Sec. 3.5.2.2), Rietveld refinements (Sec. 3.5.2.4), and polarization analysis (Sec. 3.5.2.3). Further, magnetic ground states were studied in magnetic fields along twofold $\langle 110 \rangle$ directions (Sec. 3.5.2.5).

3.5.1. Introduction to ErCu

The centrosymmetric compound ErCu exhibits properties, which are typical of rare-earth intermetallics, most notably a rich magnetic phase diagram due to numerous competing interactions. The compound is a promising candidate material for hosting novel anti-ferromagnetic ground states with non-trivial topology of the following reasons. The detection of multitudinous ground states in the isostructural compounds HoCu and TmCu (cf. Secs. 3.3 and 3.4) possessing non-trivial topology, long-wavelength modulations, and multi- k character, as well as the emergence of highly unconventional transport properties in HoCu and TmCu (cf. Refs. [18, 118]) may suggest the stabilization of topological magnetic ground states also in ErCu.

The compound ErCu crystallizes in the cubic CsCl structure with lattice constant $a = 3.431$ Å [70, 71]. At temperatures below ≈ 15 K the tripositive rare-earth ions carry magnetic long-range order. The magnetic ions may be viewed as localized moments of $9.58 \mu_B$, as inferred for Er^{3+} ($[Xe] 4f^{11}$) by means of Hund's rules ($L = 6$, $S = \frac{3}{2}$, $J = \frac{15}{2}$, and $g = \frac{6}{5}$ [30]). Complex magnetic phase diagrams evolve, as shown in Fig. 3.69 for the major cubic directions and inferred from magnetization, ac susceptibility, and specific heat [202]. The phase diagrams reflect the importance of cubic anisotropies featuring qualitative differences between the major cubic directions. Critical fields, which are much smaller for fourfold directions than for twofold and threefold directions, suggest a fourfold easy axis in agreement with neutron spectroscopy measurements [203].

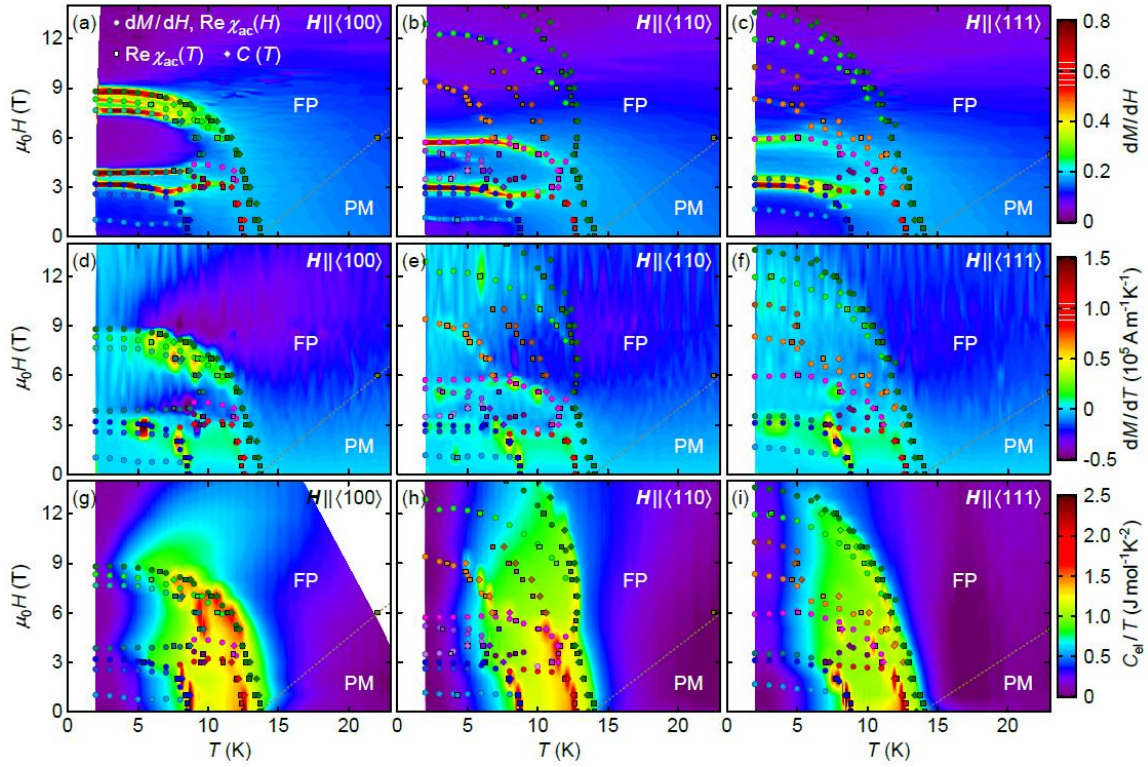


Figure 3.69.: Magnetic phase diagrams of ErCu for magnetic field applied along $\langle 100 \rangle$ (left column), $\langle 110 \rangle$ (middle column), or $\langle 111 \rangle$ (right column). The color coding in the background represents the susceptibility calculated from magnetization, i.e., dM/dH (top row), the derivative of the magnetization with respect to temperature, i.e., dM/dT (middle row), and the non-phonon contribution to the specific heat divided by temperature, i.e., C_{el}/T (bottom row). The figure was taken from Ref. [202].

In zero magnetic field, three magnetically ordered phases are established with transition temperatures $T_{N1} = 8.7$ K, $T_{N2} = 12.7$ K, and $T_{N3} = 13.8$ K [202]. Susceptibility as a function of temperature, as shown in Fig. 3.70 (a), features three clearly visible anomalies at the transition temperatures. The inverse susceptibility as a function of temperature, as shown in Fig. 3.70 (b), displays Curie-Weiss behavior with the fluctuating Curie-Weiss moment $9.9 \mu_B/\text{f.u.}$ and the Curie-Weiss temperature -18 K, which is characteristic of a non-frustrated antiferromagnet. Specific heat as a function of temperature, which is shown in Figs. 3.69 (c) and (d), features sharp peaks at T_{N1} and T_{N2} , as characteristic of first-order phase transitions, and a lambda-anomaly at T_{N3} , characteristic of a second-order phase transition (cf. Fig. 3.70). Magnetic entropy in ErCu as a function of temperature, as shown in Figs. 3.70 (e) and (f), was inferred by approximating the phonon contributions in ErCu by the phonon contributions of non-magnetic LuCu. The high temperature limit of the entropy amounts to $S_{mag} = R \cdot \ln 16$, which is consistent with the quantum mechanically predicted value $S_{mag} = R \cdot \ln(2J + 1)$ for Er^{3+} with $J = \frac{15}{2}$. Resistivity measurements were reported in Refs. [204, 205]. Typical magnetization data as a function

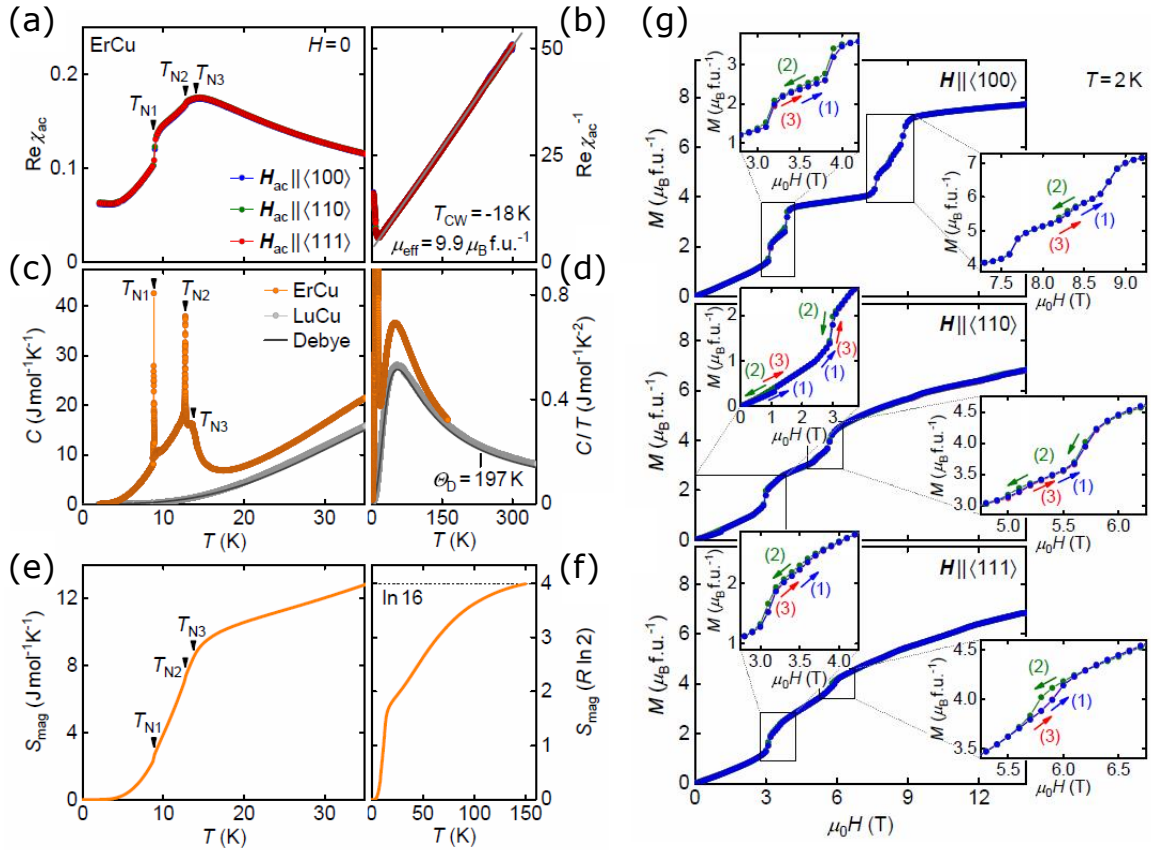


Figure 3.70.: Bulk properties of ErCu in zero magnetic field. (a) AC susceptibility in zero magnetic field as a function of temperature, the excitation fields applied along major cubic directions. Three anomalies are observed, labeled T_{N1} , T_{N2} , and T_{N3} . (b) Inverse susceptibility as a function of temperature featuring linear behavior. (c),(d) Specific heat as a function of temperature. Shown are specific heat data of ErCu and of the non-magnetic compound LuCu. Further, an estimate for the phonon contribution, which is based on the Debye model, is shown. (e),(f) Magnetic contribution to the entropy. Therefore, the phonon contributions in ErCu were approximated by the phonon contributions in LuCu. (g) Magnetization data as a function of field at low temperatures are shown for magnetic fields applied along $\langle 100 \rangle$, $\langle 110 \rangle$, and $\langle 111 \rangle$. Data were measured in three different protocols, namely for increasing field after zero-field cooling (1), for decreasing fields starting from 14 T (2), and for increasing fields starting from -14 T (3). The figures were taken from Ref. [202].

of field are shown in Fig. 3.70 (g) for the three major cubic directions. The magnetization increases monotonically as a function of field and displays multiple steps, which is reminiscent of observations in DyCu [115], PrAg [116], or NdIn₃ [95]. Relatively weak hysteresis was observed in the magnetization data, depending on whether the field was increased after zero-field cooling, increased from -14 T, or decreased from 14 T.

Magnetic structure determinations using neutron diffraction from polycrystalline samples were reported in Ref. [68]. However, only two magnetically ordered phases were studied at zero magnetic field, as the authors resolved only two transitions in specific heat, namely at 10.9 K and 13.8 K. The temperatures that were studied in Ref. [68]

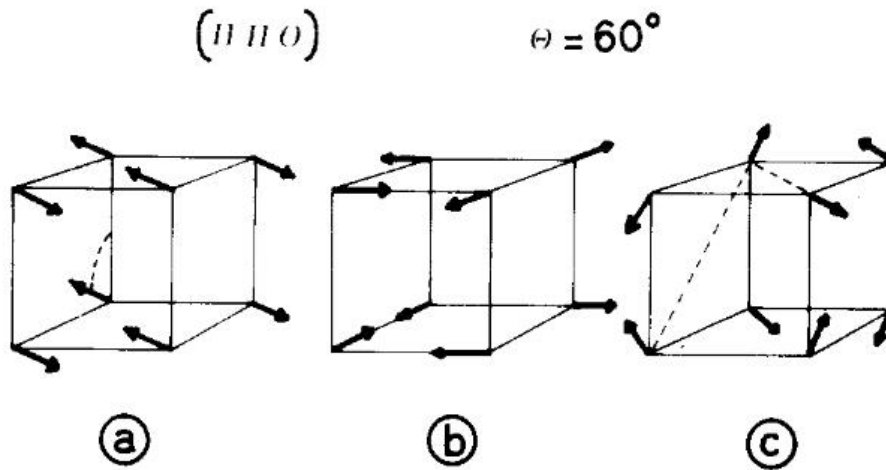


Figure 3.71.: Magnetic structure in the low-temperature phase of ErCu, which is further below labeled C. A magnetic structure determination by means of polycrystalline neutron diffraction was reported by Morin *et al.* in Ref. [68]. Three magnetic structures were found in agreement with the neutron diffraction data recorded at $T = 1.5$ K. The structure candidates were characterized by an angle $\theta = 60^\circ$. The ground state is either single-axis, double-axis, or triple-axis. (a) In the single-axis case the moments point along a direction enclosing an angle $\theta = 60^\circ$ with the $[001]$ direction. (b) The double-axis texture has moments pointing along $\langle 100 \rangle$ directions. (c) The triple-axis texture has moments pointing along $\langle 111 \rangle$ directions. The figures were taken from Ref. [68].

correspond to the phases C and either to phase IC1 or phase IC2, as referred to in our study further below. In the lowest-temperature phase C, at $T = 1.5$ K, commensurate $(\pi\pi 0)$ antiferromagnetism with an ordered moment of $5.7 \mu_B$ was observed. The authors of Ref. [68] proposed three scenarios for the magnetic ground state in this phase. Fig. 3.71 shows the three possible structures. The ground state represents either a single- k structure, the moments enclosing an angle of 60° with the $[001]$ direction, or a multi- k structure that has the same structure factor as the single- k structure (cf. Ref. [107]). The moments point along $\langle 100 \rangle$ directions, if the texture is double- k , or along $\langle 110 \rangle$ directions, if it is triple- k . Crystal electric fields, as inferred from neutron spectroscopy measurements [203], do not permit to determine the magnetic ground states unambiguously [68], as the energy for $\langle 110 \rangle$ and $\langle 111 \rangle$ directions is too similar to the energy for $\langle 100 \rangle$ directions, which had lowest energy. The authors found that distortions of the lattice are small in phase C, as only a small broadening of the nuclear (200) peak was observed. At $T = 12$ K in phase IC1 or IC2, the ground state was found to represent a superposition of incommensurate propagation vectors $(0.54, 0.5, 0)$ as well as commensurate propagation vectors. The commensurate component had a modulus of $2.4 \mu_B$ and was directed along the c -axis ($\theta = 0^\circ$), the incommensurate component was related to an amplitude modulation with maximum amplitude of $3 \mu_B$, the moments also directed along the c -axis ($\theta = 0^\circ$).

3.5.2. Neutron Diffraction Study

In the following, a neutron study of ErCu is presented. First, propagation vectors of magnetic ground states were determined in zero magnet field, which is presented in Sec. 3.5.2.1. Therefore, temperature dependences of magnetic Bragg peaks were recorded in zero magnetic field. Second, polarization analysis, representational analysis, and Rietveld refinements were carried out, as presented in Secs. 3.5.2.2, 3.5.2.3, and 3.5.2.4, respectively. Third, temperature dependences of magnetic Bragg peaks were determined at different magnetic fields along twofold $\langle 110 \rangle$ directions, as presented in Sec. 3.5.2.5.

3.5.2.1. Magnetic Propagation Vectors

To determine the magnetic propagation vectors of ErCu in zero magnetic field, neutron diffraction of the sample OFZ104-3-3 was carried out on the diffractometer E4 [206].

The main results of these measurements may be summarized as follows:

- In zero magnetic field, ErCu features three phases hosting magnetic long-range order. These phases may be labeled **C** ($T < T_{N1}$), **IC1** ($T_{N1} < T < T_{N2}$), and **IC2** ($T_{N2} < T < T_{N3}$) (cf. Ref. [202]).
- All phases display variations of $(\pi\pi 0)$ antiferromagnetism.
- In phase C, the ground state is commensurate representing a superposition of propagation vectors of the star $\langle \frac{1}{2}, \frac{1}{2}, 0 \rangle$. The structure may be single- k , double- k , or triple- k .
- In phase IC1, the ground state represents a superposition of incommensurate contributions due to propagation vectors of the star $\langle \frac{1}{2} - \delta, \frac{1}{2}, \delta \rangle$ ($\delta = 0.044$), much weaker contributions due to propagation vectors of the star $\langle \frac{1}{2} - \delta, \frac{1}{2}, 0 \rangle$, and weak contributions due to commensurate propagation vectors of the star $\langle \frac{1}{2}, \frac{1}{2}, 0 \rangle$.
- In phase IC2, the ground state represents a superposition of incommensurate contributions due to propagation vectors of the star $\langle \frac{1}{2} - \delta, \frac{1}{2}, 0 \rangle$ and much weaker incommensurate contributions due to propagation vectors of the star $\langle \frac{1}{2} - \delta, \frac{1}{2}, \epsilon \rangle$ ($\epsilon = 0.02$). The structure is multi- k . Contributions due to propagation vectors of the stars $\langle \frac{1}{2} - \delta, \frac{1}{2}, \delta \rangle$ and $\langle \frac{1}{2}, \frac{1}{2}, 0 \rangle$ are finite but relatively weak.

The study was organized as follows. First, magnetic propagation vectors were determined in phase C at $T = 4$ K. Therefore, several high-symmetry points of the first Brillouin zone were probed as putative magnetic propagation vectors and diffraction intensity was recorded by means of rocking scans. Magnetic intensity was detected at the M point. Accordingly, the magnetic ground state in phase C was confirmed to be a $(\pi\pi 0)$ antiferromagnet. Second, magnetic propagation vectors were determined in phase IC1 at

$T = 10$ K and in phase IC2 at 13 K. By means of q -scans, Bragg peaks were recorded at commensurate $(\pi\pi 0)$ positions, as well as at incommensurate positions in the vicinity of $(\pi\pi 0)$ positions. Magnetic propagation vectors were inferred by indexation of the magnetic Bragg peaks, which were observed. Third, temperature dependences of magnetic Bragg peaks were studied.

For the experiments, neutrons with a wavelength of 2.41 \AA were used. The sample was oriented such that the (110) plane corresponded to the scattering plane. While cooling the sample from room temperature to base temperature, the orientation matrix was determined at the structural reflections (002) and (110). The lattice parameter amounts to $a = 3.4166(18) \text{ \AA}$. A two dimensional detector with 256×256 pixels on an area $200 \times 200 \text{ mm}^2$ at the sample-detector distance 79.38 cm permitted to accurately determine coordinates of incommensurate Bragg peaks in reciprocal space.

To determine magnetic propagation vectors in phase C at $T = 4$ K, the following high symmetric points in reciprocal space [125] were considered as putative propagation vectors: the points (i) M and (ii) R. However, only at the M point a pronounced magnetic Bragg peak was measured. In contrast, no magnetic intensity was detected in a rocking scan around the position $(\frac{1}{2}, \frac{1}{2}, \frac{1}{2})$. Accordingly, the magnetic propagation vectors in phase C are of the star $\langle \frac{1}{2}, \frac{1}{2}, 0 \rangle$, in agreement with Ref. [68].

To record the magnetic Bragg peak $(\frac{1}{2}, -\frac{1}{2}, 0)$ in phase C at 4 K with high q -resolution, a q -scan through the position $(\frac{1}{2}, -\frac{1}{2}, 0)$ was carried out along the (001) direction in the reciprocal space. The recorded data are presented in Fig. 3.72. The q -scan with step width $\Delta l = 0.002$ along the line $(0, 0, l)$ in the reciprocal space corresponds to a rocking scan with step width $\Delta\omega \approx -0.159^\circ$. The detector changes its position only slightly during this scan, as in the center $d \sin(\theta) / dh \approx 0$. For instance, during a l -scan with 161 steps the detector changes its angular position from $\theta = 29.52^\circ$ (when $l = -0.16$) to 28.78° ($l = 0$) and back to 29.52° ($l = 0.16$). At each step during the l -scans, a detector image was recorded. Each detector image represents a 256×256 matrix $I_\omega(X, Y)$ of recorded diffraction intensities.

Fig. 3.72 (a) shows the sum over detector images $\sum_\omega I_\omega(X, Y)$ for this rocking scan at $T = 4$ K. The pronounced Bragg spot at $(\frac{1}{2}, -\frac{1}{2}, 0)$ reflects magnetic long-range order of type $(\pi\pi 0)$ in phase C.

To determine diffraction intensities of the Bragg peak $(\frac{1}{2}, -\frac{1}{2}, 0)$ as a function of ω , the region of interest ROI O was defined in the detector images and intensities were inferred by summation of the matrix entries lying in ROI O:

$$\mathcal{I}(\omega) = \sum_{(X,Y) \in O} I_\omega(X, Y) . \quad (3.78)$$

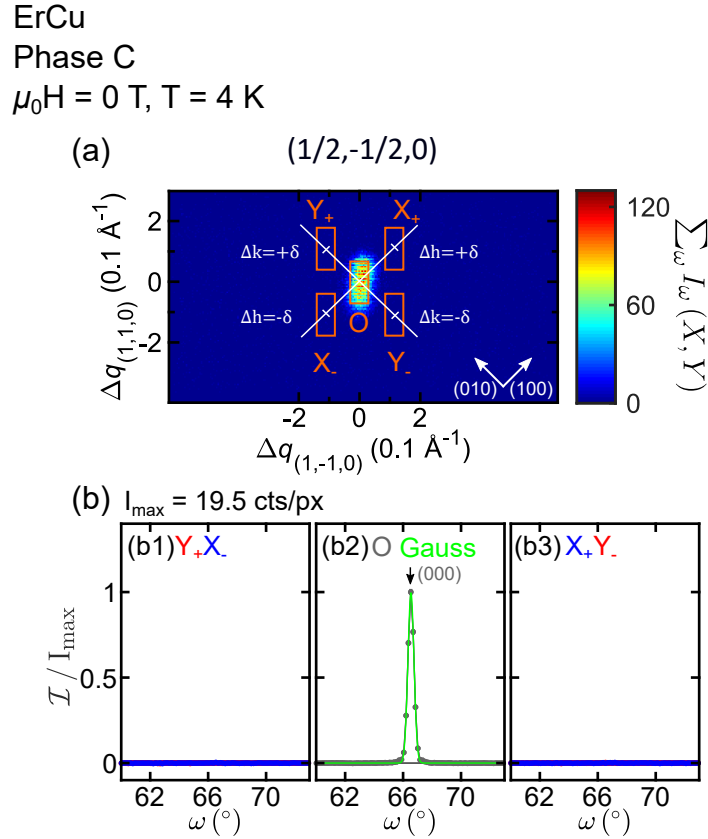


Figure 3.72.: Magnetic propagation vectors in phase C. A q -scan along (001) through the position $(\frac{1}{2}, -\frac{1}{2}, 0)$ was carried out. Propagation vectors may be inferred by indexation of the Bragg peaks. (a) Sum over detector images, which were recorded by means of the q -scan. (b) Intensities as a function of ω for the ROIs (b1) Y_+ and X_- , (b2) O , and (b3) Y_- and X_+ . A Bragg peak was observed at the position $(\frac{1}{2}, -\frac{1}{2}, 0)$. For each Bragg peak, which was observed, the q -position in reciprocal space is indicated by means of the shift with respect to the commensurate position $(\frac{1}{2}, -\frac{1}{2}, 0)$.

Fig. 3.73 (b2) shows the intensity $\mathcal{I}(\omega)$, as inferred from the rocking scan around the peak $(\frac{1}{2}, -\frac{1}{2}, 0)$. A Gaussian profile centered at $\omega_0 = 66.53^\circ$ with a FWHM 0.49° gives an excellent fit to the recorded magnetic Bragg peak as reflected by the relatively high R -value given by $R^2 = 0.9995$. Shown in Fig. 3.73 (b1) and Fig. 3.73 (b3) are intensities as a function of ω for the ROIs Y_+ , Y_- , X_+ , and X_- , which display vanishingly small intensities.

It may be concluded that the ground state in phase C is a superposition of propagation vectors of the star $\langle \frac{1}{2}, \frac{1}{2}, 0 \rangle$. This ground state may be single- k , double- k , or triple- k .

To determine the propagation vectors in phase IC1, the same reciprocal space scan, which was carried out in phase C, was repeated in phase IC1 at 10 K. Presented in Fig. 3.73 are the data, as recorded by this q -scan. Fig. 3.73 (a) shows the sum over detector images. Bragg peak intensities were observed in five different ROIs in the detector images.

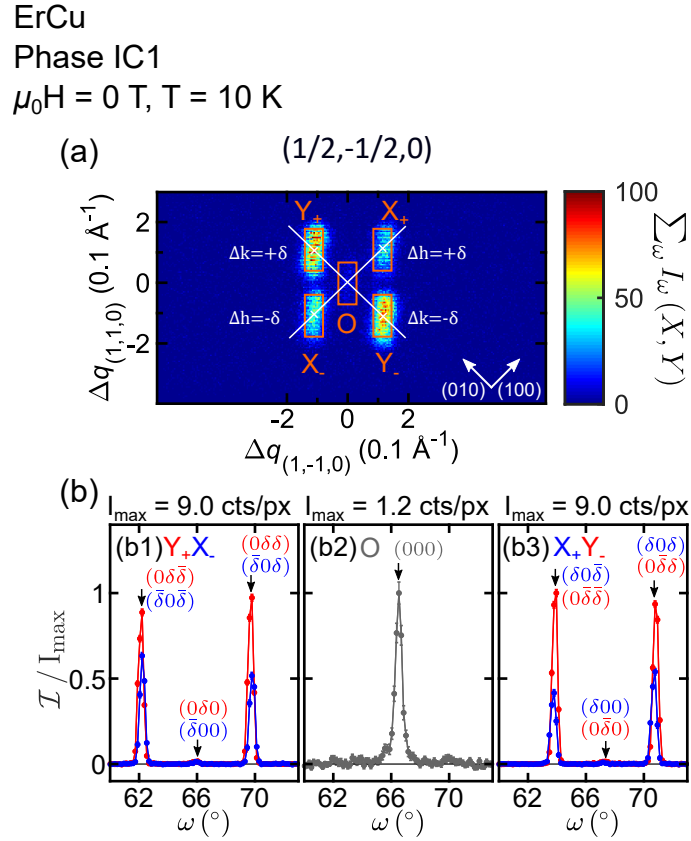


Figure 3.73.: Magnetic propagation vectors in phase IC1. A q -scan along (001) through the position $(\frac{1}{2}, -\frac{1}{2}, 0)$ was carried out. Propagation vectors may be inferred by indexation of the Bragg peaks. (a) Sum over detector images, which were recorded by means of the q -scan. (b) Intensities as a function of ω for the ROIs (b1) Y_+ and X_- , (b2) O , and (b3) Y_- and X_+ . For each Bragg peak, which was observed, the q -position in reciprocal space is indicated by means of the shift with respect to the commensurate position $(\frac{1}{2}, -\frac{1}{2}, 0)$.

Shown in Fig. 3.73 (b2) is the intensity as a function of ω , as inferred for ROI O . A Bragg peak was observed at $(\frac{1}{2}, -\frac{1}{2}, 0)$, the intensity being distinctively smaller than in phase C. Shown in Fig. 3.73 (b1) and (b2) are intensities as a function of ω , as inferred for the ROIs Y_+ , X_- , X_+ , and Y_- , respectively. In total 12 different magnetic Bragg peaks are visible in these data. In the figure, their Q -positions are indicated by their shift with respect to the Q -position $(\frac{1}{2}, -\frac{1}{2}, 0)$. Relatively strong Bragg peaks were observed at Q -positions, which are related to the star $\langle \frac{1}{2} - \delta, \frac{1}{2}, \delta \rangle$, where $\delta = 0.044 \pm 0.002$. Further, Bragg peaks with relatively weak intensities were observed at Q -positions, which are related to the star $\langle \frac{1}{2} - \delta, \frac{1}{2}, 0 \rangle$.

Accordingly, the ground state is a superposition of relatively strong contributions due to propagation vectors of the star $\langle \frac{1}{2} + \delta, \frac{1}{2}, \delta \rangle$. The ground state may also have finite contributions due to propagation vectors of the stars $\langle \frac{1}{2}, \frac{1}{2}, 0 \rangle$ and $\langle \frac{1}{2} - \delta, \frac{1}{2}, 0 \rangle$. Hence,

the magnetic ground state may be multi- k . Further it has a long-wavelength modulation of the order of $a/\delta \approx 78 \text{ \AA}$ along two cubic directions.

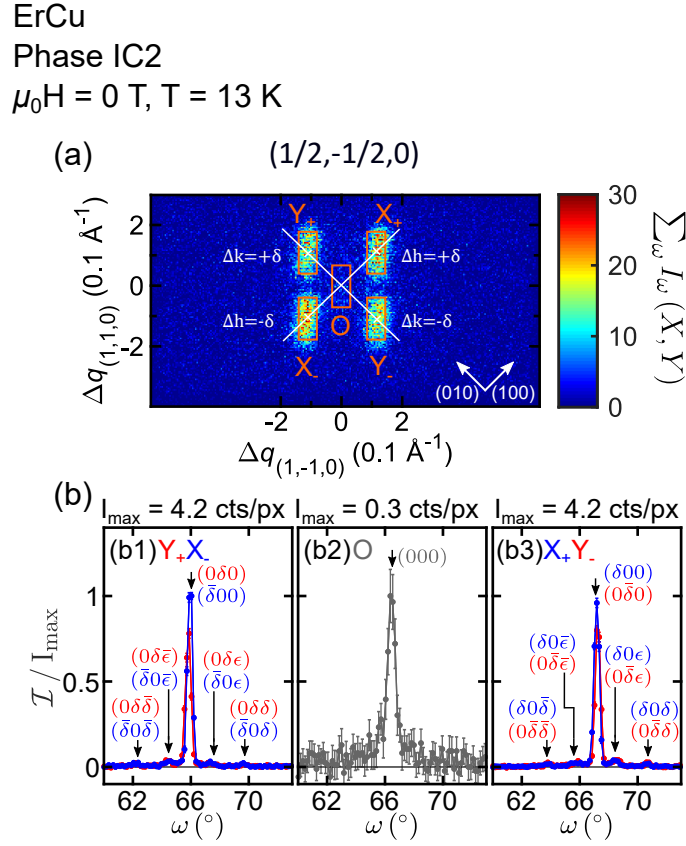


Figure 3.74.: Magnetic propagation vectors in phase IC2. A q -scan along (001) through the position $(\frac{1}{2}, -\frac{1}{2}, 0)$ was carried out. Propagation vectors may be inferred by indexation of the Bragg peaks. (a) Sum over detector images, which were recorded by means of the q -scan. (b) Intensities as a function of ω for the ROIs (b1) Y_+ and X_- , (b2) O , and (b3) Y_- and X_+ . For each Bragg peak, which was observed, the q -position in reciprocal space is indicated by means of the shift with respect to the commensurate position $(\frac{1}{2}, -\frac{1}{2}, 0)$.

To determine the propagation vectors in phase IC2, the same reciprocal space scan, which was carried out in phases C and IC1, was repeated in phase IC2 at 13 K. Presented in Fig. 3.74 are the data, as recorded by the q -scan. Shown in Fig. 3.74 (a) is the sum over detector images. Bragg peak intensities were observed in five different ROIs in the detector images. Shown in Fig. 3.74 (b2) is the intensity as a function of ω , as inferred for ROI O. A Bragg peak is present at $(\frac{1}{2}, -\frac{1}{2}, 0)$, but the intensity is relatively weak. Shown in Fig. 3.72 (b1) and (b2) are the intensities as a function of ω , as inferred for the ROIs Y_+ , X_- , X_+ , and Y_- , respectively. Bragg peaks were observed at q -positions, which are related to the star $\langle \frac{1}{2} - \delta, \frac{1}{2}, \delta \rangle$. However, their intensity is very weak. Bragg peaks with relatively strong intensities were observed at q -positions, which are related to the star $\langle \frac{1}{2} - \delta, \frac{1}{2}, 0 \rangle$. Further, peaks were observed at positions, which are related to the star

$\langle \frac{1}{2} - \delta, \frac{1}{2}, \epsilon \rangle$, where $\epsilon = 0.020 \pm 0.002$. Accordingly, the ground state is a superposition of contributions due to propagation vectors of the stars $\langle \frac{1}{2} - \delta, \frac{1}{2}, 0 \rangle$ and $\langle \frac{1}{2} + \delta, \frac{1}{2}, \epsilon \rangle$. The magnetic ground state may be multi- k and has a long-wavelength modulation of the order of $a/\delta \approx 78 \text{ \AA}$ along one cubic direction and $a/\epsilon \approx 170 \text{ \AA}$ along another cubic direction. Further, the ground state may have finite contributions due to propagation vectors of the stars $\langle \frac{1}{2}, \frac{1}{2}, 0 \rangle$ and $\langle \frac{1}{2} - \delta, \frac{1}{2}, \delta \rangle$.

The propagation vector stars $\langle \frac{1}{2} - \delta, \frac{1}{2}, \delta \rangle$, $\langle \frac{1}{2} - \delta, \frac{1}{2}, 0 \rangle$, and $\langle \frac{1}{2} - \delta, \frac{1}{2}, \epsilon \rangle$ have 24, 12, and 24 different k -arms, respectively. For the study of multi- k structures in this thesis, we do not distinguish between conjugated k -arms. Accordingly, they may be identified in terms of Ω -arms. The stars $\langle \frac{1}{2} - \delta, \frac{1}{2}, \delta \rangle$, $\langle \frac{1}{2} - \delta, \frac{1}{2}, 0 \rangle$, and $\langle \frac{1}{2} - \delta, \frac{1}{2}, \epsilon \rangle$, have 12, 6, and 12 different Ω -arms, respectively. One third of these Ω -arms possesses a pair of q -positions in the vicinity of $(\frac{1}{2}, -\frac{1}{2}, 0)$. Together with the commensurate peak at $(\frac{1}{2}, -\frac{1}{2}, 0)$ this gives in total 21 Bragg peak positions, which belong to 11 different wave-vector arms.

In the following, integrated intensities as a function of temperature are presented for these 11 wave-vector arms. Therefore, a temperature sweep was carried out starting in phase C at 4 K after zfc. During the sweep, the q -scan, which was performed in phases C, IC1, and IC2, was repeated at well defined temperatures ranging from 4 K to 14 K. The Bragg peaks, which were observed at 21 different q -positions, were fitted by Gaussian peak profiles and integrated.

Fig. 3.75 shows the temperature dependences of integrated intensities, as inferred from the 21 Bragg peak positions. Shown in Fig. 3.75 (a) is the integrated intensity as a function of temperature of the Bragg peak located at $(\frac{1}{2}, -\frac{1}{2}, 0)$ reflecting the temperature dependence of Bragg peaks of the star $\{\mathbf{k}_c\}$, where $\mathbf{k}_c := (\frac{1}{2}, \frac{1}{2}, 0)$. Presented in Figs. 3.75 (b), (c), and (d) are the integrated intensities as inferred from Bragg peaks, which are associated with the propagation vector stars $\{\mathbf{k}_{ic,1}\}$, $\{\mathbf{k}_{ic,2}\}$, and $\{\mathbf{k}_{ic,3}\}$, where $\mathbf{k}_{ic,1} := (\frac{1}{2} - \delta, \frac{1}{2}, \delta)$, $\mathbf{k}_{ic,2} := (\frac{1}{2} - \delta, \frac{1}{2}, 0)$, and $\mathbf{k}_{ic,3} := (\frac{1}{2} - \delta, \frac{1}{2}, \epsilon)$, respectively. For the pairs of incommensurate peaks, which belong to conjugated k -arms, i.e., to the same Ω -arm, the average of their integrated intensities is shown. An illustration of the location of the 21 Bragg peaks is given in Fig. 3.75 (e). The k -arms, which belong to the same star, feature the same temperature dependences, as in zero magnetic field the symmetry between different k -arms of a star is preserved.

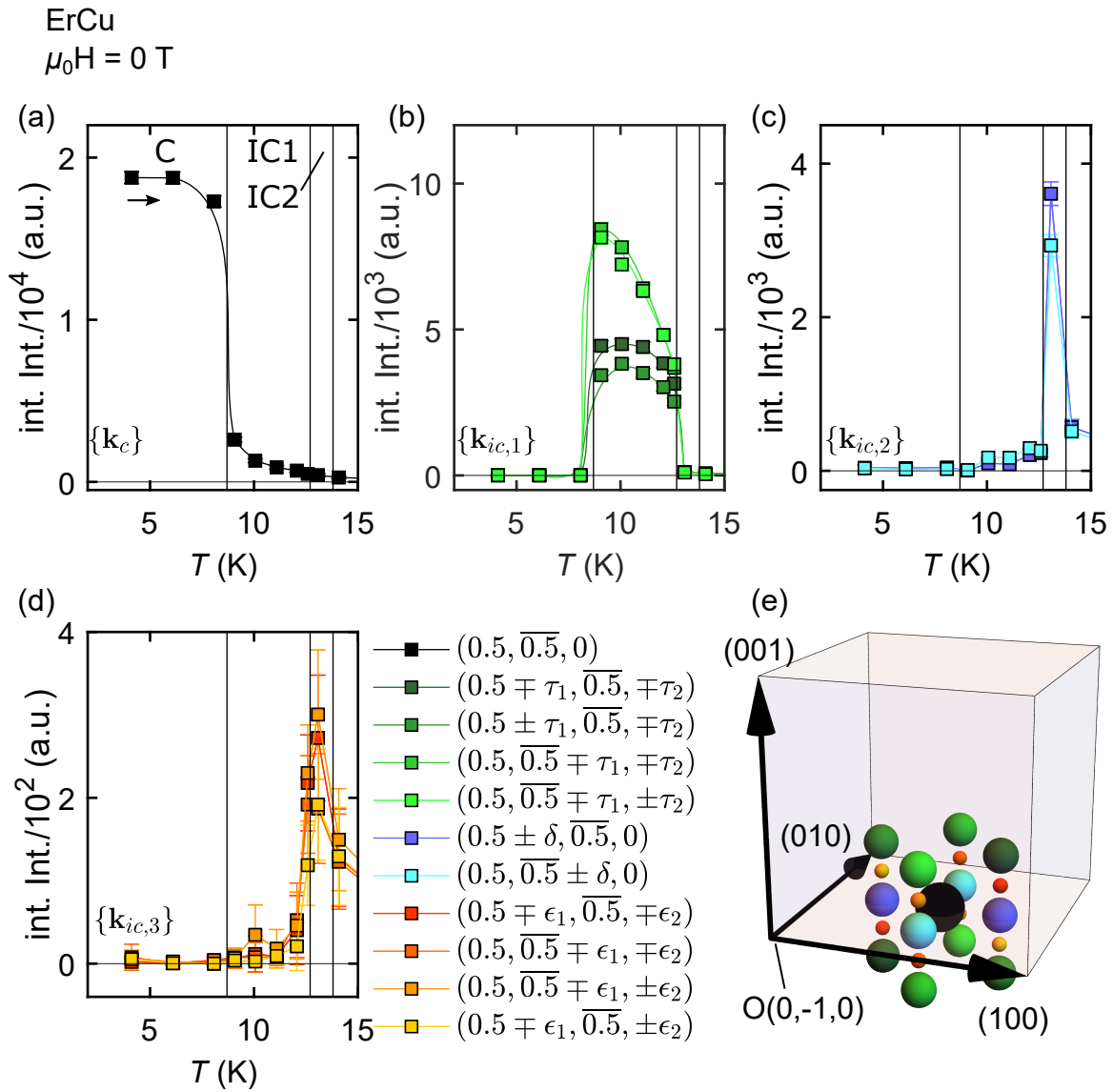


Figure 3.75.: Temperature dependences of magnetic Bragg peaks in zero magnetic field. (a) Integrated intensity as a function of temperature, of the Bragg peak, which is associated with the propagation vector k_c . (b)-(d) Temperature dependences of Bragg peak, which are associated with propagation vectors of the stars $\{k_{ic,1}\}$, $\{k_{ic,2}\}$, and $\{k_{ic,3}\}$, respectively. Shown are averages of integrated intensities of Bragg peaks, which belong to conjugated k -arms, i.e., to the same Ω -arm. (e) Illustration of the location of the 21 Bragg peak positions, which were considered in this study.

3.5.2.2. Representational Analysis

To determine all irreducible representations (IRs) as well as the corresponding basis functions that are allowed by symmetry for the four types of propagation vectors \mathbf{k}_c , $\mathbf{k}_{ic,1}$, $\mathbf{k}_{ic,2}$, and $\mathbf{k}_{ic,3}$, representational analysis was carried out by means of the software SARA h [54]. The study provides a decomposition of ground states into Fourier series.

The results of this study may be summarized as follows:

- The magnetic ground state in phase C may be decomposed into a Fourier series with propagation vectors of the star $\{\mathbf{k}_c\}$, where $\mathbf{k}_c = (\frac{1}{2}, \frac{1}{2}, 0)$. Each Fourier component can be written as superposition of $\Gamma_3(\mathbf{k}_c)$ and $\Gamma_9(\mathbf{k}_c)$ basis functions.
- The magnetic ground states in phases IC1 may be decomposed into a Fourier series with propagation vectors of the stars $\{\mathbf{k}_c\}$, $\{\mathbf{k}_{ic,1}\}$, and $\{\mathbf{k}_{ic,2}\}$, where $\mathbf{k}_{ic,1} = (\frac{1}{2} - \delta, \frac{1}{2}, \delta)$, and $\mathbf{k}_{ic,2} = (\frac{1}{2} - \delta, \frac{1}{2}, 0)$. Each commensurate Fourier component may be decomposed analogously to phase C. The incommensurate Fourier components are a superposition of $\Gamma_1(\mathbf{k}_{ic,1})$ and $\Gamma_2(\mathbf{k}_{ic,1})$ basis functions, as well as $\Gamma_2(\mathbf{k}_{ic,2})$, $\Gamma_3(\mathbf{k}_{ic,2})$, and $\Gamma_4(\mathbf{k}_{ic,2})$ basis functions.
- The magnetic ground state in phase IC2 may be decomposed into a Fourier series with propagation vectors of the stars $\{\mathbf{k}_{ic,2}\}$ and $\{\mathbf{k}_{ic,3}\}$, where $\mathbf{k}_{ic,3} = (\frac{1}{2} - \delta, \frac{1}{2}, \epsilon)$. Each incommensurate Fourier component is a superposition of $\Gamma_1(\mathbf{k}_{ic,3})$ and $\Gamma_2(\mathbf{k}_{ic,3})$ basis functions, $\Gamma_2(\mathbf{k}_{ic,2})$, $\Gamma_3(\mathbf{k}_{ic,2})$, and $\Gamma_4(\mathbf{k}_{ic,2})$ basis functions.

Propagation vector	IR	BV	BV components					
			$m_{\parallel a}$	$m_{\parallel b}$	$m_{\parallel c}$	$im_{\parallel a}$	$im_{\parallel b}$	$im_{\parallel c}$
$\mathbf{k}_c = (\frac{1}{2}, \frac{1}{2}, 0)$	Γ_3	Ψ_1	0	0	16	0	0	0
	Γ_9	Ψ_2	8	0	0	0	0	0
		Ψ_3	0	-8	0	0	0	0
$\mathbf{k}_{ic,2} = (\frac{1}{2} - \delta, \frac{1}{2}, 0)$	Γ_2	Ψ_1	4	0	0	0	0	0
	Γ_3	Ψ_2	0	4	0	0	0	0
	Γ_4	Ψ_3	0	0	4	0	0	0
$\mathbf{k}_{ic,1} = (\frac{1}{2} - \delta, \frac{1}{2}, \delta)$	Γ_1	Ψ_1	0	2	0	0	0	0
	Γ_2	Ψ_2	0	0	2	0	0	0
		Ψ_3	2	0	0	0	0	0
$\mathbf{k}_{ic,3} = (\frac{1}{2} - \delta, \frac{1}{2}, \epsilon)$	Γ_1	Ψ_1	0	2	0	0	0	0
	Γ_2	Ψ_2	0	0	2	0	0	0
		Ψ_3	2	0	0	0	0	0

Table 3.9.: Analysis of representations of the magnetic Er site in the space group $Pm\bar{3}m$. For each of the four magnetic propagation vectors \mathbf{k} that was detected in ErCu, the IRs $\Gamma(\mathbf{k})$ with non-trivial basis functions $\Psi^{\mathbf{k}}$ are listed. The analysis was carried out by means of the software SARA h .

Tab. 3.9 summarizes the results of the representational analysis as obtained for propagation vectors \mathbf{k}_c , $\mathbf{k}_{ic,1}$, $\mathbf{k}_{ic,2}$, and $\mathbf{k}_{ic,3}$ and space group $Pm\bar{3}m$. For propagation vectors \mathbf{k}_c and $\mathbf{k}_{ic,2}$ the results are analogous to the results in Sec. 3.3.3.4. For incommensurate propagation vectors $\mathbf{k}_{ic,3}$ and $\mathbf{k}_{ic,1}$, the magnetic representation splits into $\Gamma = 1\Gamma_1^1 + 1\Gamma_2^2$. The IR Γ_2 has the order $\nu = 2$ and contains two basis functions. In contrast, Γ_1 has the order $\nu = 1$ and contains one basis function.

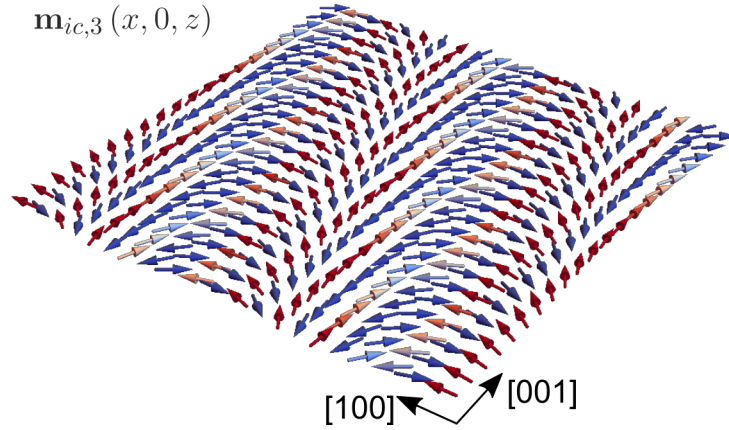


Figure 3.76.: Magnetic structure $\mathbf{m}_{ic,3}$ representing an example for a magnetic structure with propagation vector $\mathbf{k}_{ic,3}$ that is a superposition of basis functions from one IR only, namely $\Gamma_2(\mathbf{k}_{ic,3})$, and that features spatially constant modulus of magnetic moments.

Magnetic structures with propagation vectors such as $\mathbf{k}_{ic,3}$ may have intriguing properties. Namely, there are some peculiarities related to the fact that the IR $\Gamma_2(\mathbf{k}_{ic,3})$ has the order $\nu = 2$. For instance, single- k spiral structures exist that consist of basis functions from one single IR only. Consider therefore, e.g., the magnetic structure with propagation vector $\mathbf{k}_{ic,3} = (\frac{1}{2} - \delta, \frac{1}{2}, \epsilon)$, which is described in terms of:

$$\mathbf{m}_{ic,3}(\mathbf{R}) = \mathbf{m}_0 (\hat{e}_x \cos(\mathbf{k}_{ic,3} \cdot \mathbf{R}) + \hat{e}_z \sin(\mathbf{k}_{ic,3} \cdot \mathbf{R})) . \quad (3.79)$$

The structure $\mathbf{m}_{ic,3}$ is a superposition of $\Gamma_2(\mathbf{k}_{ic,3})$ basis functions and features spatially constant modulus of magnetic moments.

Fig. 3.76 shows a real-space picture of $\mathbf{m}_{ic,3}$. The structure is incommensurate with respect to the cubic directions $[100]$ and $[001]$, i.e., along x and z . Magnetic moments are perfectly antiferromagnetically coupled along y , they are antiferromagnetically coupled with cycloidal character along x , and they are ferromagnetically coupled with helical character along z . Interestingly, all moments of $\mathbf{m}_{ic,3}$ feature the same modulus. In contrast, there is no such single- k spiral structure with wave-vector $\mathbf{k}_{ic,2}$ that is a superposition of basis functions, which are related to one IR only. All single- k structures with propagation vector $\mathbf{k}_{ic,2}$ that are related to one IR only are in fact amplitude modulations.

These considerations are of particular interest, if Landau theory implies that the magnetic ground state is a superposition of basis functions from one IR only [53]. In fact, Landau theory may be applicable in phase IC2, as the phase transition at the Néel temperature was reported to be a second-order phase transition [68].

3.5.2.3. Polarization Analysis

To experimentally determine the IRs that describe the magnetic ground states in phases C and IC2, polarized neutron diffraction of the sample OFZ104-3-4-1 was carried out at the diffractometer DNS [135].

The main results of these experiments may be summarized as follows:

- In phase C, the magnetic ground state is a superposition of $\Gamma_9(\mathbf{k}_c)$ basis functions only. In particular, the ground state represents one of the five commensurate $(\pi\pi 0)$ structures s2, s4, d2, d5, and t2 (cf. Fig. 3.40).
- In phase IC2 the ground state contains $\Gamma_3(\mathbf{k}_c)$ basis functions and $\Gamma_4(\mathbf{k}_{ic,2})$ basis functions.

For the experiments the sample was oriented such that the (001) plane corresponded to the scattering plane. At the DNS diffractometer only peaks located in the scattering plane are accessible for measurements. Phase IC1 was not investigated with these experiments, as the magnetic Bragg peaks, which are indexed by propagation vectors $\mathbf{k}_{ic,1}$ or $\mathbf{k}_{ic,3}$, are not located in the (001) plane.

The study was done as follows. In phases C and IC2, diagonal entries of polarization matrices were determined for each peak in the vicinity of $(\frac{1}{2}, \frac{1}{2}, 0)$ in the reciprocal space. Irreducible representations that describe the magnetic ground states in C and IC2 were inferred by means of the Blume-Maleev equations (cf. Sec. 2.1.2).

Polarization matrices in C and IC2 were determined as follows. With the same experimental procedure as in Sec. 3.3.3.5 large maps for the vicinity of $(\frac{1}{2}, \frac{1}{2}, 0)$ in the reciprocal space were recorded in phase C at $T = 5$ K and in phase IC2 at $T = 13$ K. The maps contained two channels, one with spin-flip and the other one with non-spin-flip scattering intensities. The data permitted to study in phase C the commensurate Bragg peak $(\frac{1}{2}, \frac{1}{2}, 0)$ and in phase IC2 the commensurate Bragg peak, as well as the four Bragg peaks located at $(\frac{1}{2} \pm \delta, \frac{1}{2}, 0)$ and $(\frac{1}{2}, \frac{1}{2} \pm \delta, 0)$.

The integrated intensity of the commensurate peak was considerably weaker in phase IC2 than in phase C:

$$\frac{I\left(\frac{1}{2}, \frac{1}{2}, 0\right)_{13\text{K}}}{I\left(\frac{1}{2}, \frac{1}{2}, 0\right)_{5\text{K}}} = 0.035 \pm 0.001, \quad (3.80)$$

which is in agreement with Fig. 3.75. The determination of polarization matrices from the experimental data followed the same procedure as described in Sec. 3.3.3.5. The polarization rate of the incident neutron beam was not measured for the ErCu sample. However, the experimental setup was the same for the two sets of measurements and it

Q-position	Phase C	Phase IC2
$\left(\frac{1}{2}, \frac{1}{2}, 0\right)$	$(-0.98, +0.94, -0.97)$	$(-1.03, -, +0.96)$
$\left(\frac{1}{2} - \delta, \frac{1}{2}, 0\right)$	-	$(-1.00, -, +0.98)$
$\left(\frac{1}{2}, \frac{1}{2} - \delta, 0\right)$	-	$(-1.01, -, +0.99)$
$\left(\frac{1}{2}, \frac{1}{2} + \delta, 0\right)$	-	$(-1.01, -, +0.99)$
$\left(\frac{1}{2} + \delta, \frac{1}{2}, 0\right)$	-	$(-1.00, -, +0.94)$

Table 3.10.: Polarization matrices of magnetic peaks in phases C and IC2. Shown are the diagonal elements of polarization matrices, as determined experimentally by means of polarized neutron diffraction at 5K in phase C and at 13K in phase IC2. For the measurements, the ErCu sample was oriented such that the scattering plane corresponded to the crystallographic (001) plane. For the vectors, which are listed, the statistical errors of each entry are smaller than ± 0.02 .

was assumed that the neutron polarization rate did not change, i.e., $\alpha = 1 - \epsilon = 0.97$. Hence, all experimental polarization matrices were corrected by a factor $\gamma = \frac{1}{1-2\epsilon} \approx 1.06$ to compensate for the lack of full beam polarization.

Fig. 3.10 shows the measured polarization matrices. For all Bragg peaks, the polarization in the x -channel is consistent with $P_{xx} = -1$ reflecting the purely magnetic origin of all scattering processes (cf. Ref. [136]).

In phase C, the polarization matrix of the commensurate peak $\left(\frac{1}{2}, \frac{1}{2}, 0\right)$ satisfies $P_{yy} = 0.93 \approx -P_{zz}$. With the Blume-Maleev equations it may be established that a polarization matrix fulfilling $P_{yy} = 1 = -P_{zz}$ would imply a ground state which is described by only $\Gamma_9(\mathbf{k}_c)$ basis functions (cf. Secs. A.2 and 3.3.3.5). Here, we assume that the polarization matrix is in fact described by only $\Gamma_9(\mathbf{k}_c)$ and that the discrepancy between measured polarization ($P_{yy} = 0.93 \approx -P_{zz}$) and expected polarization ($P_{yy} = 1 = -P_{zz}$) arises due to double spin-flip scattering. Our assumption is based on the same arguments that were thoroughly explained in Sec. 3.3.3.5. Among the 21 commensurate $(\pi\pi 0)$ structures in Tab. 3.1 there are only five, which contain only $\Gamma_9(\mathbf{k}_c)$ basis functions in their Fourier decomposition, namely s2, s4, d2, d5, and t2. Hence, it is inferred, that the magnetic ground state in phase C represents one of these five structures. Note, that the five structures are associated with an angle $\theta = 90^\circ$, which stands in contrast to an angle of 60° inferred by Morin *et al.* [68].

In phase IC2, the polarization matrices of all incommensurate Bragg peaks are consistent with $P_{yy} = -1 = -P_{zz}$. As it can be shown by the Blume-Maleev equations, this polarization implies that the incommensurate components of the ground state in phase IC2 are described by $\Gamma_4(\mathbf{k}_{ic,2})$ basis functions only (cf. Sec. A.2). Similarly, the polarization matrix of the relatively weak commensurate Bragg peak is consistent with $P_{yy} = -1 = -P_{zz}$. By means of the Blume-Maleev equations it is inferred that the com-

mensurate components of the ground state in phase IC2 are described by $\Gamma_3(\mathbf{k}_c)$ basis functions only (cf. Sec. A.2). Both IRs, i.e. $\Gamma_4(\mathbf{k}_{ic,2})$ and $\Gamma_3(\mathbf{k}_c)$, are related to an angle of $\theta = 0^\circ$, which is in excellent agreement with previous findings at $T = 12$ K by Morin *et al.* [68]. The results are in total analogy to the results in phase IC1 of HoCu (cf. Sec. 3.3.3.5). Due to the lack of knowledge about the number of propagation vectors it is beyond the scope of this thesis to suggest a specific magnetic ground state for phase IC2 of ErCu.

3.5.2.4. Rietveld Refinements

To perform Rietveld refinements in phase C of ErCu, neutron diffraction of single crystal OFZ104-3-3 was carried out at the time-of-flight diffractometer SXD [207].

The main results of these experiments may be summarized as follows:

- The CsCl crystal structure of ErCu was confirmed by means of Rietveld refinements.
- The magnetic ground state in phase C represents a commensurate $(\pi\pi 0)$ antiferromagnet and is a superposition of $\Gamma_9(\mathbf{k}_c)$ basis functions only, which is in agreement with the polarization analysis. Accordingly, the ground state represents one of the five $(\pi\pi 0)$ structures s2, s4, d2, d5 and t2 (cf. Tab. 3.1).
- Time-of-flight data in this compound are contaminated by strong Renninger effects.

For the experiments, neutrons with wavelengths $0.5 \text{ \AA} < \lambda < 5.5 \text{ \AA}$ were used. In phase C at $T = 4.5 \text{ K}$ a large volume in the reciprocal space was recorded by means of time-of-flight measurements. The volume contained 1824 structural and 630 magnetic Bragg reflections of the $\langle \frac{1}{2} \frac{1}{2} 0 \rangle$ star. Integrated intensities of the Bragg reflections were inferred by means of the data reduction software SXD2001 [207]. As explained in the following, the data set could not as a whole be used for Rietveld refinements, as the data set displayed an odd behavior, which may be artifact. In particular, all attempts to carry out Rietveld refinements failed. However, refinements were successfully carried out on a reduced data set containing only Bragg peaks recorded with neutrons in the reduced wavelength range $0.9 \text{ \AA} < \lambda < 1.1 \text{ \AA}$. As explained in the following, the large data set was contaminated with unphysical wavelength dependences. Presumably multiple scattering, which is typically strongly wavelength dependent [130, 131, 208], caused the artifact wavelength dependences in the large data set.

To illustrate this untypical wavelength dependence, integrated intensities of structural reflections were plotted in Fig. 3.77. They are supposed to follow the nuclear structure factor for the CsCl structure of ErCu, which is given by:

$$F_{\text{ErCu}}^2(h, k, l) = \begin{cases} (b_{\text{Er}} + b_{\text{Cu}})^2 & h + k + l \in 2\mathbb{Z} \\ (b_{\text{Er}} - b_{\text{Cu}})^2 & h + k + l \in 2\mathbb{Z} + 1 \end{cases} . \quad (3.81)$$

As the scattering lengths of Er and Cu are very similar, $b_{\text{Er}} = 7.79 \text{ fm}$ and $b_{\text{Cu}} = 7.718 \text{ fm}$ [122], the nuclear reflections should display two groups of strongly enhanced integrated intensities, when $h + k + l$ is even, and strongly suppressed integrated intensities, when $h + k + l$ is odd.

Fig. 3.77 shows the integrated intensities of structural reflections as a function of $\sin(\theta)/\lambda$. The large data set of 1824 structural reflections recorded with neutrons of

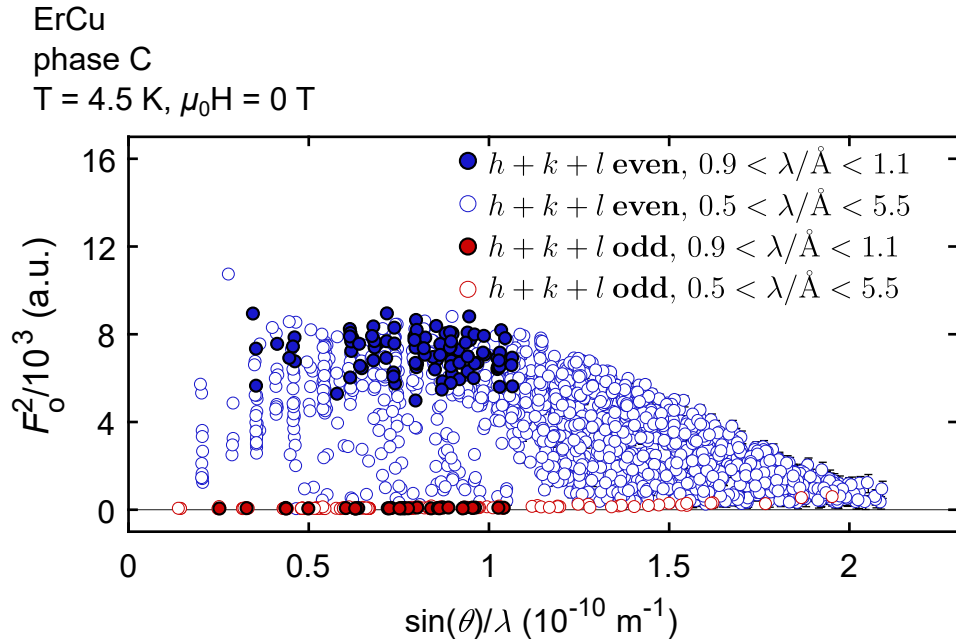


Figure 3.77.: Nuclear structure factor of ErCu. A large set of structural Bragg reflections was measured at the time-of-flight diffractometer SXD. Presented is the nuclear structure factor, as measured in phase C at 4.5 K. Therefore, integrated intensities of the recorded Bragg peaks, i.e., $I = F_o^2$, are shown as a function of $\sin(\theta)/\lambda$. The whole set of 1824 structural Bragg reflections, which were recorded with neutrons of wavelengths $0.5 \text{ \AA} < \lambda < 5.5 \text{ \AA}$, does not display the behavior expected for the CsCl crystal structure of ErCu. In contrast, Bragg reflections that were recorded with neutrons of small wavelength spread, i.e., $0.9 \text{ \AA} < \lambda < 1.1 \text{ \AA}$, display the expected behavior as they split into two groups of strongly suppressed (when $h + k + l$ is odd) and strongly enhanced reflections (when $h + k + l$ is even) following the structure factor of ErCu. Presumably, the unphysical wavelength dependence of the whole data set originates in Renninger effects, which are typically strongly wavelength dependent.

wavelengths $0.5 \text{ \AA} < \lambda < 5.5 \text{ \AA}$ are represented by non-filled circles. The red circles describe Bragg peaks with odd values of $h + k + l$ and the blue ones with even values of $h + k + l$. The pattern does not follow the structure factor $F_{\text{ErCu}}^2(h, k, l)$, but displays a strong $\sin(\theta)/\lambda$ dependence. In contrast, the 133 nuclear Bragg reflections that were recorded with neutrons of small wavelength spread $0.9 \text{ \AA} < \lambda < 1.1 \text{ \AA}$, represented by filled circles, follow the structure factor $F_{\text{ErCu}}^2(h, k, l)$, featuring two groups of strongly enhanced and strongly suppressed reflections.

Magnetic Rietveld refinements using JANA2006 [59] were carried out on the reduced data set containing 133 structural and 170 magnetic ($\pi\pi 0$) Bragg reflections. The integrated intensities were considered as nuclear and magnetic structure factors $F_o^2(h, k, l)$, respectively. For the refinement of the crystal structure, $Pm\bar{3}m$, a scale parameter, and a quadratic (isotropic) displacement parameter were introduced. For the magnetic refinements the (uniform) size of the magnetic moments, and $d - 1$ ratio parameters for d possible magnetic domains were introduced.

Magnetic structure	s1	s2	s4
Allover refinement:			
Number of reflections: 303			
$R [F^2 \geq 3\sigma (F^2)]:$	19.65	5.20	5.10
$wR (F^2):$	63.61	11.61	11.13
Nuclear refinement:			
Number of reflections: 133			
$R [F^2 \geq 3\sigma (F^2)]:$	14.61	4.19	4.10
$wR (F^2):$	34.44	10.33	10.12
Magnetic refinement:			
Number of reflections: 170			
$R [F^2 \geq 3\sigma (F^2)]:$	44.89	10.24	10.04
$wR (F^2):$	161.63	18.67	16.96
mag. moment (μ_B):	2.76(3)	4.860(4)	4.143(4)
U_{iso}	0.013932	-0.000166	0.000378

Table 3.11.: Magnetic Rietveld refinements for the ground state in phase C at 4.5 K. Integrated intensities $I = F_o^2$ of the 170 magnetic ($\pi\pi 0$) reflections and 133 structural reflections, which were recorded with neutrons of wavelengths $0.9 \text{ \AA} < \lambda < 1.1 \text{ \AA}$, were used for the refinements. The three magnetic structures s1, s2, and s4 that were considered as magnetic ground state are the only single- k structures among the 21 commensurate ($\pi\pi 0$) structures in Tab. 3.1 that consist of basis functions of one IR only. For the refinement of the crystal structure, $Pm\bar{3}m$, a scale parameter and a quadratic (isotropic) displacement parameter were introduced. For the magnetic refinements the (uniform) size of the magnetic moment and $d - 1$ ratio parameters for d possible domains were introduced.

As magnetic ground state in phase C, the three commensurate ($\pi\pi 0$) structures s1, s2, and s4 were considered. These three structures represent the only single- k structures among the 21 commensurate ($\pi\pi 0$) structures in Tab. 3.1 that contain basis functions from one IR only. s2 and s4 are superpositions of $\Gamma_9(\mathbf{k}_c)$ basis functions and s1 contains only $\Gamma_3(\mathbf{k}_c)$ basis functions. Multi- k structures were not considered due to difficulties to implement them in JANA2006 in combination with time-of-flight data. As shown in the following, excellent refinement results were obtained for the two structures s2 and s4. The five structures s2, s4, d2, d5, and t2 share the same magnetic structure factors and cannot be distinguished from each other by means of Rietveld refinements in zero magnetic field (cf. Sec. 3.3.3.6), as they all consist of $\Gamma_9(\mathbf{k}_c)$ basis functions only. Hence, the Rietveld refinements carried out on ErCu confirm that the ground state in phase C consists of $\Gamma_9(\mathbf{k}_c)$ basis functions only, which is in excellent agreement with the experiments in Sec. 3.5.2.3.

Tab. 3.11 shows the results obtained from the Rietveld refinements. The low R -values of roughly 4 for the two structures s2 and s4 confirm that the magnetic ground state in phase C consists of $\Gamma_9(\mathbf{k}_c)$ basis functions only. Further, the low R -values for the

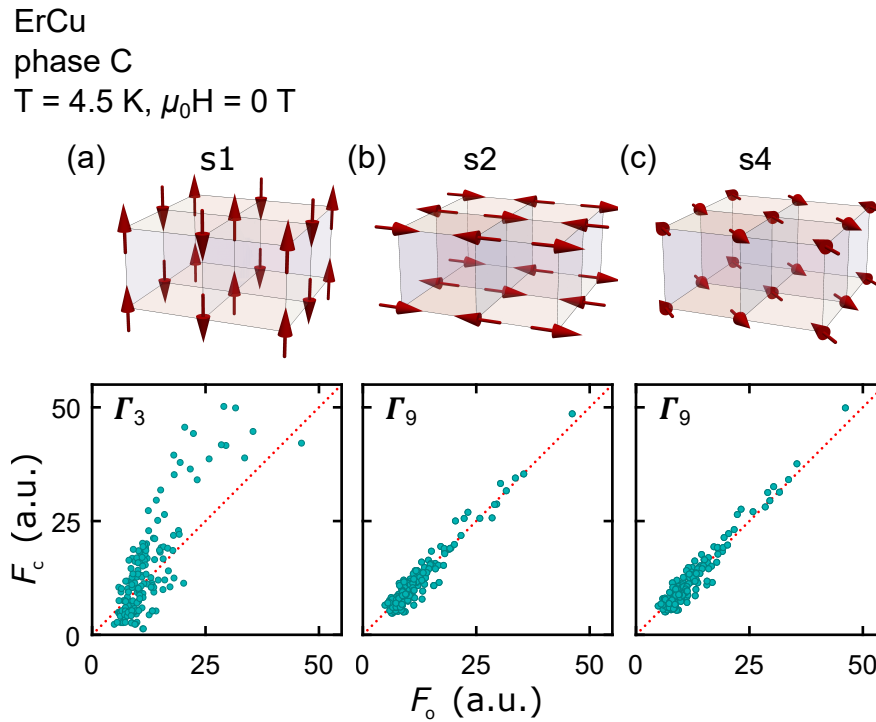


Figure 3.78.: Calculated vs. observed structure factors F_c/F_o for the magnetic Rietveld refinements, which were carried out in phase C at 4.5 K. The structure factors F_o inferred from the recorded data are compared with the structure factors F_c calculated for each of the three magnetic structures by means of JANA2006 [59]. Shown are magnetic structure factors as inferred from Bragg reflections of the reduced data set, i.e., which were recorded with neutrons of wavelengths $0.9 \text{ \AA} < \lambda < 1.1 \text{ \AA}$. The three structures taken into account are the only single- k structures among the 21 commensurate $(\pi\pi 0)$ structures (cf. Tab. 3.1) that consist of basis functions from one IR only. (a) Refinement of the structure s1, which is associated with the IR Γ_3 . (b) Refinement of the structure s2, which is associated with the IR Γ_9 . (c) Refinement of the structure s4, which is associated with the IR Γ_9 .

nuclear structure refinement of roughly 5 confirm the CsCl crystal structure of ErCu. In contrast, for the structure s1 the R -values were considerably larger. As displacement parameter U_{iso} slightly negative values were obtained for both magnetic structures s2 and s4, which is unphysical. A magnetic moment of $4.860 \mu_B$ was obtained for the structure s2 and a moment of $4.143 \mu_B$ for the structure s4. Both values are considerably smaller than $9.58 \mu_B$, the moment inferred from Hund's rules for the free Er^{3+} ion. No extinction correction was performed.

Fig. 3.78 indicates graphically the excellent agreement of the magnetic structure factors F_c , calculated for the two magnetic structures s2 and s4, with the values F_o , inferred from the recorded data. All points lie in the vicinity of the bisectrix, on which calculated and measured structure factors are equal.

3.5.2.5. Magnetic Field Along Twofold Direction

Neutron diffraction of sample OFZ104-3-3 with fields along twofold $\langle 110 \rangle$ directions was carried out at the diffractometer E4 [206]. The experimental setup was the same as for the experiments in Sec. 3.5.2.1. However, between the two sets of experiments the sample was removed.

The main results of these experiments may be summarized as follows:

- The ground states in phases C, IC1, and IC2 are relatively stable for fields up to 2 T. Accordingly, the magnetic phases at zero magnetic field, C, IC1, and IC2, extend to pockets of the $\langle 110 \rangle$ phase diagram, which may be labeled M_I , M_{II} , and M_{III} , respectively.
- Temperature dependences of the arms $A_{1,x}^{ic} = [\frac{1}{2} \pm \delta, \frac{1}{2}, 0]_{\sim}$ and $A_{1,y}^{ic} = [\frac{1}{2}, \frac{1}{2} \pm \delta, 0]_{\sim}$ are distinctively different in fields along [110], even though the symmetry between the k -arms is preserved by the [110] field direction. This is not expected in a non-chiral space-group and may be related to tiny misalignment of the sample.

The section is organized as follows. First, temperature dependences in relatively low fields of 2 T are presented. The observed Bragg peaks and their temperature dependences were very similar to the temperature dependences at zero magnetic field, which were presented in Sec. 3.5.2.1. In particular, the same types of propagation vectors were observed, namely of the stars $\{\mathbf{k}_c\}$, $\{\mathbf{k}_{ic,1}\}$, $\{\mathbf{k}_{ic,2}\}$, and $\{\mathbf{k}_{ic,3}\}$. Second, temperature dependences in relatively high fields ≥ 8 T are presented.

For these experiments, the two magnetic Bragg positions $\mathbf{q}_1 = (\frac{1}{2}, -\frac{1}{2}, 0)$ and $\mathbf{q}_2 = (\frac{1}{2}, -\frac{1}{2}, 1)$ as well as incommensurate satellites in the vicinity of the two positions were studied by means of temperature sweeps at different magnetic fields, namely 2 T, 8 T, 11 T, and 13.5 T. At zero magnetic field magnetic Bragg peaks were present at 21 different q -positions in the vicinity of $(\frac{1}{2}, -\frac{1}{2}, 0)$, as pointed out in Sec. 3.5.2.1. These peaks were indexed with propagation vectors of the stars $\{\mathbf{k}_c\}$, $\{\mathbf{k}_{ic,1}\}$, $\{\mathbf{k}_{ic,2}\}$, and $\{\mathbf{k}_{ic,3}\}$, respectively. For the study, reported here, peaks, which are associated with these four propagation vector stars were investigated in the vicinity of the two positions \mathbf{q}_1 and \mathbf{q}_2 by means of rocking scans. Integrated intensities were inferred by the same procedure as described in Sec. 3.5.2.1.

Among the Bragg peaks considered in this section some are expected to exhibit similar temperature dependences due to symmetry arguments, which may be summarized as follows:

- (s.i) Bragg peaks associated with the same k -arm or with conjugated k -arms should exhibit qualitatively similar temperature dependences, as long as the polarization

factor [21] in the structure factor does not change at the two q -positions, where the Bragg peaks are located.

(s.ii) Bragg peaks from same crystallographic stars should have similar temperature dependences, if their k -arms have the same orientation in the field.

In fact, (s.i) was confirmed in these experiments. However, (s.ii) did not hold true in general.

For each temperature sweep that was carried out at a field B , the protocol was as follows: The history was (i) zero field cooling to 2 K and (ii) increasing the field to the value B . The temperature sweep was then carried out with increasing temperature. It was avoided to approach the paramagnetic state, as in prior test experiments the sample fell from the sample holder, when critical temperatures were approached in high magnetic fields.

Fig. 3.79 shows the temperature dependences of magnetic Bragg peaks, as recorded in a field of 2 T. As seen in the following, the peaks associated with propagation vectors of the stars $\{\mathbf{k}_c\}$, $\{\mathbf{k}_{ic,1}\}$, $\{\mathbf{k}_{ic,2}\}$, and $\{\mathbf{k}_{ic,3}\}$ feature qualitatively the same temperature dependences as in zero magnetic field (cf. Fig. 3.75) revealing three magnetically ordered phases. Accordingly, the three phases C, IC1, and IC2 may be part of phase pockets M_I , M_{II} , and M_{III} that extend at least up to fields of ≈ 2 T.

Shown in Fig. 3.79 (d) are temperature dependences of the two commensurate Bragg peaks located at \mathbf{q}_1 and \mathbf{q}_2 . Both of them display similar temperature dependences, in agreement with (s.i) as they both belong to the k -arm A_1^c . In phase pocket M_I , maximum integrated intensities of the Bragg peak at \mathbf{q}_1 were twice as large as integrated intensities of the Bragg peak at \mathbf{q}_2 .

The peaks at \mathbf{q}_1 and \mathbf{q}_2 belong to the same k -arm but the size of the integrated intensities differs by a factor 2. This difference of integrated intensities at \mathbf{q}_1 , which has lower q , and at \mathbf{q}_2 , which has larger q , may be due to a combination of different effects. The magnetic cross section is namely proportional to:

- (q.i) the Debye-Waller factor [21, 22], which is smaller at \mathbf{q}_2 than at \mathbf{q}_1 .
- (q.ii) the square of the magnetic form factor [21, 22], which is smaller at \mathbf{q}_2 than at \mathbf{q}_1 .
- (q.iii) the magnetic polarization factor [21], which does not depend on the modulus q , but on the direction of magnetic moments.

Fig. 3.79 (a) and (b) show temperature dependences at 2 T of satellite Bragg peaks associated with propagation vectors of the stars $\{\mathbf{k}_{ic,2}\}$ and $\{\mathbf{k}_{ic,1}\}$, respectively. The satellites located in the vicinity of \mathbf{q}_1 (Figs. 3.79 (a1) and (b1)) and the satellites located in the vicinity of \mathbf{q}_2 (Figs. 3.79 (a2) and (b2)) feature qualitatively the same temperature dependences as corresponding peaks at zero magnetic field. The peaks associated with

the star $\{\mathbf{k}_{ic,2}\}$ are relatively strong in phase pocket M_{III} , and the peaks associated with the star $\{\mathbf{k}_{ic,1}\}$ in phase pocket M_{II} , respectively. In both phase pockets, the satellites with larger q lying in the vicinity of \mathbf{q}_2 are roughly one order of magnitude weaker than the corresponding counterparts at smaller q lying in the vicinity of \mathbf{q}_1 . This decrease as a function of q is in fact much stronger than for the commensurate Bragg peaks located at \mathbf{q}_1 and \mathbf{q}_2 in phase pocket M_I , where the factor is given by 2. Accordingly, this decrease in phases M_{II} and M_{III} when compared with M_I is mainly due to the magnetic polarization factor (q.iii). In particular, it may be inferred that the magnetic moments in phase pockets M_{II} and M_{III} are not perpendicular to \mathbf{q}_2 . Satellite peaks associated with propagation-vectors of the star $\{\mathbf{k}_{ic,3}\}$, as recorded in the vicinity of \mathbf{q}_1 , are shown in Fig. 3.79 (c). Temperature dependences are again similar to the dependences at zero magnetic field. The satellites associated with propagation vectors of the star $\{\mathbf{k}_{ic,3}\}$ and located in the vicinity of \mathbf{q}_1 are vanishingly small.

At higher magnetic fields, i.e., 8 T, 11 T, and 13.5 T, only peaks associated with propagation vector stars $\{\mathbf{k}_c\}$ and $\{\mathbf{k}_{ic,2}\}$ were investigated, as intensity at positions associated with the $\{\mathbf{k}_{ic,3}\}$ and $\{\mathbf{k}_{ic,1}\}$ propagation vector stars were vanishingly small. Fig. 3.80 shows all finite integrated intensities determined at 8 T, 11 T, and 13.5 T, respectively. Commensurate Bragg peaks were detected only at 8 T and 11 T, but not at 13.5 T.

Figs. 3.80 (d) and (e) show the integrated intensities of the commensurate $(\pi\pi 0)$ peaks located at \mathbf{q}_1 and \mathbf{q}_2 at the fields 8 T and 11 T, respectively. The temperature dependences of the two peaks were qualitatively equivalent, in agreement with (s.i). However, \mathbf{q}_1 was roughly one order of magnitude weaker than \mathbf{q}_2 . This may be explained by (q.iii) and a change of the direction of magnetic moments, when compared with the direction of moments in phase pocket M_I , where the ratio between \mathbf{q}_1 and \mathbf{q}_2 was given by a factor 2. Accordingly, at 8 T the moments are more tilted towards the $\parallel +\hat{\mathbf{q}}_1$ direction than in phase pocket M_I . At 11 T almost no intensity is visible at commensurate peak positions of the $\langle \frac{1}{2} \frac{1}{2} 0 \rangle$ star. At 13.5 T the integrated intensities of commensurate Bragg peaks are vanishingly small.

Incommensurate Bragg peaks of the $\{\mathbf{k}_{ic,2}\}$ propagation vector star were observed in all three fields, i.e., 8 T, 11 T, and 13.5 T. The following two observations were made in our study:

- (o.i) The arms $A_{1,x}^{ic} = [\frac{1}{2} \pm \delta, \frac{1}{2}, 0]_{\sim}$ and $A_{1,y}^{ic} = [\frac{1}{2}, \frac{1}{2} \pm \delta, 0]_{\sim}$ featured considerably different temperature dependences, even though the symmetry between $A_{1,x}^{ic}$ and $A_{1,y}^{ic}$ was preserved by the field direction.
- (o.ii) Temperature dependences were qualitatively different at different fields.

In the following, the temperature dependences of peaks associated with $\{\mathbf{k}_{ic,2}\}$ are

presented. We point out in detail, why our observation (o.i) stands in contrast to our expectation (s.ii), which was established by symmetry arguments.

Fig. 3.80 (a) shows temperature dependences of peaks associated with $\{\mathbf{k}_{ic,2}\}$ in a field of 8 T. Fig. 3.80 (a1) shows the integrated intensities of the peaks $(\frac{1}{2} \pm \delta, -\frac{1}{2}, 0)$ (blue) and $(\frac{1}{2}, -\frac{1}{2} \pm \delta, 0)$ (red), and Fig. 3.80 (b1) shows the counterpart satellites in the vicinity of \mathbf{q}_2 . The Bragg peak intensities reflect the temperature dependences of the arms $A_{1,x}^{ic}$ (blue) and $A_{1,y}^{ic}$ (red), respectively (cf. Sec. 3.3.4.1). The satellites in the vicinity of \mathbf{q}_2 are roughly one order of magnitude stronger than the satellites around \mathbf{q}_1 . Compared to phase M_I , where the ratio is given by 2, the polarization factor has changed (q.iii). As expected, all peaks having the same color feature the same temperature dependences, which is in agreement with (s.i). As the magnetic field along [110] preserves the symmetry between the two arms $A_{1,x}^{ic}$ and $A_{1,y}^{ic}$, their temperature dependences are also expected to be qualitatively equivalent (cf. argument (s.iii)). However, the red curves, reflecting the temperature dependence of $A_{1,x}^{ic}$, are distinctively different from the blue curves, reflecting the temperature dependence of $A_{1,y}^{ic}$. For temperatures ranging from 2 K to 5 K all integrated intensities are vanishingly small. However, above 5 K the Bragg peaks associated with $A_{1,x}^{ic}$ increase steeply, whereas the peaks associated with $A_{1,y}^{ic}$ display a shallow increase.

In Fig. 3.80 (b) the data recorded in a field of 11 T are shown. Again the integrated intensities of Bragg peaks located in the vicinity of \mathbf{q}_2 (Fig. 3.80 (b2)) were roughly one order of magnitude stronger than the peaks located in the vicinity of \mathbf{q}_1 (Fig. 3.80 (b1)). The curves in the same color feature qualitatively equivalent temperature dependences, as the peaks belong to conjugated k -arms, i.e., to the same Ω -arm (cf. argument (s.i)). The curves with different colors again feature distinctively different temperature dependences, which is again at odds with (s.ii). At low temperatures ranging from 2 K to roughly 6 K, the integrated intensities of peaks associated with $A_{1,x}^{ic}$ have a plateau, whereas the peaks associated with $A_{1,y}^{ic}$ are vanishingly small. At higher temperatures, the integrated intensities of peaks associated with $A_{1,x}^{ic}$ decrease steeply, whereas integrated intensities of peaks associated with $A_{1,y}^{ic}$ increase strongly.

In Fig. 3.80 (c) the temperature dependences in a field of 13.5 T are shown. No qualitative differences to the curves in 11 T were observed.

The distinctively different temperature dependences of arms $A_{1,x}^{ic}$ and $A_{1,y}^{ic}$ are curious and at odds with our expectations. As explained in the following, this curiosity may be related to misalignment of the sample. The k -arms are namely supposed to have similar temperature dependences which is related to the non-chirality of the space group (cf. Ref. [209]) and is explained in the following. A reflection $R_{\hat{n}}$ at the plane, which contains $(\frac{1}{2}, \frac{1}{2}, 0)$ and which is perpendicular to the reciprocal space vector $\hat{n} = (1, -1, 0)$ maps

the k -arm $A_{1,x}^{ic}$ on $A_{1,y}^{ic}$ and vice versa. The reflection $R_{\hat{n}}$ represents a good symmetry of the space group. Furthermore, the operator $R_{\hat{n}}$ maps the magnetic propagation vector $(\frac{1}{2} - \delta, \frac{1}{2}, 0)$ on the vector $(\frac{1}{2}, \frac{1}{2} - \delta, 0)$, as it is:

$$R_{\hat{n}} \left(\frac{1}{2} - \delta, \frac{1}{2}, 0 \right) = \left(\frac{1}{2}, \frac{1}{2} - \delta, 0 \right) \quad (3.82)$$

The reflection $R_{\hat{n}}$ does not affect the field direction, i.e., $R_{\hat{n}}\mathbf{B} = \mathbf{B}$. Hence, the two propagation vector arms have the same orientation in the magnetic field along [110] suggesting that temperature dependences should be qualitatively equivalent. However, in the experiments, temperature dependences were distinctively different.

We explain this curiosity by a tiny misalignment of the sample implying that the field was not perfectly directed along [110] causing an energetic difference between $A_{1,x}^{ic}$ on $A_{1,y}^{ic}$ in the field.

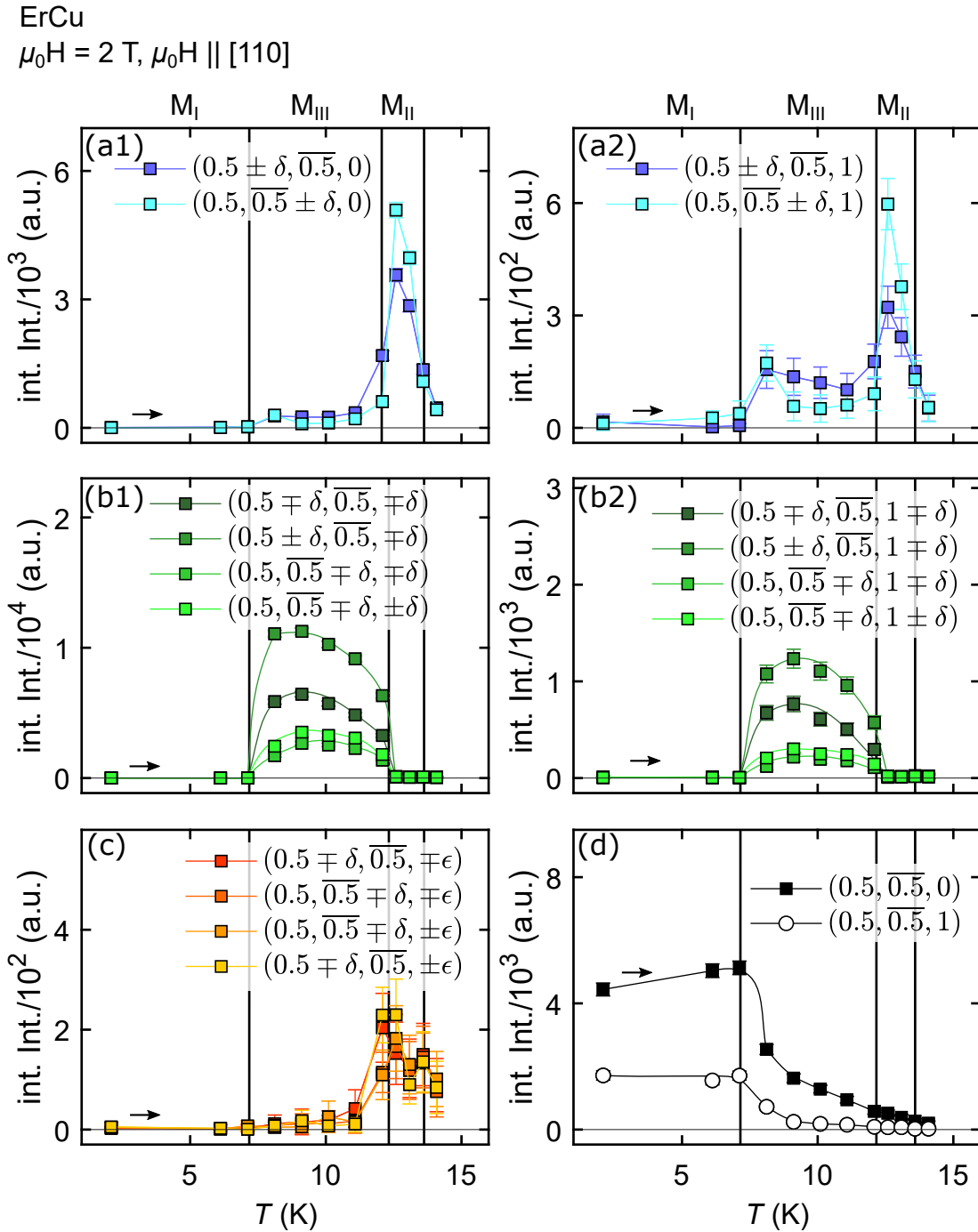


Figure 3.79.: Temperature dependences of Bragg peaks in a relatively low field of 2 T. The dependences are qualitatively equivalent to those in zero magnetic field. Integrated intensities as a function of temperature are shown of magnetic Bragg peaks located in the vicinity of $(\frac{1}{2}, -\frac{1}{2}, 0)$ and in the vicinity of $(\frac{1}{2}, -\frac{1}{2}, 1)$. (a) Incommensurate satellites indexed with propagation vectors of the star $\{\mathbf{k}_{ic,2}\}$ in the vicinity of (a1) $(\frac{1}{2}, -\frac{1}{2}, 0)$ and in the vicinity of (a2) $(\frac{1}{2}, -\frac{1}{2}, 1)$. (b) Incommensurate satellites indexed with propagation vectors of the star $\{\mathbf{k}_{ic,1}\}$ in the vicinity of (b1) $(\frac{1}{2}, -\frac{1}{2}, 0)$, and in the vicinity of (b2) $(\frac{1}{2}, -\frac{1}{2}, 1)$. (c1) Magnetic Bragg peaks that are indexed with propagation vectors of the star $\{\mathbf{k}_{ic,3}\}$, as detected in the vicinity of $(\frac{1}{2}, -\frac{1}{2}, 0)$. (d) The two commensurate magnetic Bragg peaks $(\frac{1}{2}, -\frac{1}{2}, 0)$ and $(\frac{1}{2}, -\frac{1}{2}, 1)$, both of which belong to the k -arm A_1^c .

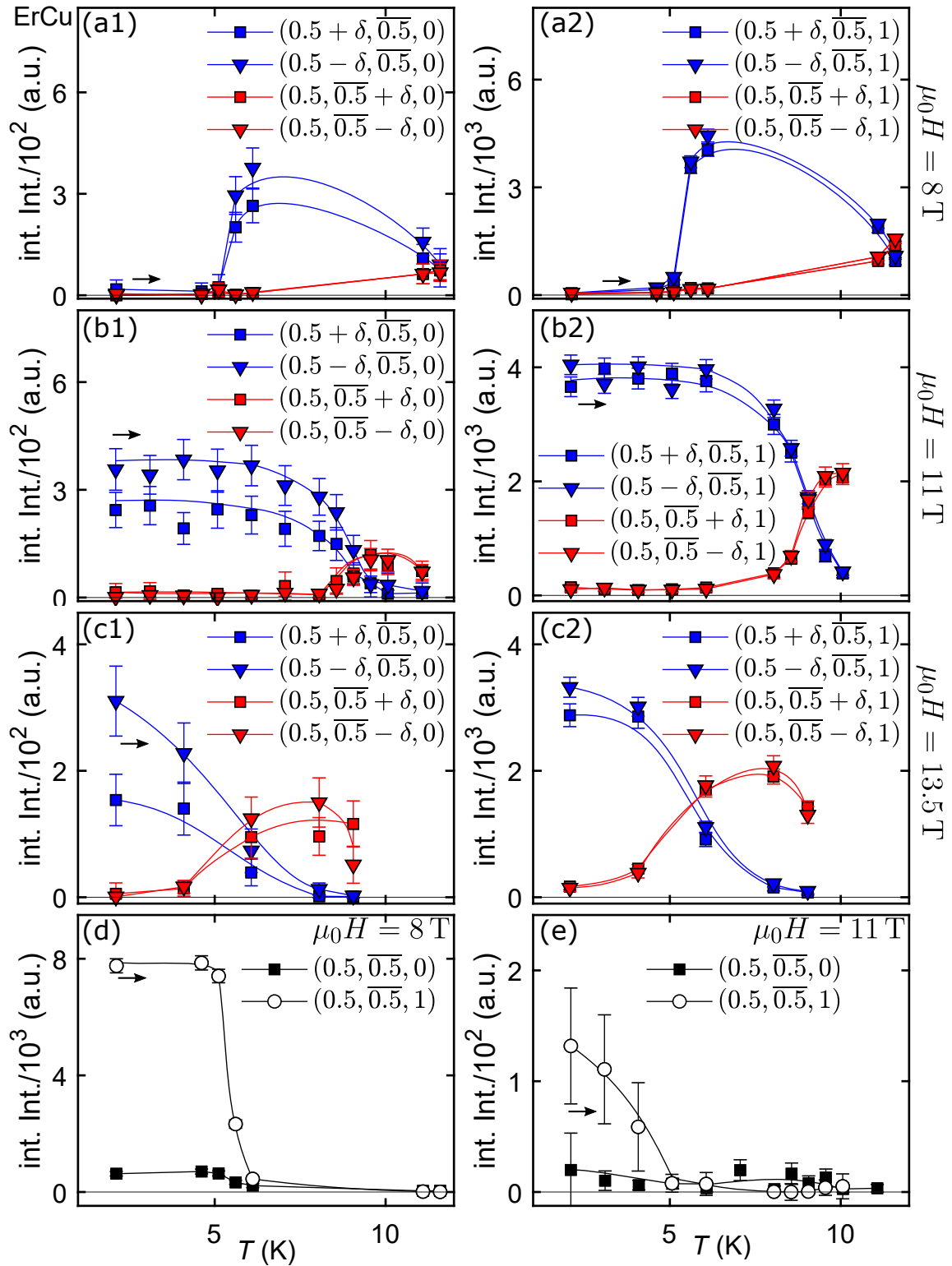


Figure 3.80.: Temperature dependences of magnetic Bragg peaks in relatively high fields along $[110]$. (a)-(c) Incommensurate peaks in the vicinity of the commensurate position $(0.5, \overline{0.5}, 0)$ that are indexed with propagation vectors of the star $\{\mathbf{k}_{ic,2}\}$ in fields of (a1) 8 T, (b1) 11 T, and (c1) 13.5 T. Corresponding satellites in the vicinity of the commensurate position $(0.5, \overline{0.5}, 1)$ in fields of (a2) 8 T, (b2) 11 T, and (c2) 13.5 T. (d) Commensurate peaks in a field of 8 T and (e) in a field of 11 T.

3.6. Summary and Outlook

In this chapter we presented microscopic studies of HoCu, TmCu, and ErCu. The main results may be summarized as follows:

- We detected multitudinous magnetic ground states, including multi- k structures, structures with long-wavelength modulations, structures that are topologically protected against unwinding, and structures giving rise to a complex electronic structure with finite Chern numbers, magnetic charges, and an orbital magnetization.
- We reported several mechanisms that suggest the emergence of an unconventional Hall effect due to Berry phases. This Hall effect is related to magnetic long-range order but does not arise due to an ordinary anomalous Hall effect depending linearly on the net magnetization.

In the first part of our **study of HoCu** a sophisticated neutron diffraction study using single crystals was presented. The aim of the neutron study was on one hand to determine the magnetic ground states at zero magnetic field. On the other hand, magnetic ground states of the $\langle 110 \rangle$ and $\langle 111 \rangle$ phase diagrams were studied. A detailed picture of the three ordered phases at zero magnetic was obtained. In phase C, the magnetic ground state represents the commensurate antiferromagnet t_2 . This structure is triple- k , highly noncoplanar featuring finite scalar spin chiralities, and may be stabilized by quadrupolar interactions. A finite Berry curvature and magnetic charges in the electronic structure may emerge together with the noncoplanar magnetic ground state. In phase IC1, the magnetic ground state represents the triple- k structure \mathcal{T}_2 , which is a superposition of one commensurate and two incommensurate propagation vectors. The ground state has a long wavelength in real space of the order of 90 \AA . The structure is highly noncoplanar and the Berry curvature may possibly be finite. The ground state possesses a non-trivial topology, which is related to a winding number. Accordingly, the ground state is protected against unwinding, i.e., it cannot be continuously transformed into a collinear antiferromagnet. Furthermore, the structure may be portrayed as an assembly of monopoles and antimonopoles in real-space. In phase IC2, the ground state is a complex multi- k structure combining several commensurate and incommensurate propagation vectors. An educated guess \mathcal{M}_1 was proposed as the magnetic ground state in this phase. The structure \mathcal{M}_1 is highly noncoplanar and its topology is non-trivial being protected against unwinding into a collinear antiferromagnet. In the second part of our study of HoCu, the interplay of magnetic order and the electronic structure was investigated. Therefore, the conduction electrons of HoCu were studied in the presence of $(\pi\pi 0)$ order. It was found, that (i) noncoplanar $(\pi\pi 0)$ structures may cause a finite Berry curvature associated with a complex assembly of magnetic monopoles and antimonopoles in the electronic structure. A lattice

distortion, which may be reflected, for instance, by the presence of magnetostriction, has a vast impact on the topology of the electronic structure and causes finite Chern numbers, an orbital magnetization and an anomalous Hall effect, which is not ordinary. Furthermore, it was found that also (ii) noncollinear $(\pi\pi 0)$ antiferromagnets, which are collinear at zero magnetic field and coplanar in fields, may induce an anomalous Hall effect. We further established, that (iii) $(\pi\pi 0)$ antiferromagnets with a long-wavelength modulation may possibly cause a topological Hall effect at finite magnetic fields.

In our **study of ErCu**, magnetic ground states were investigated by means of single-crystal neutron diffraction. First, ground states were studied at zero magnetic field. In phase C, the ground state was found to be commensurate of type $(\pi\pi 0)$. The structure may be single- k or multi- k . In phases IC1 and IC2 the ground states are multi- k and have a long wavelength in real-space exceeding 170 Å. Second, magnetic ground states at magnetic fields were investigated. At higher magnetic fields, magnetic ground states are predominantly superpositions of incommensurate propagation vectors.

In our **study of TmCu**, magnetic ground states were investigated by means of single-crystal neutron diffraction. First, ground states at zero magnetic field were investigated. In phase C the ground state is a commensurate, single- k $(\pi\pi 0)$ antiferromagnet. In phase IC, just below the ordering temperature, the ground state is multi- k and has a long wavelength in real space of the order of 110 Å. Second, magnetic ground states were investigated for fields along the major cubic directions. Multi- k structures with long-wavelength modulations were identified. For fields along $\langle 110 \rangle$ directions, an exotic phase, labeled phase M_{b1} , was observed featuring a ground state distinctively different from $(\pi\pi 0)$ antiferromagnetism. The magnetic structure in M_{b1} has a periodicity, which is 7 times as large as the crystallographic unit cell.

We turn to a conclusion of our comprehensive study on the rare-earth intermetallics RCu . In **all three compounds** competing interactions cause a variety of magnetic ground states, including long-wavelength modulations, multi- k states, ground states with non-trivial topology, and a non-trivial electronic structure. The compounds, all of which are centrosymmetric, are a playground for further studies and may be promising candidates for hosting novel stabilization mechanisms of topological order.

In fact, the complex properties, which were observed in this chapter, preclude a full microscopic understanding. We raise the following questions for future studies on the RCu series:

- What is the origin of numerous phase transitions?
- What is the origin of modulations with long wavelengths in real-space?
- Are there other ground states among the multitudinous multi- k states possessing non-trivial topology?

-
- Is there orbital order, which is related to magnetic order?
 - Are there other relevant mechanisms that induce Berry phases and have an impact on the transport properties?

4. Incommensurate Antiferromagnetism in EuPtSi_3

In this chapter, a microscopic study of the antiferromagnetic properties of the tetragonal compound EuPtSi_3 is presented. As the crystal structure lacks an inversion symmetry center, EuPtSi_3 may host ground states with non-trivial topology, as suggested by unconventional contributions to the Hall effect, which may have topological origin [19]. In our previous study (cf. Ref. [19]) the magnetic ground state at low temperatures in zero magnetic field, labeled phase A, was portrayed as antiferromagnet with an incommensurate modulation along the tetragonal c -axis, suggesting a spiral structure with a wavelength of the order of 100 \AA . However, as reported in the following, this picture is incomplete. As the main result of single-crystal neutron diffraction, we show that the ground state in phase A has an incommensurate modulation also in the tetragonal ab -plane. The wavelength is of the order of 600 \AA . The ground state is multi- k representing a superposition of at least three magnetic propagation vectors. Experimental signatures suggest an interpretation as a lattice of antiferromagnetic Skyrmions (cf. Ref. [210]).

The presentation of our study is organized as follows. First, an introduction of the properties as known prior to our study is presented in Sec. 4.2. Second, the results of the microscopic study on magnetic long-range order in zero magnetic field are presented in Sec. 4.2. The magnetic propagation vectors of the ground state in phase A at zero magnetic field were determined by means of single crystal neutron diffraction, as reported in Sec. 4.2.1. Representational analysis and magnetic structure determination are reported in Sec. 4.2.2 and Sec. 4.2.3. The solutions include structures with non-trivial topology, such as a lattice of antiferromagnetic Skyrmions, as reported in Sec. 4.2.3.

4.1. Introduction to EuPtSi_3

The fourth compound studied as part of this thesis, EuPtSi_3 , has a non-centrosymmetric space group and displays $4f$ -magnetism. It represents a promising candidate material as host for antiferromagnetic structures with non-trivial topology. The reasons are as follows. Recently, signatures of modulated spin structures with a long wavelength were

detected (cf. Ref. [19]). Due to the lack of inversion symmetry, Dzyaloshinskii-Moriya interactions [14, 15], which are crucial for the stabilization of topological spin states such as Skyrmions [6, 211–213], may cause the long-wavelength modulations in EuPtSi_3 . The unconventional Hall effect in EuPtSi_3 , which we reported in Ref. [19], may be due to non-trivial Berry phases associated with a non-trivial topology of the antiferromagnetic ground states in EuPtSi_3 (cf. Refs. [9, 109, 110]).

EuPtSi_3 crystallizes in the achiral [214], non-centrosymmetric $I4mm$ crystal structure, which is also referred to as BaNiSn_3 structure (cf. Refs. [215, 216]). The lattice parameters of the tetragonal unit cell are $a = 4.286 \text{ \AA}$ and $c = 9.795 \text{ \AA}$ [19]. Related compounds of the EuTX_3 series, where T is a d -transition element and X e.g. Ge [217], such as EuRhGe_3 [218, 219], EuIrGe_3 [218], EuCoGe_3 [219], EuPdGe_3 [220, 221], EuNiGe_3 [222] or EuPtGe_3 [223], exhibit complex magnetic phase diagrams. Accordingly, these materials may in principle also be candidates for hosting ground states with non-trivial topology. In contrast, BaPtSi_3 was found to be a BCS-like superconductor [216]. LaPdSi_3 and LaPtSi_3 are also superconductors [224].

Magnetic long-range order in EuPtSi_3 at temperatures below $< 18 \text{ K}$ originates from the Eu^{2+} rare-earth ions, where the orbital momentum is quenched [215]. The rare-earth ions may be viewed as localized moments having the free-ion value of Eu^{2+} , which is given by $\mu_{\text{eff}} = g \cdot \sqrt{J(J+1)} \mu_B = 7.94 \mu_B/\text{f.u.}$ ($J = S = \frac{7}{2}$, $L = 0$) according to Hund's rules. A complex magnetic phase diagram has been determined, as shown in Fig. 4.1 (a) for $\langle 100 \rangle$, $\langle 110 \rangle$, and $\langle 100 \rangle$ and inferred from ac susceptibility, specific heat, and magnetoresistance. Note that despite the quenched orbital momentum of Eu^{2+} , the phase diagram exhibits signatures characteristic of tetragonal anisotropies (cf. Ref. [215]). This observation is in agreement with anisotropies revealed by Mössbauer spectroscopy [215]. The tetragonal anisotropies are, e.g., reflected by the anisotropy of the critical fields, which are higher for the basal $\langle 100 \rangle$ and $\langle 110 \rangle$ directions than for the $\langle 001 \rangle$ direction. Accordingly, the $[001]$ axis may be an easy direction in agreement with Ref. [215]. The phase diagrams for fields in the basal plane feature four ordered phases, whereas for fields along the c -axis two ordered phases are observed. We note that the tetragonal anisotropies may be an indication of a mixed valence of Eu, suggesting a small ratio of Eu^{3+} valence states in addition to the prevailing Eu^{2+} valence states.

In zero magnetic field two magnetically ordered phases are established. The specific heat features a lambda-anomaly at $T_c = 17 \text{ K}$ characteristic of a second-order phase transition, as well as a small second maximum at slightly lower temperatures [19]. The existence of two anomalies may be clearly resolved when magnetic fields are applied. At $T_c = 17 \text{ K}$ in zero magnetic field, the susceptibility, $\text{Re}\chi_{\text{ac}}$, displays a maximum. Curie-Weiss behavior with positive Curie-Weiss temperature is observed in agreement with Ref. [215], regardless

whether excitation fields are directed along $\langle 100 \rangle$, $\langle 110 \rangle$, or $\langle 001 \rangle$ [19]. For the basal plane the Curie-Weiss temperature is given by 4.1 K, whereas for the c -axis it is given by 9.7 K. The positive sign of the Curie-Weiss temperature is curious in an antiferromagnet such as EuPtSi_3 , where in fact a negative value is expected. The fluctuating moment, as inferred from the slope of $\text{Re } \chi_{\text{ac}}^{-1}(T)$, amounted to $(7.8 \pm 0.1) \mu_B/\text{f.u.}$, which is slightly smaller than the free-ion value of Er^{2+} [19].

Measurements of the Hall effect reveal an unconventional contribution $\Delta\rho_{xy}$, which arises together with magnetic long-range order but is not related to a conventional anomalous Hall effect, where the Hall resistivity would scale monotonically with the net magnetization. In particular, the additional Hall contribution may be of topological origin suggesting a non-trivial topology of the magnetic ground states. Figs. 4.1 (a)-(c) show the unconventional contribution to the Hall effect as a function of field at different temperatures. The additional contribution to the Hall effect is clearly related to magnetic long-range order, as it vanishes in the field-polarized and the paramagnetic regime. The additional contribution was inferred from the Hall signal by subtracting from the total Hall effect the normal contribution and an anomalous contribution that is linear in the net magnetization (Figs. 4.1 (d)-(f)). As pointed out in Ref. [19] the additional Hall signal $\Delta\rho_{xy}$, when related to non-trivial Berry phases, may in principle be related either to real-space contributions, reciprocal-space contributions, or off-diagonal mixed contributions [9, 109, 110].

Magnetic structure determinations in the low temperature phase in zero magnetic field using neutron powder diffraction were reported in Ref. [19]. At $T = 2$ K, two different magnetic propagation vectors were observed, namely the commensurate vector $(0, 0, 1)$, as well as the incommensurate vector $(0, 0, 1 - \delta)$ with $\delta \approx 0.09$. The propagation vectors were found in agreement with results from single-crystal neutron experiments, which were resolution-limited due to the use of hot neutrons [19]. The finding suggests a spiral structure with a long wavelength along the c -axis of the order of $\lambda \sim 100 \text{ \AA}$, as pointed out in Ref. [19] by the author of this thesis. The long-wavelength modulation is possibly related to Dzyaloshinskii-Moriya interactions, which may be present in EuPtSi_3 due to the lack of an inversion center [14, 15]. However, spin-orbit interactions would be required as microscopic mechanism inducing antisymmetric exchange. Based on specific heat and Mössbauer spectroscopy the authors of Ref. [215] suggested as the ground state in phase A a commensurate antiferromagnetic structure with propagation vector $(0, 0, 1)$, as well as an amplitude modulation just below the ordering temperature in phase B [215]. By means of electronic calculations both the size of the magnetic moments and the direction of the easy axis were reproduced in Ref. [225].

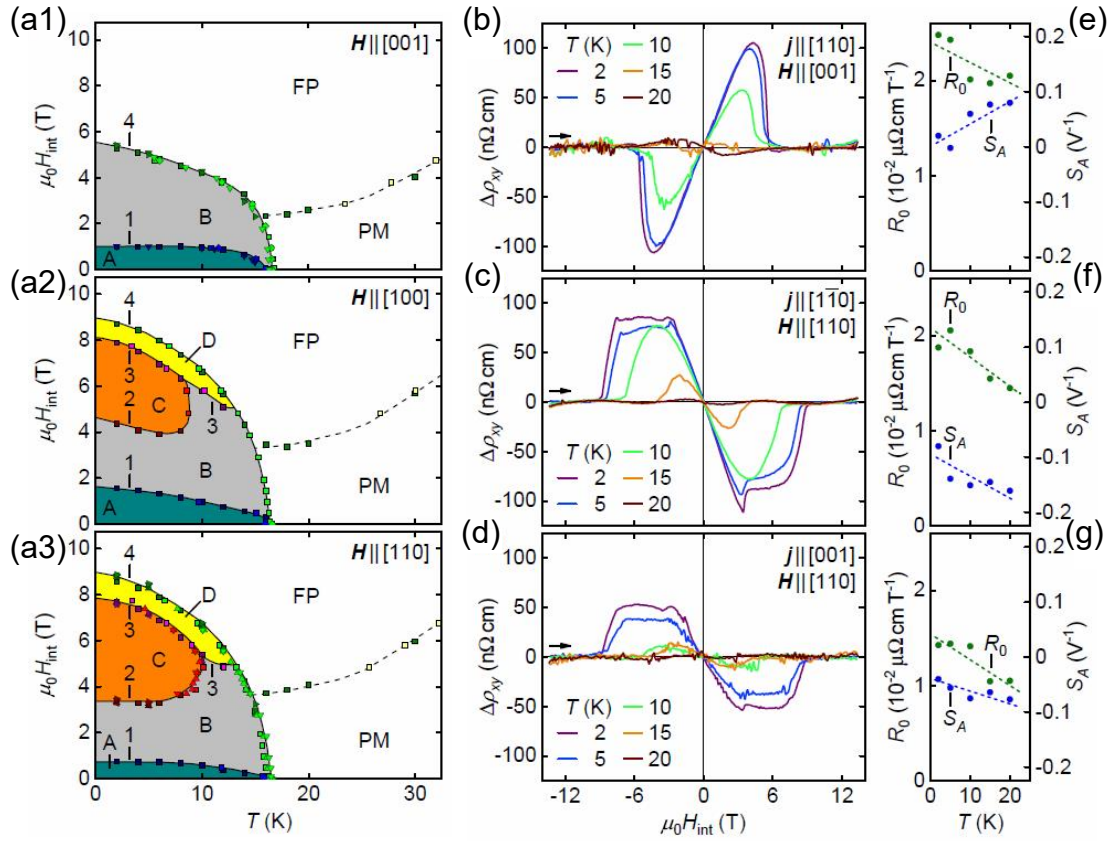


Figure 4.1.: (a) Magnetic phase diagrams of EuPtSi_3 for fields along the major tetragonal directions. Data inferred from ac susceptibility, specific heat, magnetoresistance, and Hall effect are shown on an internal field scale. (b)-(d) Additional contributions $\Delta\rho_{xy}$ to the Hall resistivity for magnetic fields along different crystallographic directions. To obtain $\Delta\rho_{xy}$, normal and conventional anomalous Hall effect were subtracted from the total Hall effect. (e)-(g) Normal and anomalous Hall coefficients R_0 and S_A as a function of temperature. The figures were taken from Ref. [19].

4.2. Magnetic Long-Range Order in Zero Magnetic Field

In the following, a study of the magnetic long-range order in phase A of EuPtSi_3 (cf. Fig. 4.1) is presented. First, the magnetic propagation vectors were determined in phase A by means of single crystal neutron diffraction, as reported in Sec. 4.2.1. Second, representational analysis was carried out, as reported in Sec. 4.2.2, and a magnetic structure determination was carried out, as reported in Sec. 4.2.3. Some of the possible ground state solutions have intriguing topological properties, which are discussed in detail in Sec. 4.2.3.

4.2.1. Magnetic Propagation Vectors

To determine the magnetic propagation vectors in phase A, single crystal neutron diffraction in zero magnetic field of sample OFZ-97-3-1-bc was carried out at BIODIFF [124].

The main results of these experiments may be summarized as follows:

- The magnetic ground state in phase A at zero magnetic field represents an antiferromagnet, which is approximately of type (00π) but additionally modulated with an incommensurate superstructure.
- This magnetic structure is a superposition of propagation vectors of the stars $\{\mathbf{k}_{ic,1}\}$, $\{\mathbf{k}_{ic,2}\}$, and $\{\mathbf{k}_{ic,3}\}$ with $\mathbf{k}_{ic,1} = (\epsilon, \epsilon, \xi_1)$, $\mathbf{k}_{ic,2} = (\epsilon, \epsilon, \xi_2)$, and $\mathbf{k}_{ic,3} = (\epsilon, \epsilon, \xi_3)$, where $\epsilon = 0.0072$, $\xi_1 = 1.0814$, $\xi_2 = 1.0713$, and $\xi_3 = 1.0604$. There is no evidence for a commensurate propagation vector $\mathbf{k} = (0, 0, 1)$.
- The magnetic ground state does not have ferromagnetic components with moments in the (001) plane. However, it may have a ferromagnetic component with moments along the c -axis $[001]$.
- The ground state in phase A is modulated with a long wavelength of $\approx 600 \text{ \AA}$ in the basal plane and $\approx 120 \text{ \AA}$ along the tetragonal c -axis.

For the experiments, neutrons of wavelength $\lambda = 3.4 \text{ \AA}$ and a relatively thin sample were used to optimize the neutron transmission through the sample. Neutron experiments with compounds containing Eu are typically difficult, as Eu is highly neutron absorbing due to the natural abundance of ^{151}Eu (cf. [122]). The neutron wavelength was chosen as a compromise, as it had to be large enough in order to have enough resolution in the q -space for the determination of incommensurate satellites, and it had to be small enough to have sufficient neutron transmission through the sample. Alternatively, a specimen purely based on the isotope ^{153}Eu (cf. Ref [226]), which is a relatively good neutron transmitter, could have been grown. The sample was oriented such that the (110) plane corresponded to the scattering plane. The maximum cross section of the sample $\sim 2 \text{ mm}^2$ was at the beginning of the experiment perpendicular to the neutron beam and the depth of the sample in beam direction amounted to 0.2 mm . A large detector with high resolution was used for these experiments.

The experiments were carried out as follows. First, rocking scans were recorded for the structural peak position $(0, 0, 2)$ in the paramagnetic regime at $T = 30 \text{ K}$ and in phase A at $T = 5 \text{ K}$. Integrated intensities were inferred for the structural peak at the two temperatures and compared in order to determine ferromagnetic components with magnetic moments in the (001) plane. Second, a rocking scan was carried out for the $(0, 0, 1)$ position at $T = 5 \text{ K}$ in order to search for magnetic Bragg peaks. Magnetic propagation vectors of the ground state in phase A were determined by indexation of magnetic Bragg peaks.

To record rocking scans for the structural $(0, 0, 2)$ position, the sample had to be rotated by $\sim \theta_{002} \approx 20.32^\circ$. Hence, the effective cross section of the sample in the neutron beam was reduced by $1 - \cos(\theta_{002}) \approx 6\%$. The two rocking scans at $T = 30 \text{ K}$ and

$T = 5\text{ K}$ were recorded with a step width of 0.2° . Integrated intensities of the peak located at $(0, 0, 2)$ were inferred from the two rocking scans as follows. First, intensities as a function of ω were inferred for the Bragg peak located at $(0, 0, 2)$. Therefore, the region of interest ROI_{In} was defined in the detector images. From the detector images $D_\omega(X, Y)$, intensities as a function of ω were obtained by summing up the intensities in ROI_{In}, i.e., $\mathcal{I}(\omega) = \sum_{(X,Y) \in \text{ROI}_{\text{In}}} D_\omega(X, Y)$. Second, the integrated intensities were inferred by summation over the rocking scan $I = \sum_\omega \mathcal{I}(\omega)$.

No difference of integrated intensities around $(0, 0, 2)$ at the two temperatures was observed:

$$\frac{I^{5\text{K}}}{I^{30\text{K}}} = 0.99 \pm 0.02. \quad (4.1)$$

Hence, the magnetic ground state in phase A does not include a ferromagnetic contribution, i.e., a component with wave vector $\mathbf{k} = 0$ that has finite moments in the basal plane (001) , as inferred by means of the magnetic structure factor [22]. However, this does not rule out a ground state with a ferromagnetic component directed along $[001]$. A component along $[001]$ cannot be detected at the (002) Bragg peak position, as the polarization factor [21] in the magnetic structure factor is entirely suppressed at this position in reciprocal space.

For the rocking scan around the magnetic position $(0, 0, 1)$, which was carried out in phase A at 5 K , the sample had to be rotated by $\sim \theta_{001} \approx 9.99^\circ$. Hence the cross section of the sample in the neutron beam was reduced by $1 - \cos(\theta_{001}) \approx 1.5\%$. The step width of the scan was 0.2° and detector images were recorded at the rocking angles $\omega_j = -14.59 + j \cdot 0.2^\circ$. Accordingly, the Bragg condition for $(0, 0, 1)$ was fulfilled at the rocking angle $\omega_{23} \approx -\theta_{001}$.

As explained in the following, 24 magnetic Bragg peaks, which are related to three different propagation vector stars, were observed during the rocking scan. However, no Bragg peak was observed at the position $(0, 0, 1)$, where scattering intensity was observed in neutron powder diffraction, as reported in our previous study (cf. Ref. [19]). The 24 magnetic Bragg peaks may be indexed by means of propagation vectors of the six stars $\{\mathbf{k}_{ic,1}\}$, $\{\mathbf{k}_{ic,2}\}$, $\{\mathbf{k}_{ic,3}\}$, $\{-\mathbf{k}_{ic,1}\}$, $\{-\mathbf{k}_{ic,2}\}$, and $\{-\mathbf{k}_{ic,3}\}$ with $\mathbf{k}_{ic,1} = (\epsilon, \epsilon, \xi_1)$, $\mathbf{k}_{ic,2} = (\epsilon, \epsilon, \xi_2)$, and $\mathbf{k}_{ic,3} = (\epsilon, \epsilon, \xi_3)$, where $\xi_1 = 1.0814$, $\xi_2 = 1.0713$, $\xi_3 = 1.0604$, and $\epsilon = 0.0072$.

As each of the six propagation vector stars has four different k -arms, there exist in total 24 k -arms of the six propagation vector stars. Each k -arm has one Bragg peak in the vicinity of the $(0, 0, 1)$ position. Note that the Bragg peaks appear in pairs, according to conjugated propagation vectors. Accordingly, the incommensurate Bragg peaks in the vicinity of the $(0, 0, 1)$ position appear in pairs.

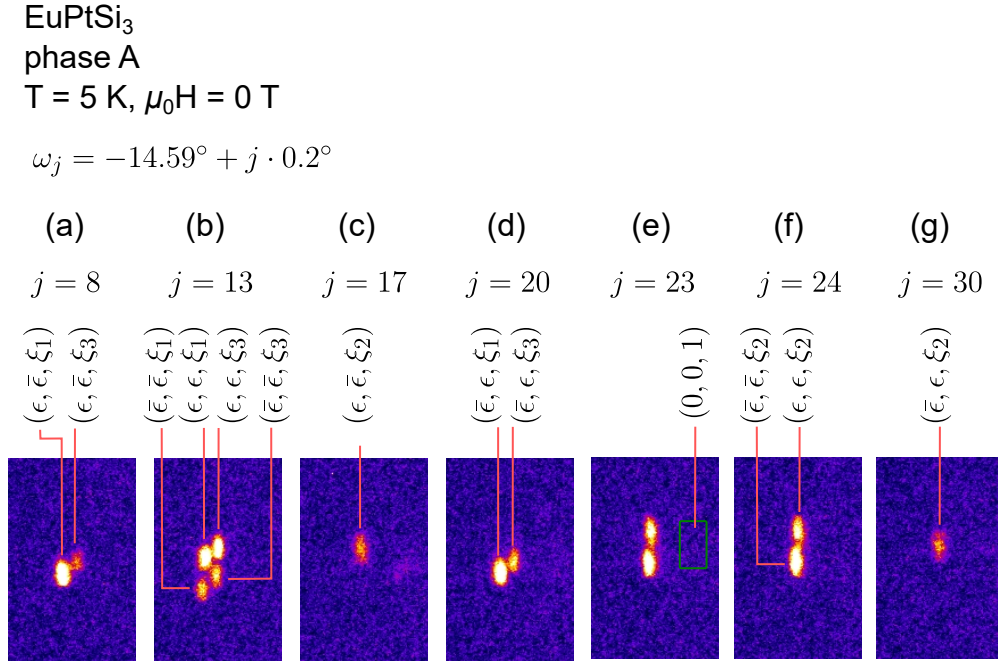


Figure 4.2.: Magnetic Bragg peaks in the vicinity of $(0, 0, 1)$, as observed in a rocking scan in phase A at 5 K. The rocking scan, which was carried out, represents approximately a q -scan along the reciprocal space direction $(\bar{1}10)$. Shown are detector images recorded at different rocking angles ω_j . (a)-(g) Detector images, recorded at angles, where the Bragg condition was fulfilled for the indicated q -positions. 12 magnetic Bragg peaks are shown and their reciprocal space positions are indicated, where $\epsilon = 0.0072$, $\xi_1 = 1.0814$, $\xi_2 = 1.0713$, and $\xi_3 = 1.0604$. The indexing of the twelve Bragg peaks requires propagation vectors of three different stars. (e) Detector image recorded at the rocking angle, where the Bragg condition is fulfilled for the q -position $(0, 0, 1)$. However, no Bragg peak intensity was observed at this position, which is indicated by a green rectangle.

The constituents of such a pair are indexed with respect to two different structural peak positions, such as

$$(0, 0, 0) + (\epsilon, \epsilon, \xi_1) \quad \text{and} \quad (0, 0, 2) - (\epsilon, \epsilon, \xi_1) . \quad (4.2)$$

In the following diffraction data are presented, which show the 12 Bragg peaks indexed with respect to the structural q -position $(0, 0, 0)$.

Fig. 4.2 shows these data, as recorded by means of the rocking scan around the q -position $(0, 0, 1)$. Shown are detector images, which were recorded at different rocking angles ω_j of the sample. The data presented in (a),(b),(c),(d),(f), and (g) show all 12 Bragg peaks, which correspond to the reciprocal space position $(0, 0, 0)$ and the propagation vectors $\mathbf{k}_{ic,1}$, $\mathbf{k}_{ic,2}$, and $\mathbf{k}_{ic,3}$. The data presented in (e) illustrate, that no Bragg peak intensity was observed at the commensurate $(0, 0, 1)$ position, which is indicated by the green rectangle.

As the indexation of the magnetic Bragg peaks requires propagation vectors of three different non-conjugated crystallographic stars, it may be concluded that the magnetic ground state in phase A is a multi- k structure with at least three propagation vector. The magnetic structure has a long wavelength in real-space. The wavelength of the modulation in the (001) plane is given by $a/\epsilon \approx 600 \text{ \AA}$ and the wavelength along the tetragonal c -axis is given by $c/[(\xi_{1/2/3} - 1)] \approx 120 \text{ \AA}$. The finding of a long wavelength modulation along the tetragonal c -axis is in agreement with our previous study (cf. Ref. [19]). The long-wavelength modulation in the basal plane, however, was not reported previously.

Note, that the propagation vectors as inferred in the present study give rise to complex magnetic structures. There are namely multitudinous ways how to superpose the propagation vectors $\mathbf{k}_{ic,1}$, $\mathbf{k}_{ic,2}$ and $\mathbf{k}_{ic,3}$ to multi- k states, as each of the three propagation vector stars possesses four k -arms. In contrast, magnetic structures with propagation vectors such as $(0, 0, 1 + \delta)$, which were reported in our previous study (cf. Ref. [19]), are single- k structures, as the wave-vector star $\{(0, 0, 1 + \delta)\}$ possesses one k -arm only.

4.2.2. Representational Analysis for Magnetic Structures

To determine all IRs as well as the corresponding basis functions for propagation vectors $\mathbf{k}_{ic,1}$, $\mathbf{k}_{ic,2}$, $\mathbf{k}_{ic,3}$ and space group $I4mm$, a representational analysis was carried out by means of the software *SARAh* [54].

Tab. 4.1 shows the results of the representational analysis, as obtained in *SARAh*. The decomposition of magnetic representations is equivalent for the propagation vectors $\mathbf{k}_{ic,1}$, $\mathbf{k}_{ic,2}$, and $\mathbf{k}_{ic,3}$, as all of them have the form $\mathbf{k}_{ic} = (\epsilon, \epsilon, z)$ with an incommensurate parameter z , i.e., $z \notin \mathbb{Q}$. The magnetic representation splits into the two IRs $\Gamma_1(\mathbf{k}_{ic})$ and $\Gamma_2(\mathbf{k}_{ic})$. The IR $\Gamma_1(\mathbf{k}_{ic})$ has the order $\nu = 1$ and the basis function is directed along the c -axis. In contrast, $\Gamma_2(\mathbf{k}_{ic})$ has the order $\nu = 2$ and the basis functions lie in the basal plane. Tab. 4.1 also shows the representational analysis for the propagation vector (001) for the sake of completeness. The representation analysis is the basis for the magnetic structure determination in Sec. 4.2.3.

Propagation vector	IR	BV	BV components					
			$m_{\parallel a}$	$m_{\parallel b}$	$m_{\parallel c}$	$im_{\parallel a}$	$im_{\parallel b}$	$im_{\parallel c}$
$\mathbf{k}_{ic} = (\epsilon, \epsilon, z), z \notin \mathbb{Q}$	Γ_1	Ψ_1	1	-1	0	0	0	0
	Γ_2	Ψ_2	1	1	0	0	0	0
		Ψ_3	0	0	2	0	0	0
$(0, 0, 1)$	Γ_2	Ψ_1	0	0	8	0	0	0
	Γ_5	Ψ_2	4	0	0	0	0	0
		Ψ_3	0	-4	0	0	0	0

Table 4.1.: Analysis of the representation of the magnetic Eu site in the space group $I4mm$. For each magnetic propagation vector \mathbf{k} (space group $I4mm$) which is given in the first column, the IRs $\Gamma(\mathbf{k})$ that contain non-trivial basis functions $\Psi^{\mathbf{k}}$ are listed. The analysis was carried out by means of the software *SARAh* [54].

4.2.3. Magnetic Structure Determination

A structure determination was carried out for the magnetic ground state in phase A at $T = 5$ K in zero magnetic field. As no data from polarized neutrons or Rietveld refinements is available, some considerations presented in this section are based on assumptions.

The main results of these considerations may be summarized as follows:

- Each of the propagation vectors $\mathbf{k}_{ic,1}$, $\mathbf{k}_{ic,2}$, and $\mathbf{k}_{ic,3}$ may be viewed as an antiferromagnetic cycloid. Putative Dzyaloshinskii-Moriya interactions in EuPtSi_3 would support cycloidal spirals as opposed to helical spirals.
- Accordingly, the ground state in phase A at 5 K represents a superposition of antiferromagnetic cycloids with propagation vectors $\mathbf{k}_{ic,1}$, $\mathbf{k}_{ic,2}$, and $\mathbf{k}_{ic,3}$.
- The geometric and topological properties of the superposition of cycloids depends mainly on the relationship between the projections of $\mathbf{k}_{ic,1}$, $\mathbf{k}_{ic,2}$, and $\mathbf{k}_{ic,3}$ in the basal $(h, k, 0)$ plane.
- The superposition of cycloids with propagation vectors $\mathbf{k}_{ic,1}$, $\mathbf{k}_{ic,2}$, and $\mathbf{k}_{ic,3}$, represents an antiferromagnetic cycloid with modulated amplitude, if the projections of the propagation vectors onto the basal plane are parallel (which is denoted as (m.i) in the text).
- The superposition of cycloids with propagation vectors $\mathbf{k}_{ic,1}$, $\mathbf{k}_{ic,2}$, and $\mathbf{k}_{ic,3}$, as well as a commensurate component, represents a topologically non-trivial structure, if at least two wave vectors have perpendicular projections in the basal (which is denoted as (m.ii) in the text).
- Case (m.ii) may be specified further: If the commensurate component is antiferromagnetic (which is denoted as (c.i) in the text), the structure represents a lattice of antiferromagnetic Skyrmions. If the commensurate component is ferromagnetic (which is denoted as (c.ii) in the text), it represents a lattice of ferrimagnetic Skyrmions.
- In case (c.i) the structure consists of sublattices with strictly opposite Skyrmion winding numbers. Accordingly, Berry phases vanish on average.
- In case (c.ii) the structure consists of sublattices with equal Skyrmion numbers. Accordingly, non-trivial Berry phases may lead to a topological Hall effect.

The presentation is organised as follows. First, it is established that each of the three propagation vectors $\mathbf{k}_{ic,1}$, $\mathbf{k}_{ic,2}$, and $\mathbf{k}_{ic,3}$ may be viewed as an antiferromagnetic cycloid. Second, superpositions of two cycloids with propagation vectors of the stars $\{\mathbf{k}_{ic,1}\}$, $\{\mathbf{k}_{ic,2}\}$, and $\{\mathbf{k}_{ic,3}\}$ are investigated. It is found that some superpositions may be viewed as a variation of $\mu(x, y, z)$ representing an antiferromagnetic or ferrimagnetic Skyrmion lattice.

Third the topological properties of μ are investigated. Fourth, it is discussed whether the topological properties may be related to unconventional transport properties.

The magnetic propagation vectors $\mathbf{k}_{ic,1}$, $\mathbf{k}_{ic,2}$, and $\mathbf{k}_{ic,3}$ represent incommensurate points in the vicinity of $(0, 0, 1)$ in the reciprocal space, which is a forbidden position in space group $I4mm$. Magnetic structures that are superpositions of propagation vectors in the vicinity of $(0, 0, 1)$ characteristically feature an antiferromagnetic coupling of magnetic moments along the $\langle 111 \rangle$ directions. The character of the propagation vectors $\mathbf{k}_{ic,1}$, $\mathbf{k}_{ic,2}$, and $\mathbf{k}_{ic,3}$, i.e., whether they are related to a helical, a cycloidal, or an amplitude modulation (cf. Ref. [30]), cannot be inferred from our experimental data. However, as explained in the following, the propagation vectors are presumably related to cycloidal propagations. The $I4mm$ crystal structure of EuPtSi_3 [215, 225] is isotypic of the BaNiSn_3 structure, which is non-centrosymmetric [216]. Due to this lack of inversion symmetry, EuPtSi_3 may host Dzyaloshinskii-Moriya interactions that favour a canting of magnetic moments [14, 15]. Further, the crystal structure of EuPtSi_3 is related to the point group C_{4v} [227, 228], where canted spiral structures typically have a cycloidal character [211–213].

A cycloidal structure with wave-vector $\sim \mathbf{k}_0 = (\epsilon, \epsilon, l_0)$ (where l_0 is either $l_1 := \xi_1$, $l_2 := \xi_2$ or $l_3 := \xi_3$) may be constructed from the basis functions in Tab. 4.1 by means of:

$$\mathbf{m}_c = m_1 \cdot \left[\frac{\hat{e}_x + \hat{e}_y}{\sqrt{2}} \cos(\mathbf{k}_0 \mathbf{R}) + \hat{e}_z \sin(\mathbf{k}_0 \mathbf{R}) \right] \quad (4.3)$$

Note, that the structure \mathbf{m}_c is a superposition of basis functions from one IR only, namely $\Gamma_2(\mathbf{k}_0)$ (cf. Tab. 4.1). Accordingly, in a situation, where the prerequisites for Landau theory are fulfilled, the structure \mathbf{m}_c is allowed as a magnetic ground state, as it is related to one IR only [53]. In fact, Landau theory may be applicable, as the transition temperature was characterized by a lambda anomaly in the specific heat [19], which is characteristic of second-order phase transitions.

Chirality domains of magnetic structures in EuPtSi_3 , i.e., domains with opposite rotation sense, should be in equilibrium, as EuPtSi_3 has an achiral crystal structure [214]. This contrasts chiral magnets, where the chiral crystal structure leads to homochiral magnetic structures [6, 229]. Hence, the chirality of the cycloid \mathbf{m}_c , i.e., the sense of rotation, may be chosen arbitrarily.

Fig. 4.3 (a) shows a real-space picture of \mathbf{m}_c in a $(1\bar{1}0)$ plane. The structure may be viewed as an antiferromagnetic cycloid propagating along an axis, that is inclined with respect to $[001]$ towards $[110]$ by an angle $\phi = \arctan(\sqrt{2}\epsilon c/l_0 a) \approx 1.2^\circ$. For the structure \mathbf{m}_c the coupling of magnetic moments along $\langle 111 \rangle$ directions is antiferromagnetic and slightly canted. Along the $\langle 100 \rangle$, $\langle 110 \rangle$, and $\langle 001 \rangle$ directions it is ferromagnetic and slightly canted.

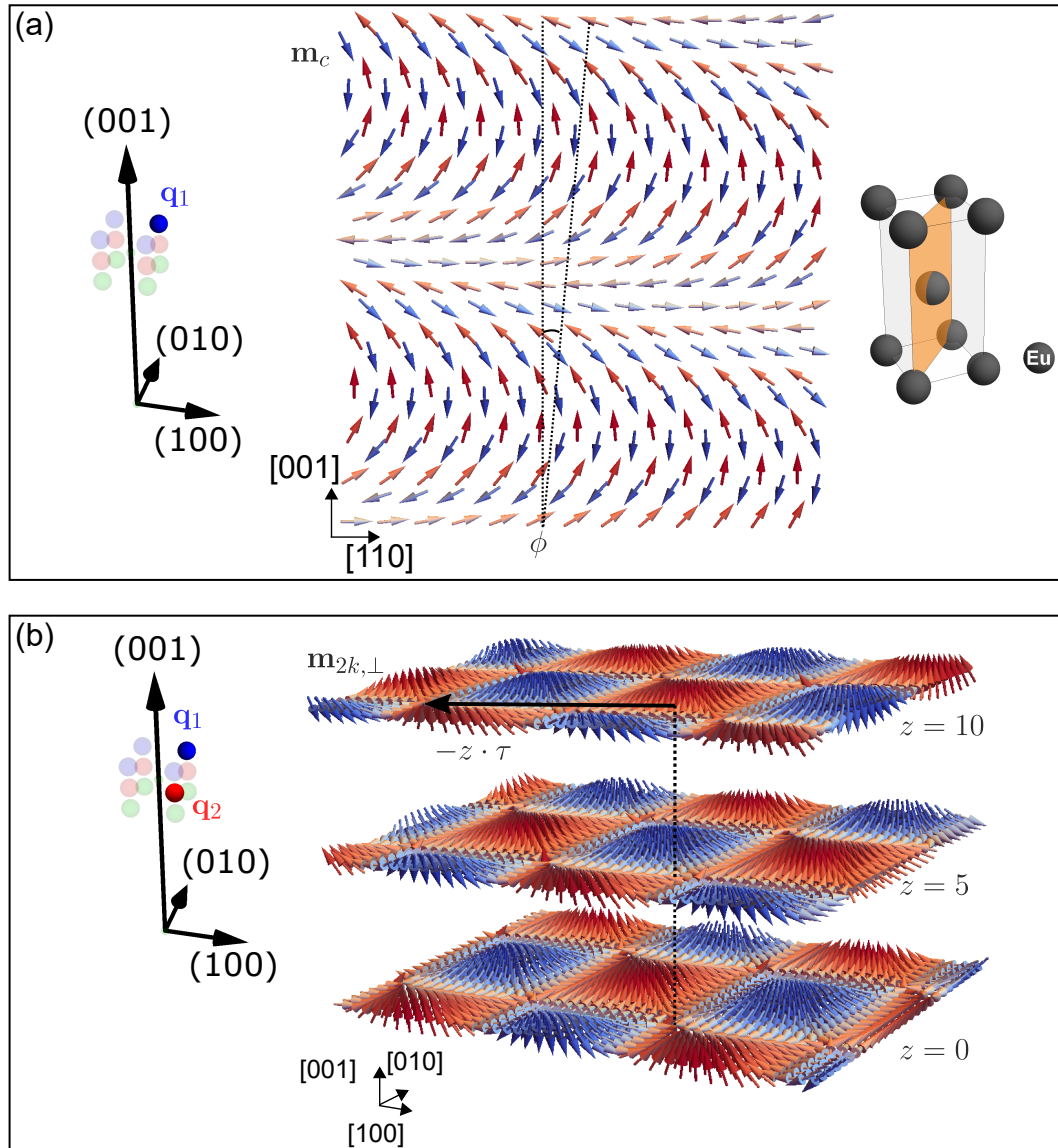


Figure 4.3.: Magnetic ground state in phase A of EuPtSi_3 representing a superposition of antiferromagnetic cycloids. (a) Each of the propagation vectors of the ground state in phase A may be viewed as an antiferromagnetic cycloid. Shown is a cycloid \mathbf{m}_c with wave vector \mathbf{k}_0 propagating along an axis, which is inclined to the axis $[001]$ by an angle ϕ towards $[110]$. (b) The superposition of two cycloids with propagation vectors $\mathbf{k}_1 = (\epsilon, \epsilon, l_1)$ and $\mathbf{k}_2 = (\epsilon, -\epsilon, l_3)$, as well as a ferromagnetic component represents a spatially modulated lattice of antiferromagnetic Skyrmions. Two AFM Skyrmion lattices, which are along the c -direction separated by a distance z , are relatively shifted by $-\tau \cdot z$ within the basal (001) plane.

It was found in Sec. 4.2.1 that the magnetic ground state at 5 K represents a superposition of propagation vectors $\mathbf{k}_{ic,1}$, $\mathbf{k}_{ic,2}$, and $\mathbf{k}_{ic,3}$. When antiferromagnetic cycloids with propagation vectors of the stars $\{\mathbf{k}_{ic,1}\}$, $\{\mathbf{k}_{ic,2}\}$, and $\{\mathbf{k}_{ic,3}\}$ are superposed, it is crucial, how the incommensurate projections of the superposed wave vectors onto the $(h, k, 0)$ plane are related to each other. These incommensurate projections are parallel

to the $\langle 110 \rangle$ directions. Hence, the projections from two propagation vectors may either be perpendicular or parallel.

If the projections in the $(h, k, 0)$ plane are parallel, the wave vectors are incommensurate with respect to the same $\langle 110 \rangle$ direction. The superposition of cycloids may then be portrayed as a complex cycloid with modulated amplitude. If the projections in the $(h, k, 0)$ plane are perpendicular, the wave vectors are incommensurate with respect to different $\langle 110 \rangle$ directions. The superposition of cycloids may then be portrayed as an antiferromagnetic Skyrmion lattice. Accordingly, the following two cases may be considered for the superposition of cycloids:

- (m.i) The superposition of wave vectors, for which the projections in the $(h, k, 0)$ plane are parallel, represents a complex cycloid with modulated amplitude. Examples are wavevectors such as $(\epsilon, \epsilon, l_1)$ and $(\epsilon, \epsilon, l_3)$.
- (m.ii) The superposition of wave vectors, for which the projections in the $(h, k, 0)$ plane are perpendicular, may represent a lattice of ferrimagnetic or antiferromagnetic Skyrmions. Examples are wavevectors such as $(\epsilon, \epsilon, l_1)$ and $(\epsilon, -\epsilon, l_3)$.

Case (m.i) may be established by simple trigonometric calculations using addition theorems. In the following, the more interesting case (m.ii) is established in detail. For this case, the superposition $\mathbf{m}_{2k,\perp}$ of two cycloids with wavevectors $\mathbf{k}_1 = (\epsilon, \epsilon, l_1)$ and $\mathbf{k}_2 = (\epsilon, -\epsilon, l_3)$, as well as a commensurate component $\parallel \hat{e}_z$ with wave vector \mathbf{k}_c that is specified further below, may be considered. The superposition of the two cycloids has the following form:

$$\begin{aligned} \mathbf{m}_{2k,\perp}(x, y, z) = & m_1 \cdot \left[\frac{\hat{e}_x + \hat{e}_y}{\sqrt{2}} \cos(\mathbf{k}_1 \cdot \mathbf{R}) + \hat{e}_z \sin(\mathbf{k}_1 \cdot \mathbf{R}) \right] + \\ & + m_1 \cdot \left[\frac{\hat{e}_x - \hat{e}_y}{\sqrt{2}} \cos(\mathbf{k}_2 \cdot \mathbf{R}) + \hat{e}_z \sin(\mathbf{k}_2 \cdot \mathbf{R}) \right] + \\ & + m_0 \cdot \hat{e}_z \cdot \exp(i \cdot \mathbf{k}_c \cdot \mathbf{R}) . \end{aligned} \quad (4.4)$$

where

$$\mathbf{k}_1 \cdot \mathbf{R} = 2\pi(\epsilon x + \epsilon y) + 2\pi z \cdot l_1 \quad (4.5)$$

$$\mathbf{k}_2 \cdot \mathbf{R} = 2\pi(\epsilon x - \epsilon y) + 2\pi z \cdot l_3 . \quad (4.6)$$

It is now established that the structure $\mathbf{m}_{2k,\perp}$ may be viewed as a spatially modulated

variation of an archetype structure μ , which describes a lattice of antiferromagnetic or ferrimagnetic Skyrmions:

$$\begin{aligned} \mu(x, y, z) := & m_0 \cdot \hat{e}_z \cdot \exp(i \cdot \mathbf{k}_c \cdot \mathbf{R}) + \\ & + m_1 \cdot \left[\frac{\hat{e}_x + \hat{e}_y}{\sqrt{2}} \cos(2\pi\epsilon(x+y) + 2\pi z) + \hat{e}_z \sin(2\pi\epsilon(x+y) + 2\pi z) \right] + \\ & + m_1 \cdot \left[\frac{\hat{e}_x - \hat{e}_y}{\sqrt{2}} \cos(2\pi\epsilon(x-y) + 2\pi z) + \hat{e}_z \sin(2\pi\epsilon(x-y) + 2\pi z) \right] \end{aligned} \quad (4.7)$$

In each basal (001) plane, the structure $\mathbf{m}_{2k,\perp}$ is equal to μ . However, for different values of z the Skyrmion layers are shifted by in-plane translations:

$$\mathbf{m}_{2k,\perp}(x, y, z) = \mu(x + z \cdot \tau_1, y + z \cdot \tau_2, z), \quad (4.8)$$

where $\tau = \frac{1}{2\epsilon}(l_1 + l_3 - 2, l_1 - l_3)$. Fig. 4.3 illustrates Eq. (4.8) showing three different z -layers of the structure $\mathbf{m}_{2k,\perp}$ with a ferromagnetic component $\mathbf{k}_c = 0$.

As the magnetic ground state in phase A represents a superposition not of two, but at least of three propagation vectors, it is even more complex than the structure $\mathbf{m}_{2k,\perp}$. However, the ground state in phase A may be portrayed as variation of the structure $\mathbf{m}_{2k,\perp}$ and hence of μ , if propagation vectors with perpendicular projections onto the basal plane are involved. In particular, topological properties of the ground state in phase A may be related to the properties of μ .

The structure μ features intriguing topological properties as follows. The topology of μ depends strongly on the commensurate component with wave vector \mathbf{k}_c . The vectorfield μ namely represents either:

- (c.i) a lattice of antiferromagnetic Skyrmions, if the commensurate component is antiferromagnetic with $\mathbf{k}_c = (0, 0, 1)$, or
- (c.ii) a lattice of ferrimagnetic Skyrmions, if the commensurate component is ferromagnetic with $\mathbf{k}_c = (0, 0, 0)$.

In case (c.i) the structure μ is bipartite with Skyrmions on one sublattice S_I and Skyrmions with opposite winding number on the other lattice S_{II} . The two sublattices of the magnetic structure μ are shifted by a translation $\sim \frac{1}{2}\sqrt{2a^2 + c^2}^{-1} \cdot (a, a, c)^T$. Along the $\langle 111 \rangle$ directions, the coupling of magnetic moments is antiferromagnetic with a small canting.

To calculate the winding numbers on the two sublattices it is convenient to consider the directorfield (cf. Ref. [6]):

$$n_{\text{AFM}} = \mu(x, y, z) / |\mu(x, y, z)| |_{\mathbf{k}_c=(0,0,1)}$$

Note, that the function n_{AFM} is well-defined for finite values of m_0 .

Fig. 4.4 (a) shows the winding numbers on the two sublattices as a function of the size of the commensurate component m_0 (where $m_1 = 1$). The winding numbers, which were determined by numerical integration of the Skyrmion density [170] over a unit cell $U = \left[0, a \cdot \frac{1}{\epsilon}\right] \times \left[0, a \cdot \frac{1}{2\epsilon}\right]$ in the basal plane, have opposite signs on the two sublattices. In particular, the winding numbers are finite, as long as $|m_0| < 2$. For positive values of $m_0 < 2$ it was obtained:

$$\text{WZ} = \int_{U, z=0} n_{\text{AFM}} \cdot (\partial_x n_{\text{AFM}} \times \partial_y n_{\text{AFM}}) \, dx \cdot dy = \begin{cases} -1 & S_{\text{I}} \\ +1 & S_{\text{II}} \end{cases} \quad (4.9)$$

Accordingly, the structure μ represents a lattice of antiferromagnetic Skyrmions and the winding numbers on the two sublattices have strictly opposite sign.

In the second case, where the commensurate component is ferromagnetic (c.ii), there are spatial regions of the structure μ , where the antiferromagnetic coupling along $\langle 111 \rangle$ directions is broken. Accordingly, the antiferromagnetic coupling along $\langle 111 \rangle$ directions is weaker and not strictly antiparallel. Note, that the Curie-Weiss temperature, which is positive even though the compound is antiferromagnetic [19, 215], may possibly be related to an antiferromagnetic coupling along $\langle 111 \rangle$ directions, which is not strictly antiparallel.

The director field is again well defined for finite values of m_0 :

$$n_{\text{FM}} = \mu(x, y, z) / |\mu(x, y, z)|_{\mathbf{k}_c=(0,0,0)}$$

Fig. 4.4 shows the winding numbers on the two sublattices, as obtained by numerical integration. The winding numbers have now the same sign on both sublattices. In particular, the winding numbers are finite, as long as $|m_0| < 2$ (again it was set $m_1 = 1$). For positive values of $m_0 < 2$ it was obtained:

$$\text{WZ} = \int_{U, z=0} n_{\text{FM}} \cdot (\partial_x n_{\text{FM}} \times \partial_y n_{\text{FM}}) \, dx \cdot dy = \begin{cases} -1 & S_{\text{I}} \\ -1 & S_{\text{II}} \end{cases}$$

Accordingly, the winding numbers have strictly the same sign on both sublattices and the structure represents a lattice of ferrimagnetic Skyrmions.

In the following, it is argued, that the structure μ and hence $\mathbf{m}_{2k,\perp}$ may cause a topological Hall effect. In particular, we note that the existence of a topological Hall effect crucially depends on whether the commensurate component is antiferromagnetic (c.i) or ferromagnetic (c.ii). For antiferromagnetic Skyrmions (c.i) no finite topological Hall effect

is expected, as the winding numbers on the two sublattices have opposite sign. Accordingly, the emergent magnetic fields [9] acting on the conduction electrons are zero in average. Related studies discussed antiferromagnetic Skyrmions on a honeycomb lattice [230], where the topological Hall effect should also vanish. However, it was pointed out that the topological Hall effect may become finite, if the two sublattices become inequivalent. Similarly we find that a topological Hall signal may be caused by a structure μ , which has a ferromagnetic component (c.ii). In the case of a ferromagnetic component, the winding numbers on the two sublattices have the same sign. Accordingly, an emergent magnetic field on the conduction electrons may be caused by the structure μ .

4.3. Summary, Outlook and Open Questions

In this chapter we presented a microscopic study of magnetic long-range order in EuPtSi_3 . We reported a magnetic ground state, which is multi- k and may possess non-trivial topological properties.

First, the magnetic ground state in phase A at zero magnetic field was studied by means of single crystal neutron diffraction. At first the magnetic propagation vectors were determined. The magnetic ground was found to have a long-wavelength modulation of the order of 500 Å in the basal plane, as well as a modulation with a wavelength of the order of 120 Å along the c -axis. The structure was found to represent a superposition of at least three different propagation vectors. In particular, the ground state is multi- k . It was further established that the ground state does not have a commensurate antiferromagnetic propagation vector $(0, 0, 1)$. There was no evidence for ferromagnetic propagation vectors with moments in the plane (001) , but ferromagnetic contributions with moments along the c -axis $[001]$ may possibly be finite. However, the neutron study did not allow to determine the magnetic ground state unambiguously. Nonetheless, striking arguments were found that each magnetic propagation vector is related to an antiferromagnetic cycloid. As superposition of at least three cycloids the magnetic ground state in phase A may represent a variation of an antiferromagnetic or ferrimagnetic Skyrmion lattice. The topological properties of the structure crucially depend on the nature of commensurate components. In particular, when superposed with a ferromagnetic component, the superposition of antiferromagnetic cycloids may have finite winding numbers that are related to Berry phases and that may cause a topological Hall effect.

A major goal in future studies may be to obtain a full microscopic picture of the magnetic long-range order. The next experimental step is to carry out neutron or resonant X-ray scattering in magnetic fields.

The following questions may be raised for future studies:

- What are the mechanisms causing a magnetic ground state with a large wavelength in real-space?
- What is the origin for unconventional contributions to the Hall effect, which arise together with magnetic long-range order but are not related to an anomalous Hall effect, which depends linearly on the net magnetization?
- What is the origin of magnetic anisotropies? Does europium represent a mixed valence state or can it be described as Eu^{2+} ?
- Why is the Curie-Weiss temperature positive, even though the compound is antiferromagnetic?

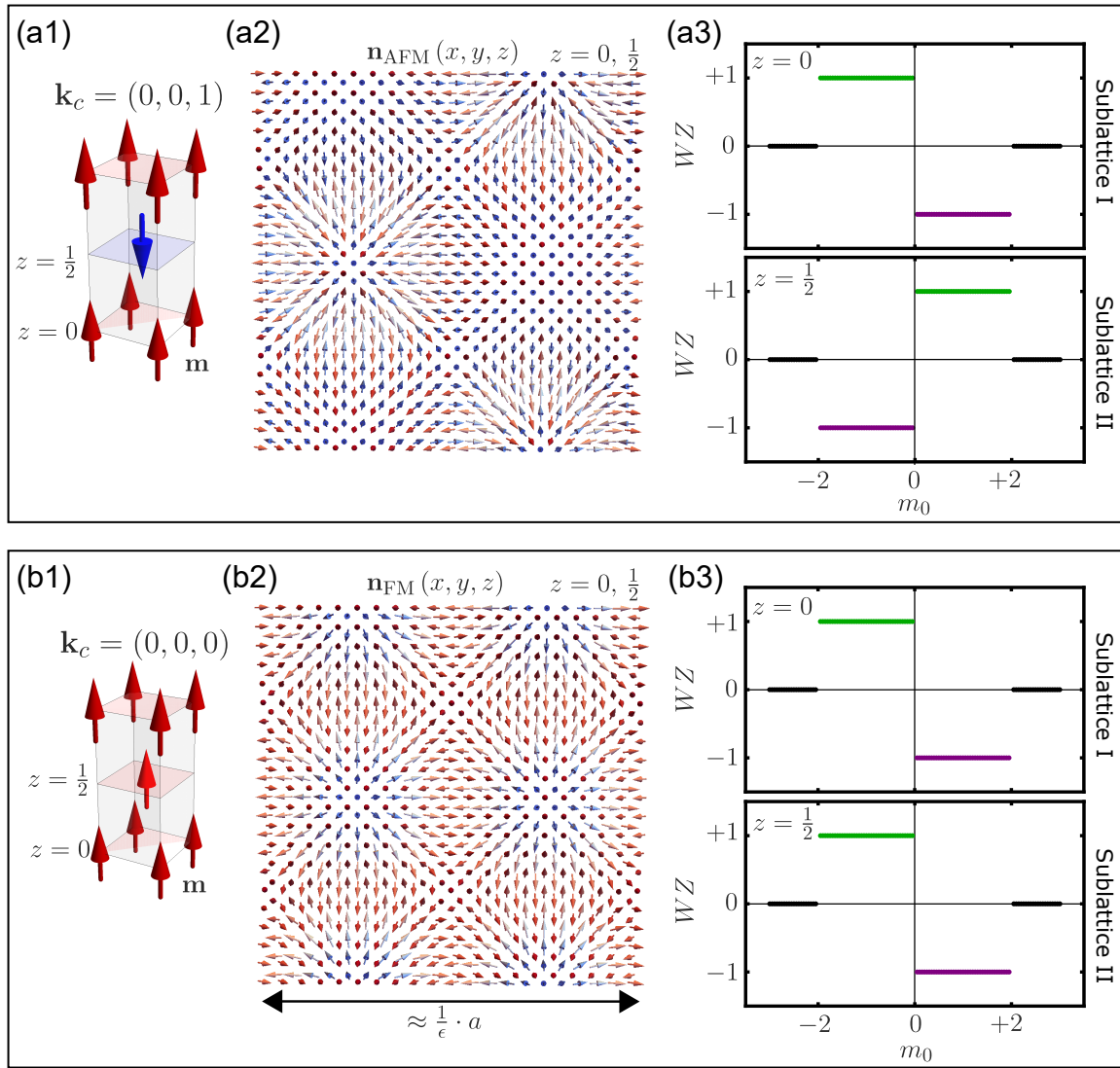


Figure 4.4.: Topological properties of the structure μ . (a) If the commensurate component in μ is antiferromagnetic (a1), the corresponding structure μ_{AFM} has two sublattices that are antiferromagnetically coupled. Shown in (a2) is the directorfield \mathbf{n}_{AFM} of μ_{AFM} . The winding numbers, which were calculated by means of $\text{WZ} = \int_{U, z=0} \mathbf{n}_{\text{AFM}} \cdot (\partial_x \mathbf{n}_{\text{AFM}} \times \partial_y \mathbf{n}_{\text{AFM}}) dx \cdot dy$, have opposite signs on the two sublattices, as shown by numerical integration (a3). Accordingly, the structure μ_{AFM} represents a lattice of antiferromagnetic Skyrmions. (b) If the commensurate component is ferromagnetic (b1), the corresponding structure \mathbf{n}_{FM} has two sublattices, which are almost antiferromagnetically coupled. Shown in (b2) is the directorfield \mathbf{n}_{FM} of μ_{FM} . Winding numbers, which were calculated by means of $\text{WZ} = \int_{U, z=0} \mathbf{n}_{\text{FM}} \cdot (\partial_x \mathbf{n}_{\text{FM}} \times \partial_y \mathbf{n}_{\text{FM}}) dx \cdot dy$, have the same sign on the two sublattices. Accordingly, the structure μ_{FM} represents a lattice of ferrimagnetic Skyrmions.

5. Conclusions

The focus of this work was the study of antiferromagnetic superstructures in rare-earth compounds. The materials, which were studied, are candidates for hosting magnetic ground states with nontrivial topology. We reported microscopic studies of the four materials HoCu, TmCu, ErCu, and EuPtSi₃ by means of single-crystal neutron diffraction. Magnetic structure determinations were carried out. Of particular interest was the identification of multi- k structures and structures with nontrivial topology. Furthermore, the interplay of magnetic order and the electronic structure was investigated.

In the first part of the thesis, experimental methods were introduced. It was explained, how magnetic ground states may be determined by means of neutron scattering. Strategies were presented, how multi- k structures may be distinguished from single- k structures.

In the second part of the thesis, microscopic studies of the RCu compounds were presented. As the main results, a multitude of antiferromagnetic ground states was identified, including highly noncoplanar multi- k states with long-wavelength modulations and ground states that are topologically protected against unwinding into a collinear antiferromagnet. The interplay between the magnetic ground states and the electronic structure was investigated. We reported, that a finite Berry curvature with Chern numbers, an orbital magnetization, and a finite intrinsic anomalous Hall effect may emerge. This class of centrosymmetric compounds, in which Dzyaloshinski-Moriya interactions are absent, may be playground for the detection of novel mechanisms stabilizing topological order.

In the third part of the thesis, a magnetic structure determination in the noncentrosymmetric compound EuPtSi₃, where Dzyaloshinski-Moriya interactions may stabilize topological order, was reported. In the study by means of neutrons signatures of a multi- k ground state with long-wavelength modulation were observed. The experimental signatures allowed for an interpretation of the magnetic ground state as antiferromagnetic Skyrmion lattice.

A. Appendix

A.1. Magnetic Structure Factors in the RCu Compounds

In the following, structure factors are calculated for antiferromagnetic ($\pi\pi 0$) structures, which are described in terms of:

$$\mathbf{m}(\mathbf{R}) = \sum_{i=0}^{N_k} \mathbf{r}(\mathbf{k}_i^c) \exp(i \cdot \mathbf{k}_i^c \cdot \mathbf{R}), \quad (\text{A.1})$$

where $1 \leq N_k \leq 3$.

The cross section, which is proportional to the magnetic structure factor, is obtained by inserting Eq. (A.1) into Eq. (2.4):

$$\sigma(\mathbf{q}) = F^2(h, k, l) \sim \sum_{\mathbf{R}_1, \mathbf{R}_2, \alpha, \beta} \sum_{i, j=0}^{N_k} \mathbf{r}^\alpha(\mathbf{k}_i^c) \mathbf{r}^\beta(\mathbf{k}_j^c) \cdot (\delta_{\alpha\beta} - \hat{q}_\alpha \hat{q}_\beta) \cdot \quad (\text{A.2})$$

$$\cdot \exp \left[i \cdot \mathbf{q} \cdot (\mathbf{R}_1 + \mathbf{R}_2) + i \cdot \mathbf{k}_i^c \cdot \mathbf{R}_1 + i \cdot \mathbf{k}_j^c \cdot \mathbf{R}_2 \right]. \quad (\text{A.3})$$

As $\exp(i\mathbf{k}_i^c) = \exp(-i\mathbf{k}_i^c)$ for the three commensurate propagation vectors, the sums over the spatial coordinates may be simplified as follows:

$$\sum_{\mathbf{R}_1, \mathbf{R}_2} \exp \left[i \cdot \mathbf{q} \cdot (\mathbf{R}_1 + \mathbf{R}_2) + i \cdot \mathbf{k}_i^c \cdot \mathbf{R}_1 + i \cdot \mathbf{k}_j^c \cdot \mathbf{R}_2 \right] = \quad (\text{A.4})$$

$$\begin{aligned} &= \sum_{i, j} \sum_{\mathbf{R}_1} \exp \left[i \cdot \mathbf{q} \cdot \mathbf{R}_1 - i \cdot \mathbf{k}_i^c \cdot \mathbf{R}_1 \right] + \sum_{\mathbf{R}_1} \exp \left[i \cdot \mathbf{q} \cdot \mathbf{R}_2 - i \cdot \mathbf{k}_j^c \cdot \mathbf{R}_2 \right] = \\ &= \left(\frac{N (2\pi)^3}{v_0} \right)^2 \sum_{i, j} \sum_{\mathbf{G}, \mathbf{G}'} \delta(\mathbf{k}_i^c + \mathbf{G} - \mathbf{q}) \cdot \delta(\mathbf{k}_j^c + \mathbf{G}' - \mathbf{q}). \end{aligned} \quad (\text{A.5})$$

The last line particularly implies $\mathbf{q} = \mathbf{k}_i^c + \mathbf{G}$ and $\mathbf{q} = \mathbf{k}_j^c + \mathbf{G}'$. As (i) \mathbf{k}_i^c and \mathbf{k}_j^c for $i \neq j$ belong to different arms of the $\langle \pi\pi 0 \rangle$ star, and (ii) two wave vectors of different arms of the same star by definition cannot differ by a reciprocal lattice vector, the terms with $i \neq j$ vanish.

In our study we are particularly interested in the case $\mathbf{q}_0 = \left(\frac{1}{2}, \frac{1}{2}, 0\right)$. Inserting Eq. (A.5) into Eq. (A.3) yields:

$$\sigma(\mathbf{q}_0) = C \cdot \delta(\mathbf{k}_1^c + \mathbf{G} - \mathbf{q}_0) \cdot \left(\frac{1}{2} (\mathbf{r}_1(\mathbf{k}_1^c) - \mathbf{r}_2(\mathbf{k}_1^c))^2 + (\mathbf{r}_3(\mathbf{k}_1^c))^2 \right) \quad (\text{A.6})$$

Note, that in zero magnetic field typically all domains of a magnetic structure have to be taken into account. As Eq. (A.1) describes only one magnetic domain, the cross section and the structure factor in Eq. (A.6) also accounts for one magnetic domain only.

A.2. Polarization Matrices in the RCu Compounds

In the following, we consider $(\pi\pi 0)$ ground states and derive properties of polarization matrices, which were used in our study on HoCu and ErCu.

Let $\mathbf{m} = \mathbf{m}^d(\mathbf{R})$ be a $(\pi\pi 0)$ magnetic ground state. Note that there may be several domains $d \in D$ of the ground state. The propagation vectors of \mathbf{m}^d are of the star $\{\mathbf{k}_c\}$, where $\mathbf{k}_c = (\frac{1}{2}, \frac{1}{2}, 0)$.

P shall be the polarization matrix of a scattering process with wave-vector $\mathbf{Q} = (\frac{1}{2}, \frac{1}{2}, 0)$. The sample orientation in the experiments, where we measure P , shall be such that the (001) plane corresponds to the scattering plane. Relations between P and \mathbf{m} may be derived by means of the Blume-Maleev equations (cf. Sec. 2.1.2 for further information). We may define $\mathbf{M}_{\perp}^d = \hat{\mathbf{Q}} \times (\mathbf{m}^d(\mathbf{Q}) \times \hat{\mathbf{Q}})$.

We consider the following two cases, where the polarization matrix satisfies (i) $P_{yy} = -P_{zz} = 1$, as well as (ii) $P_{yy} = -P_{zz} = -1$. Note that polarization matrices satisfying these conditions (i) were observed in phase C of HoCu and in phase C of ErCu (ii) in phase IC1 of HoCu and in phase IC2 of ErCu.

For contributions in the Fourier series of \mathbf{m} (Fourier components), which are related to \mathbf{k}_c , we show in the following, that:

- (i) if $P_{yy} = -P_{zz} = 1$, there are no Fourier components along the z -axis. The ground state consists of $\Gamma_9(\mathbf{k}_c)$ basis functions only.
- (ii) if $P_{yy} = -P_{zz} = -1$, there are no Fourier components perpendicular to the z -axis. The ground state consists of $\Gamma_3(\mathbf{k}_c)$ basis functions only.

In this section we address only commensurate structures. However, the same arguments hold true for incommensurate structures. For Fourier components related to $\mathbf{k}_{ic} = (\frac{1}{2} \pm \delta, \frac{1}{2}, 0)$ we may summarize:

- if $P_{yy} = -P_{zz} = 1$, there are no Fourier components along the z -axis. The ground state consists of $\Gamma_2(\mathbf{k}_{ic})$ and $\Gamma_3(\mathbf{k}_{ic})$ basis functions only (cf. case (i)).
- if $P_{yy} = -P_{zz} = -1$, there are no Fourier components perpendicular to the z -axis. The ground state consists of $\Gamma_4(\mathbf{k}_{ic})$ basis functions only (cf. case (ii)).

In the following, (i) and (ii) are established. The Fourier series of the commensurate $(\pi\pi 0)$ ground state may be written in terms of:

$$\mathbf{m}^d(\mathbf{R}) = \sum_n \mathbf{r}^d(\mathbf{k}_n^c) \exp(i\mathbf{k}_n^c \cdot \mathbf{R}) \quad (\text{A.7})$$

$$\Rightarrow \mathbf{M}^d(\mathbf{Q}) = \int \mathbf{m}^d(\mathbf{R}) d^3R = \sum_{\mathbf{G}} \sum_{n \in \{1,2,3\}} \mathbf{r}^d(\mathbf{k}_n^c) \delta(\mathbf{Q} - \mathbf{k}_n^c - \mathbf{G}) \quad (\text{A.8})$$

The off-diagonal chiral terms vanish for all commensurate $\langle \pi\pi 0 \rangle$ structures, since

$$\text{Im}(M_{\perp,i}^d M_{\perp,j}^{d*}) = 0. \quad (\text{A.9})$$

Accordingly, the equations reduce to:

$$P_{yy}^d = -P_{zz}^d = \frac{1}{|M_{\perp}^d|^2} \left(|M_{\perp,y}^d|^2 - |M_{\perp,z}^d|^2 \right) \quad (\text{A.10})$$

Note that \mathbf{m}^d represents only one single magnetic domain. In experiments carried out at zero magnetic field, all possible domains are typically equally populated. The average over all magnetic domains yields:

$$P_{yy} = \frac{1}{\sum_d \sigma^d(\mathbf{Q})} \cdot \sum_d \sigma^d(\mathbf{Q}) P_{yy}^d \quad (\text{A.11})$$

$$\Rightarrow P = \frac{1}{\sum_d \sigma^d(\mathbf{Q})} \sum_d \frac{1}{|M_{\perp}^d|^2} \sigma^d(\mathbf{Q}) \cdot \left((M_{\perp,y}^d)^2 - (M_{\perp,z}^d)^2 \right) \quad (\text{A.12})$$

For the calculation, all those domains $d \in D$ have to be considered, for which the k -arm $\left[\frac{1}{2}, \frac{1}{2}, 0\right]_{\sim}$ is participating, i.e., all domains, for which the corresponding vectorfield \mathbf{m}^d has a finite component $\mathbf{r}^d \left(\left(\frac{1}{2}, \frac{1}{2}, 0 \right) \right)$.

For calculations by means of the Blume-Maleev equations, the cartesian coordinates are defined with respect to the reciprocal space position \mathbf{Q} , such that \mathbf{e}_z is vertical and $\mathbf{e}_x = \hat{Q}$, \mathbf{e}_y , \mathbf{e}_z represent an orthonormal basis. The variables \mathbf{r}_d can be expanded in that basis as follows:

$$\mathbf{r}^d = \mu_x^d \cdot \mathbf{e}_x + \mu_y^d \cdot \mathbf{e}_y + \mu_z^d \cdot \mathbf{e}_z \quad (\text{A.13})$$

$$\Rightarrow \mathbf{M}_{\perp}^d = \hat{Q} \times (\mathbf{M}_{\perp}^d \times \hat{Q}) = \quad (\text{A.14})$$

$$= \sum_{\mathbf{G}} \sum_{n \in \{1,2,3\}} \hat{Q} \times (\mathbf{r}^d(\mathbf{k}_n^c) \times \hat{Q}) \cdot \delta(\mathbf{Q} - \mathbf{k}_n^c - \mathbf{G}) \quad (\text{A.15})$$

As is $\mathbf{Q} = (\frac{1}{2}, \frac{1}{2}, 0) = \mathbf{k}_1^c$, the equation reduces to:

$$\Rightarrow \mathbf{M}_\perp^d \sim \hat{Q} \times (\mathbf{r}^d(\mathbf{k}_1^c) \times \hat{Q}) = \quad (\text{A.16})$$

$$= \hat{Q} \times [(\mu_x^d(\mathbf{k}_1^c) \cdot \mathbf{e}_x + \mu_y^d(\mathbf{k}_1^c) \cdot \mathbf{e}_y + \mu_z^d(\mathbf{k}_1^c) \cdot \mathbf{e}_z) \times \hat{Q}] \quad (\text{A.17})$$

A short calculation provides:

$$\frac{1}{|\mathbf{M}_\perp^d|^2} \left(+ (\mathbf{M}_{\perp,y}^d)^2 - (\mathbf{M}_{\perp,z}^d)^2 \right) = \frac{+(\mu_y^d(\mathbf{k}_1^c))^2 - (\mu_z^d(\mathbf{k}_1^c))^2}{(\mu_y^d(\mathbf{k}_1^c))^2 + (\mu_z^d(\mathbf{k}_1^c))^2} \quad (\text{A.18})$$

Inserting this into Eq. (A.12) gives:

$$P_{yy} = \frac{1}{\sum_d \sigma_d(\mathbf{Q})} \sum_d \sigma_d(\mathbf{Q}) \frac{(\mu_y^d(\mathbf{k}_1^c))^2 - (\mu_z^d(\mathbf{k}_1^c))^2}{(\mu_y^d(\mathbf{k}_1^c))^2 + (\mu_z^d(\mathbf{k}_1^c))^2} \quad (\text{A.19})$$

From $P_{yy} = +1$ it follows for all domains with $\sigma_d(\mathbf{Q}) > 0$:

$$\frac{(\mu_y^d(\mathbf{k}_1^c))^2 - (\mu_z^d(\mathbf{k}_1^c))^2}{(\mu_y^d(\mathbf{k}_1^c))^2 + (\mu_z^d(\mathbf{k}_1^c))^2} = +1 \quad (\text{A.20})$$

$$\Rightarrow (\mu_z^d(\mathbf{k}_1^c))^2 = 0 \text{ and } (\mu_y^d(\mathbf{k}_1^c))^2 > 0 \quad (\text{A.21})$$

This shows that only $\Gamma_9(\mathbf{k}_c)$ basis functions occur in the Fourier decomposition of \mathbf{m}_d , if $\sigma_d(\mathbf{Q}) > 0$.

Further, this holds true for all other domains, as argued in the following. Consider the specific case of a domain D_{d_1} , which has a propagation vector of the k -arm A_1^c with $\sigma^{d_1}(\mathbf{Q}) = 0$. As the structure factor vanishes at \mathbf{Q} , the magnetic moments must fulfill $\mathbf{r}(\mathbf{k}_1^c) \parallel \mathbf{Q}$.

However, from the symmetries of the space group it follows that there is a second domain D_{d_2} that originates from D_{d_1} by a rotation around [001] by an angle $\theta = 90^\circ$. In particular, the domains have the same propagation vector \mathbf{k}_1^c and components along the z -axis are equivalent, i.e., $\mu_z^{d_1}(\mathbf{k}_1^c) = \mu_z^{d_2}(\mathbf{k}_1^c)$. In this second domain, the polarization factor of the structure factor is not suppressed at the position \mathbf{Q} , i.e., $\sigma_{d_2}(\mathbf{Q}) > 0$. It follows $\mu_z^{d_1}(\mathbf{k}_1^c) = \mu_z^{d_2}(\mathbf{k}_1^c) = 0$, and $\mu_x^{d_1}(\mathbf{k}_1^c) = \mu_y^{d_2}(\mathbf{k}_1^c) > 0$. This implies for both domains D_{d_1} and D_{d_2} that all components of \mathbf{m} along the z -axis vanish.

Second, we consider (ii). From Eq. (A.19) it may be inferred:

$$\frac{(\mu_y^d(\mathbf{k}_1^c))^2 - (\mu_z^d(\mathbf{k}_1^c))^2}{(\mu_y^d(\mathbf{k}_1^c))^2 + (\mu_z^d(\mathbf{k}_1^c))^2} = -1 \quad (\text{A.22})$$

$$\Rightarrow (\mu_y^d(\mathbf{k}_1^c))^2 = 0 \text{ and } (\mu_z^d(\mathbf{k}_1^c))^2 > 0 \quad (\text{A.23})$$

The same argument as before shows, that Eq. (A.23) holds for all domains. Hence, all components of moments in the basal plane vanish and the ground state consists of only $\Gamma_3(\mathbf{k}_c)$ basis functions.

A.3. Stoke's Theorem for Chern Numbers

In the following, a variation of Stoke's theorem is derived, which describes the relation between Chern-numbers and the distribution of magnetic monopoles in the first Brillouin zone of the electronic structure. The theorem is discussed further in the study presented in Sec. 3.3.7.2.

In Sec. 3.3.7.2 an electron band $|v_1\rangle$ with Berry curvature $\Omega(\mathbf{k})$ was considered. The band $|v_1\rangle$ features magnetic charges in the first Brillouin zone. The Chern numbers follow the following variation of Stoke's law given by:

$$\gamma(k_z) = \sum_{k < k_z} Q(k) - \sum_{k > k_z} Q(k). \quad (\text{A.24})$$

This law may be derived by basic vector analysis calculations as follows. We consider the following two cuboid regions in the reciprocal space defined by:

$$V_<(k_z) := \left\{ (\kappa_x, \kappa_y, \kappa_z) : -\frac{\pi}{a} \leq \kappa_x, \kappa_y \leq \frac{\pi}{a}; -\frac{\pi}{a} \leq \kappa_z \leq k_z \right\} \quad (\text{A.25})$$

$$V_>(k_z) := \left\{ (\kappa_x, \kappa_y, \kappa_z) : -\frac{\pi}{a} \leq \kappa_x, \kappa_y \leq \frac{\pi}{a}; k_z \leq \kappa_z \leq \frac{\pi}{a} \right\}. \quad (\text{A.26})$$

The first BZ is the union of $V_<(k_z)$ and $V_>(k_z)$. The Berry curvature fulfills (cf. Ref. [164]):

$$\text{rot } \Omega(\mathbf{k}_0) = 4\pi i \cdot \sum_{\mathbf{k}} \delta(\mathbf{k} - \mathbf{k}_0) Q(\mathbf{k}). \quad (\text{A.27})$$

On the other hand, conventional Stoke's theorem provides:

$$\begin{aligned} \int_{V_<(k_z)} \text{rot } \Omega(\mathbf{k}_0) &= \int_{\partial V_<(k_z)} \Omega \cdot d\mathbf{S} \\ \int_{V_>(k_z)} \text{rot } \Omega(\mathbf{k}_0) &= \int_{\partial V_>(k_z)} \Omega \cdot d\mathbf{S}. \end{aligned} \quad (\text{A.28})$$

Note, that the sum of surface integrals over the facets of the first Brillouin zone vanishes due to the periodicity of Ω . Eqs. (A.27) and Eqs. (A.28) provide further:

$$4\pi i \sum_{\mathbf{k} \in V_<(k_z)} Q(\mathbf{k}) = 2\pi i \left[\gamma(k_z) - \gamma\left(-\frac{\pi}{a}\right) \right] \quad (\text{A.29})$$

$$4\pi i \sum_{\mathbf{k} \in V_>(k_z)} Q(\mathbf{k}) = 2\pi i \left[\gamma\left(\frac{\pi}{a}\right) - \gamma(k_z) \right]. \quad (\text{A.30})$$

Note, that is $\gamma\left(\frac{\pi}{a}\right) = \gamma\left(-\frac{\pi}{a}\right) = 0$, as the charges in the first Brillouin zone add up to zero. Subtraction of the two formulas gives:

$$2 \sum_{\mathbf{k} \in V_{<}(k_z)} Q(\mathbf{k}) - 2 \sum_{\mathbf{k} \in V_{>}(k_z)} Q(\mathbf{k}) = \left[2\gamma(k_z) - 2\gamma\left(\frac{\pi}{a}\right) \right] \quad (\text{A.31})$$

As $\gamma\left(\frac{\pi}{a}\right) = 0$, Eq. (A.24) follows directly from Eq. (A.31).

A.4. Neutron Diffraction on HoCu with Magnetic Field along Twofold Directions

As reported in Sec. 3.3.4.1, field and temperature dependencies of magnetic Bragg peaks were determined for fields along twofold $\langle 110 \rangle$ directions. In the following, we present integrated intensities as a function of temperature of magnetic Bragg peaks, as inferred from sweepT1, sweepT2, sweepT3, sweepT4, sweepT5, and sweepT6 (Fig. 3.21).

Shown in Fig. A.1 are temperature dependences of integrated intensities of Bragg peaks of the stars $\langle \mathbf{q}_{I,\alpha} \rangle$ and $\langle \mathbf{q}_{I,\beta} \rangle$.

Shown in Fig. A.2 are the temperature dependences of the Bragg peaks located at positions of the stars $\langle \pi\pi 0 \rangle$ and $\langle \pi - \delta, \pi, 0 \rangle$.

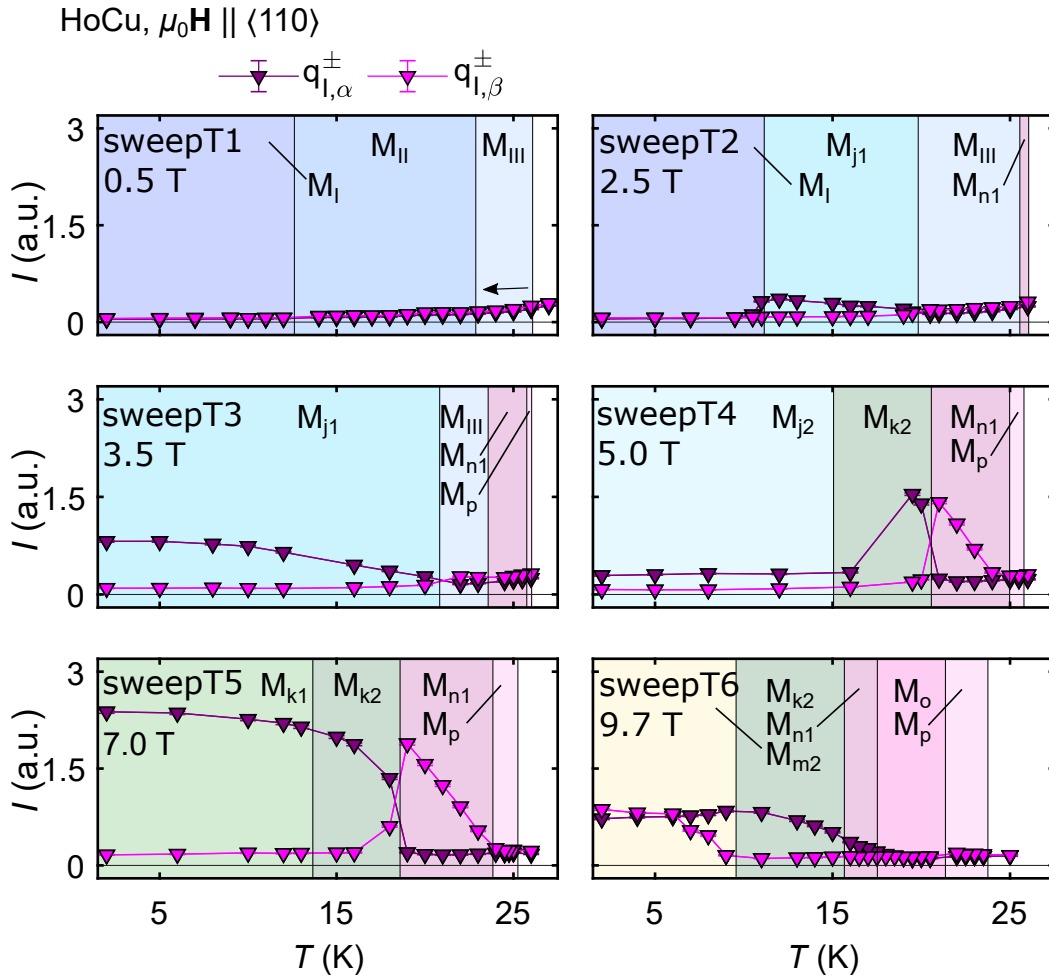


Figure A.1.: Integrated intensities of Bragg peaks the stars $\langle \mathbf{q}_{I,\alpha} \rangle$ and $\langle \mathbf{q}_{I,\beta} \rangle$, as inferred from sweepT1, sweepT2, sweepT3, sweepT4, sweepT5, and sweepT6. Data were recorded for decreasing fields.

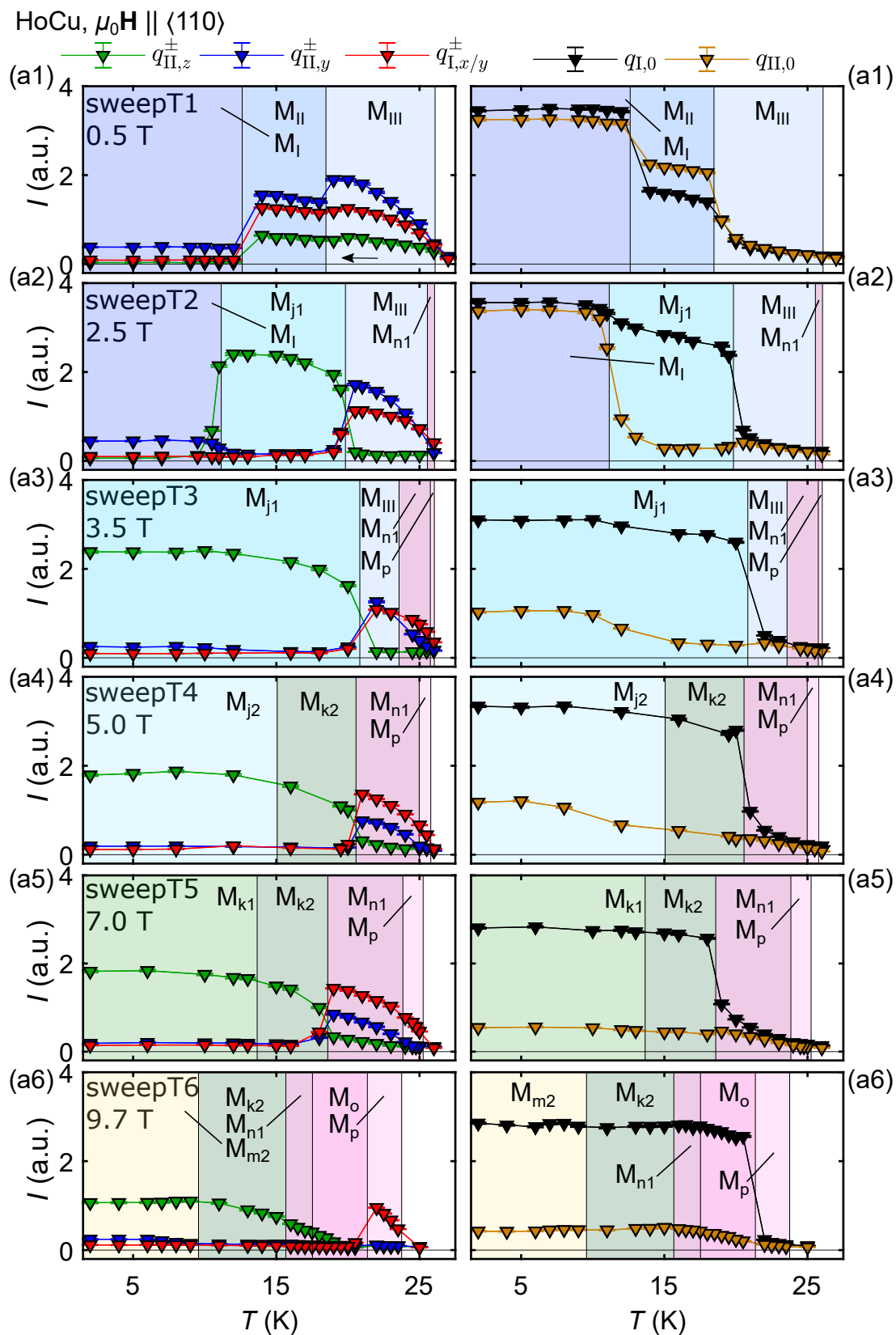


Figure A.2.: Integrated intensities of Bragg peaks the stars (a) $\langle \pi - \delta, \pi, 0 \rangle$ and (b) $\langle \pi\pi 0 \rangle$, as inferred from sweepT1, sweepT2, sweepT3, sweepT4, sweepT5, and sweepT6. Data were recorded for decreasing fields.

A.5. Neutron Diffraction on TmCu with Field along Twofold Directions

In Sec. 3.4.3, an unconventional phase M_{b1} of the $\langle 110 \rangle$ phase diagram of TmCu was identified. Fig. A.3 shows the diffraction intensity in this phase, as recorded in the $(h, k, 1.5)$ plane. The Bragg peaks, which were observed, may be indexed by propagation vectors $(0, \frac{1}{2}, \frac{1}{2})$, $(\frac{1}{7}, \frac{1}{2}, \frac{1}{2})$, $(\frac{2}{7}, \frac{1}{2}, \frac{1}{2})$, and $(\frac{3}{7}, \frac{1}{2}, \frac{1}{2})$. Accordingly, the ground state in M_{b1} is distinctively different from a $(\pi\pi 0)$ antiferromagnet.

TmCu
Orientation O2, $\mu_0\mathbf{H} \parallel [0, -1, 1]$
phase M_{b1} , $\mu_0H = 5$ T, $T = 2$ K

$(h, k, 1.5)$ -plane

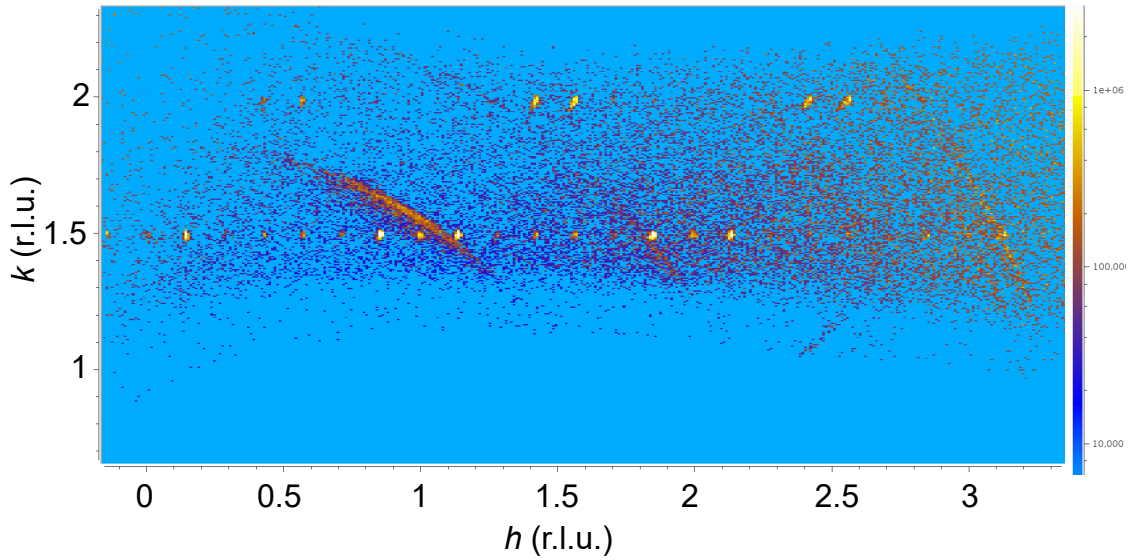


Figure A.3.: Scattering intensity in phase M_{b1} of TmCu. Shown is the diffraction intensity as recorded in the $(h, k, 1.5)$ plane. Along the line $(h, 1.5, 1.5)$ Bragg peaks are present at positions $h = j \cdot \frac{1}{7}$ with $j = \{-1, 4, 5, 6, 7, \dots, 21\}$. Peaks are also present at the positions $(\frac{3}{7}, 2, 1.5)$, $(\frac{4}{7}, 2, 1.5)$, $(\frac{10}{7}, 2, 1.5)$ and $(\frac{11}{7}, 2, 1.5)$. Accordingly, the magnetic ground state is multi- k and a superposition of propagation vectors such as $(0, \frac{1}{2}, \frac{1}{2})$, $(\frac{1}{7}, \frac{1}{2}, \frac{1}{2})$, $(\frac{2}{7}, \frac{1}{2}, \frac{1}{2})$, and $(\frac{3}{7}, \frac{1}{2}, \frac{1}{2})$.

Bibliography

- [1] J. M. Kosterlitz and D. J. Thouless, Long range order and metastability in two dimensional solids and superfluids. (Application of dislocation theory), [J. Phys. C **5**, L124 \(1972\)](#).
- [2] J. M. Kosterlitz and D. J. Thouless, Ordering, metastability and phase transitions in two-dimensional systems, [J. Phys. C **6**, 1181 \(1973\)](#).
- [3] D. J. Thouless, M. Kohmoto, M. P. Nightingale, and M. den Nijs, Quantized Hall Conductance in a Two-Dimensional Periodic Potential, [Phys. Rev. Lett. **49**, 405 \(1982\)](#).
- [4] F. D. M. Haldane, Continuum dynamics of the 1-D Heisenberg antiferromagnet: Identification with the $O(3)$ nonlinear sigma model, [Phys. Lett. A **93**, 464 \(1983\)](#).
- [5] F. D. M. Haldane, Nonlinear Field Theory of Large-Spin Heisenberg Antiferromagnets: Semiclassically Quantized Solitons of the One-Dimensional Easy-Axis Néel State, [Phys. Rev. Lett. **50**, 1153 \(1983\)](#).
- [6] S. Mühlbauer, B. Binz, F. Jonietz, C. Pfleiderer, A. Rosch, A. Neubauer, R. Georgii, and P. Böni, Skyrmion Lattice in a Chiral Magnet, [Science **323**, 915 \(2009\)](#).
- [7] Y. Ishikawa, K. Tajima, D. Bloch, and M. Roth, Helical spin structure in manganese silicide MnSi, [Solid State Commun. **19**, 525 \(1976\)](#).
- [8] T. Adams, S. Mühlbauer, C. Pfleiderer, F. Jonietz, A. Bauer, A. Neubauer, R. Georgii, P. Böni, U. Keiderling, K. Everschor, M. Garst, and A. Rosch, Long-Range Crystalline Nature of the Skyrmion Lattice in MnSi, [Phys. Rev. Lett. **107**, 217206 \(2011\)](#).
- [9] A. Neubauer, C. Pfleiderer, B. Binz, A. Rosch, R. Ritz, P. G. Niklowitz, and P. Böni, Topological Hall Effect in the *A* Phase of MnSi, [Phys. Rev. Lett. **102**, 186602 \(2009\)](#).
- [10] T. Schulz, R. Ritz, A. Bauer, M. Halder, M. Wagner, C. Franz, C. Pfleiderer, K. Everschor, M. Garst, and A. Rosch, Emergent electrodynamics of skyrmions in a chiral magnet, [Nat. Phys. **8**, 301 \(2012\)](#).

- [11] W. Münzer, A. Neubauer, T. Adams, S. Mühlbauer, C. Franz, F. Jonietz, R. Georgii, P. Böni, B. Pedersen, M. Schmidt, A. Rosch, and C. Pfleiderer, Skyrmion lattice in the doped semiconductor $\text{Fe}_{1-x}\text{Co}_x\text{Si}$, *Phys. Rev. B* **81**, 041203 (2010).
- [12] S. Seki, X. Z. Yu, S. Ishiwata, and Y. Tokura, Observation of Skyrmions in a Multiferroic Material, *Science* **336**, 198 (2012).
- [13] T. Schwarze, J. Waizner, M. Garst, A. Bauer, I. Stasinopoulos, H. Berger, C. Pfleiderer, and D. Grundler, Universal helimagnon and skyrmion excitations in metallic, semiconducting and insulating chiral magnets, *Nat. Mater.* **14**, 478 (2015).
- [14] T. Moriya, Anisotropic Superexchange Interaction and Weak Ferromagnetism, *Phys. Rev.* **120**, 91 (1960).
- [15] I. Dzyaloshinsky, A thermodynamic theory of “weak” ferromagnetism of antiferromagnetics, *J. Phys. Chem. Solids* **4**, 241 (1958).
- [16] Z. Wang, E. Ruff, M. Schmidt, V. Tsurkan, I. Kézsmárki, P. Lunkenheimer, and A. Loidl, Polar Dynamics at the Jahn-Teller Transition in Ferroelectric GaV_4S_8 , *Phys. Rev. Lett.* **115**, 207601 (2015).
- [17] A. K. Nayak, V. Kumar, T. Ma, P. Werner, E. Pippel, R. Sahoo, F. Damay, U. K. Rößler, C. Felser, and S. S. P. Parkin, Magnetic antiskyrmions above room temperature in tetragonal Heusler materials, *Nature* **548**, 561 (2017).
- [18] M. Rahn, *Search for Topological Properties in Multi-k Magnetic Structures*, Diploma thesis, Technische Universität München (2013).
- [19] A. Bauer, A. Senyshyn, C. Franz, W. Simeth, S. Bozhanova, S. Gottlieb-Schönmeyer, and C. Pfleiderer, Long-wavelength magnetic texture and unconventional hall effect in EuPtSi_3 , (2019), unpublished.
- [20] C. G. Shull, W. A. Strauser, and E. O. Wollan, Neutron Diffraction by Paramagnetic and Antiferromagnetic Substances, *Phys. Rev.* **83**, 333 (1951).
- [21] S. W. Lovesey, *Theory of Neutron Scattering from Condensed Matter. Vol. 2: Polarization Effects and Magnetic Scattering* (Clarendon Press: Oxford, 1984).
- [22] G. L. Squires, *Introduction to the theory of Thermal Neutron Scattering* (Cambridge University Press, 1978).
- [23] P. M. Chaikin and T. C. Lubensky, *Principles of condensed matter theory* (Cambridge University Press, 1995).

- [24] N. W. Ashcroft and N. Mermin, *Solid State Physics* (Harcourt: New York, 1976).
- [25] P. J. Brown, A. G. Fox, E. N. Maslen, M. A. O'Keefe, and B. T. M. Willis, *International Tables for Crystallography* (International Union of Crystallography, 2006).
- [26] K. Gottfried and T. Yan, *Quantum mechanics: fundamentals* (Springer Science & Business Media, 2013).
- [27] P. Debye, Interferenz von Röntgenstrahlen und Wärmebewegung, *Ann. Phys. (N. Y.)* **348**, 49 (1913).
- [28] I. Waller, Zur Frage der Einwirkung der Wärmebewegung auf die Interferenz von Röntgenstrahlen, *Zeitschrift für Physik A Hadrons and Nuclei* **17**, 398 (1923).
- [29] C. G. Shull and J. S. Smart, Detection of Antiferromagnetism by Neutron Diffraction, *Phys. Rev.* **76**, 1256 (1949).
- [30] J. Jensen and A. R. Mackintosh, *Rare earth magnetism* (Clarendon Oxford, 1991).
- [31] J. B. Forsyth and M. Wells, On an analytic approximation to the atomic scattering factor, *Acta Crystallogr.* **12**, 412 (1959).
- [32] J. Schweizer, CHAPTER 4 - Polarized Neutrons and Polarization Analysis, in *Neutron Scattering from Magnetic Materials*, edited by T. Chatterji (Elsevier Science, 2006) pp. 153–213.
- [33] P. J. Brown, CHAPTER 5 - Spherical Neutron Polarimetry, in *Neutron Scattering from Magnetic Materials*, edited by T. Chatterji (Elsevier Science, 2006) pp. 215–244.
- [34] C. J. Joachain, *Quantum collision theory* (North-Holland, Amsterdam, 1983).
- [35] M. Blume, Polarization Effects in the Magnetic Elastic Scattering of Slow Neutrons, *Phys. Rev.* **130**, 1670 (1963).
- [36] S. V. Maleev, V. G. Bar'yakhtar, and R. A. Suris, THE SCATTERING OF SLOW NEUTRONS BY COMPLEX MAGNETIC STRUCTURES, *Soviet Phys.-Solid State (English Transl.)* **Vol: 4** (1963).
- [37] M. Janoschek, S. Klimko, R. Gähler, B. Roessli, and P. Böni, Spherical neutron polarimetry with MuPAD, *Physica B* **397**, 125 (2007).
- [38] M. Janoscheck, *Investigation of the chiral magnets $NdFe_3(^{11}BO_3)_4$ and $MnSi$ by means of neutron scattering*, Ph.D. thesis, Technische Universität München (2008).

- [39] J. Kindervater, *Fluctuation-induced magnetic phase transitions in Fe and MnSi studied by neutron scattering*, Ph.D. thesis, Technische Universität München (2015).
- [40] E. F. Bertaut, Representation analysis of magnetic structures, *Acta Crystallogr. A* **24**, 217 (1968).
- [41] J. M. Perez-Mato, J. L. Ribeiro, V. Petricek, and M. I. Aroyo, Magnetic superspace groups and symmetry constraints in incommensurate magnetic phases, *J. Phys. Condens. Matter* **24**, 163201 (2012).
- [42] J. Rodríguez-Carvajal and F. Bourée, Symmetry and magnetic structures, *EPJ Web of Conferences* **22**, 00010 (2012).
- [43] V. Petříček, J. Fuksa, and M. Dušek, Magnetic space and superspace groups, representation analysis: competing or friendly concepts? *Acta Crystallogr. A* **66**, 649 (2010).
- [44] A. Wills, Magnetic structures and their determination using group theory, *J. Phys. IV France* **11**, Pr9 (2001).
- [45] T. Chatterji, CHAPTER 2 - Magnetic Structures, in *Neutron Scattering from Magnetic Materials*, edited by T. Chatterji (Elsevier Science, 2006) pp. 25–91.
- [46] R. Ballou and B. Ouladdiaf, CHAPTER 3 - Representation Analysis of Magnetic Structures, in *Neutron Scattering from Magnetic Materials*, edited by T. Chatterji (Elsevier Science, 2006) pp. 93–151.
- [47] Y. A. Izyumov, V. E. Naish, and R. P. Ozerov, *Neutron Diffraction of Magnetic Materials* (Consultants Bureau, Plenum Publishing Corporation, New York, 1991).
- [48] Y. A. Izyumov and V. E. Naish, Symmetry analysis in neutron diffraction studies of magnetic structures: 1. A phase transition concept to describe magnetic structures in crystals, *J. Magn. Magn. Mater.* **12**, 239 (1979).
- [49] Y. A. Izyumov, V. E. Naish, and S. B. Petrov, Symmetry analysis in neutron diffraction studies of magnetic structures: 3. An example: The magnetic structure of spinels, *J. Magn. Magn. Mater.* **13**, 267 (1979).
- [50] Y. A. Izyumov, V. E. Naish, and S. B. Petrov, Symmetry analysis in neutron diffraction studies of magnetic structures: 4. Theoretical group analysis of exchange Hamiltonian, *J. Magn. Magn. Mater.* **13**, 275 (1979).

- [51] J. Rodríguez-Carvajal and J. Villain, Magnetic structures, *Comptes Rendus Physique* (2019), in press.
- [52] Y. A. Izyumov, V. E. Naish, and V. N. Syromiatnikov, Symmetry analysis in neutron diffraction studies of magnetic structures: 2. Changes in periodicity at magnetic phase transitions, *J. Magn. Magn. Mater.* **12**, 249 (1979).
- [53] J. Rossat-Mignod, Magnetic Structures, in *Methods in Experimental Physics*, Vol. 23, edited by K. Sköld and D. L. Price (Academic Press, 1987) pp. 69–157.
- [54] A. S. Wills, A new protocol for the determination of magnetic structures using simulated annealing and representational analysis (SARAh), *Physica B* **276-278**, 680 (2000).
- [55] O. V. Kovalev, *Representations of the Crystallographic Space Groups: Irreducible Representations, Induced Representations, and Corepresentations* (Gordon and Breach Science, 1993).
- [56] B. J. Campbell, H. T. Stokes, D. E. Tanner, and D. M. Hatch, ISODISPLACE: A web-based tool for exploring structural distortions, *J. Appl. Crystallogr.* **39**, 607 (2006).
- [57] H. M. Rietveld, A profile refinement method for nuclear and magnetic structures, *J. Appl. Crystallogr.* **2**, 65 (1969).
- [58] W. R. Inc., Mathematica, Version 11.3, (2018).
- [59] V. Petříček, M. Dušek, and L. Palatinus, Crystallographic Computing System JANA2006, *Z. Kristallogr. Cryst. Mater.* **229**, 345 (2014).
- [60] J. Rodríguez-Carvajal and A. FULLPROF, Program for rietveld refinement and pattern matching analysis, in *Satellite Meeting on Powder Diffraction of the 15th International Congress of the IUCr, Toulouse (France)* (1990) p. 127.
- [61] D. E. Moncton, J. D. Axe, and F. J. DiSalvo, Neutron scattering study of the charge-density wave transitions in $2H - \text{TaSe}_2$ and $2H - \text{NbSe}_2$, *Phys. Rev. B* **16**, 801 (1977).
- [62] G. Shirane, M. Shapiro, and J. Tranquada, *Neutron Scattering with a Triple-Axis Spectrometer – Basic Techniques* (Cambridge University Press, 2002).
- [63] E. M. Forgan, E. P. Gibbons, K. A. McEwen, and D. Fort, Observation of a Quadruple- q Magnetic Structure in Neodymium, *Phys. Rev. Lett.* **62**, 470 (1989).

- [64] E. M. Forgan, The magnetic structure of neodymium below 20k: a first-principles mean field theory for two-dimensionally modulated spin patterns in an antiferromagnet, *J. Phys. F* **12**, 779 (1982).
- [65] K. A. McEwen, C. Vettier, and B. Lebech, Uniaxial stress dependence of the magnetic structure of neodymium, *J. Magn. Magn. Mater.* **31-34**, 171 (1983).
- [66] B. Lebech, Neutron diffraction studies of the modulated magnetic structures of CeSb and Nd metal (invited), *J. Appl. Phys.* **52**, 2019 (1981).
- [67] A. Bauer, G. Benka, A. Regnat, C. Franz, and C. Pfleiderer, Ultra-high vacuum compatible preparation chain for intermetallic compounds, *Rev. Sci. Instrum.* **87**, 113902 (2016).
- [68] P. Morin and D. Schmitt, Competition between multi- q antiferromagnetic structures in cubic rare earth-copper compounds, *J. Magn. Magn. Mater.* **21**, 243 (1980).
- [69] P. Morin and D. Schmitt, Quadrupolar Interactions and Magneto-elastic Effects in Rare-earth Intermetallic Compounds, in *Handbook of Ferromagnetic Materials*, Vol. 5, edited by K. H. J. Buschow and E. P. Wohlfahrt (Elsevier, 1990) pp. 1–132.
- [70] R. E. Walline and W. E. Wallace, Magnetic and Structural Characteristics of Lanthanide—Copper Compounds, *J. Chem. Phys.* **42**, 604 (1965).
- [71] K. Buschow, Intermetallic compounds of rare earths and non-magnetic metals, *Rep. Prog. Phys.* **42**, 1373 (1979).
- [72] Y. Gefen and M. Rosen, Anomalous elasticity and anelasticity of GdCu at low temperatures, *J. Phys. Chem. Solids* **42**, 857 (1981).
- [73] J. Pierre and B. Hennion, Crystalline Electric Field Effects in f-electron Magnetism, in *Martensitic Transformation Triggered by Magnetic Ordering*, edited by Z. Z. R. P. Guertin, W. Suski (Plenum, New York, 1982) p. 275.
- [74] K. Buschow, Intermetallic compounds of rare-earth and 3d transition metals, *Rep. Prog. Phys.* **40**, 1179 (1977).
- [75] K. H. J. Buschow and J. F. Fast, Magnetic Properties of Some Rare-Earth Aluminium Compounds, *Z. für Phys. Chem.* **50**, 1 (2011).
- [76] H. A. Gersch and W. C. Koehler, Types of magnetically ordered configurations on simple lattices, *J. Phys. Chem. Solids* **5**, 180 (1958).

- [77] J. Sakurai, Y. Kubo, T. Kondo, J. Pierre, and E. F. Bertaut, Relations between the Ruderman-Kittel-Kasuya-Yosida interaction electron concentration and crystal structure, *J. Phys. Chem. Solids* **34**, 1305 (1973).
- [78] R. Aléonard and P. Morin, TmCd quadrupolar ordering and magnetic interactions, *Phys. Rev. B* **19**, 3868 (1979).
- [79] M. T. Hutchings, Point-Charge Calculations of Energy Levels of Magnetic Ions in Crystalline Electric Fields, in *Solid State Physics*, Vol. 16, edited by F. Seitz and D. Turnbull (Academic Press, 1964) pp. 227–273.
- [80] K. R. Lea, M. J. M. Leask, and W. P. Wolf, The raising of angular momentum degeneracy of f-Electron terms by cubic crystal fields, *J. Phys. Chem. Solids* **23**, 1381 (1962).
- [81] P. Santini, S. Carretta, G. Amoretti, R. Caciuffo, N. Magnani, and G. H. Lander, Multipolar interactions in *f*-electron systems: The paradigm of actinide dioxides, *Rev. Mod. Phys.* **81**, 807 (2009).
- [82] P. M. Levy, P. Morin, and D. Schmitt, Large Quadrupolar Interactions in Rare-Earth Compounds, *Phys. Rev. Lett.* **42**, 1417 (1979).
- [83] R. Aléonard and P. Morin, Magnetic properties of equiatomic rare earth cadmium compounds, *J. Magn. Magn. Mater.* **50**, 128 (1985).
- [84] C. Jaussaud, P. Morin, and D. Schmitt, Quadrupolar interactions in TmCu, *J. Magn. Magn. Mater.* **22**, 98 (1980).
- [85] D. Givord, P. Morin, and D. Schmitt, Magnetic properties of TmZn in the ordered phase, *J. Magn. Magn. Mater.* **40**, 121 (1983).
- [86] R. Aléonard, P. Morin, and J. Rouchy, Magnetic and quadrupolar properties of DyCu and related dysprosium cubic compounds, *J. Magn. Magn. Mater.* **46**, 233 (1984).
- [87] P. Morin, J. Rouchy, and D. Schmitt, Cooperative Jahn-Teller effect in TmZn, *Phys. Rev. B* **17**, 3684 (1978).
- [88] P. Morin, Quadrupolar ordering in CeAg, *J. Magn. Magn. Mater.* **71**, 151 (1988).
- [89] A. Czopnik, N. Iliew, B. Staliński, H. Mädge, C. Bazan, and R. Pott, Magnetic and structural transitions in TmGa₃, *Physica B+C* **130**, 262 (1985).

- [90] P. Morin, M. Giraud, P. Burlet, and A. Czopnik, Antiferroquadrupolar and antiferromagnetic structures in TmGa_3 , *J. Magn. Magn. Mater.* **68**, 107 (1987).
- [91] T. Onimaru, T. Sakakibara, N. Aso, H. Yoshizawa, H. S. Suzuki, and T. Takeuchi, Observation of Modulated Quadrupolar Structures in PrPb_3 , *Phys. Rev. Lett.* **94**, 197201 (2005).
- [92] J. M. Effantin, J. Rossat-Mignod, P. Burlet, H. Bartholin, S. Kunii, and T. Kasuya, Magnetic phase diagram of CeB_6 , *J. Magn. Magn. Mater.* **47-48**, 145 (1985).
- [93] I. Kakeya, T. Kakeshita, K. Kindo, Y. Yamamoto, and T. Saburi, High Field Magnetization in DyCu , *J. Phys. Soc. Jpn.* **68**, 1025 (1999).
- [94] E. Stryjewski and N. Giordano, Metamagnetism, *Adv. Phys.* **26**, 487 (1977).
- [95] M. Amara, R. M. Galéra, P. Morin, J. Voiron, and P. Burlet, Magnetic phase diagram in NdIn_3 antiferromagnet, *J. Magn. Magn. Mater.* **131**, 402 (1994).
- [96] A. Yamagishi, K. Yonenobu, O. Kondo, P. Morin, and M. Date, Metamagnetic transitions of DyAg in pulsed high magnetic field, *J. Magn. Magn. Mater.* **90-91**, 51 (1990).
- [97] P. Morin, J. Rouchy, D. Schmitt, and E. du Tremolet de Lacheisserie, Interplay between quadrupolar and bilinear interactions in rare earth intermetallics, *J. Magn. Magn. Mater.* **90-91**, 105 (1990).
- [98] D. Gignoux and D. Schmitt, Rare earth intermetallics, *J. Magn. Magn. Mater.* **100**, 99 (1991).
- [99] D. Gignoux and D. Schmitt, Competition between commensurate and incommensurate phases in rare-earth systems: Effects on H-T magnetic phase diagrams, *Phys. Rev. B* **48**, 12682 (1993).
- [100] J. Jensen and A. R. Mackintosh, Novel magnetic phases in holmium, *J. Magn. Magn. Mater.* **104-107**, 1481 (1992).
- [101] S. W. Zochowski, K. A. McEwen, and E. Fawcett, Magnetic phase diagrams of neodymium, *J. Phys. Condens. Matter* **3**, 8079 (1991).
- [102] R. M. Moon, J. W. Cable, and W. C. Koehler, Magnetic Structure of Neodymium, *J. Appl. Phys.* **35**, 1041 (1964).
- [103] J. Schweizer, J. Villain, and A. B. Harris, Symmetry of magnetic structures: the case of CeAl_2 , *Eur. Phys. J. Appl. Phys.* **38**, 41 (2007).

- [104] S. M. Shapiro, E. Gurewitz, R. D. Parks, and L. C. Kupferberg, Multiple- q Magnetic Structure in CeAl_2 , *Phys. Rev. Lett.* **43**, 1748 (1979).
- [105] E. M. Forgan, B. D. Rainford, S. L. Lee, J. S. Abell, and Y. Bi, The magnetic structure of CeAl_2 is a non-chiral spiral, *J. Phys. Condens. Matter* **2**, 10211 (1990).
- [106] M. Amara and P. Morin, Multiaxial antiferromagnetic structures and quadrupolar interactions, *Physica B* **205**, 379 (1995).
- [107] M. Wintenberger and R. Chamard-Bois, Indétermination sur les dimensions de la maille magnétique dans l'étude par diffraction neutronique sur poudres de corps cubiques ou uniaxes, *Acta Crystallogr. A* **28**, 341 (1972).
- [108] G. Shirane, A note on the magnetic intensities of powder neutron diffraction, *Acta Crystallogr.* , 282 (1959).
- [109] R. Ritz, M. Halder, C. Franz, A. Bauer, M. Wagner, R. Bamler, A. Rosch, and C. Pfleiderer, Giant generic topological Hall resistivity of MnSi under pressure, *Phys. Rev. B* **87**, 134424 (2013).
- [110] C. Franz, F. Freimuth, A. Bauer, R. Ritz, C. Schnarr, C. Duvinage, T. Adams, S. Blügel, A. Rosch, Y. Mokrousov, and C. Pfleiderer, Real-Space and Reciprocal-Space Berry Phases in the Hall Effect of $\text{Mn}_{1-x}\text{Fe}_x\text{Si}$, *Phys. Rev. Lett.* **112**, 186601 (2014).
- [111] C.-C. Chao, Electrical Resistivity of Equiatomic Rare-Earth-Noble-Metal Compounds, *J. Appl. Phys.* **37**, 2081 (1966).
- [112] R. R. Birss, R. V. Houldsworth, and D. G. Lord, Magnetoresistance in holmium copper compounds, *J. Magn. Magn. Mater.* **15-18**, 917 (1980).
- [113] D. Schmitt, P. Morin, and J. Pierre, Crystal field and magnetic properties in some cubic holmium compounds, *Phys. Rev. B* **15**, 1698 (1977).
- [114] P. Morin, J. Pierre, and J. Chaussy, Specific Heat in TbZn and HoZn Compounds, *Phys. Status Solidi A* **24**, 425 (1974).
- [115] I. Kakeya, T. Kakeshita, K. Kindo, Y. Yamamoto, and T. Saburi, High Field Magnetization in DyCu , *J. Phys. Soc. Jpn.* **68**, 1025 (1999).
- [116] P. Morin and D. Schmitt, Magnetic properties and quadrupolar interactions in PrAg , *Phys. Rev. B* **26**, 3891 (1982).

- [117] D. Xiao, M.-C. Chang, and Q. Niu, Berry phase effects on electronic properties, [Rev. Mod. Phys. **82**, 1959 \(2010\)](#).
- [118] M. Rahn, *Magnetic properties, magnetoresistance and Hall effect of RCu (R= Ho, Er, Tm)*, Personal Summary, Technische Universität München (2013).
- [119] M. R. Ibarra, P. A. Algarabel, and A. S. Pavlovic, High-field magnetostriction of TbCu, DyCu, and HoCu, [J. Appl. Phys. **67**, 4814 \(1990\)](#).
- [120] K. Tajima, P. Böni, G. Shirane, Y. Ishikawa, and M. Kohgi, Paramagnetic spin fluctuations in an Fe₆₅Ni₃₅ alloy, [Phys. Rev. B **35**, 274 \(1987\)](#).
- [121] M. Meven and A. Sazonov, HEiDi: Single crystal diffractometer at hot source, [JLSRF **1**, 7 \(2015\)](#).
- [122] V. F. Sears, Neutron scattering lengths and cross sections, [Neutron News **3**, 26 \(1992\)](#).
- [123] H. M. Rietveld, The Rietveld Method: A Retrospection, [Z. Kristallogr. Cryst. Mater. **225**, 545 \(2010\)](#).
- [124] A. Ostermann and T. Schrader, BIODIFF: Diffractometer for large unit cells, [JLSRF **1**, 2 \(2015\)](#).
- [125] W. Setyawan and S. Curtarolo, High-throughput electronic band structure calculations: Challenges and tools, [Comput. Mater. Sci. **49**, 299 \(2010\)](#).
- [126] W. C. Koehler, J. W. Cable, M. K. Wilkinson, and E. O. Wollan, Magnetic Structures of Holmium. I. The Virgin State, [Phys. Rev. **151**, 414 \(1966\)](#).
- [127] A. Heinemann and S. Mühlbauer, SANS-1: Small angle neutron scattering, [JLSRF **1**, 10 \(2015\)](#).
- [128] R. Gilles, A. Ostermann, and W. Petry, Monte Carlo simulations of the new small-angle neutron scattering instrument SANS-1 at the Heinz Maier-Leibnitz Forschungsneutronenquelle, [J. Appl. Crystallogr. **40**, s428 \(2007\)](#).
- [129] R. Gilles, A. Ostermann, C. Schanzer, B. Krimmer, and W. Petry, The concept of the new small-angle scattering instrument SANS-1 at the FRM-II, [Physica B **385-386**, 1174 \(2006\)](#).
- [130] M. Renninger, "Umweganregung", eine bisher unbeachtete Wechselwirkungserscheinung bei Raumgitterinterferenzen, [Z. Physik **106**, 141 \(1937\)](#).

- [131] E. Rossmannith, Multiple diffraction in the kinematical approach, *Acta Crystallogr. A* **62**, 174 (2006).
- [132] T. M. Giebultowicz, A. W. Overhauser, and S. A. Werner, Direct Observation of the Charge-Density Wave in Potassium by Neutron Diffraction, *Phys. Rev. Lett.* **56**, 1485 (1986).
- [133] L. Pintschovius, O. Blaschko, G. Krexner, M. de Podesta, and R. Currat, Search for charge-density waves in potassium by neutron diffraction, *Phys. Rev. B* **35**, 9330 (1987).
- [134] A. S. Wills, Validation of magnetic structures, *Z. Kristallogr. Suppl.* **2007**, 53 (2007).
- [135] Y. Su, K. Nemkovskiy, and S. Demirdiř, DNS: Diffuse scattering neutron time-of-flight spectrometer, *JLSRF* **1**, 27 (2015).
- [136] Q. Huang, P. Karen, V. L. Karen, A. Kjekshus, J. W. Lynn, A. D. Mighell, I. N. Sora, N. Rosov, and A. Santoro, Neutron Powder Diffraction Study of the Nuclear and Magnetic Structures of the Oxygen-Deficient Perovskite YBaCuCoO_5 , *J. Solid State Chem.* **108**, 80 (1994).
- [137] M. Janoschek, P. Fischer, J. Schefer, B. Roessli, V. Pomjakushin, M. Meven, V. Petricek, G. Petrakovskii, and L. Bezmaternikh, Single magnetic chirality in the magnetoelectric $\text{NdFe}_3(^{11}\text{BO}_3)_4$, *Phys. Rev. B* **81**, 094429 (2010).
- [138] R. Georgii, T. Weber, G. Brandl, M. Skoulatos, M. Janoschek, S. Mühlbauer, C. Pfeleiderer, and P. Böni, The multi-purpose three-axis spectrometer (TAS) MIRA at FRM II, *Nucl. Instrum. Methods Phys. Res. A* **881**, 60 (2018).
- [139] L. Landau, The Theory of Phase Transitions, *Nature* **138**, 840 (1936).
- [140] L. C. Chapon, P. Manuel, P. G. Radaelli, C. Benson, L. Perrott, S. Ansell, N. J. Rhodes, D. Raspino, D. Duxbury, E. Spill, and J. Norris, Wish: The New Powder and Single Crystal Magnetic Diffractometer on the Second Target Station, *Neutron News* **22**, 22 (2011).
- [141] O. Arnold, J. C. Bilheux, J. M. Borreguero, A. Buts, S. I. Campbell, L. Chapon, M. Doucet, N. Draper, R. Ferraz Leal, M. A. Gigg, V. E. Lynch, A. Markvardsen, D. J. Mikkelson, R. L. Mikkelson, R. Miller, K. Palmen, P. Parker, G. Passos, T. G. Perring, P. F. Peterson, S. Ren, M. A. Reuter, A. T. Savici, J. W. Taylor, R. J. Taylor, R. Tolchenov, W. Zhou, and J. Zikovsky, Mantid—Data analysis and visualization package for neutron scattering and μ SR experiments, *Nucl. Instrum. Methods Phys. Res. A* **764**, 156 (2014).

- [142] P. Bak and B. Lebech, "Triple- q " Modulated Magnetic Structure and Critical Behavior of Neodymium, *Phys. Rev. Lett.* **40**, 800 (1978).
- [143] E. Fawcett, Spin-density-wave antiferromagnetism in chromium, *Rev. Mod. Phys.* **60**, 209 (1988).
- [144] P. A. Lee, N. Nagaosa, and X.-G. Wen, Doping a Mott insulator: Physics of high-temperature superconductivity, *Rev. Mod. Phys.* **78**, 17 (2006).
- [145] N. Nagaosa, J. Sinova, S. Onoda, A. MacDonald, and N. Ong, Anomalous Hall effect, *Rev. Mod. Phys.* **82**, 1539 (2010).
- [146] A. P. Ramirez, Strongly Geometrically Frustrated Magnets, *Annu. Rev. Mater. Sci.* **24**, 453 (1994).
- [147] H. Kawamura and S. Miyashita, Phase Transition of the Two-Dimensional Heisenberg Antiferromagnet on the Triangular Lattice, *J. Phys. Soc. Jpn.* **53**, 4138 (1984).
- [148] M. Becker, M. Hermanns, B. Bauer, M. Garst, and S. Trebst, Spin-orbit physics of $j = \frac{1}{2}$ Mott insulators on the triangular lattice, *Phys. Rev. B* **91**, 155135 (2015).
- [149] D. J. Thouless, *Topological Quantum Numbers in Nonrelativistic Physics* (World Scientific, 1998).
- [150] A. Altland and B. D. Simons, *Condensed matter field theory* (Cambridge University Press, 2010).
- [151] S. Mühlbauer, G. Brandl, M. Månsson, and M. Garst, Formation of incommensurate long-range magnetic order in the Dzyaloshinskii-Moriya antiferromagnet $\text{Ba}_2\text{CuGe}_2\text{O}_7$ studied by neutron diffraction, *Phys. Rev. B* **96**, 134409 (2017).
- [152] N. D. Mermin, The topological theory of defects in ordered media, *Rev. Mod. Phys.* **51**, 591 (1979).
- [153] N. D. Mermin, The homotopy groups of condensed matter physics, *J. Math. Phys.* **19**, 1457 (1978).
- [154] A. Hatcher, *Algebraic topology* (Cambridge University Press, 2002).
- [155] T. H. R. Skyrme, A unified field theory of mesons and baryons, *Nucl. Phys.* **31**, 556 (1962).
- [156] T. H. R. Skyrme and B. F. J. Schonland, A non-linear field theory, *Proc. R. Soc. Lond. A* **260**, 127 (1961).

- [157] T. H. R. Skyrme and W. G. Penney, Particle states of a quantized meson field, *Proc. R. Soc. Lond. A* **262**, 237 (1961).
- [158] L. E. J. Brouwer, Über Abbildung von Mannigfaltigkeiten, *Math. Ann.* **71**, 97 (1911).
- [159] H. Hopf, Über die Abbildungen der dreidimensionalen Sphäre auf die Kugelfläche, *Math. Ann.* **104**, 637 (1931).
- [160] P. J. Ackerman and I. I. Smalyukh, Static three-dimensional topological solitons in fluid chiral ferromagnets and colloids, *Nat. Mater.* **16**, 426 (2017).
- [161] H. A. Kramers, General theory of paramagnetic rotation in crystals, *Proc. Amsterdam Acad.* **33**, 959 (1930).
- [162] C. Herring, *Magnetism: a treatise on modern theory and materials*, edited by G. T. Rado and H. Suhl, Vol. IV (Academic Press, 1966).
- [163] H. Chen, Q. Niu, and A. MacDonald, Anomalous Hall Effect Arising from Non-collinear Antiferromagnetism, *Phys. Rev. Lett.* **112**, 017205 (2014).
- [164] F. D. M. Haldane, Berry Curvature on the Fermi Surface: Anomalous Hall Effect as a Topological Fermi-Liquid Property, *Phys. Rev. Lett.* **93**, 206602 (2004).
- [165] H. Chen, T.-C. Wang, D. Xiao, G.-Y. Guo, Q. Niu, and A. H. MacDonald, Manipulating Anomalous Hall Antiferromagnets with Magnetic Fields, [arXiv:1802.03044](https://arxiv.org/abs/1802.03044) [cond-mat] (2018).
- [166] R. Aldrovandi and J. G. Pereira, *An Introduction to Geometrical Physics* (World Scientific, 1995).
- [167] C. Castelnovo, R. Moessner, and S. L. Sondhi, Magnetic monopoles in spin ice, *Nature* **451**, 42 (2008).
- [168] L. D. C. Jaubert and P. C. W. Holdsworth, Signature of magnetic monopole and Dirac string dynamics in spin ice, *Nat. Phys.* **5**, 258 (2009).
- [169] N. Kanazawa, Y. Nii, X. X. Zhang, A. S. Mishchenko, G. De Filippis, F. Kagawa, Y. Iwasa, N. Nagaosa, and Y. Tokura, Critical phenomena of emergent magnetic monopoles in a chiral magnet, *Nat. Commun.* **7**, 11622 (2016).
- [170] B. Binz and A. Vishwanath, Chirality induced anomalous-Hall effect in helical spin crystals, *Physica B* **403**, 1336 (2008).

- [171] G. H. Derrick, Comments on Nonlinear Wave Equations as Models for Elementary Particles, *J. Math. Phys.* **5**, 1252 (1964).
- [172] R. H. Hobart, On the Instability of a Class of Unitary Field Models, *Proc. Phys. Soc.* **82**, 201 (1963).
- [173] R. A. Battye and P. M. Sutcliffe, Knots as Stable Soliton Solutions in a Three-Dimensional Classical Field Theory, *Phys. Rev. Lett.* **81**, 4798 (1998).
- [174] P. J. Ackerman and I. I. Smalyukh, Diversity of Knot Solitons in Liquid Crystals Manifested by Linking of Preimages in Torons and Hopfions, *Phys. Rev. X* **7**, 011006 (2017).
- [175] M. Kobayashi and M. Nitta, Torus knots as Hopfions, *Phys. Lett. B* **728**, 314 (2014).
- [176] E. A. Kuznetsov and V. P. Ruban, Collapse of vortex lines in hydrodynamics, *J. Exp. Theor. Phys.* **91**, 775 (2000).
- [177] W. T. M. Irvine and D. Bouwmeester, Linked and knotted beams of light, *Nat. Phys.* **4**, 716 (2008).
- [178] H. Kedia, I. Bialynicki-Birula, D. Peralta-Salas, and W. T. M. Irvine, Tying Knots in Light Fields, *Phys. Rev. Lett.* **111**, 150404 (2013).
- [179] D. Proment, M. Onorato, and C. F. Barenghi, Vortex knots in a Bose-Einstein condensate, *Phys. Rev. E* **85**, 036306 (2012).
- [180] J. Jäykkä and J. Hietarinta, Unwinding in Hopfion vortex bunches, *Phys. Rev. D* **79**, 125027 (2009).
- [181] K. Königsberger, *Analysis 2* (Springer-Verlag, 2013).
- [182] J.-S. B. Tai, P. J. Ackerman, and I. I. Smalyukh, Topological transformations of Hopf solitons in chiral ferromagnets and liquid crystals, *PNAS* , 201716887 (2018).
- [183] E. H. Hall, On a New Action of the Magnet on Electric Currents, *Am. J. Math.* **2**, 287 (1879).
- [184] E. H. Hall, On the possibility of transverse currents in ferromagnets, *Philos. Mag.* **12**, 157 (1881).
- [185] E. M. Pugh and T. W. Lippert, Hall e.m.f. and Intensity of Magnetization, *Phys. Rev.* **42**, 709 (1932).

- [186] K. Ohgushi, S. Murakami, and N. Nagaosa, Spin anisotropy and quantum Hall effect in the *kagomé* lattice: Chiral spin state based on a ferromagnet, *Phys. Rev. B* **62**, R6065 (2000).
- [187] Y. Taguchi, Y. Oohara, H. Yoshizawa, N. Nagaosa, and Y. Tokura, Spin Chirality, Berry Phase, and Anomalous Hall Effect in a Frustrated Ferromagnet, *Science* **291**, 2573 (2001).
- [188] S. Nakatsuji, N. Kiyohara, and T. Higo, Large anomalous Hall effect in a non-collinear antiferromagnet at room temperature, *Nature* **527**, 212 (2015).
- [189] A. K. Nayak, J. E. Fischer, Y. Sun, B. Yan, J. Karel, A. C. Komarek, C. Shekhar, N. Kumar, W. Schnelle, J. Kübler, C. Felser, and S. Parkin, Large anomalous Hall effect driven by a nonvanishing Berry curvature in the noncolinear antiferromagnet Mn_3Ge , *Sci. Adv.* **2**, e1501870 (2016).
- [190] R. Shindou and N. Nagaosa, Orbital Ferromagnetism and Anomalous Hall Effect in Antiferromagnets on the Distorted fcc Lattice, *Phys. Rev. Lett.* **87**, 116801 (2001).
- [191] J. J. Rhyne, Anomalous Hall Effect in Single-Crystal Dysprosium, *Phys. Rev.* **172**, 523 (1968).
- [192] P. Anderson and H. Hasegawa, Considerations on Double Exchange, *Phys. Rev.* **100**, 675 (1955).
- [193] M. Onoda, G. Tatara, and N. Nagaosa, Anomalous Hall Effect and Skyrmion Number in Real and Momentum Spaces, *J. Phys. Soc. Jpn.* **73**, 2624 (2004).
- [194] S. Hayami, T. Misawa, Y. Yamaji, and Y. Motome, Three-dimensional Dirac electrons on a cubic lattice with noncoplanar multiple- Q order, *Phys. Rev. B* **89**, 085124 (2014).
- [195] M. Kohmoto, Topological invariant and the quantization of the Hall conductance, *Ann. Phys. (N. Y.)* **160**, 343 (1985).
- [196] T. Thonhauser, D. Ceresoli, D. Vanderbilt, and R. Resta, Orbital Magnetization in Periodic Insulators, *Phys. Rev. Lett.* **95**, 137205 (2005).
- [197] D. Xiao, J. Shi, and Q. Niu, Berry Phase Correction to Electron Density of States in Solids, *Phys. Rev. Lett.* **95**, 137204 (2005).
- [198] J. Shi, G. Vignale, D. Xiao, and Q. Niu, Quantum Theory of Orbital Magnetization and Its Generalization to Interacting Systems, *Phys. Rev. Lett.* **99**, 197202 (2007).

- [199] P. Morin, D. Schmitt, and C. Vettier, Magnetic excitations in TmCu, *J. Magn. Magn. Mater.* **40**, 287 (1984).
- [200] H. Lin, M. F. Collins, T. M. Holden, and W. Wei, Magnetic structure of erbium, *Phys. Rev. B* **45**, 12873 (1992).
- [201] J. Bohr, D. Gibbs, J. D. Axe, D. E. Moncton, K. L. D'amico, C. F. Majkrzak, J. Kwo, M. Hong, C. L. Chien, and J. Jensen, Diffraction studies of rare earth metals and superlattices, *Physica B* **159**, 93 (1989).
- [202] N. Bonacic, C. Duvinage, M. Rahn, W. Simeth, H. Hautmann, M. Halder, A. Bauer, and C. Pfleiderer, Specific heat across the complex anisotropic magnetic phase diagram of ErCu, (2019), unpublished.
- [203] P. Morin, J. Pierre, J. Rossat-Mignod, K. Knorr, and W. Drexel, Crystal fields in ErCu, ErAg, and ErZn, *Phys. Rev. B* **9**, 4932 (1974).
- [204] A. Fote, H. Lutz, T. Mihalisin, and J. Crow, Electrical resistance of three low temperature antiferromagnets near their Néel temperatures, *Phys. Lett. A* **33**, 416 (1970).
- [205] E. Boling, J. E. Crow, and T. Mihalisin, Antiferromagnetic Ordering in ErCu: Resistivity and Specific Heat, in *Crystalline Electric Field and Structural Effects in f-electron Systems*, edited by J. E. Crow, R. P. Guertin, and T. Mikalisin (Plenum, New York, 1980) p. 415.
- [206] K. Prokes and F. Yokoachiya, E4: The 2-Axis Diffractometer at BER II, *JLSRF* **3**, 104 (2017).
- [207] D. A. Keen, M. J. Gutmann, and C. C. Wilson, SXD – the single-crystal diffractometer at the ISIS spallation neutron source, *J. Appl. Crystallogr.* **39**, 714 (2006).
- [208] A. Sazonov, M. Meven, G. Roth, R. Georgii, I. Kézsmárki, V. Kocsis, Y. Tokunaga, Y. Taguchi, Y. Tokura, and V. Hutanu, Origin of forbidden reflections in multiferroic Ba₂coge₂o₇ by neutron diffraction: symmetry lowering or Renninger effect? *J. Appl. Crystallogr.* **49**, 556 (2016).
- [209] M. Glazer, G. Burns, and A. N. Glazer, *Space groups for solid state scientists* (Elsevier, 2012).
- [210] W. Legrand, D. Maccariello, F. Ajejas, S. Collin, A. Vecchiola, K. Bouzehouane, N. Reyren, V. Cros, and A. Fert, Room-temperature stabilization of antiferromagnetic skyrmions in synthetic antiferromagnets, *Nat. Mater.* , 1 (2019).

- [211] A. Bogdanov and A. Hubert, The stability of vortex-like structures in uniaxial ferromagnets, *J. Magn. Magn. Mater.* **195**, 182 (1999).
- [212] A. Bogdanov and A. Hubert, Thermodynamically stable magnetic vortex states in magnetic crystals, *J. Magn. Magn. Mater.* **138**, 255 (1994).
- [213] A. N. Bogdanov and D. A. Yablonskii, Thermodynamically stable "vortices" in magnetically ordered crystals. the mixed state of magnets, *J. Exp. Theor. Phys.* **95** (1989).
- [214] H. D. Flack, Chiral and Achiral Crystal Structures, *Helv. Chim.* **86**, 905 (2003).
- [215] N. Kumar, S. K. Dhar, A. Thamizhavel, P. Bonville, and P. Manfrinetti, Magnetic properties of EuPtSi₃ single crystals, *Phys. Rev. B* **81**, 144414 (2010).
- [216] E. Bauer, R. T. Khan, H. Michor, E. Royanian, A. Grytsiv, N. Melnychenko-Koblyuk, P. Rogl, D. Reith, R. Podloucky, E.-W. Scheidt, W. Wolf, and M. Marsman, BaPtSi₃: A noncentrosymmetric BCS-like superconductor, *Phys. Rev. B* **80**, 064504 (2009).
- [217] O. Bednarchuk, A. Gagor, and D. Kaczorowski, Synthesis, crystal structure and physical properties of EuTGe₃ (T=Co, Ni, Rh, Pd, Ir, Pt) single crystals, *J. Alloys Compd.* **622**, 432 (2015).
- [218] A. Maurya, P. Bonville, R. Kulkarni, A. Thamizhavel, and S. K. Dhar, Magnetic properties and complex magnetic phase diagram in non-centrosymmetric EuRhGe₃ and EuIrGe₃ single crystals, *J. Magn. Magn. Mater.* **401**, 823 (2016).
- [219] O. Bednarchuk and D. Kaczorowski, Low-Temperature Physical Properties of Single-Crystalline EuCoGe₃ and EuRhGe₃, *Acta Phys. Pol. A* **127**, 418 (2015).
- [220] D. Kaczorowski, B. Belan, and R. Gladyshevskii, Magnetic and electrical properties of EuPdGe₃, *Solid State Commun.* **152**, 839 (2012).
- [221] M. A. Albedah, K. Al-Qadi, Z. M. Stadnik, and J. Przewoźnik, Antiferromagnetism in EuPdGe₃, *J. Alloys Compd.* **613**, 344 (2014).
- [222] A. Maurya, P. Bonville, A. Thamizhavel, and S. K. Dhar, EuNiGe₃, an anisotropic antiferromagnet, *J. Phys. Condens. Matter* **26**, 216001 (2014).
- [223] N. Kumar, P. K. Das, R. Kulkarni, A. Thamizhavel, S. K. Dhar, and P. Bonville, Antiferromagnetic ordering in EuPtGe₃, *J. Phys. Condens. Matter* **24**, 036005 (2012).

- [224] M. Smidman, A. D. Hillier, D. T. Adroja, M. R. Lees, V. K. Anand, R. P. Singh, R. I. Smith, D. M. Paul, and G. Balakrishnan, Investigations of the superconducting states of noncentrosymmetric LaPdSi₃ and LaPtSi₃, *Phys. Rev. B* **89**, 094509 (2014).
- [225] D. Pan and X. G. Wan, Electronic structure of EuPtSi₃ studied from the first principles calculation, *Physica B* **406**, 1129 (2011).
- [226] L. Passell, O. W. Dietrich, and J. Als-Nielsen, Neutron scattering from the Heisenberg ferromagnets EuO and EuS. I. The exchange interactions, *Phys. Rev. B* **14**, 4897 (1976).
- [227] C. Franz, A. Senyshyn, A. Regnat, C. Duvinage, R. Schönmann, A. Bauer, Y. Prots, L. Akselrud, V. Hlukhyy, V. Baran, and C. Pfleiderer, Single crystal growth of CeTAl₃ (T = Cu, Ag, Au, Pd and Pt), *J. Alloys Compd.* **688**, 978 (2016).
- [228] S. Paschen, E. Felder, and H. Ott, Transport and thermodynamic properties of CeAuAl₃, *Eur. Phys. J. B* **2**, 169 (1998).
- [229] S. V. Grigoriev, N. M. Potapova, S.-A. Siegfried, V. A. Dyadkin, E. V. Moskvina, V. Dmitriev, D. Menzel, C. D. Dewhurst, D. Chernyshov, R. A. Sadykov, L. N. Fomicheva, and A. V. Tsvyashchenko, Chiral Properties of Structure and Magnetism in Mn_{1-x}Fe_xGe Compounds: When the Left and the Right are Fighting, Who Wins? *Phys. Rev. Lett.* **110**, 207201 (2013).
- [230] B. Göbel, A. Mook, J. Henk, and I. Mertig, Antiferromagnetic skyrmion crystals: Generation, topological Hall, and topological spin Hall effect, *Phys. Rev. B* **96**, 060406 (2017).

Publications

1. **Non-local order in Mott insulators, duality and Wilson loops**
SP Rath, W Simeth, M Endres, W Zwerger
[Annals of Physics **334**, 256–271 \(2013\)](#)
2. **Observation of two independent skyrmion phases in a chiral magnetic material**
A Chacon, L Heinen, M Halder, A Bauer, W Simeth, S Mühlbauer, H Berger, M Garst, A Rosch, C Pfleiderer
[Nature Physics **14**, 936-941 \(2018\)](#)
3. **Thermodynamic evidence of a second skyrmion lattice phase and tilted conical phase in Cu_2OSeO_3**
M Halder, A Chacon, A Bauer, W Simeth, S Mühlbauer, H Berger, L Heinen, M Garst, A Rosch, C Pfleiderer
[Physical Review B **98**, 144429 \(2018\)](#)

Acknowledgments

An dieser Stelle möchte mich bei all den lieben Personen bedanken, die zu dieser Arbeit beigetragen haben und die mich unterstützt haben. Insbesondere möchte ich danken:

- Allen voran meinem Doktorvater Christian Pfeiderer. Vielen, vielen Dank! Du warst ein super Betreuer, der mich unterstützend durch die letzten Jahre geführt hat. Danke, dass Du stets für alle Ideen offen warst!
- Peter Böni, für Deine Expertise in der Neutronenstreuung. Ebenso danke ich Dir für die angenehme lehrstuhlübergreifende Zusammenarbeit.
- Besonderer Dank gilt den Wissenschaftlern, dem technischen Personal und den Mitarbeitern, die die Neutronenstreuxperimente möglich gemacht haben: Robert Georgii, Matthias Gutmann, André Heinemann, Vladimir Hutanu, Uwe Keiderling, Andreas Mantwill, Martin Meven, Sebastian Mühlbauer, Kirill Nemkovski, Bachir Ouladdiaf, Manuel Pascal, Björn Pedersen, Karel Prokes, Navid Quereshi, Tobias Schrader, Reinhard Schwikowski, Anatoliy Senyshyn, Markos Skoulatos, Tobias Weber, Andreas Wilhelm und Fabiano Yokaichiya.
- Susanne Mayr und Katarzyna Danielewicz für oftmals kurzfristige Arbeiten im Kristalllabor.
- Vaclav Petricek, der mich beim Verfeinern magnetischer Strukturen intensiv beraten hat.
- Marein Rahn, Andi Bauer und Michi Wagner. Ohne euch wären die Projekte meiner Arbeit nicht möglich gewesen.
- Besonderer Dank gilt allen Kollegen in Garching, hauptsächlich an E21 und E51, ohne die die letzten Jahre langweilig gewesen wären: Tim Adams, Aisha Aqeel, Andi Bauer, Georg Benka, Grace Causer, Alfonso Chacon, Christopher Duvinage, Chris Franz, Stefan Giemsa, Marco Halder, Franz Haslbeck, Johanna Jochum, Pau Jorba, Jonas Kindervater, Markus Kleinhans, Martina Meven, Martina Michel, Christoph Morkel, Astrid Mühlberg, Alex Regnat, Robert Ritz, Felix Rucker, Jan Sahliger, Steffen Säubert, Schorsch Sauther, Christoph Schnarr, Astrid Schneidewind, Thorsten Schröder, Marc Seifert, Lisa Seitz, Olaf Soltwedel, Jan Spallek,

Michael Wagner, Andreas Wendl, Birgit Wiedemann, Marc Wilde und allen Studenten, die bei uns am Lehrstuhl arbeiten oder gearbeitet haben.

- Felix und Steffen für unsere vielen außercurricularen Treffen.
- All meinen Freunden.
- Meiner Verwandtschaft, die mich besonders auf meinem Weg geprägt hat: Lina Simeth, Edeltraud Auburger, Eduart Schleinkofer, Margit Schleinkofer, Inge Birn, Josef Schleinkofer, Rolf Birn, Tobias Birn, Elfriede Schleinkofer, Lenz Auburger, Sonja Auburger, Florian Auburger und Betty Auburger.
- Meinem Bruder Stephan Simeth.
- Meinen Eltern Anna Elisabeth und Manfred Simeth. Danke dafür, dass Ihr hinter mir gestanden seid.
- Meiner Freundin Andrea. Danke, dass Du mich die gesamte Zeit über uneingeschränkt unterstützt hast. Ich freue mich auf die gemeinsame Zeit mit unserer Tochter Hannah Elisabeth.